UNIVERSITY OF COPENHAGEN

PhD in Biophysics

Reconstitution of viral budding

A study on phase separation and spontaneous curvature in plasma membranes

Victoria Thusgaard Ruhoff

The Niels Bohr Institute

Supervisor: Poul Martin Bendix
Co-supervisor: Guillermo Moreno-Pescador

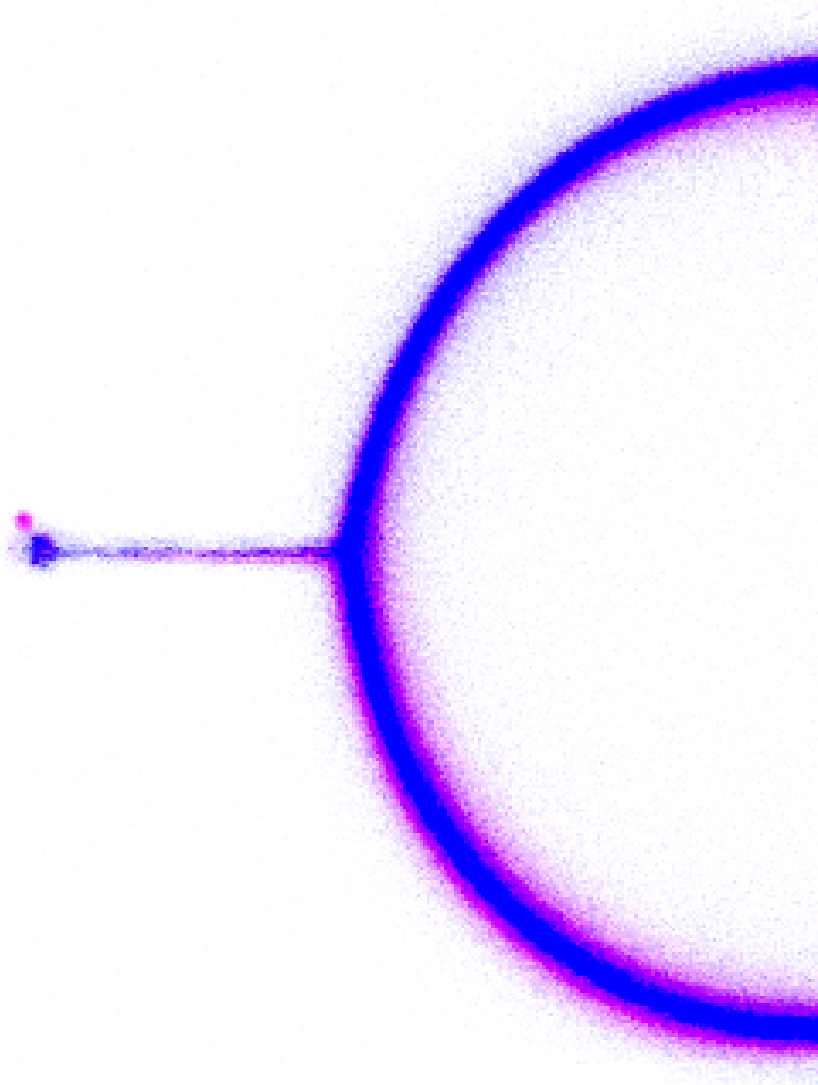

This thesis has been submitted to the PhD School of The Faculty of Science, University of Copenhagen

November 30th 2024

"I am among those who think that science has great beauty."

- Maria Salomea Skłodowska-Curie

"I would rather have questions that can't be answered than answers that can't be questioned."

- Richard Phillips Feynman

Acknowledgements

Reaching the end of this PhD journey feels both surreal and deeply satisfying. Along the way, I've been fortunate to have the support, guidance, and encouragement of many incredible people, without whom this experience would not have been the same.

First, I want to thank my supervisor, Poul Martin Bendix for giving me free reins to explore my research interests, while always being available to provide guidance and constructive feedback when I needed it. Your trust in my independence has been a cornerstone of this work, and I am incredibly grateful for your mentorship, wisdom, and ability to keep a straight face during my more creative proposals throughout this PhD journey.

I want to thank my co-supervisor Guillermo Moreno-Pescador for extensive feedback regarding experimental design and ideation throughout this entire journey. In addition, a thanks to Mohammad Reza Arastoo and Younes Farhangibarooji for invaluable training in the lab and great fun at the office! Thanks to our lab manger Marianne Lund Jensen, who was always happy to assist and kept the lab running smoothly. A special thanks to Luis Hamel Ascanio whom I supervised during his time as a master student and research assistant in the lab, during which he contributed significantly to parts of the research presented in this thesis. Your incredible dedication and countless hours spent tackling challenging experiments was admirable. Guiding you was a rewarding experience —and an excellent exercise in answering questions I didn't even know I had never asked.

In addition I want to extend my thanks to my collaborators Robert Daniels, Salvatore Chiantia, Weria Pezeshkian, Natascha Leijnse, Amin Doostmohammadi and Tommas Nielsen for their valuable scientific contributions to manuscripts and experimental designs during my time at NBI. In addition, I want to thank Raya Sorkin for hosting me for 2 weeks and allowing me to exchange experimental techniques with the scientists working in her lab.

I want extend my gratitude to Neha Kamat and all the people in the Kamat Lab at Northwestern University. Thank you for inspiring and challenging me academically, and always being available to answer my questions —I learned so much from all of you. Thank you for welcoming me with open arms into your community (and for attending my numerous "creative" lab outing events) and for broadening my scientific expertise and toolkit. It was a pleasure spending 5 months at your lab!

To Bente Markussen, thank you for being the best academic officer one could wish for! Without your countless administrative advice, daily positivity, timely minion memes, and magical ability to navigate organizational black holes, I would have been reduced to a pile of bureaucratic despair long ago. Thank you for brightening our days and being the source of social energy at Biocomplexity.

To my colleagues in all of Biocomplexity, thank you. Whether it was troubleshooting experiments, planning Christmas parties, playing board games or just collectively complaining over approaching deadlines, your company and input was always valued. Especially thanks to Mireia, for your unwavering encouragement over the past three years —through the highs, the lows, and the "I'm just going to scream into a centrifuge" moments. I deeply admire your scientific mind and generosity, and the way you lift up everyone around you. Biocomplexity (and the lab supplies stock) would not have been the same without you. To the Kinder Egg Club, you have my thanks for the steady stream of adorable tiny animals that brightened my desk. Also a shout-out to the Badminton Club, for helping me forget about science and just have fun!

To my family, thank you for your unending support and for pretending to understand what my research was about. To my loving parents, thank you for countless meals and pep talks during the final weeks.

To my partner, Justus, thank you for believing in me even when I doubted myself. Your unlimited patience and support, even when I was keeping you up in the middle of the night, made the last tough stretch possible. I couldn't have wished for a better partner for science and shenanigans.

A massive shout-out to my friends who stuck by me through this academic marathon. Thank you for listening to my rants, even when I spiraled into obscure academic jargon. And for those who checked in with variations of "So, is it done yet?" —I know it was out of love.

Completing this thesis is a milestone I will always be proud of. I hope you enjoy it!

Abstract

Every year, influenza cause global outbreaks and substantial research has been carried out to understand this infectious disease and develop effective treatments and prevention strategies. On a molecular level, the cell-to-cell transmission of influenza virus is critically dependent on formation of spherical and cylindrical protrusions from the cell surface. The degree of membrane bending observed in these progeny virion structures requires generation of significant forces, the origin of which are an active area of research. Influenza viruses bud from infected cells just after gathering a number of spike-proteins in a nanoscale budding region followed by outward bulging of the membrane. It has been suggested that this process could be driven or enhanced by crowding of spike proteins which are present at the budding region during initiation of the bud. The bulky spike proteins may collide stochastically (crowd) to create a lateral entropic pressure capable of inducing membrane bending, however the proteins must be highly concentrated to provide sufficient lateral crowding to generate such curvature. A long-standing hypothesis in the field is that membrane nanodomains are responsible for this protein clustering.

In this thesis, it was investigated whether membrane nanodomains can efficiently relocated and cluster virus proteins in a novel model system which allows generic testing of the membrane phase affinity of any membrane protein. It was found that all tested virus proteins exhibited strong phase affinity, but surprisingly for more fluid domains rather than for liquid ordered domains, which stands in contrast to previously observed behavior. The ability of virus proteins to generate membrane bending in cells and membrane vesicles was further assessed by development of a second novel assay which can directly measure the spontaneous curvature of a membrane containing integral membrane proteins. By measuring the potential of a membrane to bend inward versus outwards it is possible to directly measure the spontaneous curvature of a cell membrane and future work will reveal the effect of viral proteins on the tendency of a membrane to bend. Overall, it can be concluded that virus spike proteins are still likely candidates in assisting or even driving the budding process of progeny viruses and therefore a deeper understanding of how these proteins interact with membranes is of critical importance for understanding how viruses disseminate in our body.

Resumé

Hvert år forårsager influenza globale epidemier, og betydelig forskning er blevet udarbejdet i et forsøg på at forstå denne infektionssygdom og udvikle effektive behandlinger og forebyggelsesstrategier. På molekylært niveau er overførslen af influenzavirus imellem celler kritisk afhængig af dannelsen af sfæriske og cylindriske fremspring fra celleoverfladen. Den grad af membranbøjning, der observeres i disse virus strukturer, kræver generering af betydelige kræfter, hvis oprindelse aktivt debatteres inden for feltet. Influenzavirus knopskyder fra inficerede celler umiddelbart efter samling af de indlejrede virus proteiner i nanoskopiske membranregioner hvorfra membranen begynder at bule ud. Det er blevet foreslået, at denne proces er drevet eller forstærket af trængsel mellem spike-proteiner, som er til stede i knopskydningsregionen under initieringen af den nye virus partikel. De voluminøse spike-proteiner kan kollidere stokastisk (forårsage trængsel) og skabe et lateralt entropisk tryk, der kan fremkalde membranbøjning, men proteinerne skal være meget koncentrerede for at skabe tilstrækkeligt tryk til at generere en sådan krumning. En mangeårig hypotese på området er, at membranens nanodomæner er ansvarlige for denne proteinklynge.

I denne afhandling blev det undersøgt, om membran-nanodomæner effektivt kan flytte og gruppere virusproteiner ved brug af et nyt modelsystem, der tillader generel efterprøvning af membranproteiners affinitet for forskellige membranfaser. Det blev vist, at alle de heri testede virusproteiner udviste stærk faseaffinitet, men overraskende nok for mere flydende faser snarere end flydende-ordnet faser, hvilket står i kontrast til tidligere observeret adfærd. Virusproteinernes evne til at generere membranbøjning i celler og membranvesikler blev yderligere vurderet ved at udvikle en teknik, som kan måle den spontane krumning af en membran, der indeholder indlejrede membranproteiner. Ved at måle en membrans potentiale til at bøje indad i forhold til udad er det muligt direkte at måle den spontane krumning af en cellemembran, og fremtidigt arbejde vil afsløre virale proteiners effekt på en membrans tendens til at bøje. Samlet set kan det konkluderes, at virus spike-proteiner stadig er sandsynlige kandidater til at forstærke eller endda drive knopskydningen af nye virus partikler. Derfor er en dybere forståelse af, hvordan disse proteiner interagerer med membraner, af afgørende betydning for at forstå, hvordan vira spredes i kroppen.

List of Publications

1. Victoria Thusgaard Ruhoff, Guillermo Moreno-Pescador, Weria Pezeshkian, and Poul Martin Bendix. Strength in numbers: effect of protein crowding on the shape of cell membranes. *Biochemical Society Transactions*, 50(5):1257–1267, 2022.

2. Guillermo Moreno-Pescador, Mohammad Reza Arastoo, Victoria Thusgaard Ruhoff, Salvatore Chiantia, Robert Daniels, and Poul Martin Bendix. Thermoplasmonic vesicle fusion reveals membrane phase segregation of influenza spike proteins. *Nano Letters*, 23(8):3377–3384, 2023

3. Victoria Thusgaard Ruhoff, Poul Martin Bendix, and Weria Pezeshkian. Close, but not too close: a mesoscopic description of (a) symmetry and membrane shaping mechanisms. *Emerging Topics in Life Sciences*, 7(1):81-93, 2023.

4. Victoria Thusgaard Ruhoff, Mohammad Reza Arastoo, Guillermo Moreno-Pescador, and Poul Martin Bendix. Biological Applications of Thermoplasmonics. *Nano Letters*, 24(3):777-789, 2024

5. Victoria Thusgaard Ruhoff, Natascha Leijnse, Amin Doostmohammadi, and Poul Martin Bendix. Filopodia: integrating cellular functions with theoretical models. *Trends in Cell Biology*, 2024.

Table of contents

List of figures

Nomenclature

Acronyms / Abbreviations

λ	Wavelength
3D	Three-dimensional
AuNP	Gold nanoparticle
AuNS	Gold nano shell
Brain SM	Brain sphingomyelin
CoV-S	SARS-CoV-2 spike protein
CTxB	Cholera Toxin B
DiD	Vybrant DiD cell-labeling solution
DiO	Vybrant DiO cell-labeling solution
DOPC	1,2-dioleoyl-sn-glycero-3-phosphocholine
DTT	Dithiothreitol (reagent inducing blebbing in cells)
ENTH	Epsin N-terminal homology
GFP	Green fluorescent protein
GPI	Glycosylphosphatidylinositol lipid anchor
GPMV	Giant plasma membrane vesicle
GUV	Giant unilamellar vesicle
H-C	Helfrich-Canham

HA	Hemagglutinin spike protein from Influenza A virus
HA-TMD	Hemagglutinin transmembrane domain
HEK293T	Human embryonic kidney cells
HPβCD	Hydroxypropyl-β-cyclodextrin
I1061T	HeLa NPC1-I1061T mutant
IAV	Influenza A virus
K_B	Boltzmann constant
KO	NPC1 knock-out
L_d	Liquid disordered
L_o	Liquid ordered
MβCD	Methyl-β-cyclodextrin
M1	Matrix protein 1 from Influenza A virus
M2	Matrix protein 2 from Influenza A virus
MDCK	Madin-Darby canine kidney cell
mRNA	Messenger ribonucleic acid
NA	Neruaminidase spike protein from Influenza A virus
NA	Numerical aperture
NA-42	Neruaminidase mutated protein that forms a dimer void of the neuraminidase 'crown'
NA-62	Neuraminidase mutated protein forming tetramers without the large spike 'crown'
NA-FL	Neruaminidase full length protein
NEM	N-Ethylmaleimide (reagent inducing blebbing in cells)
NIR	Near-infrared

NP	Nucleoprotein
NPC1	Niemann-Pick type C1
NPs	Nanoparticles
PA	Polymerase acidic protein
PB1	Polymerase basic 1 protein
PB2	Polymerase basic 2 protein
PE lipid	Phosphatidylethanolamine lipid
PFA	Paraformaldehyde
PM	Plasma membrane
RNA	Ribonucleic acid
SD	Standard deviation
T	Temperature
Tm	Miscibility temperature
VLP	Virus like particle
vRNP	Viral ribonucleaoprotein
WT	Wild type

Chapter 1

Motivation and thesis overview

The plasma membrane functions as a protective barrier for living cells, and is the site of a plethora of essential cellular functions. It consists of an approximately 5 nm thick lipid bilayer that is embedded with numerous integral membrane proteins, working together in complex dynamics to perform essential cellular tasks, many of which require membrane shape deformations. Such deformations include spherical and cylindrical protrusions from the membrane surface, which are critical shapes involved in the dissemination of diseases such as influenza A virus (IAV) infection.

To form progeny virions from infected cells, influenza proteins must co-localize at certain 'budzones' from which the new spherical virion protrusion is initiated. To bend the plasma to such a degree, however, requires forces that are strong enough to break the energy barrier for membrane bending. The mechanism behind the lateral organization of membrane proteins, as well as the origin of the membrane bending forces, are active research areas, both of which were investigated in this thesis in relation to the budding process of IAV.

First, the relevant biological background is covered, highlighting the theory behind membrane shaping mechanisms investigated in this work. Then current literature describing the IAV virion and proteins are presented, with emphasis on the current hypotheses on how viral budding occurs and which proteins are thought to be involved. Finally, the motivation for investigating the lateral organization of viral proteins at the budding site and their inherent ability to generate enough surface pressure to initiate membrane bending is presented. A paragraph on the motivation for investigating the lateral organization of viral proteins at the budding site and their inherent ability to generate enough surface pressure to initiate membrane bending concludes the background section.

Next, the experimental techniques employed in this thesis to design novel assays are introduced, starting with the choice of model membranes for protein expression, followed by an introduction to optical trapping with an emphasis on how force spectroscopy and thermoplasmonic heating shaped the design of the studies completed. The techniques are subsequently presented in relation to their general relevance in the field of biophysics.

In chapter 4, the first experimental results are presented, investigating the phase affinity of viral proteins in phase-separated hybrid vesicles, to determine lateral organization of the proteins in their native orientation at physiologically relevant conditions. In chapter 5, the second completed study is introduced, quantifying the spontaneous curvature induction of viral proteins crowding on the cell membrane. Both studies are presented with an introduction, results and discussion, and followed by a collective conclusion that synthesizes the obtained results and their relevance to the current knowledge in the field.

Lastly, chapter 7 includes an overview of the research collaborations completed as part of the 'change of scientific environment' requirement of the PhD degree, investigating the biophysical changes of cell membranes in diseased and healthy cells.

Chapter 2

Biological background

In the presented work, the biophysical questions investigated pertain to the organization of proteins on the cell surface of mammalian cells. In the following, I will provide a thorough description of some of the complex biophysical processes taking place on the cell membrane and introduce their suggested roles in viral budding.

The plasma membrane of cells exhibits a fascinating degree of molecular activity and membrane dynamics and our understanding of it has expanding greatly during the last decade. The plasma membrane simultaneously provides a protective barrier and constitutes the interface in which all interactions between a cell and its environment take place. It is composed of a lipid bilayer maintained by hydrophobic and hydrophilic forces, and densely packed with proteins estimated at around 30.000 proteins in each μm^2 on the cell surface[1]. The plasma membrane is thus a very crowded environment, requiring complex orchestration of protein interactions to facilitate their purpose, as organization of proteins together with vast remodeling of the membrane structure is what allows for many cellular events to take place. Without membrane remodeling, allowing for e.g. intra- and extracellular signaling and uptake of nutrients[2,3,4], the basis of cell viability and proliferation is lost. In the following it will be discussed how lateral organization of proteins in the plasma membrane can provide the foundation of essential processes, followed by how a newly discovered mechanism of protein crowding can contribute to membrane remodeling in vivo. The concepts will provide the foundation for investigating influenza budding, an event crucial for the cell to cell spread of this infectious disease.

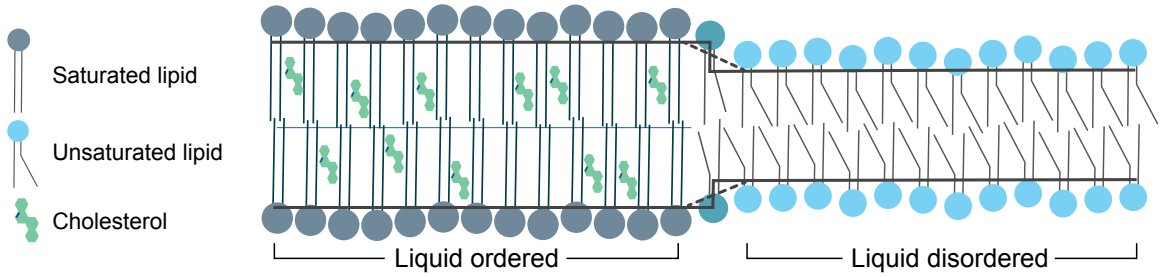

Fig. 2.1 Lipid bilayers can phase separate into liquid ordered and disordered domains. The schematic shows such ordered (gray) and disordered (blue) domains formed by saturated and unsaturated lipids and cholesterol in a lipid bilayer. Line tension (solid line) from the hydrophobic mismatch of the lipid tail regions at the interphase between domains is minimized (dashed line) from deformation of the lipids.

2.1 Lateral organization in cells membranes

Cells are thought to organize the proteins on the plasma membrane to complete various cellular tasks. Protein interactions such as oligomerization and scaffolding provides a degree of organization in the plasma membrane[5,6,7]. The membrane itself has also been proposed to contain organized nanodomains attracting proteins. The various lipids in the bilayer diffusive freely in the lateral direction, however their different packing properties allow for the emergence of ordered lipid phases enriched in sterol- and sphingolipids. These domains are liquid ordered (L_o) in nature, and at the edge of the domain, the change to liquid disorder (L_d) results in line tension due to the mismatch of the hydrophobic region, which is minimized by deformation at the interphase[8] (figure 2.1). These domains where originally termed 'rafts', however it is suggested now that such domains are referred to as transient nanodomains[9] for the sake of consistency in the membrane field. In this thesis, liquid ordered domains are used to refer to these nanodomains, however the word 'raft' is occasionally used in this thesis when discussing literature using this nomenclature.

The formation of transient lipid domains existing in the ordered phase, has long been suggested in literature to serve as platform for protein organization and accumulation[10,11]. The ability of certain proteins to recognize and associate with such domains have thus been rigorously investigated and triggered an interest in the biological relevance of such domains[12]. Experiments carried out with giant unilamellar vesicles (GUVs) or giant plasma membrane vesicles (GPMVs) have identified numerous proteins that show a preference for either the ordered or disordered liquid phase depending on membrane conditions[13,14,15,16,17]. Although these macroscopic L_o domains can be made in model membranes, such domains in cells are difficult to visualize as they are

nanoscopic and transient in nature, thus their in vivo ability to organize proteins is still disputed[11].

2.2 Protein crowding in membrane re-modeling

Disclaimer: This section provides an introduction to the putative membrane bending mechanism, *crowding*. The thoughts presented in this section led to the first author review "Strength in numbers: effect of protein crowding on the shape of cell membranes"[18]. In the following I will highlight a few important points from the paper for the benefit of the reader of this thesis. For further discussion on this topic the reader is referred to the published article (appendix B.2).

The plasma membrane naturally resists bending because the hydrophobic and hydrophilic forces acting on the lipids in the bilayer are generally balanced when the membrane is flat. Beside these inherent forces governing the structure of the membrane, the cytoskeleton of eukaryotic cells also serves to structure and stabilize the membrane[19]. Despite these inherent characteristics, the plasma membrane exhibits numerous shapes and the cell require significant membrane remodeling for essential tasks e.g. intra- and extracellular signaling and uptake of nutrients[2,3,4], where the formation of spherical vesicles from the membrane surface is imperative.

Asymmetric lipid distribution can account for some of the observed curvature generation in membranes, however not nearly the vast amount of membrane bending found at the cell surface[20,21]. Instead protein organization and activity is employed by the cell to generate the curvature needed for cell survival. Exactly how such remodeling is driven by proteins, has been extensively researched, leading to discovery of structurally important protein features for curvature generation[22]. Proteins are often driving curvature by collective contributions, and some of the identified features include intrinsic curvature of membrane binding proteins and scaffolds[23,24] and insertion of wedges such as amphiphatic helices into the bilayer[25,26,27]. Despite a large body of research demonstrating how these structural features govern membrane re-modeling, a recently discovered mechanism of protein-protein crowding, devoid of conserved structural features, have emerged to challenge the prevailing views on the drivers of membrane bending[28,29,30].

This overlooked entropic model describes how the stochastic collisions of proteins can cause sufficient surface pressure to induce membrane bending, if the collective

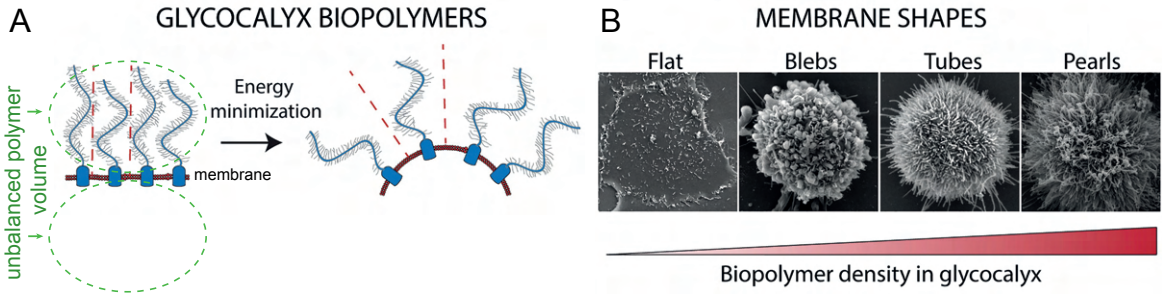

Fig. 2.2 Crowding modulates cell membrane shapes. A) Schematic of the glycocalyx biopolymer on a membrane surface. As the membrane bends, each biopolymer effectively occupies a larger volume, decreasing the pressure from crowding on the surface and in turn minimizing the energy. Green dashed circles highlight the imbalance in protein occupying the area just above and below the membrane. B) SEM images showing morphological changes of the cell surface upon increased density of biopolymers. A) and B) are adapted with permission from [31].

protein volume is not equally distributed on the outer and inner membrane surface (figure 2.2A). Shurer et al. have beautifully demonstrated how such simple protein crowding governs the overall shapes of the cell membrane, by expressing various concentrations of the large biopolymer, glycocalyx, in various concentration on the plasma membrane[31] (figure 2.2B). As the pressure from crowding increases, different predicted structures such as blebs, tubes and pearls appear on the cell surface, in agreement with shape predictions from suggested models[32]. Stochastic protein-protein crowding is thus emerging as a relevant player to describe the physical mechanisms at play on the membrane surface, and has even been theoretically suggested to play a potential role in viral budding due to the large spike proteins[33]. Such suggestions has motivated parts of the research conducted in this thesis.

To understand the impact of protein crowding, the entropic pressure can be modeled using the Carnahan-Starling equations of state, and compared to experimentally observed results[29]. This model describes the ectodomains of membrane bound proteins as non-interactive spheres, colliding stochastically. The pressure generated by these lateral collisions can be described quite well, at protein densities up to 70%[34], by

$$p_{crowding} = \frac{\eta}{a_p}[1 + \frac{2\eta(1 - 0.44\eta)}{(1-\eta)^2}]K_BT \tag{2.1}$$

with η being the fraction of the membrane covered by protein given by $\eta = \frac{N_p a_p}{a_v}$ where N_p is the number of proteins, a_p is the 2D occupied area of the protein on the membrane surface, a_v is the surface area of the membrane[29,34]. The continuously diffusing proteins are confined to the narrow region right above the membrane, and the proteins have a translational entropy in relation to this available volume. When

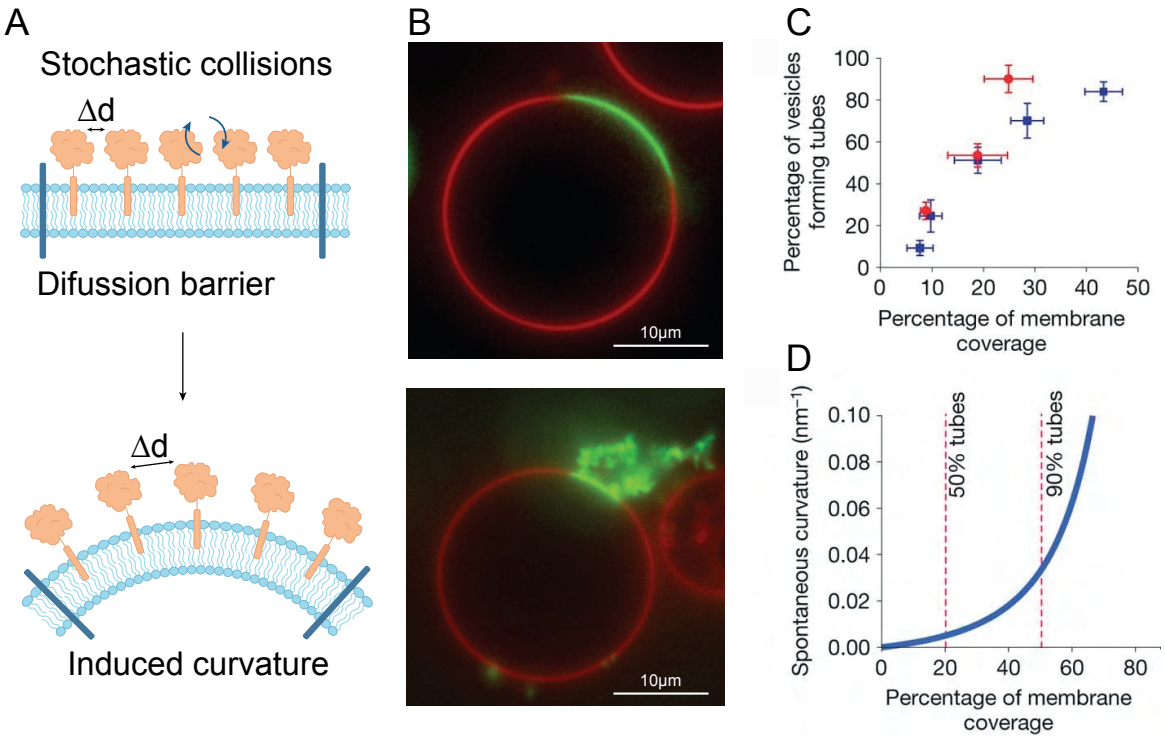

Fig. 2.3 Protein-protein crowding inducing tubule formations in membranes. A) Schematic demonstrating the increase in the distance (d) between proteins crowded on a membrane surface upon bending. Here the proteins are confined by a diffusion barrier, mimicking the lipid domain containing the proteins shown in (B). Original figure reprinted with permission from [18]. B) Wide-field fluorescent micrographs of phase-separated GUVs with a membrane-bound ENTH protein domain (green) in a low (top) and high concentration (bottom), the difference being a 10x increase in protein binding sites in the lipid domain (green due to protein binding). The high protein concentration creates spontaneous membrane curvature in the lipid domain, resulting in the tubules seen protruding from the domain (bottom). C) Data for experiments with an ENTH lacking an amphiphatic helix structure. As the percent membrane coverage increases, the number of vesicles with tubes increase, showing that the protein can induce spontaneous curvature in the bilayer. D) Model prediction of spontaneous curvature from percent membrane coverage, with red dashed lines indicating the experimentally observed tube formation in the vesicle sample at the given coverage. B), C) and D) reprinted with permission from [29].

the membrane bends, the volume of this region increases, effectively increasing the translational entropy and lowering the pressure, as the proteins have more space to move (figure 2.3A). With increasing protein density this energy contribution will eventually out-compete the elastic energy cost associated with membrane bending. This pressure generation and consequent spontaneous curvature have been measured experimentally showing tubulation in GUVs, cargo sorting in cells and morphology changes of cells membranes[29,35,28,31,30,36]. For instance, for a membrane-anchored epsin1 ENTH protein domain lacking an amphiphatic helix (generally thought to be responsible for its curvature inducing capabilities), it was experimentally shown that

increasing the concentration of this protein domain on the surface of GUVs resulted in spontaneous tubule formation on a high fraction of the vesicles, directly correlated with the protein density[29] (figure 2.3B,C). The experimental results correlate with theoretical predictions from the Carnahan-Starling pressure model and provides and estimate of spontaneous curvature of the membrane that agrees with experimentally observe tube formation (figure 2.3D). Interesting to highlight, is that fact that intrinsically disordered protein domains (IDPs) show the most potent crowding effect due to the relative large volume of such unstructured domains[28]. This type of mechanism provides thus provides an explicit use for IDP domains which have previously been thought of as unusual regions of proteins. Such domains have a large crowding effect and could therefore play very important roles in cellular trafficking.

In relation to earlier discussions regarding lateral organization of proteins in membranes (section 2.1), it is important to highlight that due to its inherent nature, the crowding effect is enhanced when proteins are confined by a diffusion barrier[34] (figure 2.4A,B) . As discussed in relation to figure 2.3, by confining proteins in a lipid domain by means of strong phase partitioning, a high pressure can be generated which produces curvature. Even steric confinement of GFP -which has no intrinsic curvature

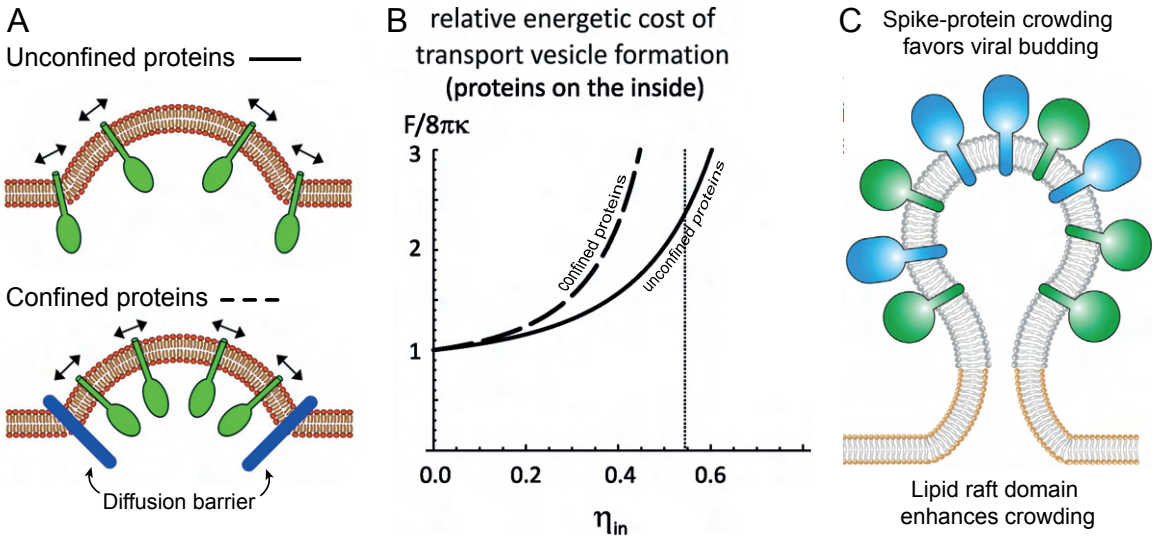

Fig. 2.4 Diffusion barriers enhance crowding. A) Schematic of unconfined and confined proteins crowding on the inside of a membrane protrusion without (top) or with a diffusion barrier (bottom). B) The modeled relative energy cost of this protrusion from (A) during formation of transport vesicles with unconfined (solid line) and confined proteins (dashed line) as a function of the protein density. The energetic cost is plotted on the y-axis in relation to the cost in a pure lipid membrane ($8\pi\kappa$). The vertical dotted line represents the tight packing limit for confined proteins. A) and B) are modified with permission from [34]. C) Schematic of suggested viral budding from raft domains (gray) with spike proteins (green and blue) generating pressure from crowding among the large ectodomains. Reprinted from [18] modified with permission from [33].

capabilities- has been shown to induce curvature[35]. It is thus relevant to consider the possibility of various membrane organization barriers (section 2.1) consisting of cortical actin or lipid separation in nanodomains as means of generating crowding platforms in vivo. Such L_o nanodomains have for instance been suggested to play a role in orchestrating crowding during influenza budding, as the virus is thought to bud from L_o domains in the membrane[33] (figure 2.4C). Still, it is questionable whether lipid domains in the plasma membrane can withstand the pressure, as its has also ben demonstrated that protein-protein crowding can instead oppose phase separation, dissolving the phases by inducing lipid mixing[37]. In addition, if protein accumulation is achieved through attractive protein interactions or oligomerization, then this inherently counteracts the energy generated from free diffusion and stochastic collisions of crowded proteins[38].

In this thesis, both lateral membrane organization and protein-protein crowding effects are investigated in relation to the mechanisms driving the formation of new virion particles allowing for the spread of the infection. In the following a thorough introduction to influenza A and the viral proteins participating in the critical formation step, "budding" is provided, guiding the reader to a final discussions on their involvement in viral budding and the motivation for this thesis.

2.3 Influenza A virus

Influenza virus is a common viral infection in humans and presents with slight genomic variations, classified as type A, B, C, and D. In this thesis, type A is investigated as it is a major contributor to the yearly influenza outbreaks, and is a well characterized system. The nature of the influenza A virus (IAV) replication and infection mechanism has been scrutinized since the isolation of the first virus almost 100 years ago, to elucidate the biological machinery behind these recurring global infections and develop antiviral strategies. Like any viral organism, IAV needs a host to replicate and spread, and cannot survive long-term in the external environment. Viruses have thus, in general, developed ways of hijacking cellular machinery for their replication and are often quite simple in their structure with a small genome. IAV is an enveloped virus, meaning it derives its protective shell from the host. Viruses that use the host cell membrane to derive their particle envelope, are dependent on the successful organization of viral protein in the membrane and subsequently a complex membrane re-modeling process to

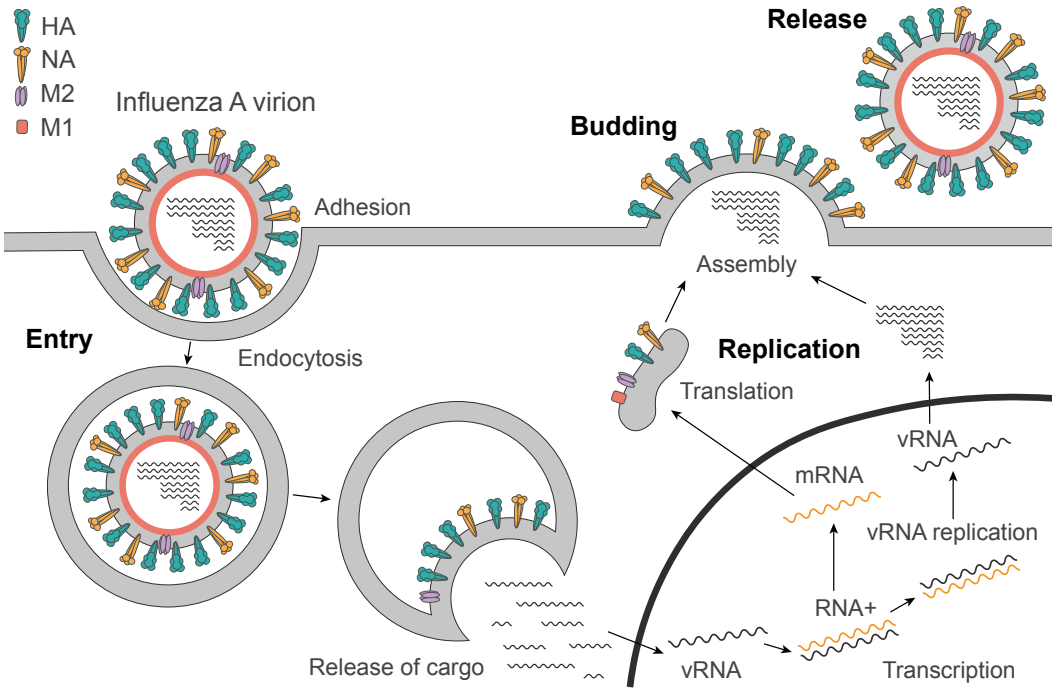

Fig. 2.5 Schematic of the influenza A viral life cycle. The 4 main steps of the life cycle are highlighted in **bold** and further descriptions in gray.

ensure proper budding and release. Indeed, the lack of any safeguards preventing release of incomplete particles, results in the majority of progeny virions being non-infectious in vivo[39]. In certain cell types, viral particles can show defects including slow uptake from impaired fusion or tethering of new virus particles to the cell surface, countering release[40]. The viral life cycle is complex but can be described in simple terms with 4 events: 1) entry 2) replication 3) budding and 4) release (figure 2.5). These events are summarized below based on the thorough review on the IAV life cycle by Dou et al.[41].

Entry:

The virus enters a cell by first binding to receptors in the cell surface. This adhesion is mediated by the spike proteins that decorate the virus, and induces the uptake of the virion via the endocytic pathway, eventually transporting the virus into the endosomes. In the endosomes the pH of the solution changes and mediates the fusion of the viral envelope and endosomal membrane. This fusion releases the genetic material of the virus into the cytosol of the cell.

Replication:

The genetic material release from the endsome, is first transported to the nucleus of the cell. The negative-sense RNA strands, encoding the viral genome, are then are duplicated for incorporation into a new virus. In addition the RNA strands are transcribed into mRNA for the production of the viral proteins. These strands get transported to the cytosol where the ribosomes translate the genetic code and synthesize the viral proteins.

Budding:

In order to initiate budding the viral membrane proteins must be located to the plasma membrane and become laterally organized into a budding zone containing all the viral components. The transmembrane proteins are recruited to the apical membrane of polarized cells and thought to associate with L_o membrane domains. This assembly of the proteins generates curvature, leading to the initiation of membrane budding and growth. The capsid enclosed proteins and genome are transported to the budding site and incorporated into the forming vesicle.

Release:

The progeny virion grows as a spherical bud from the surface and eventually forms a tight neck where membrane scission can occur, separating the virus envelope from the plasma membrane. To release the new virion from the membrane, siliac acid residues that tether the virion to the cell surface are cleaved. The particle thus pinches off from the host and circulates to infect a new cell.

In this thesis, the biophysical dynamics of the membrane processes involved in the budding event is scrutinized, thus the role of budding and its effect on the viral particles is expanded upon throughout this background section.

2.3.1 Structure and function of the virion

The virion consists of a protective shell encapsulating 8 helical viral ribonucleaoprotein (vRNP) complexes that encode the entire viral genome, consisting of 11 genes. Each vRNP is composed of a single strand of viral RNA wrapped around several copies of the viral nucleoprotein (NP) in a helical structure. Bound to one end of each vRNP, is a single copy of the heteromeric polymerase complex consisting of PB1, PB2 and PA[41]

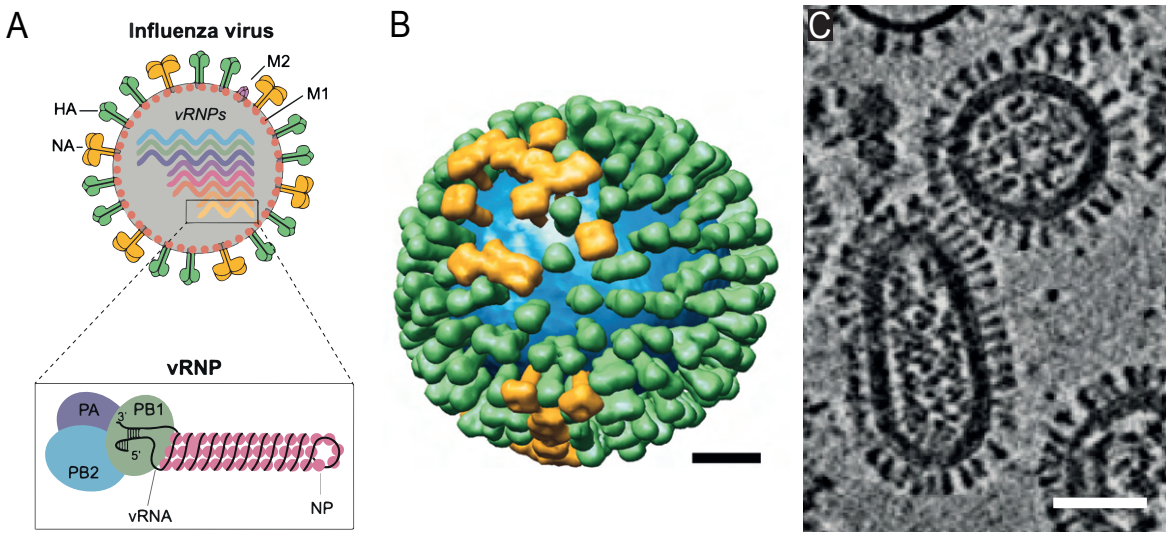

Fig. 2.6 A) Schematic structure of the virion, showing NA, HA and M2 decorating the envelope and M1 supporting the bilayer. Encapsulated are the 8 viral ribonucleaproteins (vRNP) and an insert shows the structure of the vRNP where the genetic material is wrapped around several NPs, with a heterotrimeric RNA polymerase complex attached at the end. Adapted with permission from [41]. B) Model of an influenza virion showing the distribution of spike proteins HA (green) and NA (yellow) on the membrane surface (blue). (Scale bar is 20 nm). Reprinted with permission from [42]. C) Central slice of a tomogram showing a spherical (top) and elongated (bottom) influenza A virus structure. (Scale bar is 50 nm). Reprinted with permission from [43].

(figure 2.6A). The virion shell is a host-derived lipid membrane, called the envelope, which is formed when the virion buds off from the surface of the host cell, using the host plasma membrane to encapsulate the viral components. This protective membrane barrier is covered in the rod-shaped HA and the mushroom shaped NA spike protein, approximately in the ratio 1:5[43] (figure 2.6B and figure 2.7B)). Morphologically, the virus particle size can vary, however for spheres of around 120 nm in diameter, it is estimated that 300-400 spike proteins on average populates the membrane, with a median spacing of $\approx$ 10 nm[42,43]. The spike proteins radiating from the surface, can be recognized by the host immune system and elicits an immune response. Thus the spike proteins are a common target for development of vaccines against influenza[44], however loss of efficacy of vaccines due to antigenetic drift has pushed for development of other anti viral strategies[45,46]. In addition to the spike proteins Hemagglutinin (HA) and Neuraminidase (NA), the Matrix protein 2 (M2) is also located in the viral envelope, although to a much smaller extent. The inside of the envelope is supported by an abundance of Matrix protein1 (M1) binding as a scaffold to the inside membrane surface. HA, NA M2 and M1 are all associated with the membrane and have been shown to be implicated in some way in the budding event of viruses. Since the envelop is derived from the host cell, it is not surprising that it contains host specific membrane

proteins at a low abundance, however interestingly some proteins such as tetraspanins have been found in similar amounts as some of the viral membrane proteins[47].

The influenza is a pleomorphic pathogen, meaning the virion can present in various shapes ranging from simply spherical with a diameter approx. 120 nm to long filamentous particles, stretching upwards of 20 um in lengths (figure 2.6C). The morphology depends on the strain of virus and also the conditions the viruses are studied in[48], as filamentous morphology has been shown to be either lost or regained in various cells types in vitro[49,50]. The pleomorphic ability of virions has recently been shown to provide advantages to the virus under various pressure, such as inhibition of the viral glycoproteins. Thus these filamentous participles could be the main cause of persistent viral circulation even under changing environmental conditions, and can potentially be targeted to overcome antiviral drug resistance[51].

2.3.2 Hemagglutinin

Hemagglutinin is a glycoprotein that forms a trimer in the lipid membrane, consisting of 3 identical subunits forming the characteristic viral spike protein. At the membrane-distal tip, each monomer presents a sialic acid receptor binding site, responsible for tethering the virion to the cell surface and inducing receptor-mediated endocytosis[53]. The protein consists of two domains connected by a disulfide bond: the HA_1 domain,

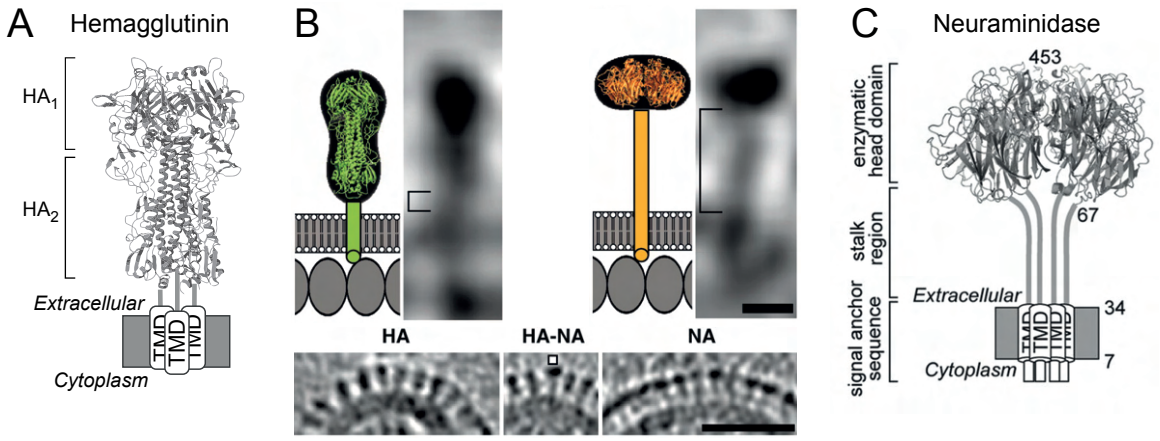

Fig. 2.7 Shapes and virion distribution of spike proteins HA and NA. A) Hemagglutinin protein structure with marked HA_1 and HA_2 domains. Created from PDB entry 1HA0. B) (Top) CryoET structures of HA (left) and NA (right) next to their respective schematic structure. The stem lengths (square brackets) are marked in the cryoET images. (Scale bar 5 nm). (Bottom) Images showing an HA cluster (left), an HA cluster with a single marked NA (middle) and an NA cluster (right) on virion surfaces. (Scale bar 50 nm). Reprinted with permission from [42]. C) Neuraminidase protein structure with marked head domain, stalk region and transmembrane domain. Reprinted with permission from [52].

which binds surface receptors and the membrane-fusion domain HA_2 (figure 2.7A). The low pH in the endosomes triggers conformational changes of the protein and a dissociation of the HA_1 and HA_2 domains, exposing fusion peptides responsible for mediating the fusion of the viral and endosomal membranes[54,55]. HA is a critical player in viral receptor binding and fusion, but has also been shown to generate membrane curvature and initiate budding on its own[56]. HA is the primary protein found on the surface of the virion, and together with NA clusters in the viral envelope with a median spacing of $\approx$ 10 nm (figure 2.7B).

2.3.3 Neuraminidase

Neuraminidase is transmembrane protein with a large, extracellular crown domain at the end of a long stalk region (figure 2.7C). In the membrane, it assembles as a homotetramer and covers around 20% of the virion surface. The catalytic headgroup of NA is responsible for cleaving siliac acid on the membrane surface of the host, thus NA enzymatic activity is critical in the final step of the viral cycle, release from the host. If NA is inhibited or absent from the virion, the particles will bind to the host membrane and start to form aggregates decreasing infectivity[57]. Although each monomer has a catalytic site, the tetrameric structure is imperative, as mutation-induced instability of the tetramer is reported to decrease the enzymatic activity of the protein[58]. HA and NA are both distributed across the entire membrane, yet the organization is not entirely random. Instead NA seems to exists primarily in local clusters surrounded by HA as demonstrated by cryoET analysis[42] (figure 2.6B and 2.7B bottom).

2.3.4 Matrix protein 1

M1 is the most abundant protein in the virion, supporting the internal membrane layer as a scaffold (figure 2.8A). M1 binds the vRNPs and is indicated to be responsible for incorporation and packing of the viral genome[59]. It associates with the inner leaflet of the virion and is postulated to interact with the cytoplasmic tails of NA and HA, recruiting it to the budding zone. This peripheral protein consists of two domains and forms a dimer in the membrane and is shown to multimerize upon contact with the inner leaflet[60]. Some discrepancies exists in early studies describing the role of M1 in the viral cycle. M1 has been reported to be capable of contributing to the release of spikeless VLPs[61], indicating M1 as an initiator of budding. However, using different techniques, M1 by itself does not drive budding or structural assembly of VLPs[56], and

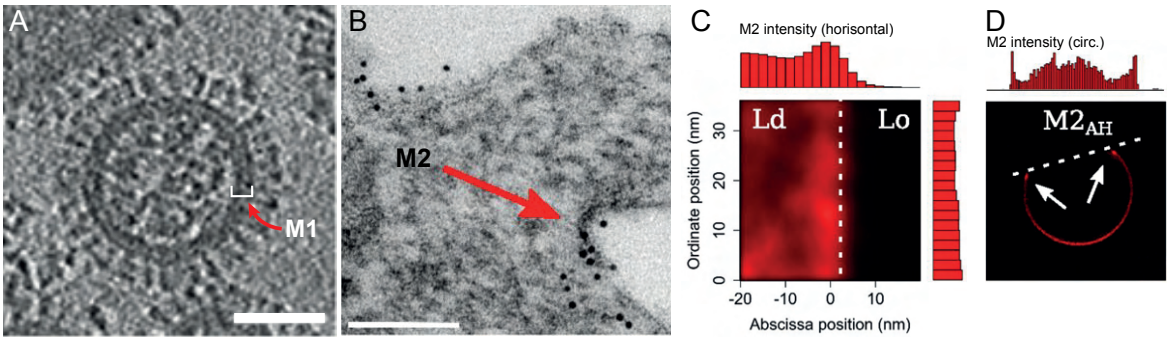

Fig. 2.8 Localization of M1 and M2 in influenza A. A) Influenza A virion imaged by Zernike phase contrast cryo-electron microscopy. Black arrows show lipid bilayer and matrix layer. M1 marked with red arrow. (Scale bar 50 nm). Reprinted with permission from [67]. B) Infected MDCK cells fixed and the immunogold labeled M2 protein shown to localize at the neck of a budding virion (black dots). (Scale bar 100 nm). C) Density map of M2 positions in a liquid ordered and ordered boundary environment, averaged over three independent trajectories. D) Confocal image of phase-separated GUV treated for 1 h with 10 mM M2AH-TMR peptide (red). Increased intensity at the boundary of L_d (red) and L_o (dark) phase is is highlighted by the histogram intensity profile of the GUV circumference. B) C) and D) are reprinted with permission from [66].

some virions that lack M1 binding in parts of the envelope membrane have also been identified[42].

2.3.5 Matrix protein 2

M2 is an integral membrane protein, forming a dimeric tetramer in the membrane and composition analysis demonstrates that it is largely excluded from viral particles. It functions as a proton channel activated by change in pH, and is crucial for the release of genetic material into the host cell as proton influx weakens the inner virion core, releasing the vRNPs from the M1 packing[62]. M2 is therefor a target of antiviral drugs[63]. M2 has been shown to bind to the neck of budding viruses (figure 2.8B) and is thought to be responsible for efficient scission of the progeny virus, as alterations of M2 lead to a morphology resembling pearls on a string[64]. The formation of filamentous viral particles have been shown to depend on the function of M2, and it has been suggested that M2 possible stabilizes the budding site, allowing for continuous polymerization of M1 into the forming virion, and thereby elongating the viral filament[50]. Due to its low frequency in viral particles, M2 has been postulated to sort to the edge of L_o nanodomains (figure 2.8C,D), however conflicting results have been observed on this notion[65,66].

2.3.6 The impact of membrane proteins on the budding of progeny virions

Budding from the membrane is initiated in small domains, termed the budzone of the virus. For a newly formed virion to be infectious it requires the assembly of all the viral components at the budding site and effective incorporation into the viral envelope. It is a highly complex recruitment system, thus many of the excreted particles are non-infectious or defective in some way[39], highlighting that not all the proteins are required for the initiation of a bud. Although correct viral production can fail at numerous points in the replication cycle, effective budding from the membrane is one of the key mechanisms for the spread and survival of the virus. Effective budding requires three steps: 1) Association of the viral proteins with the plasma membrane 2) Membrane remodeling and formation of a budding vesicle containing the genome 3) Effective scission of the budding neck and separation from the plasma membrane to release the progeny virions. Escaping the host cell can only be accomplished with significant membrane remodeling to overcome the energy barrier of membrane bending and allow bud formation. Investigating membrane budding can provide new avenues for pandemic control via alternative anti-viral drugs targeting budding rather than the continuously mutating spikes targeted in classical vaccines. Despite the simple composition of the virus, and the involvement of only 4 envelope associated proteins, the mechanism of budding in its entirety remains enigmatic.

There are various methods of investigating the role of the viral membrane associated proteins in the bud formation. The production of viral like particles (VLPs) via transfection of cells with plasmids encoding the proteins, and reverse genetics to create mutant viruses, are two commonly used cellular based techniques, and much knowledge of IAV has been gained from these experiments[68]. The advantage of reverse genetics is that the system highly mimics the viral behavior, by including all the cellular machinery involved. In turn, elucidating the mechanistic processes at play can be difficult due to the complexity of the system. VLP provide an opportunity to show the effect of selective expression of viral membrane proteins, providing a platform to determine the minimal required characteristics to replicate effective budding, yet these studies are devoid of cellular and genetic influence. Expression of viral proteins in model membranes, can provide inside into isolated biophysical behaviors of the individual viral proteins, such as receptor interaction for fusion and liquid ordered partitioning. It is important to highlight that such techniques have provided various -sometimes even contradictory- results in regards to the role of the viral proteins in budding. The

reader is referred to Nayak et al, for an overview of viral budding and morphogenesis, discussing discrepancies in studies using VLP versus virus-infected cell techniques[39].

The virion morphology is influenced by what happens at the budding site of the virion (figure 2.9A). It is generally accepted that from analysis of morphology and composition of excreted virions the impact on the budding event can be inferred. The membrane associated proteins can all play a role during the budding process to impact the virions. M1, M2 and NA have been postulated to have important roles in the final release of the budding vesicles, as mutations in all three cause changes in the morphology of either the budding site or the released virions[69,70,71]. By using a natively filamentous or spherical virus strain, the affect of the protein mutations can be examine. Mutations of M1 was shown to promote spherical morphology in a filamentous strain[69], similarly, a C-terminal mutation in M2 can induce filaments in an otherwise spherical viral strain[50]. It has been shown that the M1 protein itself does not initiate membrane budding of VLPs, contrary to earlier results obtained in virus polymerase driven systems, where M1 was shown to drive budding[72], however this latter result might have been affected by cell necrosis[56]. Instead, VLPs are produced effectively from expression of the spike proteins HA and NA, especially HA has been shown in numerous system to be able to drive budding of spherical vesicles[50].

Considering the complexity of the dynamics of membrane remodeling in bud formation, it is no wonder that the processes of viral budding remains enigmatic, with contradictory observations presented in the literature. In the following, how lateral organization and protein crowding can influence the budding event is discussed.

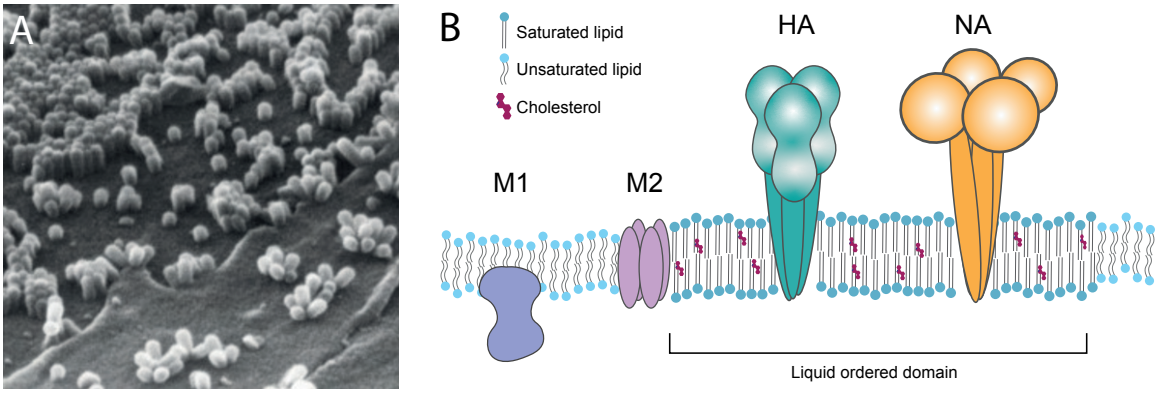

Fig. 2.9 Lateral membrane organization of proteins at budding site. A) Scanning electron micrograph of spheroidal influenza virus buds attached to infected cells (40,000×). Reprinted with permission from [39]. B) Schematic of proposed model of lateral membrane organization of the viral envelope proteins. It is suggested that NA and HA localize in the L_o domain, M2 on the boundary and M1 in the L_d domain. Inspired by [73].

2.3.7 Lateral organization of viral proteins in the host membrane

A well accepted model of viral organization in the membrane postulates that HA and NA are both recruited to small L_o domains in the plasma membrane, as multiple in vitro studies have shown an association of the spike proteins with L_o domains[74,75,76,71,73] (figure 2.9B). The cytoplasmic tails of the proteins are thought to be responsible for the nanodomain-targeting abilities. Since L_o nanodomains are thought to be transiently existing domains in cells, it is an obvious candidate for the localization and concentration of the viral proteins before bud initiation, and HA and to some extent NA have been postulated to stabilize the existence of these domains forming 'long-lived' domains from which budding can occur. However, more recent studies assessing phase partitioning of HA and NA in macroscopic L_o domains in plasma membrane vesicles, have shown that both proteins prefer the (L_d) phase[14,13]. In addition it has also been suggested that HA does not associate with existing membrane rafts but induces its own L_o-like domain[77]. Conflicting results can potentially be explained by distinct lipid packing variations with the model system or unexplored protein-protein interactions responsible for the translocation of HA and NA not captured in such isolated membrane systems[73]. Still, non-L_o domain associated mutants of HA show significantly decreased budding in infected cells, supporting the notion that virus budding could be initiated in L_o nanodomains in vivo[75].

M1 is thought to interact with the cytoplasmic tails of HA and NA and get recruited to the budding zone via these interactions[78]. It has been reported that M1 does not end up in VLP in absence of the spike protein HA and NA, but that the presence of either of these lead to incorporation of M1, however greatly enhanced with HA expression[56]. In addition, mutations of the cytoplasmic tails of NA and HA (palmitoylation sites on HA) has been shown in a variety of studies to decrease the amount of M1 in the released VLP[79,80]. This suggest that NA and HA are possibly responsible for recruiting M1 to the budzone. However it is also possible that M1 has an increased affinity for the lipid profile of NA and HA containing budding zones[41]. M2 has been postulated to sort to the edge of L_o domains depending on the membrane composition and elegant simulations have backed this notions[66], however conflicting results have been observed[65].

Finally, the cytoskeleton of the host cell might be responsible for some of the sorting mechanisms driving the viral assembly in vivo, as both M2 and HA clustering in cells have been shown to be dependent on the presence of cortical actin[81]. HA clusters appear with irregular domain boundaries, which could indicate that they are not simply

clusters of nanodomains (which would be perimeter minimized), but could be the result of a meshwork of inner leaflet associated microfilaments, trapping and organizing the HA clusters[73,82].

Lateral organization of membrane proteins in viruses and general cellular machinery deserve the attention of vigorous research as it can heighten our general understanding of health and disease. In this thesis, a novel assay is presented to further address the contradictory sorting results and contribute to the general understanding of viral protein assembly.

2.3.8 Crowding at the budding site

The mechanism by which viral proteins contribute to budding or reshaping of the membrane could well originate from a crowding mechanism. Considering the protein densities and small separation distance between these large asymmetric proteins, shown in figure 2.10A, a significant lateral pressure could be anticipated on the outer leaflet. As described in the section 2.2, stochastic surface collisions i.e. crowding of proteins with confined lateral diffusion on a membrane surface creates a uneven lateral pressure between the outer and inner membrane leaflet. The pressure induces curvature generation and bends the membrane to relieve the pressure. Both spike proteins of influenza have been shown to induce budding and release spherical vesicles from membranes, and the structural features of the proteins with large ectodomains suggest that they could be excellent crowders. Estimating the energy generated by crowding of the surface protein is not straight forward but can be achieved using the Carnahan-Starling equation of state, modeling the proteins as non-interacting spheres on the membrane as in [34, 84]. The energy from the crowding pressure can be calculated using

$$E_{crowding} = \frac{\eta a_v}{a_p}[1 + \frac{2\eta(1 - 0.44\eta)}{(1-\eta)^2}]K_BT \tag{2.2}$$

with η being the fraction of the membrane covered by protein given by $\eta = \frac{N_p a_p}{a_v}$ where N_p is the number of proteins, a_p is the 2D occupied area of the protein on the membrane surface, a_v is the surface area of the membrane (here the virion surface). Using equation 2.2, HA and NA was estimated to provide enough energy to break the typical energy bending threshold for a plasma membrane (here $\approx$ 500 K_BT). This happens at around 30% protein coverage of NA and 20% coverage of HA (figure 2.10). The structure of HA and NA differs, with the NA crown occupying more space than HA spike, therefore the size of the modeled spheres used were NA_d = 8 nm and HA_d = 5.5 nm, representing the average occupancy of the extracellular head domain for each

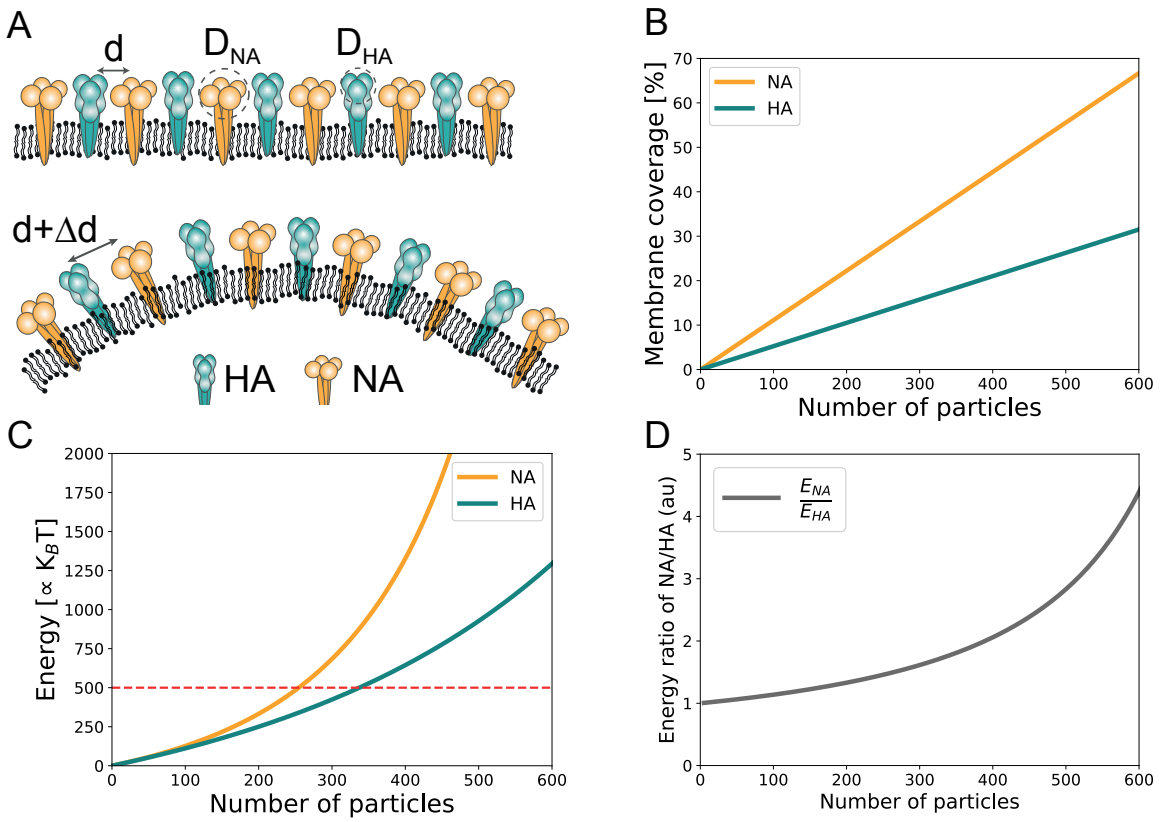

Fig. 2.10 Curvature generation from crowding of HA and NA. A) Schematic showing NA (orange) and HA (green) proteins confined laterally in a membrane, i.e crowding at the surface and inducing membrane bending to increase the lateral distance and minimize the steric pressure. B) Plot of the percent membrane coverage per number of particles (NA or HA proteins). C) Plot of energy from crowding vs. number of particles (surface coverage). The plot was generated based on the Carnahan-Starling equation[29,34] with the modeling parameters used: vesicle diameter = 120 nm, NA diameter = 8 nm, HA diameter = 5.5 nm. The dashed red line represents a typical plasma membrane bending energy of $8\pi\kappa \approx 500K_BT$. The protein diameters used are based on literature reported size of the lateral profile of the extracellular domains. The NA crown is reported to measure 8 nm[58] and the HA protein ranges from 3 to 8 nm, thus is estimated as 5.5 nm here[83]. A larger number of HA proteins are needed to reach the energy barrier compared to NA. D) The energy ratio created by crowding from NA and HA. At low protein density, the crowding effect is similar, with NA crowding being more prominent at particle numbers comparable to that on a virion (≈ 500).

protein[83,58]. From the model it was determined that at 500 particles one NA protein was needed for every three HA proteins, to contribute the same crowding, mimicking the 1:5 ratio of NA:HA proteins present on the virion surface[43].

Both HA and NA have been reported in literature to induce non-specific membrane curvature leading to release of spherical particles, suggesting they have curvature generating capabilities. These findings highlight that NA and HA could both be driving the initial budding of viruses on the surface, possibly from crowding via their ecto domains. In addition, further analysis of the protrusion indicate that NA

prefers the tip region, where curvature is 2 dimensional, whereas HA prefers the one dimensional curvature at the site of elongated cylindrical virion protrusions[85]. Such sorting of the spike proteins into curved regions, could stem from crowding ability of the ectodomain. NA has a larger crown and has a higher crowding ability than HA, which could drive it into the distal tips. Measuring any budding initiation from HA crowding can be difficult by analyzing the release of viral particles from cells, as the sialidase activity of NA is needed to release particles tethered to the surface. Thus removing NA always lowers the measurable amount of VLP in the supernatant of a cell culture, unless cells are incubated with an exogenous NA instead.

Crowding is an entirely stochastic process, therefore it is required that the proteins can diffuse laterally in a confined region where budding is desired. As mentioned above, L_o domains in the plasma membrane could account for the assembly of viral proteins, and with its composition could provide such a confined domain where protein crowding could overcome the membrane bending barrier and induce curvature. Studies in vitro have indeed demonstrated how proteins anchored in high concentration to a L_o domain, induce spontaneous tubulations from simple stochastic protein crowding[35,29]. Interestingly, this only happens in very stable domains, as crowding inherently contributes energy to the system that instead of crowding could simple induce lipid mixing and the loss of phases[86]. Indeed, the steric pressure from proteins has been shown to induce homogeneous mixing in model systems, when it exceeds the enthalpy of lipid mixing[37]. This notion support the proposed model where clustering of the viral envelope proteins stabilizes the budzones, forming a distinct membrane composition that could confine the proteins and allow efficient membrane bending via crowding to initiate the virus particles. Although, recent studies showing that HA and NA are not associated with L_o domains in model membranes questions this theory. Still more complex membrane organization could be at play in vivo[87], than simple replicable nanodomain association of the isolated proteins, and indeed many cellular processes can lead to diffusion barriers in vivo[87].

A certain degree of membrane organization is indeed plausible in vivo and, as mentioned earlier, studies have indicated the role of the cytoskeleton in stabilizing the coalescence of HA clusters. In addition M1 oligomerization at the budding site could stabilize the budzone creating the diffusion barrier needed to create significant pressure and membrane bending[34]. Indeed, only in combinations with the matrix proteins do the released particles, from NA and HA covered cell membranes, become truly virus like in their morphology, where filamentous protrusion are release through a constricted

neck scission at the base[88,85]. Much is still to be uncovered to determine the role of protein crowding in viral budding.

Crowding is a putative mechanism that has been suggested to play a role in many curvature generating processes in the cell[28,31] and has been proposed as a mechanism for virus budding[33]. Traditionally the morphology of membranes is the indicator of crowding on a surface, and the forces needed to generate such curvature have been estimated in simulation[31]. However, to our knowledge, the direct impact and forces at play during curvature have not been measured quantitatively in membranes. In this thesis, a novel assay is presented to directly measure any crowding contribution of viral proteins and the plasma membrane, utilizing optical tweezers to probe the forces at play, as reviewed in the following chapter.

Chapter 3

Optical manipulation of model membranes

In this chapter, I introduce the experimental techniques employed to conduct the presented research. First, I discuss the choice of model membranes, followed by a detailed introduction to optical trapping and its applicability to study membranes. Finally, I present the theoretical foundation for the assays developed in this work.

3.1 Model membrane systems to investigate viral protein behavior

This thesis explores the involvement of proteins in the formation of new influenza A viral particles to answer fundamental questions about the viral machinery. To investigate the contribution of single proteins, they can be examined in isolation from the complexity of the mammalian cell, obscuring the relatively small protein dynamics of interest. To investigate the phase affinity of the proteins, they can be isolated in hybrid vesicles-a fusion product of GUVs and GPMVs which are models systems introduced below that resemble the natural environment of the plasma membrane. In the following, the model systems used are described in detail, followed by an introduction to the experimental optical techniques used to manipulate and study these model membranes.

3.1.1 Giant unilamellar vesicles

Giant unilamellar vesicles (GUVs) are a model membrane system that consist of a lipid bilayer vesicle, mimicking the membrane of eukaryotic cells. GUVs are made synthetically and can consist of a single lipid type or a mix of a variety. Depending on the conditions of their formation procedure and their constituents, they can exhibit a variety of biophysical properties. Their easy tunability makes them a great platform for investi-

gating membrane phenomena, and they have been used in studying membrane curvature and reshaping by cellular mechanisms[89,90,29], membrane repair mechanisms[91,92] lateral protein organization[93,94], synthetic cells[95,96], microtubule-kinesin transport system[97] and more.

Reconstituting proteins into Giant Unilamellar Vesicles (GUVs) is necessary for using such a model systems to investigate protein behavior and function. Multiple methods exists for this purpose, each presenting unique challenges as well described in [98]. Spontaneous swelling is commonly used to form GUVs, however including proteins in the mix is not straight forward as the dehydration step can lead to protein denaturation[99,100]. In addition, the necessity to form GUVs above the lipid phase transition temperature (Tm) for homogeneous membranes, can further impact protein functionality. Detergent-mediated reconstitution, while feasible, is labor-intensive and necessitates meticulous detergent removal to avoid compromising the vesicle integrity. Alternatively, pre-made GUVs can be fused with small membrane vesicles[101] or proteoliposomes and liposomes reconstituted with proteins via cell-free expression systems[102,103,104]. Despite advancements in the development techniques, the reconstitution of proteins into GUVs remains a complex task, particularly in regards to maintaining the correct orientation and functionality of the proteins.

Various protocols have been designed to synthesize GUVs with distinct biophysical properties, and advantages and disadvantages such methods are well described in 105. In this thesis, GUVs were made by gel assisted vesicle hydration, where GUVs are formed by swelling from a lipid coated polyvinyl alcohol gel surface[99]. This method minimizes degradation of relevant molecules, a common side effect of electroformation protocols[106] while allowing the growing buffer to contain physiologically relevant salt concentrations. The vesicles grow rapidly and consistently using the method and bio-molecules of interest can easily be encapsulated during formation. By tuning the lipid composition used, the GUVs can show distinct membrane properties.

One such useful feature is the emergence of stable, co-existent L_o and L_d domains. These macroscopic domains resemble ordered domains transiently existing in the plasma membrane and used to laterally organize membrane proteins. These GUVs thus form a simple model system for investigation protein organization by lipid packing. L_o domains arise due to tight packing of saturated lipid molecules with cholesterol, where separation into a Lo and L_d domain is energetically favorable, thus the emergence of such domains happen below a certain temperature, namely the miscibility temperature (Tm). In this thesis, phase-separated GUVs are made by mixing DOPC (an unsaturated lipid) with

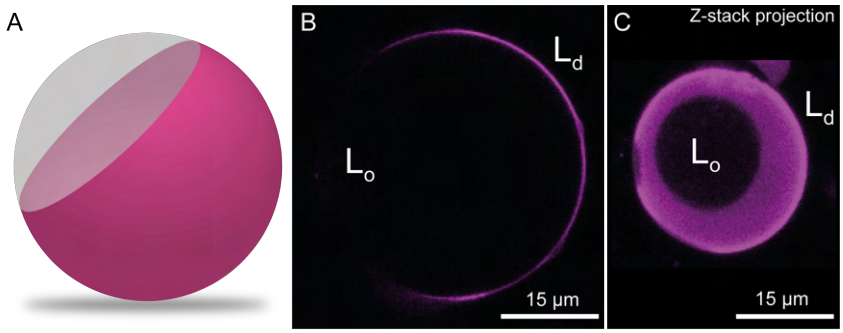

Fig. 3.1 Phase-separated GUV. A) Illustration of a phase-separated vesicle with an L_o (gray) and L_d (violet) domain. B) Representative confocal microscopy image of the center of a phase-separated vesicle showing L_o (dark) and L_d (violet) domains. C) Z-stack projection (max intensity) of the top half of a phase-separated vesicle, showing a large L_o domain on the top of the vesicle.

Brain SM (saturated lipid) and cholesterol in a stoichiometric relation allowing the emergence of L_d and L_o domains (figure 3.1).

3.1.2 GPMV

Synthetic vesicles such as GUVs lack a native representation of the cell membrane, missing the diversity of leaflet composition and asymmetry found in natural cells. Introducing a variety of lipids can also reduce control over the physical properties of the membrane. Additionally, the extensive presence of proteins on the cell surface is a significant factor, as proteins occupy approximately 30-55% of the plasma membrane, imparting various properties to it[107]. Reconstituting transmembrane proteins in GUVs is challenging and time-consuming, often resulting in incorrect orientation of the proteins within the membrane.

Giant Plasma Membrane Vesicles (GPMVs) offer an alternative model membrane, inspired by naturally occurring processes in cells, such as the formation of giant vesicles during cell migration and cell death[108,109]. GPMVs, also known as 'blebs', form as a result of a local disruption of the strong interactions between the cytoskeleton and the plasma membrane in cells, and present as spherical protrusions on the membrane (figure 3.2). GPMVs retain the lipid and protein complexity of the parent cell's plasma membrane, providing a more accurate representation of in vivo conditions compared to synthetic vesicles. Additionally, transmembrane protein expression in such membranes is relatively straightforward, requiring only transient expression of the protein in the originator cell. This ensures that the proteins are expressed in the membrane in correct orientation close to their native state. GPMVs are void of larger intracellular structures

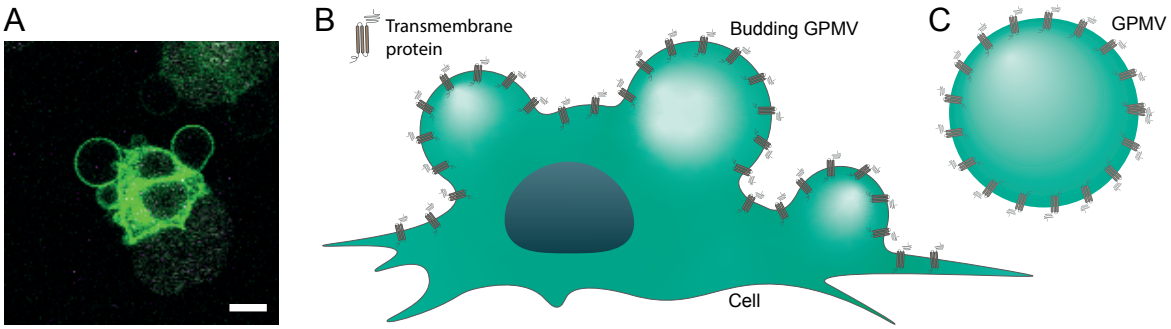

Fig. 3.2 GPMVs protruding from cells. A) Representative microscopy image of HEK293T cells expressing an NA protein with GFP tags (green). (Scale bar 10 μm). B) Illustration of blebbing cell and C) de-attached GPMV.

such as the cytoskeleton, and thus are an excellent platform to study protein behavior in absence of the complex cellular dynamics[110,111]. GPMVs are thought to retain protein asymmetry while the lipid asymmetry of the plasma membrane is partially lost in GPMVs[112]. GPMVs can be isolated from the cells or can be used while still attached to the cells depending on the nature of the experiments. GPMVs have been used to study numerous biophysical phenomena[113] including protein features for nanodomain partitioning[12], lipid dynamics of the plasma membrane[114,112] and drug delivery to cells[115,116,117].

GPMVs can be obtained from cells by subjecting them to a blebbing reagent, causing the plasma membrane to bud and eventually release vesicles. However, blebbing can also be induced without chemical agents as shown where cells irradiated with an NIR laser resulting in the formation of blebs[118]. Numerous extraction methods and usages have been published and are well-reviewed in [119]. Most commonly, GPMVs are formed by incubation of cells with a vesiculation buffer containing either dithiothreitol (DTT) in combination with paraformaldehyde (PFA), or N-Ethylmaleimide (NEM). Both methods yield GPMVs in an appropriate amount for the experiment, however in this thesis, NEM was chosen to avoid changes to the proteins that could affect the results in the studies. DTT is a reducing agent, known to cut disulfide bonds in proteins, releasing them from interactions with the cytoskeleton making the membrane relaxed and able to bud. Under certain conditions DTT might affect thioester bonds and could thus impact palmitoylation, which have been shown to be important for L_o-association[16]. This could potentially affect the L_o domain targeting of the proteins in question. In addition, DTT/PFA vesicles show corsslinking of membrane proteins with PE lipids, resulting in exclusion from L_o phases due to the unsaturated chain of the lipid[120]. NEM is a strong alkylating agent that can block free thiol groups, however

does not have an impact on already formed palmitoylation. Here NEM was used, to minimize affect on domain preference of the studied proteins, and has been found to reflect the native PM to a higher degree than DTT/PFA vesicles[120].

3.2 Assessing protein crowding with sensitive optical force spectroscopy

This thesis leverages optical trapping to explore biological phenomena, making an introduction to its applications in this field particularly relevant. Optical trapping is a versatile technique that can be applied across a wide range of scales, from nanometers to micrometers. It not only facilitates the organization and manipulation of matter but also enables the observation and measurement of dynamic processes in various objects. The technique is based on optical forces of light, which when focused appropriately can create a trap in which particles can be moved around with nanoscopic accuracy and forces can both be applied and quantified in the piconewton range (0.1 pN - 200 pN). The tool is therefore readily applicable for probing biological samples, as forces acting on a cellular level and between biomolecules are on this scale[121,122,123,124]. In addition, due to the existence of the biological transparency window for NIR lasers, the technique can be used with limited impact from the light on the specimen.

The concept of optical trapping was first introduced by Arthur Ashkin in 1970[125], which eventually led to the creation of the optical tweezer[126]. Ashkin's pioneering work in this area, along with contributions from others, earned them the Nobel Prize in Physics in 2018. This groundbreaking technique is a fundamental aspect of this thesis, especially when combined with confocal microscopy, which allows for precise and controlled visual manipulation of biological samples. The ability to use light to probe at the nanoscale is truly remarkable.

Later in this thesis, the ability of an optical trap to mechanically probe a surface and simultaneously provide a force read-out from a trapped object, is exploited to pull tethers from protein crowded plasma membranes and quantify the relevant forces.

3.2.1 Principles of optical trapping

The following technical description of optical trapping is based on information drawn from [127], [128], [129].

Optical trapping is based on the principle that light, consisting of photons, car-

ries momentum in their propagation direction. When a laser beam is focused through lenses, a Gaussian light distribution is created, with a peak in the center of the beam allowing for 3D trapping. When this beam interacts with an object, the refracted and reflected light gives rise to forces acting on the object due to transfer of momentum, namely the gradient force and the scattering force. In simple terms, the scattering force is a result of light reflecting off the object, and will push the object in the direction of the propagating beam. The fundamental force allowing optical trapping occur, is the gradient force that arises from the change in momentum when photons are refracted by and object, essentially pushing the object towards the center of the focused laser (trap). Trapping at the center only occurs if the refractive index of the trapped object is larger than the surrounding media, otherwise the object is repelled from the light. Consequently this is the most critical feature to consider when designing optical trapping experiments. For the experimental work of this thesis, polystyrene beads in various forms are used for biological probing, as $n_{polyS} = 1.59 > n_{water} = 1.33$. In addition this refractive index dependency also allows for the translocation of membrane vesicles, with a denser content than the surrounding environment, for fusion experiments to be carried out[130].

To describe the forces acting on trapped objects one needs to consider their dimensions (D) in relation to the wavelength (λ) of the trapping laser. Three regimes exists to describe the theory: The Rayleigh regime, where $\lambda \gg$ D, the Mie regime, where $\lambda \ll$ D and the intermediate regime where $\lambda =$ D, and the physics of the two extreme cases can be explained in relatively simple terms.

Mie regime

In the Mie regime an intuitive trapping mechanism exists that can be explained and visualized using optic rays. Assuming a bead is positioned unevenly in the lateral direction of a focused laser beam with a Gaussian intensity profile (figure 3.3A), it follows that the ray intensities are not symmetrically distributed around the bead. As the photons in the beam center are carrying more momentum than the peripheral photons, the change in the refracted momentum will be unequal (see dp1 and dp2). As momentum is always conserved, and $F = \frac{dp}{dt}$, the bead will experience a force acting opposite to the sum of dp1 and dp2, pushing the bead into the center of the trap, achieving stable trapping over the entire lateral intensity profile. In the axial direction a similar argument can be visualized. Assuming a bead is positioned slightly above the focal spot of the focused laser, the refracted momentum will be symmetrical dp1 and dp2 (figure 3.3B). The opposite and equal momentum, will thus force the bead

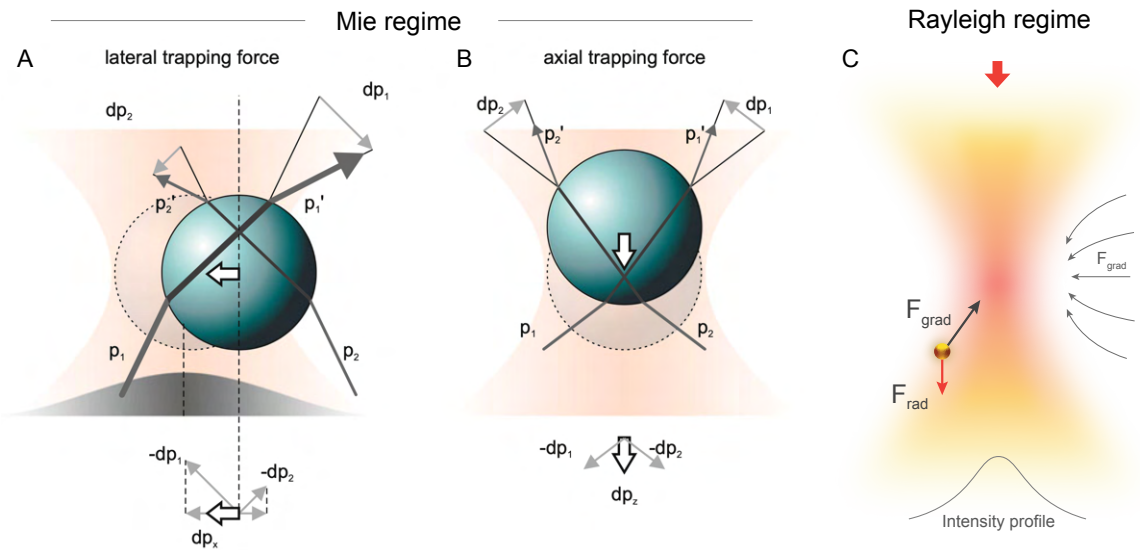

Fig. 3.3 Forces in an optical trap. A) Forces on an optically trapped bead in the Mie regime. The bead is displaced laterally in a Gaussian laser profile. Change in momentum of p1 and p2 pushes the bead towards the center (white arrow), due to the asymmetry in the ray intensity. B) Axial gradient force towards the focus of the trapping light. Bead displacement in the axial direction causes a change in momentum (dp1 and dp2) that is symmetric laterally, but not vertically resulting in the object being pushed to the axial focus point. The white arrows indicate the net restoring force, due to conservation of momentum. Reprinted with permission from [127]. C) Schematic of optical trapping in the Rayleigh regime. Particle is affected by the radiation force F_{rad} and the gradient force F_{grad}. Inspired by [128].

down into the focal plane of the trap. This argument can be repeated for the integral laser profile to explain how optical trapping follows the intensity gradient.

Rayleigh regime

For particles where $\lambda \gg$ D, the electromagnetic wave properties of light must be considered. The particle will experience a constant electric field due to its dimensions, and can be treated as an induced electric dipole, characterized by its polarizability α. The energy of the induced dipole from the interaction with the field E is the given by $U = -\alpha \vec{E} \cdot \vec{E}$. The force is given by the gradient of the potential energy, $F = -\nabla U$, and inferring that the squared electric field is proportional to the intensity of the laser, the gradient force is given by[128]

$$F_{grad} \propto \alpha \nabla I \tag{3.1}$$

This gradient force always directs particles with positive polarizability to the center of the trap where the light intensity is at its maximum, which will be the focal point

of focused laser beams (figure 3.3C). In addition to the gradient force, particle will also experience a scattering and absorption force from the light being reflected and absorbed by the particle defined, and together these are termed the radiation force

$$F_{rad} = \frac{n\langle S\rangle}{c}\sigma_{scat} + \frac{n\langle S\rangle}{c}\sigma_{abs} \tag{3.2}$$

where n describes the index of refraction of the object, $\langle S\rangle$ is the Poynting vector describing the power flow of the field, c is the speed of light and σ_{scat} and σ_{abs} are the respective scattering and absorption cross sections of the trapped object. Ultimately, stable trapping in 3D requires $F_{grad} > F_{rad}$. To ensure this, tightly focused beams are used, where the size of the gradient force will compensate for the scattering and maintain stable axial trapping, although the ratio of the forces affect whether the object will get trapped slightly downstream of the focal spot[131]. The optical tweezers and material composition of the particles can be tuned to achieve stable trapping of various shapes and sizes[132].

In this thesis project, various particle types are trapped in optical tweezers to perform the experiments. Polystyrene beads with diameters of 1.05 μm and 4.95 μm are used for probing membrane surfaces, pulling tubes from GPMVs and cells, falling in the Mie and intermediate regimes as the NIR laser used for trapping has a wavelength of 1064nm. For fusion of membranes AuNS with a diameter of 150 nm are used, representing the Rayleigh regime. Electromagnetic theory can be applied to describe the intermediate regime, however this task is non-trivial[133,129]. In practice, the optical trap is calibrated to determine the direct force measurements, and a theoretical description of the trapping is redundant as long as the trap has a harmonic potential.

3.2.2 Force calibration

To quantify the forces acting in the optical trap, a calibration is carried out, most commonly using Stokes drag calibration of Brownian motion analysis. The physics of the trap can be modeled as a spring, allowing the quantification of the spring constant and stiffness. By applying a constant external forces, such as a drag force created by applying a continuous fluid flow or moving the rap at constant speed, the trap stiffness can be estimated from the displacement of the object in the trap. The drag force will displace the object until the restoring forces is equal an opposite given by Hooke's law

$$\mathbf{F}_{drag} = \mathbf{F}_{spring} \Rightarrow -\gamma\mathbf{v} = -\kappa\mathbf{x} \tag{3.3}$$

where γ is the drag coefficient given by the viscosity of the medium ν and the object diameter via $\gamma = 3\pi\nu d$, $\mathbf{v}$ the velocity vector, κ is the spring constant and $\mathbf{x}$ is the displacement of the object in the trap. Hence the stiffens of the trap can be experimentally measured by relating the displacement of an object of known size with the flow of a fluid of known velocity and viscosity

$$\kappa = \frac{\gamma \mathbf{v}}{\mathbf{x}}. \tag{3.4}$$

Here, the Brownian motion calibration is used, which is typically more accurate. Due to the continuous stochastic forces acting on a trapped object from the surrounding media, the object will experience Brownian motion and the forces acting on the object described by the Langevin equation of motion

$$m\mathbf{a} = -\kappa\mathbf{x} - \gamma\mathbf{v} + \mathcal{F}(\mathbf{T}, \mathbf{t}) \tag{3.5}$$

where $-\kappa\mathbf{x}$ is the harmonic force, $\gamma\mathbf{v}$ the stokes drag force and the stochastic force in time dependent on the temperature of the system $\mathcal{F}(\mathbf{T}, \mathbf{t}$. The Fourier transformation of this equation relates the power spectrum for the displacement fluctuations in the trap to the corner frequency[134]

$$S_x(f) = \frac{k_B T}{\gamma\pi^2(f_c^2 + f^2)}. \tag{3.6}$$

By experimentally collecting and fitting a power spectrum, f_c can be extracted and the trap stiffness determined using[129]

$$f_c = \frac{\kappa}{2\pi\gamma}, \tag{3.7}$$

.

3.2.3 The optical and combined imaging set-up

Combining optical trapping with confocal microscopy provides a powerful set-up with the ability to probe and observe biological phenomena in real time. Combining these techniques we can manipulate fluorescent cell membranes and vesicles in solution, moving objects into contact and probing samples while recording signal responses of fluorescent molecules. The set-up used for fusion experiments consists of a Leica SP5 confocal scanning microscope combined with a trap with a focused 1064 nm Nd:YV04 NIR continous wave laser (figure 3.4). The trapping laser was focused by

a 63x water-immersion objective (NA 1.2) and directed through the samples before being collected by an oil immersion condenser (NA 1.4). The signal is detected by a quadrant photodiode recording the information of the trapped object[135]. During experiments, a pinhole size of 111.4 μm was used. The confocal microscope contains built-in lasers of various wavelengths ranging from 458 to 633 nm.

Confocal microscopy provides the advantage that it can block out-of-focus light that normally disturbs conventional microscopy images, creating a thin highly resolved slice of information in the X-Y plane. As fluorescence from the sample is collected through a pinhole, detecting only the light from the focal point of the laser, the beam is scanned across the sample to generate the images. It is noted that this scanning does no affect the optical trapping in the set-up as galvanic mirrors are employed to move only the scanning lasers across the sample. By scanning at different focal planes (Z direction) and subsequently stacking them, 3D representation of the specimen can

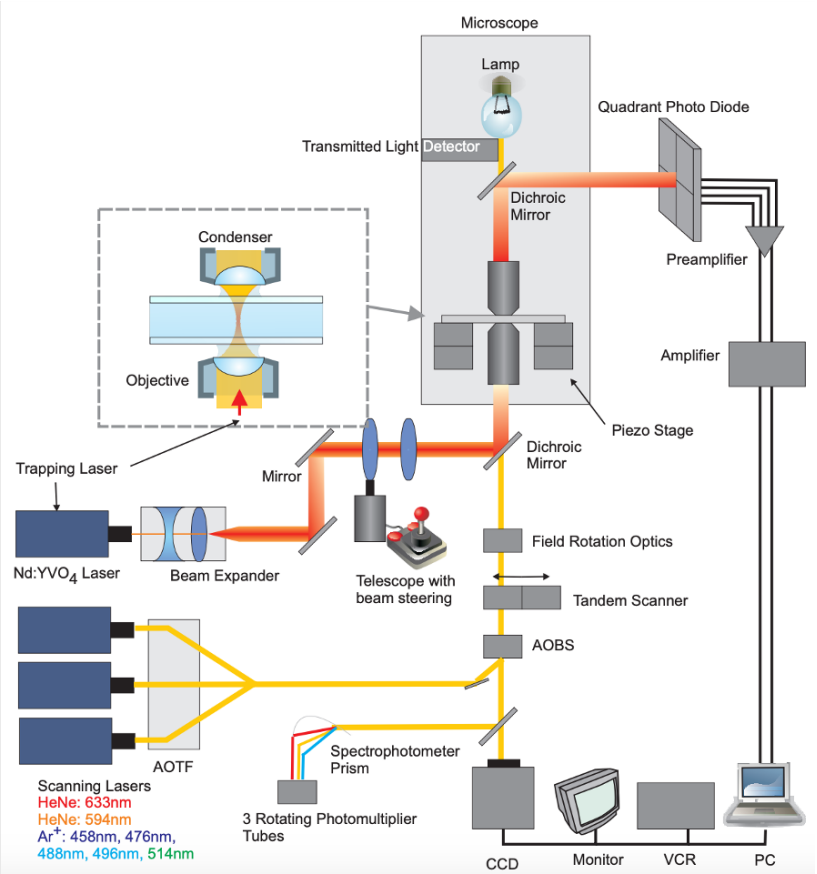

Fig. 3.4 Combined confocal microscopy and optical tweezer. Schematic of the used set-up where a confocal microscope is combined with a 1064 nm optical trap. Reprinted with permission from [135].

be visualized and is effective for determining both lateral and axial location of tagged molecules.

The image resolution is limited by the diffraction of light, with typical resolutions ranging from 200-350 nm in the lateral plane and this number reduced by roughly 2.5 for the axial resolution[136]. In general, the minimal resolved distance for confocal microscopy can be described by

$$r_{confocal} = \frac{0.4 \cdot \lambda}{\mathrm{NA}} \tag{3.8}$$

where lambda is the wavelength of the excitation laser and NA is the numeric aperture of the objective[137].

For data showing tethers pulled from GPMVs on cells, a commercial version of the above described set-up was used: Lumicks C-trap Optical Tweezers – Fluorescence & Label-free Microscopy. The theory relating the forces measured in membrane tethers to the spontaneous curvature generated by crowdin gis explianed in the following.

3.2.4 Spontaneous curvature in model membranes from protein crowding

This thesis explores the effect of bulky, viral proteins on the reshaping of membranes and for this purpose the theory of membrane tubes is applied to the model system used for experiments.

A lipid bilayer is a flexible membrane that can be deformed in various ways but this requires a change to the free energy of the system. This inherent barrier is determined by the characteristics of the membrane dynamics, classically described via the bending rigidity and membrane tension of the system. A common method to study the properties of a given membrane, is by pulling membrane tubes from the surface of membrane vesicles[138]. A membrane-binding bead attached to a vesicle, can be pulled from the membrane by applying a force on the bead, e.g. via an optical trap. Upon pulling, the bead drags the membrane along, creating first a protrusion that upon breaking the energy barrier of bending is broken and the system collapses into a tube extended from the vesicle. The shape evolution of the tube during the pull is visualized in figure 3.5A.

The tubular shape emerges as minimizing the surface area minimizes the tension of the system, but is balanced by the membrane rigidity, fighting the large curvature of extremely thin tubes. The tube can be elongated without the need of additional force but with a slight relaxation in the force from lipid relaxation once the pull is completed

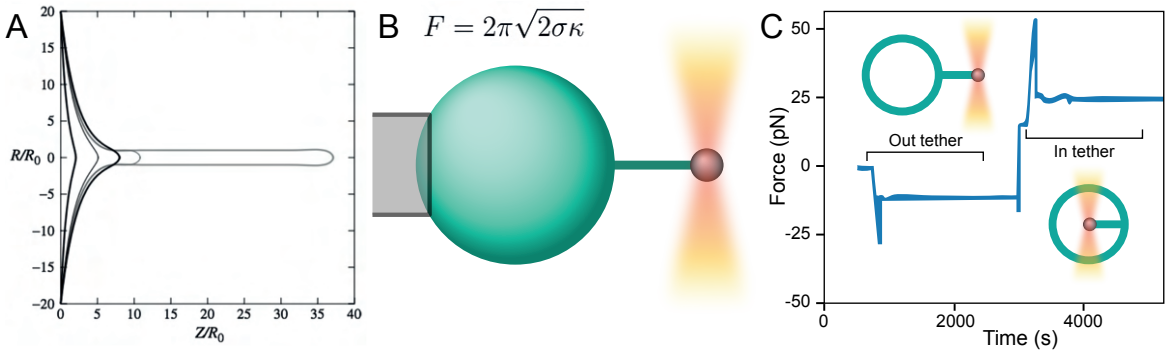

Fig. 3.5 Membrane tubes pulled from a GUV. A) Computed tube shape evolution. The graph illustrates the catenoidal tube conversion upon applied force for a circular patch with radius, R, and tube extended to a distance Z. Adapted with permission from [139]. B) Schematic of a GUV with a tube pulled with an optical tweezer with the tube force shown. C) Example force profile from experiments (in Chapter 5) with negative force values when pulling to the right (out) and positive when pulling to the left (in).

(figure 3.5B,C). The force and the radius of a membrane tubed that is equilibrated can be determined by minimizing the free energy of the vesicle-tube system with respect to the length, L, and radius of the tether, R. Considering a membrane vesicle, e.g. a GUV, with an inherent spontaneous curvature of zero and an empty tube held by a force, the mechanical parameters simplifies to

$$F = 2\pi\sqrt{2\sigma\kappa} \tag{3.9}$$

$$R = \sqrt{\frac{\kappa}{2\sigma}} \tag{3.10}$$

where σ is the membrane tension and κ is the bending rigidity. These theoretical predictions, indeed match well experimental data and from these two equations force and the tube radius can be related via

$$F = 4\pi\sigma R. \tag{3.11}$$

Mechanical analyses of model membranes such as GUVs is typically completed by aspirating a vesicle in a micropipette. Since this systems applies a constant tension on the membrane, relevant membrane properties can be determined, following the above equations. By measuring the force, the radius of the pulled tube can be determined. If a fluorescent membrane dye is added, the fluorescent intensity can provide a second independent measure of the radius, and both values of R can be used to calculate the value of the bending rigidity, κ, for the membrane (under constant σ).

To describe the energy of a vesicle-tube system with a spontaneous curvature, C_s, elastic theory where membranes are treated as thin sheets locally characterized by their mean curvature, can be applied[140,141,142]. The Helfrich-Canham free energy of the membrane can be described by integrating over the area of the system such that

$$\mathcal{F}_{H-C} = \int [\frac{\kappa}{2}(2H + C_s)^2] dA \tag{3.12}$$

where, H is the mean curvature of the membrane, κ is the bending modulus, C_s is the spontaneous curvature. The equilibrium membrane shape can be found by minimizing this energy with specific boundary constraints given by the system. For a cylindrical tube of length L, extracted with a pulling force F from a vesicle with tension σ and surface area A the energy equation can be described as

$$\mathcal{F} = \mathcal{F}_{H-C} + \sigma A - FL. \tag{3.13}$$

For the cylindrical tube of radius R, $2H = \frac{1}{R}$ and $A = 2\pi RL$ and the energy equation to minimize with respect to boundary constraints becomes

$$\mathcal{F} = \pi\kappa RL(\frac{1}{R} + C_s)^2 + 2\pi\sigma RL - FL. \tag{3.14}$$

By minimizing the free energy with respect to R, $\frac{d\mathcal{F}}{dR} = 0$, the equilibrium radius can be found and is described by

$$R_{out} = \sqrt{\frac{\kappa}{2\sigma + \kappa} C_s^2}. \tag{3.15}$$

Additionally, when minimizing the free energy with respect to L, $\frac{d\mathcal{F}}{dL} = 0$, and solving for the force F the following expression for the tube-holding force in equilibrium is obtained

$$F = \pi\kappa(\frac{1}{R} - 2C_s) + (C_s^2\pi\kappa + 2\pi\sigma)R \tag{3.16}$$

and further, when inserting the expression for R (equation 3.15)

$$F = 2\pi\sqrt{2\sigma\kappa + \kappa^2 C_s^2} - 2\pi\kappa C_s. \tag{3.17}$$

When aspirating a membrane vesicle, it is possible to pull tubes both in and out of the vesicle[143], and this additional tube force provide extra information regarding the system[144]. Deriving R for vesicle with a tube pulled into sphere, instead of out, yields the same results as in eq. 3.15 while the force is larger than for the out-tube and given

by

$$F_{in} = 2\pi\sqrt{2\sigma\kappa + \kappa^2 C_s^2} + 2\pi\kappa C_s \tag{3.18}$$

By subtracting eq. 3.17 with eq. 3.18 it becomes evident that by measuring the out-force and the in-force, the spontaneous curvature of the membrane can be estimated without controlling or knowing the tension of the system[144]

$$\Delta F = F_{out} - F_{in} = -4\pi\kappa C_s \tag{3.19}$$

This notion lays the basis for the assay presented in Chapter 5 of this thesis.

3.3 Fusion of biological membranes by thermoplasmonics heating

In addition to optical trapping, the thermoplasmonic properties of trapped metallic particles is exploited to fuse biological membranes to investigate phase separation. Thermoplasmonics, or plasmonic heating, refers to generation of heat from the interaction between metallic nanoparticles (NPs) and light. Metallic NPs exhibit what is known as surface plasmonic resonance, where an incoming electromagnetic wave induces synchronized oscillation of the free electrons in the material (figure 3.6A). This oscillation leads to friction between the metal lattice and the electrons, resulting in excellent light to heat conversion. Combining optical trapping and plasmonic particles, allows for a most advantageous generation of nanoscopic heat, which can be used to manipulate biological membranes.

3.3.1 Surface plasmon resonance on metallic particles

Plasmons describe the collective oscillation of free electrons. Surface plasmonic resonance happens when the incident electromagnetic wave, matches the systems eigenfrequency, causing maximum oscillation of the free electrons in the particle. The oscillating electrons results in a charge separation, a dipole, and to describe the optics we can consider the NPs as having dipole-like scattering and absorption of light. The extinction coefficient characterizes the optical response of a certain nanoparticles, and is described as

$$C_{ext} = C_{abs} + C_{scat} \tag{3.20}$$

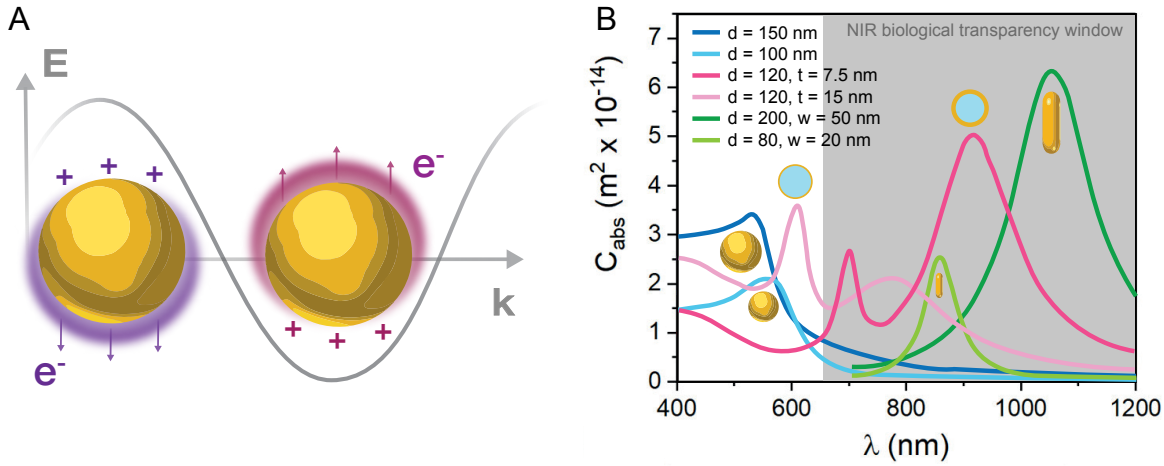

Fig. 3.6 Surface plasmonic resonance and absorption spectra for nanoparticles of various shapes. A) Schematic illustration of the interaction between the electromagnetic fields from incoming light and the conduction electrons in a metallic nanoparticle. Figure reprinted with permission from [145]. B) Schematic of representative C_{abs} spectra for gold spherical nanoparticles (blue, light blue), nanoshells with constant diameter and thickness t (pink, light pink), rods with constant aspect ratio (green, light green). NIR biological transparency window is shown with gray shading. Figure is based (with permission) on [146].

where C_{abs} is the absorption cross section and C_{scat} is the scattering cross section of the particle. For situations where the nanoparticle is much smaller than the wavelength of the light, the scattering is negligible and we can approximate[147]

$$C_{ext} = C_{abs} = 4\pi\kappa Im(\alpha) \tag{3.21}$$

Where κ is the wavenumber given by $2\pi\sqrt{\frac{\varepsilon_m}{\lambda}}$, and α is the polarizability of the particle, generally given by

$$\alpha = \frac{3V}{4\pi}\frac{\varepsilon(\omega) - \varepsilon_m}{\varepsilon(\omega) + \phi\varepsilon_m} \tag{3.22}$$

where V is the volume of the particle,ε is the dielectric permittivity of the particle at the frequency given by ω, ε_m is the dielectric permittivity of the medium and ϕ is a shape-dependent parameter. For spherical NPs $\phi = 2$, but for nanoshells (as used in this thesis) it can be calculated from[148]

$$\phi = \frac{3}{f_s}(1 + \frac{\varepsilon_c}{2\varepsilon_m}) \tag{3.23}$$

where f_s is the volume fraction given by $f_s = 1 - (\frac{a_c}{a})^3$, ε_m and ε_c are the dielectric function of the medium and the dielectric core of the shell.

From the presented equations, it is evident that changing the geometry of the particle, i.e. changing the surface electron charge density, will change the spectral location of its resonance frequency as well as the shape of the absorption spectra (3.6B). This has allowed for extensive exploration, designing NPs with desired properties by changing the size, shape, and material composition of NPs, and has lead to current commercial availability of nano- shells, rods, stars, cubes, spheres etc, having distinct absorptions spectra with ω_{max} extending into the NIR region.

3.3.2 Thermal heat profile

Thermoplasmonics, the conversion of light to heat by metallic nanoparticles when exposed to resonant electromagnetic waves, is particularly effective when combined with optical trapping. This combination creates highly localized heat sources that can precisely perturb cells and membranes, and has shown great potential for many biological applications[145]. The applicability of thermoplasmonics for such studies, lies predominantly in the ability of irradiated particles to generate heat at a level that can remodel membranes, e.g. via fusion or pore formation[149,92,150].

Gold nanoparticles are particularly effective due to their high absorption efficiency, making them ideal for applications requiring precise control over light interaction. Especially gold nanoshells and nanorods have been used in a plethora of research due

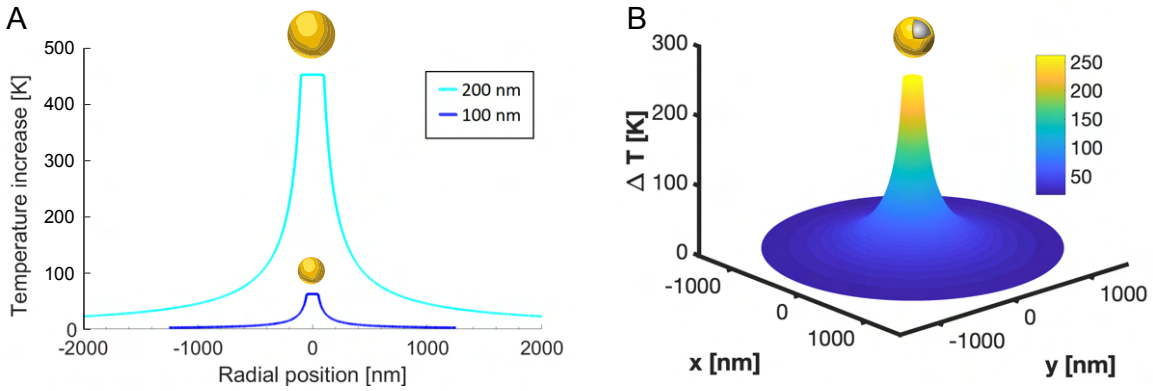

Fig. 3.7 Heat profile from irradiated AuNPs. A) Plot shows the temperature increase (ΔT) for gold nanoparticles with diameters of 100 and 200 nm. The generated heat is highly concentrated around the particle, allowing for local heating with nanoscopic precision. Plots were created considering water as the surrounding medium, and laser irradiation at wavelength 1064 nm and intensity of $I = 9 \cdot 10^{10}$ W/m^2. B) 3D rendering of the heat profile generated from a 150 nm gold nanoshell with a silica core. Same conditions for calculations as used in (A) but applied to a spherical shell. The plots were generated using an in-house script calculating the C_{abs} from Mie equations as in [151].

to their easy absorption spectra tunability, allowing maximum absorption in the NIR region (figure 3.6B).

The temperature increase in the vicinity of the irradiated NP can be calculated by solving the heat transfer equation and relating it to the C_{abs} to get

$$\Delta T(r) = \frac{I}{4\pi K r} C_{abs} \tag{3.24}$$

where r is the distance from the center of the irradiated particle, I is the laser intensity, K is the thermal conductivity of the medium and C_{abs} is the absorption cross section defined in Eq. 3.21. By determining C_{abs} for an NP, the temperature increase upon irradiation can thus be predicted (3.7 A,B). Experimental validation of the generated heat profile has been done for several NPs[151,152].

3.4 Biological applications of optical trapping and thermoplasmonics

Disclaimer: This section provides an overview of how optical trapping and thermoplasmonic heating can be applied to biological questions. The thoughts presented here led to the first-author review "Biological applications of Thermoplasmonic"[145]. Here, the major points are reproduced with modifications for the benefit of the reader of this thesis. For further discussion of this topic the reader is referred to the published article (appendix B.4).

Optical tweezers are a highly specialized instrument that can measure forces with pico newton precision by optical trapping nanoscopic objects and analyzing their movements[128] (see section 3.2.2). The tool is extremely useful for biological probing, since the forces that are acting in microscopic organisms such as cells, are on this scale.

One of the earliest uses of optical tweezers in the study of biomolecules involved measuring the movement of silica beads, which had kinesin motors attached, along microtubules[153,154,155]. The displacement of the bead within the trap demonstrated that kinesin moves in distinct steps, and since then many molecules such as DNA have been investigated with optical tweezers[156,157]. Optical forces can be employed to reposition cellular compartments, facilitating the study of organelle activity[121,158]. Additionally, this technique can be used to assess the viscoelastic properties of the cell cytosol during various stages of the cell cycle[159,160,161]. By attaching a membrane-

binding bead to a small section of the plasma membrane and pulling tubes from it, researchers have investigated numerous cellular dynamics, such as cell tension underlying cell motility, protein organization through curvature sensing[142,13], and the formation of microsomes during cell migration[162]. Furthermore, optical tweezers have been instrumental in studying the dynamics of filopodia—long, slender projections that cells use for communication and movement[124]. By mimicking these cellular extensions, optical trapping has revealed the mechanisms of their retraction, which involves actin polymerization. Additionally, by applying pressure to cell surfaces and nuclei, researchers can explore how cells respond to mechanical stimuli and how these stimuli might influence the activation of mechanosensitive proteins and molecules[163,164].

Thermoplasmonics refers to the generation of heat from nanomaterials that possess plasmonic properties (see section 3.3). The localized nanoscopic heating produced by lasers has shown significant potential not only for investigating biological materials but also for controlling biomolecular dynamics. This technique has been extensively used in various ways to manipulate cells, including directing cell differentiation[165], locally

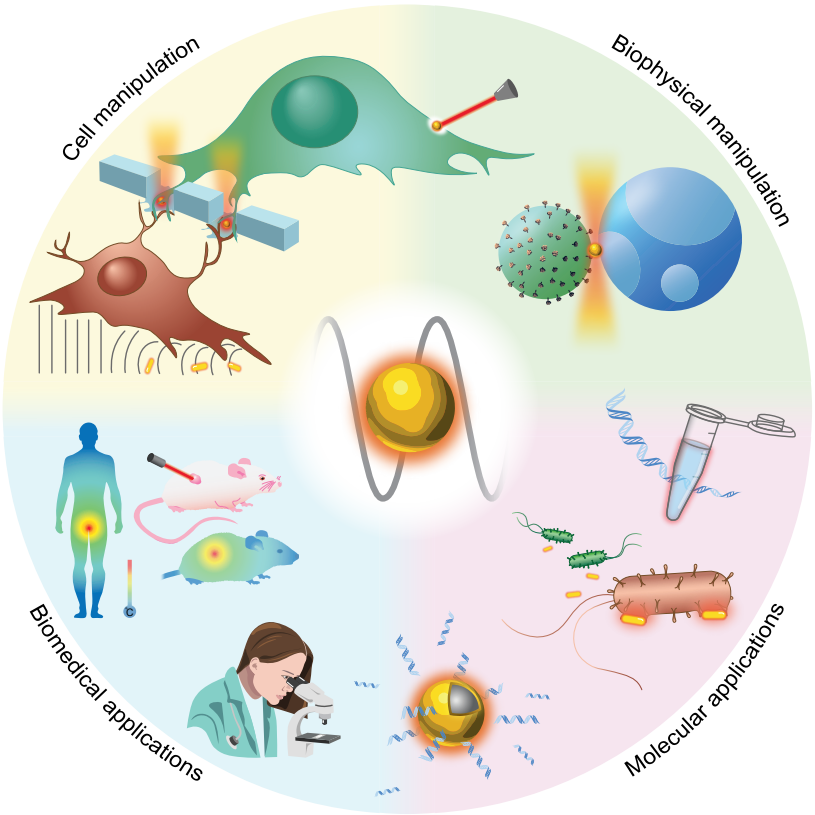

Fig. 3.8 Biological applications of thermoplasmonics. Original illustration, published in Ruhoff et al [145] showing examples of thermoplasmonics used in cell and biophysical manipulation as well as molecular and biomedical applications. Reprinted with permission.

modifying cell networks[166], and studying cell signaling and mechanical stresses[167,168]. In the context of gene therapy and drug delivery, thermoplasmonics has demonstrated numerous benefits, such as investigating and controlling uptake mechanisms[169] and remote triggering of drug release[170]. Additionally, new light-based therapeutics for cancer treatment have shown promising preclinical results[171]. Overall, thermoplasmonics has a broad range of applications in biology, which are comprehensively reviewed in the aforementioned review, focusing on cell manipulation, biophysical manipulation, and molecular and biomedical applications (figure 3.8). In the following research, the biophysical manipulation capabilities of thermoplasmonics have been utilized to study protein behavior on membrane surfaces.

The combination of thermoplasmonic and optical trapping provides an excellent platform for extremely controlled and nanoscopic use of heating to manipulate for example cells and model membranes. When using a focused laser to trap particles that show plasmonic properties,, the particles get localized to the center of the trap where they will exhibit plasmonic heating at nanoscopic scale, depending on the particle. This allows for direct control of where exactly the heating shall be applied, and this feature can be utilize to puncture cell membranes for the delivery and extraction of objects to and from the cell cytoplasm[172,149] and study of membrane repair mechanisms[92]. In addition, such heating can lead to fusion of membrane vesicles by heating exactly at the interphase between vesicles.

In the next chapter, thermoplasmonics is utilized in a novel assay to fuse model membranes with distinct membrane compositions, to investigate the membrane phase partitioning of influenza proteins embedded in the viral envelope.

Chapter 4

Study 1: Phase affinity of viral proteins

4.1 Introduction

Disclaimer: The motivation and results of the study presented in this chapter, led to the publication "Thermoplasmonic vesicle fusion reveals membrane phase segregation of influenza spike proteins" in Nano letters[93] (appendix B.1). The study is presented here with additional discussion and experiments.

The lipids comprising the plasma membrane are capable of forming tightly packed, transient lipid domains on the cell surface, suggested to be involved in the lateral organization of proteins[10] for vital cellular processes ranging from membrane trafficking and signaling[173,12,174] to cell apoptosis[175,176]. In addition, liquid ordered domains have been shown to play an important role host-pathogen interactions[177,178,179] and for budding of enveloped viruses[41,78].

Enveloped viruses such as Influenza A virus (IAV), are dependent on correct orchestration of viral proteins in the host membrane to initiate formation of infectious progeny virions (section 2.3.6). Collective clustering of the IAV spike proteins Hemagglutinin (HA) and Neuraminidase (NA) and the matrix proteins (M1 and M2) is needed at the budding site of infected cells, and such clustering has been proposed to be driven by association of particularly the spike proteins with transient liquid ordered domains in the host membrane[73]. Such domain co-localization could provide a platform for protein-protein crowding capable of driving membrane remodeling and virion formation as discussed in section 2.3.8.

Detection of liquid ordered nanodomains in cells is extremely challenging due to the transient nature of these dynamic domains, and as such their existence in vivo is still disputed[11]. Current methods for studying protein-nanodomain interactions

include molecular simulations of L_o association[180], compositional analysis of detergent resistant membrane domains in cells[181,177,75], and reconstitution in domain forming model membranes[113,13,182] as well as some recent advances in cell imaging[11], with many of these requiring tedious (and questionable) sample preparation. Using model GPMVs, HA and NA have recently been shown to partition into liquid disordered phases upon membrane partitioning at low temperatures and the addition of the cross-linker cholera toxin B (CTxB)[14,13]. These findings challenge earlier accepted models of viral budding mediated by L_o domain-association and have opened up for new questions regarding how viral assembly of proteins happens in the plasma membrane. Still, the procedures involved in these studies can be questioned due to the non-physiological temperatures at play and chemical agents involved, and this applies to earlier studies showing L_o domain localization as well. Developing more diverse methods for investigating protein-nanodomain interactions will help elucidate the mechanism behind assembly of viral proteins in the plasma membrane.

Here, a novel assay is presented, capable of addressing association of transmembrane proteins with liquid ordered domains in phase-separated model membranes, without the need for chemical cross-linking and at physiological temperatures set by the miscibility transition of the lipid mixture. The assay employs thermoplasmonics to fuse a GPMVs expressing the protein of interest in native orientation with phase-separated GUVs, to create phase-separated hybrid vesicles in which the proteins partition into preferred phases. The method does not require tedious protein purification and can easily be applied to any cell expressed membrane proteins. In addition, the controlled fusion allows for live observation of diffusion and provides the ability to study protein-protein interactions by combining multiple proteins in membranes in a controlled manner. The phase preference of IAV proteins is investigated to demonstrate the applicability of this assay.

4.2 Objective and contribution

The objective of this study was to investigate phase partitioning of viral proteins into L_o and L_d domains, to elucidate the underlying mechanisms involved in viral protein assembly at the budding site.

For this study, I contributed with replication of preliminary data and a number of control experiments for the paper, which provided substantial discussion points for the Supplementary Information. I contributed all data for M2 and SARS-CoV-2 spike phase partitioning (only presented in this thesis) and the majority of fusions for

NA, HA and NA42, which was further used to investigate limits and advantages of the method as well as characterize the success of hybrid vesicle formation with intact phases based on biophysical features. The scientific design and method development was completed by Mohammad Reza Arastoo and Guillermo Moreno-Pescador together with supervisor Poul Martin Bendix, and Mohammad carried out the first experimental data for the constructs HA-FL, HA-TMD, NA-FL, NA-62, NA-42, GPI. Salvatore Chiantia and Robert Daniels were involved in idea generation and development of the tested plasmids.

4.3 Results

4.3.1 Novel assay transferring proteins to phase-separated model membranes

To study the organization of plasma membrane proteins in membranes with distinct biophysical properties while preserving physiological conditions, we developed an assay to transport cellular expressed transmembrane proteins into synthetic membranes showing macroscopic L_d and L_o domains. By utilizing the nanoscopic heating generated upon NIR laser irradiation of thermoplasmonic nanoparticles, we fuse native and synthetic membrane vesicles and observe in real time, employing confocal microscopy, the protein dynamics at the surface leading to eventual phase separation at single vesicle level in L_o and L_d domains.

A sample of HEK293T cells transfected with the protein of interest is subjected to a vesiculation reagent, causing the development of GPMVs that protrude from the plasma membrane, eventually detaching from the cells and floating in the surrounding solution. The cells continue to supply the sample with GPMVs of various sizes, containing the protein of interest given that the cell was effectively transfected. The fluorescence intensity of the proteins in the GPMVs depend on the transfection efficiency. The proteins have the correct orientation in the GPMVs as they bud from the cells, compared to the random orientation of transmembrane proteins observed in many other methods (see section 3.1.1).

Phase-separated GUVs and AuNS are added to the sample, the AuNS binding to the GUVs via a streptavidin-biotin connection. A GPMV with high fluorescent intensity is then trapped with the optical laser and moved in close proximity to a GUV showing clear L_d and L_o phases (figure 4.1A). Once in contact the laser is moved to the intersection of the two vesicles and pulsed to create short bursts of nanoscopic heating,

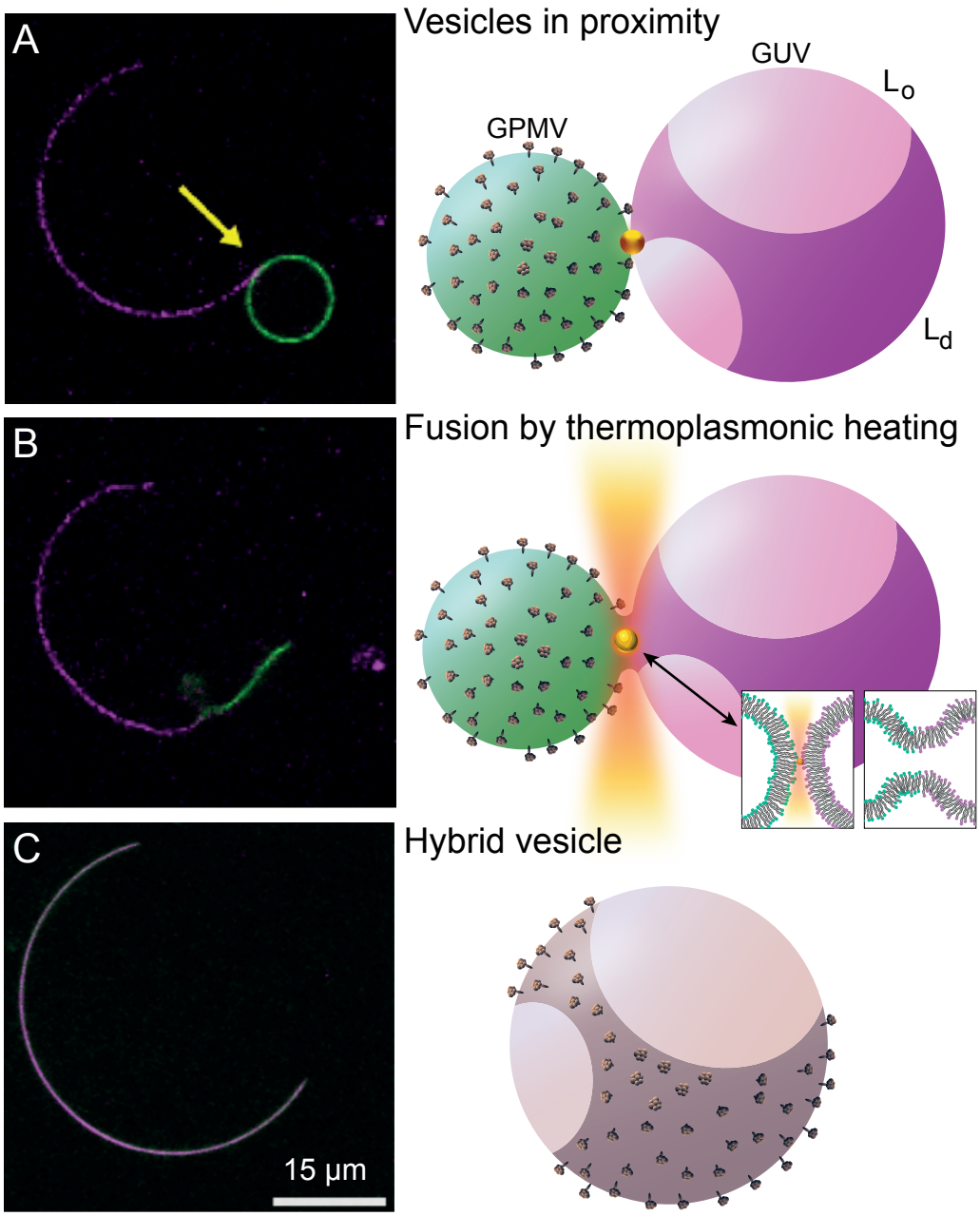

Fig. 4.1 Novel membrane fusion assay utilizing thermoplasmonics. (left) microscopy images from fusion experiments (right) schematic showing the fusion step. A) A phase-separated GUV (violet) placed in contact with a GPMV containing a protein of interest (green). Yellow arrow highlights the intersection and placement of laser. B) (left) Image showing the instant fusion of the two vesicles. (right) Schematic of irradiated nanoparticle at the vesicle interphase. Insert shows the change in the lipid bilayer upon fusion. C) (right) The hybrid vesicle post fusion when lipids and proteins have mixed. (left) Schematic fo the hybrid vesicle with proteins preferentially located in the L_d domain.

as AuNS are briefly trapped and heated in the laser focus at the intersection of the vesicles. When the AuNS enter the optical trap, they quickly disintegrate structurally

or escape the focus, providing shortlived thermal pulses at the interphase, still the laser is additionally manually pulsed, in order to avoid excessive heating at the interphase from a vast amount of AuNS continuously heating and disintegrating.

In addition, the transiently headed region around the AuNS is highly localized, with high temperatues ($\Delta T > 100$ °C) only achieved within 100 nm of the nanoparticle, as confirmed both experimentally and theoretically[151,146]. Any thermal damage to lipids and proteins during exposure to heating from this method is expected to be minor and can be neglected. Evidently, constant and prolonged heating of the membrane with high laser power will eventually affect the proteins and damage the lipids. Thus, if fusion does not happen within the timescale of a few minutes, the fusion pair is abandoned.

AuNS can move into the trap from the surrounding medium, however by using streptavidin coated particles and adding biotin on the GUV the AuNS are concentrated at the vesicle surface where they are mobile and get pulled into the optical focus at the membrane interphase. Ensuring the contact point of the two apposing vesicles is in the same focal plane as the optical trap is essential for efficient thermoplasmonic heating. Upon irradiation the lipid bilayers briefly melt (figure 4.1B), allowing the two distinct membranes to fuse to together, becoming a single hybrid vesicle[183]. Fusion into a single expanded vesicle is instant and the diffusive mixing of the membrane components can be tracked in real time in confocal microscopy. The hybrid vesicle will now have the characteristics of both the synthetic and plasma membrane, containing the protein of interest from the GPMV while maintaining the phase separation of the GUV. If the protein has a phase preference it will diffuse to this preferred phase accordingly, allowing us to investigate how membrane compositions affect lateral protein organization (figure 4.1C).

In this assay the experiments can be performed close to physiological temperatures, as the hybrid vesicles show a miscibility temperature of ≈ 30 degrees for a few examples (figure 4.2). More vesicles should be analyzed to get a more accurate read on the Tm, however, the single vesicles nature of the fusion limits the collection of a statistically significant sample, in addition, the various size range in the fusions will impact the composition of the hybrid vesicles and thus also the Tm. When raising the temperature of the chamber, the phases dissolve and mix completely (figure 4.2), upon cooling the phases re-appear confirming the protein phase preference and ensuring it was not affected by the pre-existing bilayer conditions, nor governed by whether the fusion was performed into an L_o or L_d domain. In addition, any boundary clustering that might happen very close to transition temperatures can potentially be observed.

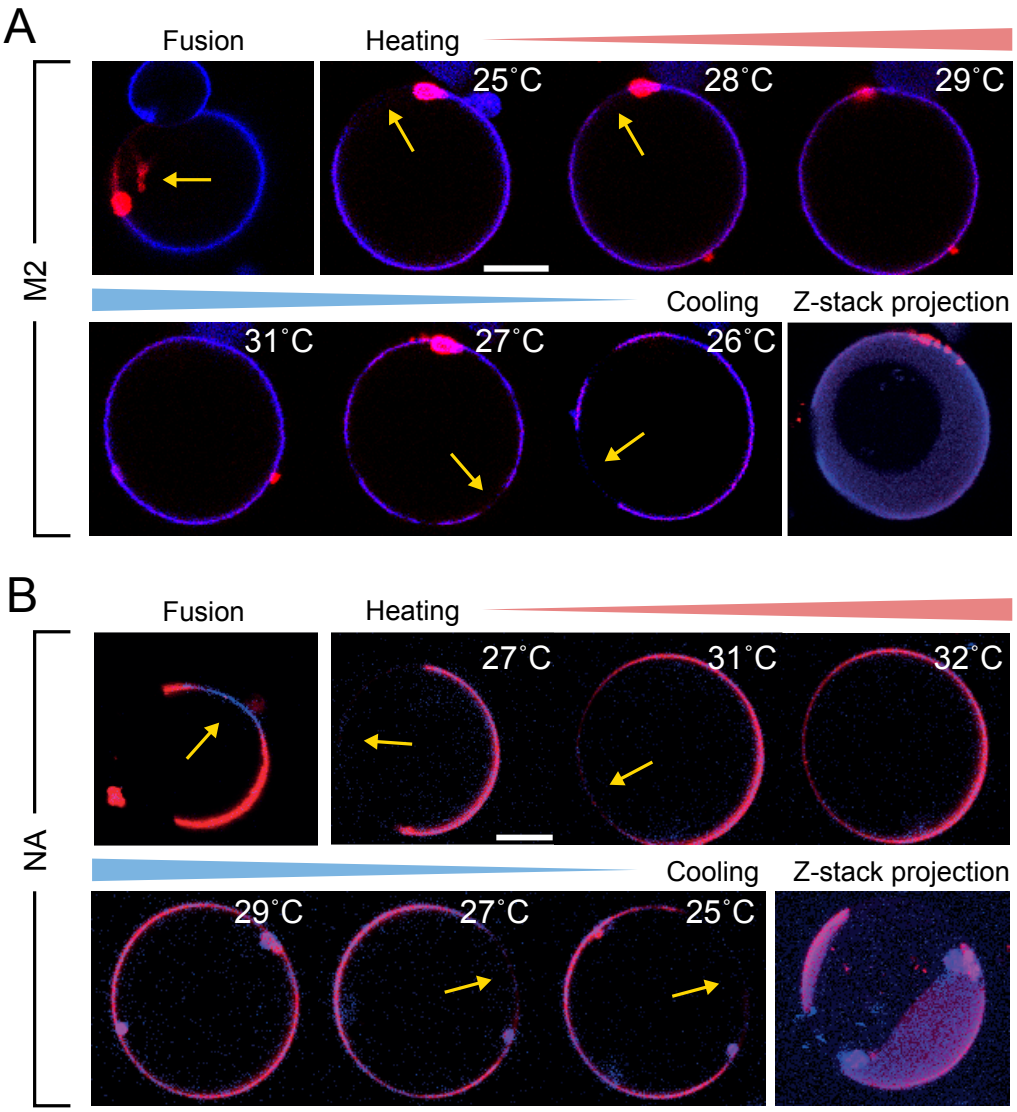

Fig. 4.2 Phase preference at phase transition temperatures. A) M2-mCherry GPMV (red) fused into L_o domain of a phase-separated GUV with DiO labeled L_d phase (blue). Yellow arrows mark place of fusion (most left panel) and placement of L*o* domains. B) NA-FL-GFP GPMV (blue) fused into L_d domain of a phase-separated GUV with DiD labeled L_d domain (red). Z-stack projection (max) of top half vesicles. Scale bars are 10 μm.

The assay stands apart from previously described techniques for investigating phase separation. It does not require cooling of the membrane to sub 20°C nor the addition of cholera toxin B which are common conditions for achieving phase separation GPMVs. Often DTT is used for preparing phase-separated GPMVs as it is shown to cause a much higher miscibility temperature when compared to NEM[120]. However DTT might have an adverse affect on the dynamics of proteins in the membrane[16,120] (see section

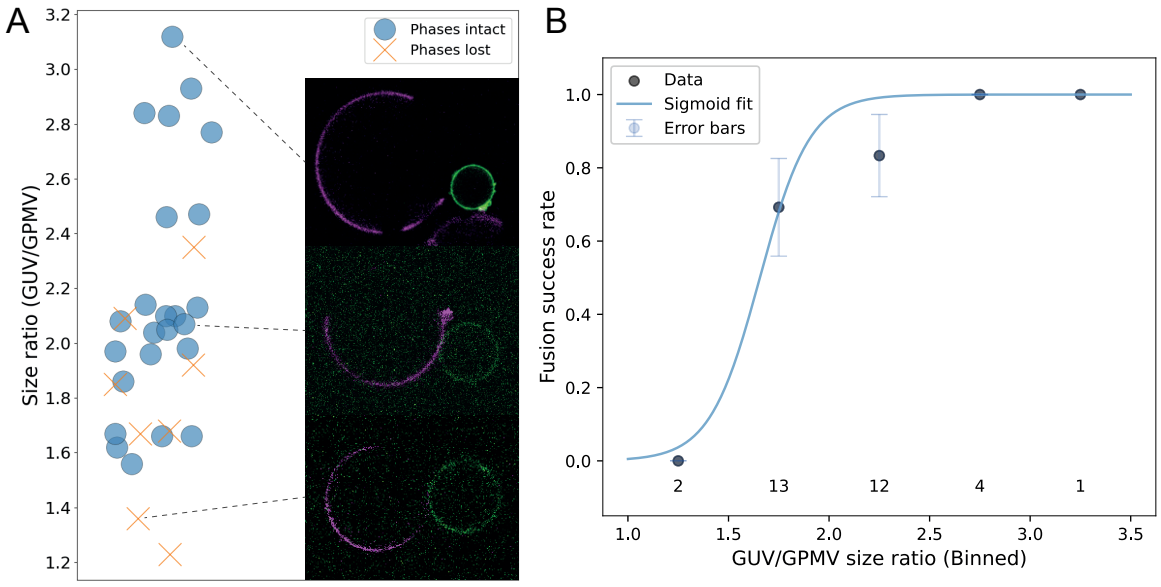

Fig. 4.3 Quantification of GUV:GPMV size ratio. A) Random scatter of the size ratio (GUV/GPMV) of 32 attempted vesicle fusions resulting in intact phase separation (blue circle) and lost phase separation (orange cross). Inserts of 2 fusions with phases retained and one with phases lost are shown for visualization. Data indicates that a large size ratio is optimal, however this might result in the loss of protein signal upon diffusion into a large GUV. To minimize bleaching, vesicles are imaged during the fusion process at low laser power, resulting in the variety of background noise seen in the inserts. Data shown represent fusion experiments where a pre-fusion video was recorded. Ratios were estimated from an average of 3 independent measurements of vesicle diameter using Fiji[184]. Depending on individual GUV composition phase loss can happen at various size ratios, yet, as expected, is most common at lower ratios. B) GUV/GPMV size ratios shown in (A) was binned and a sigmoidal curve fitted to the data, to show the rate of fusion success - here indicating that phases were intact in the hybrid vesicle.

3.1.2). In addition, in the assay the proteins are incorporated into the phase-separated membranes in their correct orientation as natively expressed in the plasma membrane.

4.3.2 Size ratio of vesicle fusion pairs impacts phase retention

As the GUV and GPMV membranes mix, the hybrid membrane will show a miscibility temperature of the combined lipid composition. For the GUV composition used here the miscibility temperature (Tm) is estimated to be around 33°C. GPMVs in general show phase separation from 5-25°C, with virtually all GPMVs showing L_o domains at 5°C[182]. GPMVs from HEK cells have been reported to phase separate around 10-15°C[185,13]. Fusing the GUV with the GPMV will substantially lower the Tm of the hybrid vesicle compared to the GUV, which can cause the loss of phases at the observing conditions (20-25°C). Thus the relative size of the GUV to the GPMV is an essential factor for

forming a hybrid vesicle with intact phases. For the constructs HA-FL, NA-FL and NA-42, all fusion videos obtained were analyzed, determining the GUV:GPMV ratio and noting whether the phases remained intact post fusion (figure 4.3A). There were no hybrid vesicles with intact phases below a 1.5 ratio. The range 1.5-2.3 showed both intact and dissolved phases, and solely intact phases above ratio of 2.3. The data was binned and the probability of fusion success (hybrid vesicles with intact phases) was calculated and fitted with a sigmoidal function (figure 4.3B). Based on this, it is recommended for future studies with this assay, that only ratios >2 are used for fusion pairs. It should be noted that during experiments, it was observed that very small GPMVs provide a challenge for fusion, thus upholding the ratio requirement requires large GUVs.

4.3.3 Fusion into L_d and L_o domain

The assay allows for selected fusion into L_d and L_o domains or the boundary between the phases. Creation of hybrid vesicles with intact phases were achieved for all three fusion sites (figure 4.4 and appendix figure A.2), demonstrating the versatility of the method. For fusions into the L_d domain and the phase boundary $\approx$ 20% resulted in phases lost, while for the L_o domain this number was $\approx$ 40% (figure 4.4A). This could suggest that fusion into L_o domains makes the hybrid vesicle more susceptible to phase disintegration, however close to a third of these fusions occurred below the 2.0 vesicle ratio (figure 4.4C), thus more data in this category would possibly increase the number of hybrid vesicles with intact phases observed. Still, fusion into the L_o domain causes direct disruption of the phase stability, and might have an impact on the phase separation if the hybrid Tm is close to room temperature, but stochastic diffusion on the membrane should eventually lead to phase separation if possible. During experiments the vesicles were imaged >15 min (up to 1 h for select data) post fusion to observe potential phase separation, or loss of phases.

GPMVs containing the constructs HA-FL, NA-FL and NA-42 were fused with GUVs at all domain sites for each construct (Appendix figure A.2). Still $\approx$ 40% of NA-FL fusions lost the phases, compared with $\approx$ 25% and $\approx$ 10% for HA-FL and NA-42 respectively. As discussed previously (section 2.2) the crowding of proteins on a membrane can provide enough pressure to counteract phase separation[37], destabilizing the domain when the steric pressure from crowding exceeds the enthalpy of membrane mixing in the observed system. For the proteins examined, NA shows the highest crowding ability, due to its large extracellular domain (section 2.3.8 figure 2.10), suggesting crowding could play a role in increasing the chance of phase loss in the hybrid

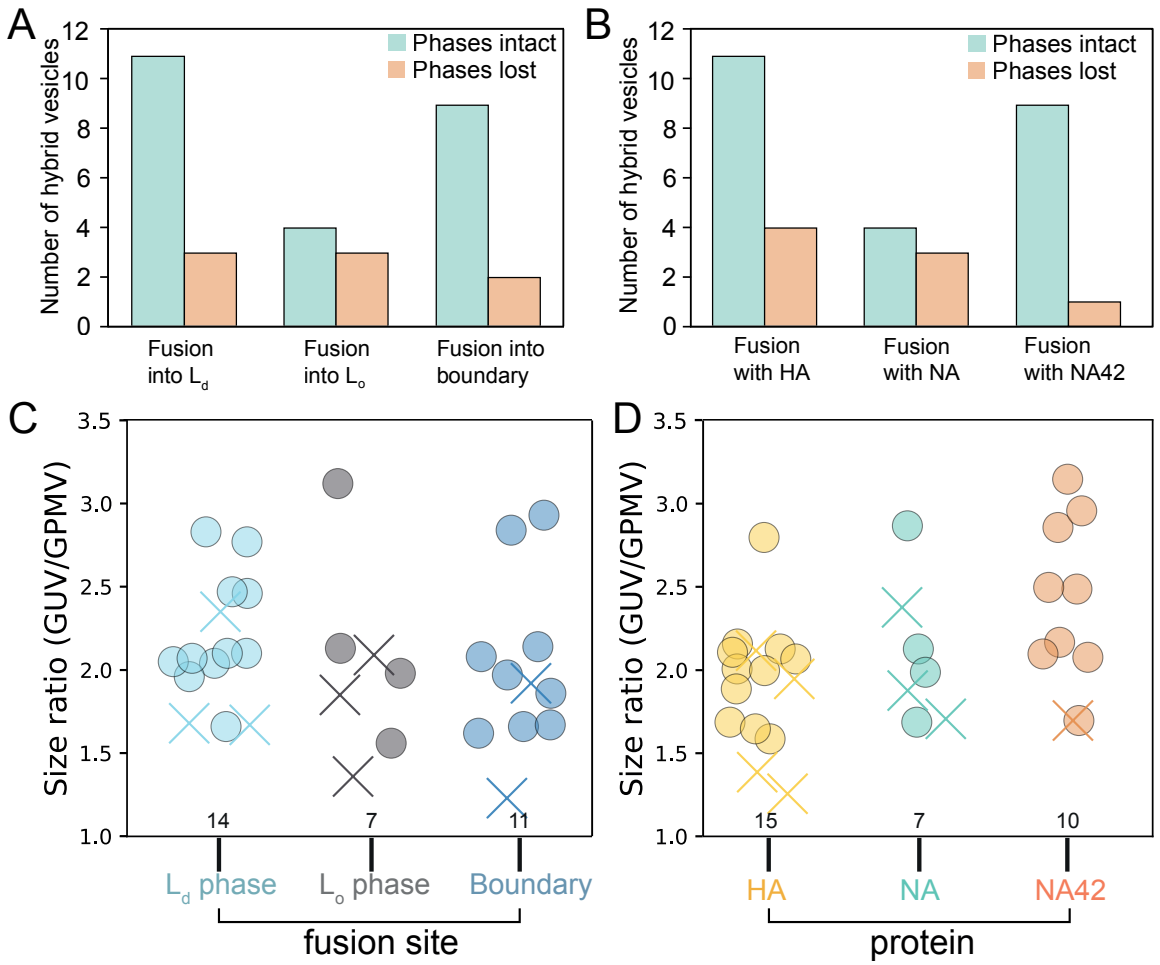

Fig. 4.4 Hybrid vesicle phase retention analysis. A,B) Bar graph showing the number of fusions experimentally completed (y-axis) in the 3 phase types (L_d, L_o and boundary) (A) as well as 3 representative protein constructs (B). Phases that are intact in the hybrid vesicle (green) and phases that were lost in the hybrid vesicle (red) post fusion are shown. From the plot, it is evident that during data collection, hybrid vesicles showed loss of phases in a number of experiments, and the loss could not be attributed to a single phase type or protein expressed. C) Size ratios for fusions initiated at the L_d phase (light blue), L_o phase (gray) and the phase boundary (blue) respectively. Fusions with intact phases (circle) and lost phases (cross) are plotted for a similar range of size ratios, and indicate no immediate effect on the phase integrity post fusion. Similarly, when the data is grouped by protein embedded in the GPMVs (D), there is no significant effect on the outcome of phase integrity post fusion.

vesicle post fusion. Whether the proteins are expressed in high enough concentration on the membrane to have an effect would require measuring the membrane properties of the hybrid vesicle (energy for lipid mixing) as well as determining the protein concentration on the surface. The latter can be done by calibrating the fluorescence from GFP to the number of GFP molecules in the microscopy system used, which has been proposed for

other proteins[186]. The pressure can be calculated using the Carnahan-Starling equation (as in section 2.3.8) and related to the enthalpy for mixing[37].

On average, transfection with NA-42 was most effective, with a greater chance of yielding GPMVs with high fluorescent intensities (Appendix figure A.1), indicating a higher concentration of this protein in the membrane compared to HA-FL and NA-FL. In addition, the NA-42 construct only exhibits two GFP conjugates, compared to four on HA-FL and NA-FL (figure 4.8), thus any increase in protein signal of NA-42 represents a 2-fold difference in protein density as compared to HA-FL and NA-FL. Since, close to all NA-42 fusions resulted in intact phases, crowding of proteins is less likely to be a driving factor in the loss of phases observed here. Overall the assay presented here has not been proven to be significantly affected by the type of proteins, however, a very high protein density (and resulting crowding) could potentially affect the ability to analyze phase preference with the presented assay.

4.3.4 Fusion timescales

The assay provides a novel way of observing real time diffusion in membrane systems. Commonly, protein preference is determined by phase separating GPMVs containing the protein, by cooling the vesicle to 10°C[182,13,187], or introducing recombinant proteins into synthetic GUVs with low Tm during formation (see section 3.1.1). These methods do not allow for direct observation of protein diffusion behavior within the non-preferred phase. Nor do they allow live observation of their behavior upon fusion *into* the non-preferred lipid domain, where proteins might clump together to from transient traveling domains before coalescence with the preferred phase.

The time scale of protein partitioning into the preferred phase, was observed to be on the order of ten to hundreds of seconds for the tested constructs. As expected, partitioning times increased as the GUV size increased, as shown for example for SARS-CoV-2 spike protein, (CoV-S), where a GUV ≈ 20 μm diameter, showed complete phase separation after about 35 s, while a GUV ≈ 40 μm diameter achieved this in around 135 s (figure 4.5). Both were the result of fusion into the preferred phase of the protein, here the L_d domain. Similar time scales were observed in general for the constructs examined, but was not characterized further for each protein. Neuraminidase mobility in GPMVs has previously been observed to have diffusion coefficients on the order of ~ 1 $\mu m^2/s$[13]. The observed time scales for complete partitioning observed are similar to such reported values. When fusion occurs in the non-preferred phase of the protein the complete partitioning was delayed, as shown for e.g. CoV-S in figure 4.5.

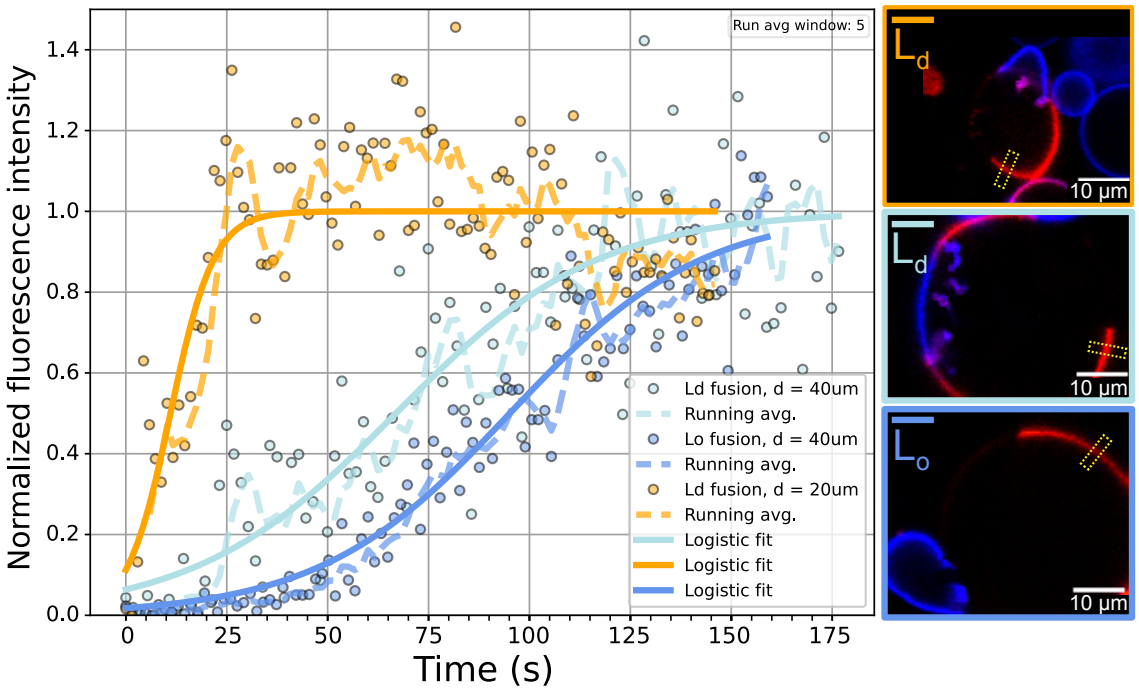

Fig. 4.5 Time scales of fusion in L_d and L_o domains of different sized vesicles. Plot shows normalized intensity of the protein (CoV-S) in the region marked (yellow dotted square) in the confocal image inserts (right side). The marked region was analyzed over time to determine the partitioning time for the protein into the L_d phase. (Vesicle diameters: light blue = 37.9 μm, dark blue = 39.4 μm, orange = 19.5 μm). The smallest vesicle (orange) equilibrates after $\sim$ 35 s and the larger (light blue) after $\sim$ 135 s which yields at time ratio of $t_{ratio} = 135/35 = 3.86$. From the diameters we get the estimated surface area ratio $s_{ratio} = 3.78$, showing that our measurements are in accordance with theory. The fusion into L_o domain (dark blue) was not imaged long enough to ensure complete partitioning, as the running average shows intensity increase in the final 5 seconds, however the logistic fit still gives an indication of the behavior observed. From a surface area difference between 37.9 μm and 39.4 μm in diameter, we get the ratio $s_{ratio} = 1.08$. Estimating the fusion (dark blue) to equilibrate around 175 s we get $t_{ratio} = 175/135 = 1.3$. This indicates that the size ratio is not enough to explain the difference in observed equilibration delay, but the slower diffusion through the L_o domain could explain this instead.

Interestingly, for the NA-42 construct, a fusion into the non-preferred domain (L_o) showed that the protein did not travel homogeneously through the L_o phase, and eventually partitioned into the L_d. Rather it seemed to be traveling in small tight domains of high protein concentration around the L_o phase, before these coalesced with the L_d domain and showed complete partitioning at 10 min post fusion (figure 4.6). It is to be noted that images were not collected between 3 and 10 minutes, so it is possible that the complete partitioning happened earlier. Here the protein does not mix well in the L_o phase, and prefers to travel in tight packs, eventually distributing equally when reaching the L_d phase. Such behavior is possible to observe with this assay, and provides new insight into the phase behavior of membrane proteins.

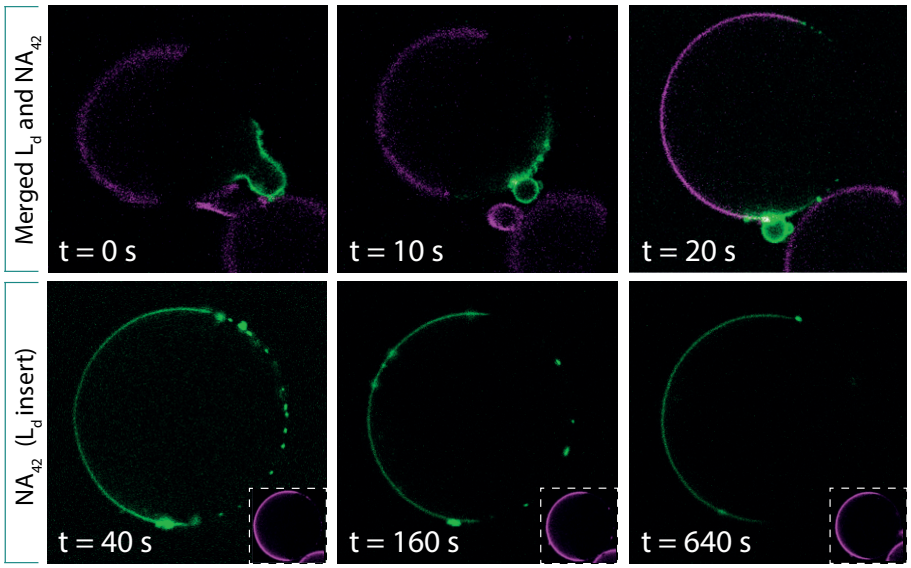

Fig. 4.6 Time scale of equilibrated protein diffusion into L_d domain. A) An example of a fusion event into the L_o domain, where diffusion of the NA-42 protein to the preferred phase (L_d) had a duration of 160s. Channels are merged (top panel) and then separated (bottom panel) for better visualization of the protein distribution. This time series represents the slowest observed diffusion in the data collected. Reprinted from [93].

4.3.5 Partitioning of viral proteins

Using the presented method, various viral protein constructs were examined for their phase preference in the hybrid vesicles. A total of 44 successful fusion were examined and the collected results are presented in figure 4.7 and each protein result is presented in the following subsections. A GPI anchored GFP construct was used as a control to confirm the presence of phases in the hybrid vesicles, and did indeed show a preference for the L_o domain as previously reported[16] (figure 4.7A.H). For GPI, the partition coefficient could be calculated using $K_{p,L_o} = I_{L_o}/I_{L_d}$[16] and was found to be $K_{p,L_o} = 1.4$. For all other constructs tested here, the proteins showed complete phase partitioning (100%) in the L_d domain. If any partial partitioning in the L_o domain exits for the tested constructs, it could not be revealed within the experimental conditions and sensitivity of the imaging system used here. Thus no partition coefficient was calculated for these constructs and were omitted from the following discussion.

NA prefers liquid disordered domains in model membranes

Influenza spike protein NA, is a transmembrane protein with a large ectodomain. NA appears on the surface of virions and is thought to cluster in localized budzones on the plasma membrane of an infected cell. This clustering has been postulated

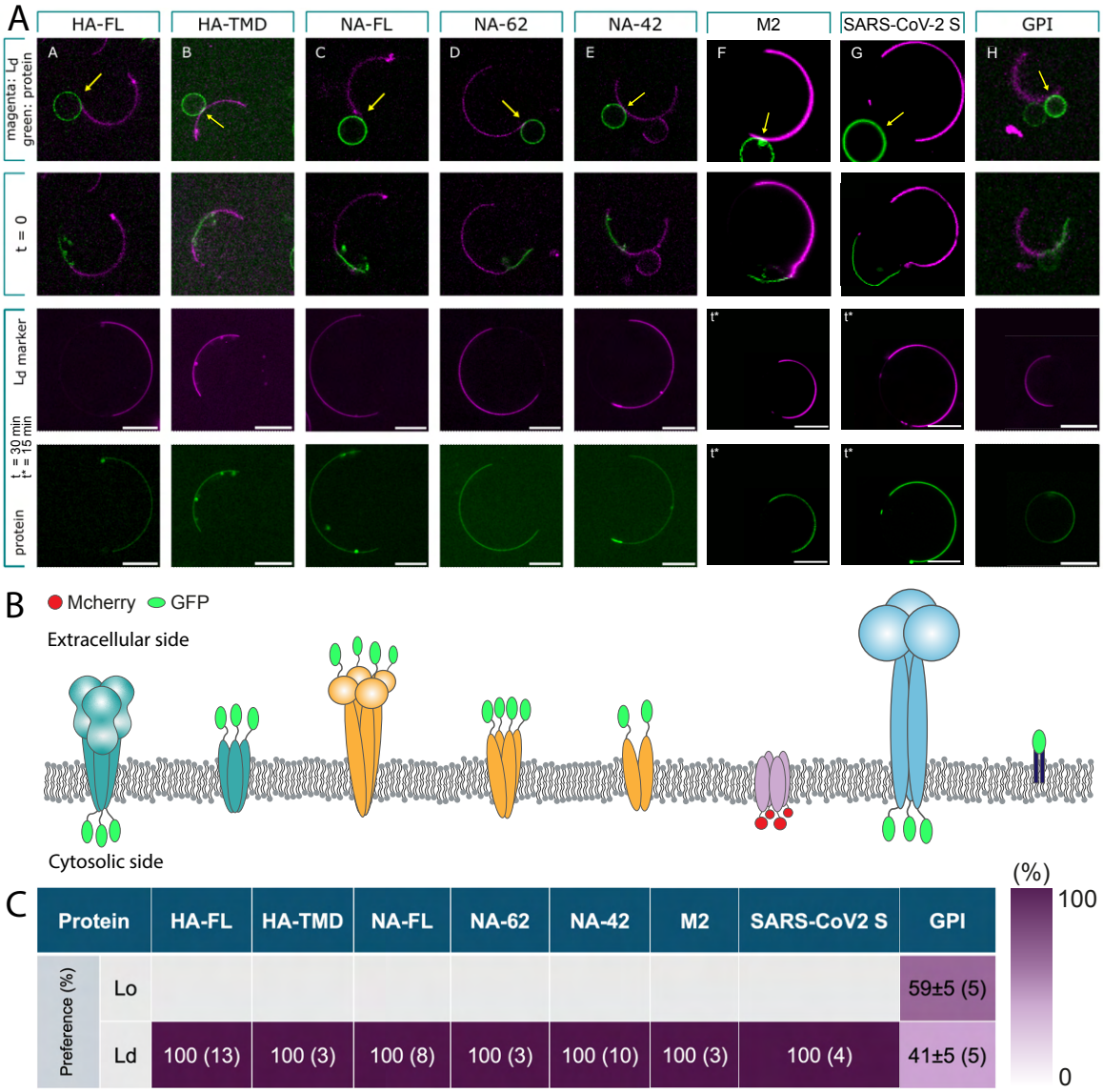

Fig. 4.7 Viral proteins show phase preference for the L_d domain. A) Example of fusion and separation of each construct tested. (top panel) Images show the phase-separated GUV (magenta) and protein-containing GPMV (green) pre-fusion, with the point of interaction of the vesicle membranes and the placement of the focused laser indicated by yellow arrows. (second panel) Images show the instance of fusion. (third panel) Images show the L_d marker channel (magenta) of the hybrid vesicle post 30 mins (15 mins for select experiments marked t*). (bottom panel) Images show the protein GFP channel (green) of the hybrid vesicle. B) Cartoon of each protein structure (relative scale). C) Overview of the percent phase separation for each protein. Numbers in purple boxes show percent preference for the given phase. All construct except GPI show 100% preference for L_d domains. Number in "()" is the amount of fusions collected for the construct, resulting in the indicated phase preference. A,B,C is adapted from [93]

to be the result of preferred association of NA with L_o nanodomains, together with other viral proteins. Although viral budding from such nanodomains has long been

postulated and early studies have shown partitioning of NA into L_o domains in in vitro studies, recent studies have shown that NA is recruited to the liquid disordered domains of phase-separated model membranes[13]. In this study, a GFP-tagged wild type NA construct was transiently expressed in GPMVs, which was subsequently fused to phase-separated GUVs (figure 4.1). The protein was found to exclusively prefer the liquid disordered domain of the hybrid vesicle, with no protein signal in the unlabeled L_d phase (figure 4.7A.C). This finding is supported by recent studies, and questions the ability of transient L_o domains to recruit NA to budzones in vivo. In addition, heating and subsequent cooling of vesicles transitioning above and below the Tm of the vesicle, did not show any change in the phase preference (figure 4.2B), yet this data was only collected for 2 NA-FL hybrid vesicles.

NA oligomerizes into tetramers on the membrane, each protein contributing to a large crown presented above the membrane surface. As crowding of proteins on a membrane surface has shown to impact the organization of lipid domains, countering phase separation[37], it is possible that NA, in the absence of other viral proteins, is repelled from the tight packing of the L_o domain due to the emerging lateral pressure from the crowding of these head groups. This hypothesis was tested by expressing a truncated version of the NA protein (figure 4.8), where the head group is removed from the stalk of the protein. This truncated version, NA-62, has significantly less crowding ability yet the protein was similarly found to partition exclusively in the L_d domain, indicating that the head group of the NA protein does not alter the phase preference of the protein when expressed in HEKT293 cells in the absence of other viral proteins (figure 4.7A.D).

Oligomerization of proteins in the plasma membrane has been shown to affect the lateral organization of the proteins in the lipid membrane, driving L_o domain association[188]. It has been proposed that cells can tune the organization of membrane proteins by altering protein oligomerization, and thereby L_o domain association, on and off as required using molecular signals[189]. To test for the effect of the tetrameric state of the protein, a truncated NA mutant similar to NA-62, that dimerizes in the membrane was investigated. This NA-42 construct was observed to behave similarly to NA and NA-62, partitioning solely in the L_d domain (figure 4.7A.E). The nature of the phase the fusion was initiated in did not affect the partitioning result (appendix figure A.2). From these experiments it can be reasoned that the oligomeric state of the protein does not affect the phase preference of the truncated construct, and that in general NA and relevant mutants partition exclusively into the L_d domain when expressed in isolation.

HA partitions into liquid disordered domains in model membranes

Similarly to NA, the viral spike protein HA localizes in viral budding zones of infected cells, and is presented on the viral envelope of progeny virus in a 6:1 ratio to NA. HA is also postulated to be recruited to site of liquid order in the plasma membrane, and has been widely studied. HA has been reported to associate with L_o domains in infected cells and GPMVs[17,190] and 'non-raft' associated derivatives of HA, show decreased infectivity[75]. Modifications to the cytoplasmic tail of HA, as well as NA, have also been shown to decrease association with detergent-insoluble glycolipids, indicating that such modifications shift the protein association to 'non-raft' domains[79].

Contradictory more recent studies report the association of HA with L_d domains in model membranes[14], as opposed to detergent based studies[79]. Here a GFP tagged HA construct, forming primarily trimers in the plasma membrane, was observed to segregate completely into L_d domains in hybrid vesicles post fusion (figure 4.7A.A), indicating that contrary to popular belief, HA expressed alone in GPMVs is not recruited by liquid ordered domains. The lateral sorting did not depend on the nature of the liquid domain that fusion was initiated in (Appendix figure A.2)

The lateral sorting of HA has been found to depend heavily on palmitoylations at the cytoplasmic tail[191], thus a truncated version of HA, HA-TMD, with the GFP tag placed at the N terminus instead of C-terminus was engineered and tested, ensuring no interference at the palmitoylation sites of the protein due to hindrance from the tag. HA-TMD was also found to exclusively sort into the L_d domain of the hybrid vesicle (figure 4.7A.B), confirming that the cytosolic fluorescent tag did not impact the protein behavior. The results obtained, question the ability of L_o nanodomains to recruit the viral spike proteins, when expressed in isolation of the other viral proteins.

M2 partitions into L_d domain and does not show phase boundary localization

The M2 is a vital player in virion escape from the host cell, thought to be involved in scission and release of viral progeny from the plasma membrane. M2 is largely excluded from the viral envelope, and has been shown to localize at the budding neck of protruding virions[64]. It has been postulated that M2 partitions to the phase boundary of L_d and L_o domains in membranes, thus facilitating localization of the protein at the budding neck as a new progeny virus buds from and L_o domain. With the presented assay, M2 phase preference was investigated in model membranes and was found to prefer the L_d domain in hybrid vesicles containing both L_o and L_d domains (figure 4.7A.F). Contrary to previously observed behavior, M2 was not shown to localize at

the boundary of L_d and L_o in the hybrid vesicles. Heating and subsequent cooling of vesicles did not reveal any localization at the boundary close to Tm.

CoV-S prefers L_d domain

In context of the recent pandemic COVID-19, it was immediate to include this protein in the study, to ascertain if any such phase preference exists for a virus that, contrary to influenza, does not bud from the plasma membrane, but into the ER–Golgi intermediate compartment of the host cell[192,193]. It should be noted that a detailed introduction to this spike protein is out of scope for this thesis, still the results obtained pertain to the phase preference study of viral proteins conducted here. The CoV-S is similar to the influenza spike proteins as it has a large ecto domain and forms trimers in the membrane, however size-wise it is significantly larger compared to neuraminidase tetramer[58,194]. Molecular simulations have suggested that the spike protein associates with L_o nanodomains through S-acylation in the TMD[177]. This predicted domain preference was tested in cells by comparing spike protein concentration in detergent resistant membrane domains, however to our knowledge its phase partitioning has not been investigated in model membrane vesicles.

The plasmid encoding the CoV-S was modified to localize the protein to the plasma membrane, such that the protein could be expressed in GPMVs for this study. Here it was shown that CoV-S spike protein partitions completely into L_d domain of hybrid membrane vesicles (figure 4.7A.G), which, similar to the influenza proteins tested, contradicts previous findings.

4.4 Discussion

Association of viral proteins with membrane nanodomains is still a highly disputed phenomenon. In this study, the phase preference of four native viral proteins and three selected mutations were studied with a total of 44 single vesicle fusions. For the influenza spike proteins NA and HA both showed complete partitioning into Ld domains. The partitioning of NA was not affected by the presence of the extracellular crown, nor the oligomerization state of the protein, and access to the palmoytylation site of HA did not affect its phase preference either. Influenza M2 was shown to prefer the Ld domain, and although it has previously been reported to favor the boundary between L_d and L_o, no such behavior was observed. The SARS-CoV-2 spike protein was similarly found to partition completely in the L_d domain. The known L_o phase associated anchor GPI confirms that L_o and L_d phases exists in the hybrid vesicle.

The GPI anchor was found to partition into both phases with a slight preference for L_o phase, however all other tested constructs show no L_o association, not even partially. These results contradict some earlier findings of L_o domain association for viral membrane proteins. The result are representative of how the proteins behave when expressed in the absence of other viral membrane proteins as well as in the absence of the cytoskeleton of the host cell. These results, together with previous conflicting findings, demonstrate that there are more complex factors at play than simple and definitive L_o domain association of the viral proteins in plasma membranes.

The interaction and clustering between the different viral proteins on the host plasma membrane could potentially affect their organization and phase preference, functioning to concentrate all the viral proteins needed for a progeny virion in one place at the cell surface. For example it has been demonstrated that M2 recruits M1 to the plasma membrane[195]. Dynamic change of phase preference from co-existence of viral proteins in model membranes could easily be investigated with the presented assay by co-transfection of various protein combinations in the GPMVs. In addition, an exciting prospect of the assay is the possibility of subsequent fusion of GPMVs containing distinct viral proteins to observe any dynamic changes in phase affinity or membrane remodeling live as the proteins interact in the fused hybrid vesicle.

The methodology used to investigate L_o domain association of proteins can have a large impact on the results obtained and the biological relevance of such results. With various methods proteins have been shown to sort into both L_d and L_o domains depending on the conditions of the experimental set-up. In early studies, L_o domain association was determined by examining the solubility of lipids in detergents, and concluding the insoluble fractions indicating presence of these nanodomains and the presence of proteins in these fractions indicating the association of that protein with L_o domains. This method has however been criticized due to the impact of such detergents on the membrane properties[196,11]. As highlighted in section 2.3.7, much research have looked at viral infection capability by the removal of L_o associating protein sequences and found them to play an important role in viral budding, indicating L_o association is critical for establishing budzones for new viruses. In various model membranes, such as GPMVs, some viral proteins have been found to show preference for all phases depending on the conditions of the membranes[190]. As GPMVs only show macroscopic phase separation at temperatures around 10 degrees, the biological relevance of these studies is questionable. In addition, the chemicals used to prepare GPMVs, e.g. DTT, have been shown to affect the phase preferences of some proteins[16], while for other proteins no significant effect was observed[190]. Furthermore, the markers used for

identifying the different domains could impact the lateral lipid organization. CTxB has been shown to partition into L_o domains, and thus is often used as a marker of this domain in vesicles[182], however, the cross-linking properties of this sub-unit is suggested to impact the lipids and reorganize transient rafts into larger domains[197]. The notion that influenza proteins are thought to cluster in transient L_o domains of the plasma membrane, is corroborated by the finding that the viral envelope contains high level of cholesterol and lipids that are traditionally associated with L_o domains[198,199]. It is therefore logical that influenza virus might bud from liquid ordered domains, as this budzone becomes the viral envelope. Interestingly, it has been shown that influenza envelope isolated lipids only start to show progressive ordering at temperatures below 40 degree and primarily exhibit liquid disorder at physiological temperatures[200]. Stiffness studies of the viral envelope corroborates this, demonstrating no major phase transition of the bilayer at lower temperatures[201]. Thus the notion of the need for L_o association for the proteins to end up in the progeny viral envelope can be disputed and help explain the L_d association of the proteins found in this study.

Hydrophobic mismatch could be an underlying factor at play in the lateral organization of proteins in membrane domains. It has been shown that the transmembrane domain length is a predictor of phase association of transmembrane proteins[202,12]. In addition, hydrophobic mismatch between the hydrophobic thickness of a membrane vesicle and a transmembrane protein can drive protein sorting and hinder proper folding of transmembrane proteins when using cell free expression systems[203]. The plasma membrane shows a wide distribution of lipid sizes and shapes, and a significant asymmetry even between the leaflet compositions[21]. Lateral organization in the plasma membrane can thus be very dependent on local packing of hydrophobically matched lipids, and the static nature of the GUV phases examined here, might not reflect that actual partitioning in vivo. The method is easily modifiable however, and a variety of of phase-separated GUVs exhibiting various hydrophobic bilayer thicknesses could be tested for the proteins investigated in this study.

The presented technique adds a new biologically relevant model system to investigate lateral protein organization in membranes, where phase partitioning can be studied without the need of chemical cross-linkers. It allows for tuning of the Tm of the system to physiologically relevant conditions, using the GUV lipid mix composition. In addition, it provides the advantage of introducing natively expressed proteins into the model system in a way that ensures the correct orientation of the transmembrane proteins, which can be crucial for native-like observation of protein behavior and interactions. The method can be easily adapted to a variety of proteins and membranes

and allows for generic investigations of how protein behavior is affected by membrane order and vice versa, elucidating the complex dynamics of cellular organization at the plasma membrane.

4.5 Materials and Methods

Disclaimer: The methods in this chapter are published and available in Moreno-Pescador et al[93] (appendix B.1). They are reproduced here (with small modifications) for the benefit of the reader of this thesis.

4.5.1 Cell culture

Human Embryonic Kidney Cells (HEK293T) were cultured at standard conditions in 25T flasks at 37°C and 5% CO2. Cells were grown in Dulbecco's Modified Eagle Medium (DMEM, high glucose, pyruvate cat. no. 11995065) which was supplemented with 10% fetal bovine serum (FBS, Gibco, cat. no. 11550356) and 1% Penicillin-Streptomycin (Gibco cat. no. 15140122).

4.5.2 Transfection

In order to observe the dynamics of a certain protein on a cell surface, we can utilize the intrinsic cellular machinery and trick cells into expressing our protein of interest on the plasma membrane. This is done by introducing genetic material such as an engineered plasmid DNA into the cell, allowing the cell to express the protein that our engineered sequence encodes. By adding a fluorescent tag to this sequence, the protein can be observed in fluorescent imaging of the cell membrane. In this chapter, cells have been transfected with plasmids encoding for 1) GPI, 2) the influenza A virus proteins Neuraminidase, Hemagglutinin and mutations of these (NA-62, NA-42 and HA-TMD) (figure 4.8), 3) influenza A matrix protein 2 and 3) SARS-CoV-2.

The following procedure was used for transfection: A 35mm glass bottom dish (MatTek, cat. no. P35G-1.5-14- C) was pre-coated for 15 minutes with 0.01% poly-L-lysine (Sigma-Aldrich, cat. no. P8920) and washed with PBS. 300.000 HEK293T cells were then seeded in the dish and grown for 24 h. The cells were transiently transfected with the desired plasmid using Lipofectamine™ LTX and PLUS Reagent (Invitrogen, cat. no. 15338030) in accordance with the manufacturer's protocol. Minor optimizations was implemented to improve expression yield. Briefly, 1.5 µg plasmid was diluted in 75 µL Opti-MEM (Gibco, cat. no. 31985070) together with 3 µL PLUS

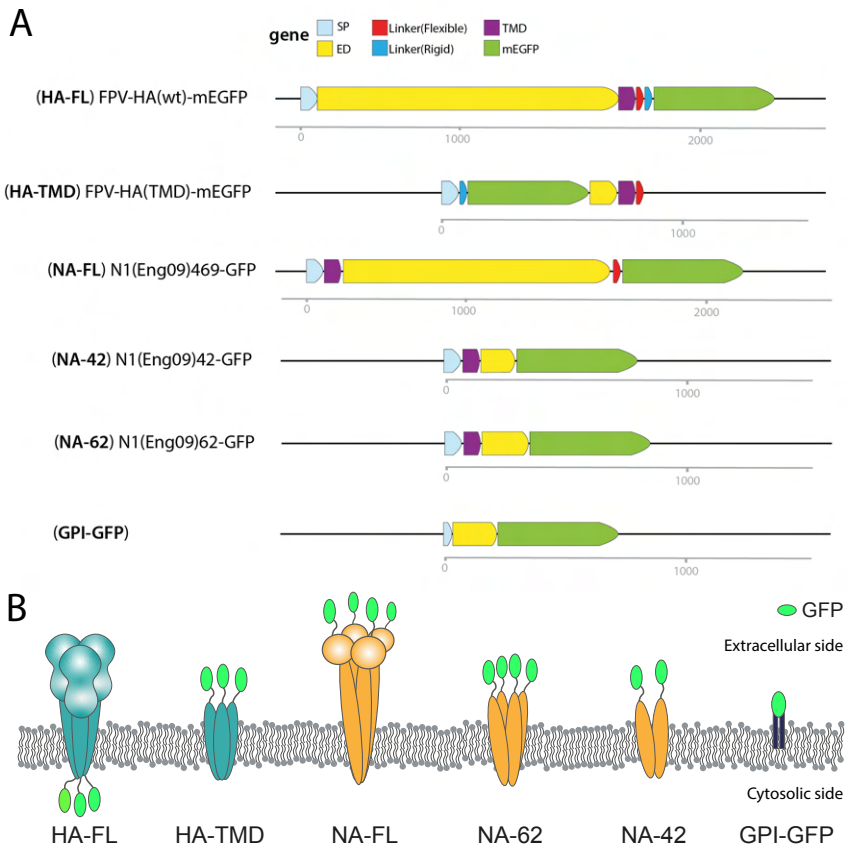

Fig. 4.8 Schematic representation of the constructs of the HA and NA protein variations as well as GPI used in this chapter. B) Schematic illustrating how the proteins assemble in the membrane adn the location of attached fluorescent GFP molecules (not to scale). Reprinted with permission from [93]

Reagent (Invitrogen, cat. no. 15338030) in an Eppendorf tube and incubated at room temperature for 5 minutes. In a separate Eppendorf tube, 3 µL Lipofectamine LTX Reagent was added to 75 µL Opti-MEM and incubated for 5 minutes, after which the content of the tubes was mixed together and incubated at room temperature for 30 minutes. The culture medium in the glass bottom dish was replaced by Opti-MEM and the prepared plasmid mix added to it drop wise. After 4 hours of incubation at 37°C, the culture medium was changed to normal growth media.

4.5.3 Giant plasma membrane vesicle (GPMV) preparation

GPMVs were obtained according to the protocol presented by Sezgin et al.[187]. Transfected cells were grown for 24 h in the glass bottom dish at 37°C and 5% CO_2. Before vesiculation the cells were washed with PBS (Gibco, cat. no. 10010023) and GPMV buffer (10 mM HEPES, 150 mM NaCl, 2 mM CaCl2, pH7.4) in succession. The

Name	Volume (ml)	Solvent (ml)	Mass (mg)	Mol (µmol)	Concentration (µmol/ml)		
SM-PC-Chol.	1.00	0.854	1.00	1.427	1.427		
Lipids			**Stock**		**Mix**		
ID-L	**Name**	**MW (g/mol)**	**g/L**	**mmol/L**	**Molar ratio**	**µmol**	**µL of stock**
AVANTI, 860062	Brain SM	760.2	10.00	13.15	40.00	0.569	43.5
AVANTI, 850375	18:1 (Δ9-Cis) PC	785.6	10.00	12.73	40.00	0.569	45
AVANTI, 700000	Cholesterol	386.4	5.00	12.94	20.00	0.284	22
AVANTI, 810150	18:1 Liss Rhod PE	1301	0.100	0.077	0.100	0.0014	18.5
AVANTI, 880129	DSPE-PEG (2000) biotin	3015	0.500	0.165	0.200	0.0028	17

Fig. 4.9 The lipid specification of phase-separated GUVs. The ternary lipid mixture consisting of Brain SM, DOPC and Cholesterol in the molar ration 40:40:20 results in phase-separated GUVs. Liss Rhod PE lipids are added to the mixture to mark the L_d domain. The biotin conjugated lipids are added to facilitate binding of streptavidin coated gold nanoshells to the GUV, to mediate the membrane-fusion event. The talbe was generated using the LIPID MIXATOR at https://nicokiaru.github.io/LipidMixator/LipidMixato. Reprinted with permission from [93].

vesiculation process was triggered by adding 1 mL GPMV buffer containing 2mM N-Ethylmaleimide (NEM, Sigma-Aldrich, cat. no. E3876), to the cells. After 2 h of incubation at 37°C, GPMVs had started to detach from cells, and were ready to be used for the fusion experiment.

4.5.4 Giant unilamellar vesicle (GUV) preparation

GUVs were synthesized using a PVA gel-assisted hydration method[99] and consisted of a mixture of DOPC (1,2-dioleoyl-sn-glycero-3-phosphocholine, Avanti Polar Lipids, cat. no. 850375), Brain SM (Avanti Polar Lipids, cat. no. 860062) and Cholesterol (Avanti Polar Lipids, cat. no. 700000) dissolved in a molar ratio of 2:2:1 in chloroform (figure 4.9). Furthermore, the lipids were mixed with the L_d marker 18:1 Liss Rhod PE (1,2-dioleoyl-sn-glycero-3-phosphoethanolamine-N-lissamine rhodamine B sulfonyl, Avanti Polar Lipids, cat. no. 810150) at 0.1 mol% to visualize the GUVs in the fluorescent microscope. 90 µL of PVA gel 5% (Sigma-Aldrich, cat. no. 363065) was spread on a clean glass slide and placed in an oven to dry at 50°C for 50 minutes. After drying, 30 µL of the lipid mix was spread on the dried PVA film and left under vacuum in a desiccator for 2 h. The GUVs were then grown by adding growing buffer (70 mM NaCl, 80 mM sucrose, 25 mM Tris) to the prepared lipid coat and incubated at 55°C for 1 h. Finally, the GUVs were harvested and kept at 4°C prior to the fusion experiment.

4.5.5 Fusion experiment

To improve the fusion of GUV-GPMV a 0.2 mol% of DSPE-PEG(2000) Biotin (1,2-distearoyl-sn-glycero-3- phosphoethanolamine-N-[biotinyl(polyethylene glycol)-2000], Avanti Polar Lipids, cat. no. 880129) were added to the lipid mix to bind streptavidin-coated beads to the surface. The streptavidin-coated gold nanoshells (AuNSs, nanoComposix, cat. no. GSIR150) were diluted in observation buffer (70mM NaCl, 55mM Glucose and 50mM Tris) with a ratio of approximately 1:20 (i.e. 12 µL AuNSs in 240 µL observation buffer) and briefly sonicated. Then, equal volume of this AuNS-containing buffer (i.e. 250 µL) was mixed with the prepared GUVs (i.e. 250 µL). Finally, 150 µL of this mix was added to the GPMV-producing cells just before the fusion experiment. The fusion experiments were carried out at room temperature which varied, according to the season, between 20°C - 25°C. Fusion were achieved by optically trapping GPMVs and moving them in vicinity of the GUVs. At the intersection point between a GUV and GPMV the trapping laser was pulsed and fusion was achieved. Cell samples were used for up to 2 hours in the optical set-up, and on average images were collected for 30 minutes after fusion, all the way up to an hour for selected vesicles as a control for long-term changes.

4.5.6 Optical and imaging set-up

A Leica SP5 confocal microscope was used for imaging of the fusions. The microscope is combined with an optical trapping laser with a wavelength of 1064 nm (Spectra Physics J201-BL-106C)[135]. The microscope was fitted with a Leica PL APO 63X water immersion objective (NA = 1.2) which was also used to focus the trapping laser. The sample contained a protein GPF tag and a lipid Rhodamine Liss tag, which were excited with a 488 nm and 594 nm laser line, respectively. The fluorescent emission was recorded in the spectral range of 493-553 nm and 598-700 nm. The trapping laser was operated with an output power of 45 mW (intensity of 3 x 10^{10} W m^{-2}) for the irradiation of streptavidin-coated 150 nm AuNSs (nanoComposix, cat. no. GSIR150) at the interface of a GUV-GPMV triggering the fusion event. The AuNSs were visualized in the sample using a 476 nm argon laser line in reflection mode, captured in the spectral range of 476-488 nm. The methodology behind optical trapping and thermoplasmonic is explained in section 3.3.

4.5.7 Data analysis

The image processing was carried out using the image analysis software Fiji[184]. A script using macro language commands was made to unwrap the vesicle signals and extract the fluorescence intensity of the protein and lipid dye along the membrane. For each image of a hybrid vesicle (post fusion), the contours of the membrane were manually selected in Fiji. The designed macro program unwrapped the marked vesicle area (with a selectable width, normally in between 5-10 pixels) creating a flat membrane from the selection. The membrane signal was determined by thresholding the intensity values and the background was subsequently removed by multiplying the masked membrane signal by the original image. The entire membrane signal was averaged by a moving window in the x direction of 3 pixels. Afterwards the intensity of each vertical pixel column was averaged and the collapsed intensities plotted (figure 4.10). The obtained intensity profiles of the unwrapped vesicle membrane clearly shows the separated L_d and L_o domains, and were used to determine the percent phase partitioning of the protein into each phase. The whole workflow can be found in the following Github repository https://github.com/GMorenoPescador/vesicle_unwrapper.

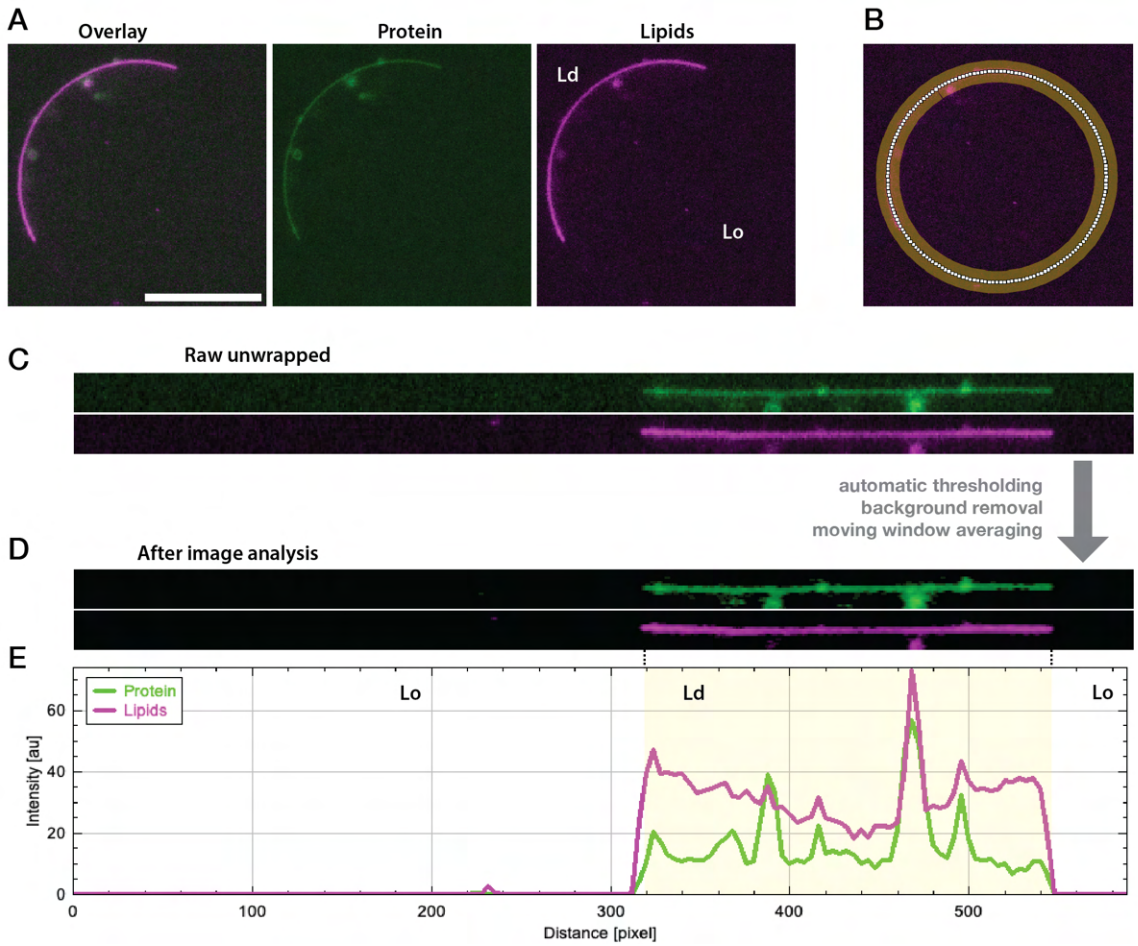

Fig. 4.10 Phase preference data analysis workflow. A) Raw data from fusion experiment show the channel overlay of GFP-tagged HA-TMD (green), and DiD lipid dye (magenta). (Scale bar 15 μm). B) The vesicle is marked using an oval selection tool. C) Resulting raw, unwrapped vesicle membranae for each channel. D) Unwrapped vesicles after image processing steps specified next to gray arrow. (E) Fluorescent intensity plot from the unwrapped vesicles in (D). L_d region is highlighted in yellow. Reprinted with permission from [93].

Chapter 5

Study 2: Induction of spontaneous curvature by viral proteins

5.1 Introduction

On the plasma membrane, constant membrane remodeling is happening while bending and breaking of the bilayer allows for the complex transport of nutrients, waste and information across the cell barrier. Numerous proteins facilitate this complex task, and conserved structural protein features have been identified as drivers of such curvature generation[22]. Yet, a structure-independent mechanism has recently been identified, indicating that the lateral pressure generated by stochastic protein-protein collisions on the membrane can drive bending to relieve the pressure (as discussed in section 2.2). This mechanism termed protein-protein crowding, relies on an imbalanced distribution of large proteins on the out and inner leaflet of the membrane, and has shown experimentally and theoretically to be able to generate enough stochastic pressure to drive membrane deformations[35,34,31]. As the spike proteins on the surface of influenza virions contain large ectodomains that are not balanced on the inside of the viral envelope, it is conceivable that they drive membrane bending through crowding to initiate viral budding from the host membrane. Modeling of the pressure generation from HA and NA, showed that they, at relevant concentrations, indeed can generate enough crowding energy to overcome the energy barrier of bending at relevant densities (figure 2.10). This theoretical insight has inspired the research presented in this study, attempting to experimentally quantify spontaneous curvature generation from viral proteins.

Measuring the spontaneous curvature of a membrane experimentally is challenging, and usually requires control of tension in the membrane. Typically micro-pipette aspiration is employed to hold membrane vesicles at a constant pressure, in order

to determine and control the tension in the lipid bilayer[204]. Although aspiration is a well known technique to study mechanical properties of membranes it requires a high technical expertise and time-consuming, tedious procedures[205] to generate reliable data, rendering such mechanical studies difficult and inaccessible. Moreover, performing micropipette aspiration studies on native membranes like GPMVs might require additional efforts due to the small sizes of these vesicles. It was recently suggested that by quantifying the forces when pulling membrane tethers in and out of stationary model membrane vesicles (GUVs), the spontaneous curvature can be inferred, without the need of tension control with aspiration[144].

Here, a novel assay is introduced, which provides a simple strategy for measuring spontaneous curvature, as well as sorting of proteins, in GPMVs without tension control by aspiration. Although GPMVs have received attraction in recent years due to their cell mimicking properties[206,207], the spontaneous curvature generation of proteins embedded in GPMVs have not been quantified experimentally to my knowledge. The assay employs optical trapping of streptavidin-coated polystyrene beads, to pull and push membrane tubes from cell-attached GPMVs expressing proteins of interest. It is demonstrated that the technique provides quantitative results on the equilibrated forces of tubes pulled both out of and into GPMVs in addition to protein sorting. Preliminary results show the possibilities of quantifying spontaneous curvature generation for selected membrane embedded proteins. With this assay, the inherent spontaneous curvature (C_s) of the plasma membrane and changes in C_s induced by expression of influenza A proteins on the surface are measured for the first time. Finally, the current limitations and future prospects of this assay are discussed. This method decreases the complexity of measuring the mechanical properties of membranes and can be extended to study protein and polymer crowding on any cell type capable of producing GPMVs.

5.2 Objective and contributions

In this project the objective was to measure experimentally whether influenza A spike proteins expressed at high densities can induce membrane spontaneous curvature via crowding.

Together with my supervisor Poul Martin Bendix, I participated in the ideation of this project. Initially, I contributed with pulling membrane tubes from cells with influenza proteins in the membrane. I then designed and carried out experiments pulling tubes inside cell-attached GPMVs for the first time in the lab, with technical assistance from Younes Farhangi Barooji, to quantify sorting of proteins in negative

curvature environments. Based on the successful in-pulls, I designed in collaboration with Poul Martin Bendix, the experimental set-up for collecting the forces from out- and in-pulls of cell-attached GPMVS to quantify spontanous curvature without tension control inspired by [144]. Small modifications to improve the technique was carried out in collaboration with research assistant (now PhD candidate) Luis Hamel Ascanio. The script used for extracting and analyzing the forces and confocal images of the tubes was written by Luis Hamel Ascanio with continuous input and guidance by me. I collected a large part of the data shown in this chapter (especially for the M2, NA-FL and NA-delta constructs), and supervised research assistant (now PhD candidate) Luis Hamel Ascanio in the collection of data with additional proteins. Finally, I carried out the statistical analyzes and prepared all figures presented in this chapter.

5.3 Results

5.3.1 Novel assay to quantify spontaneous membrane curvature

Our assay is inspired by Dasgupta et al.[144] who measured spontaneous curvature induced by glycolipids in GUVs. The assay can elucidate protein effects via protein organization at various curvatures (sorting) and forces involved in pulling membrane tubes. HEK293T cells are transiently expressed with the protein of interest and subjected to a vesiculation buffer, resulting in large GPMVs forming from the cells. The GPMVs are spherical yet firmly attached at the cell membrane for an extended time. With an optical trapping laser, a streptavidin-coated 1 μm polystyrene bead is brought in contact with the membrane and subsequently used to pull a tube with positive curvature from the GPMV surface (figure 5.1A,B). This tube is reffered to as the 'out-tube' in this chapter. Similarly, the bead can be pushed into the GPMV, to form the complementary 'in-tube' with negative curvature on the inside of the vesicle (figure 5.1C,D). The in- and out-tubes and the GPMV membrane are imaged in the confocal plane and the fluorescent intensities of the lipid dye and protein can be used to gain insight into the sorting behavior of the proteins on various membrane curvatures. The tube holding force of both the out- and in-tube can be measured with the optical trap, and this force is related to the parameters of the vesicle membrane (see section 3.2.4)

$$F_{out} = 2\pi\sqrt{2\sigma\kappa + \kappa^2 C_s^2} - 2\pi\kappa C_s. \tag{5.1}$$

for the out-tube and

$$F_{in} = 2\pi\sqrt{2\sigma\kappa + \kappa^2 C_s^2} + 2\pi\kappa C_s. \tag{5.2}$$

for the in-tube, where κ is the bending rigidity, σ is the tension and C_s is the spontaneous curvature of the membrane. κ for isolated GPMVs has previously been estimated[207] and is assumed to be 20 k_BT. Measuring either the out- or in-force can thus provide information regarding any changes in the spontaneous curvature of the membrane upon addition of crowding proteins. The out-force is predicted to decrease with increasing spontaneous curvatures, however the force measurements are influenced by the tension of the system, which can vary. The tension of a membrane vesicle is most commonly controlled using micropipette aspiration, however this requires a tedious procedure. Here, the tension of the cell-attached GPMV cannot be controlled, and results in a

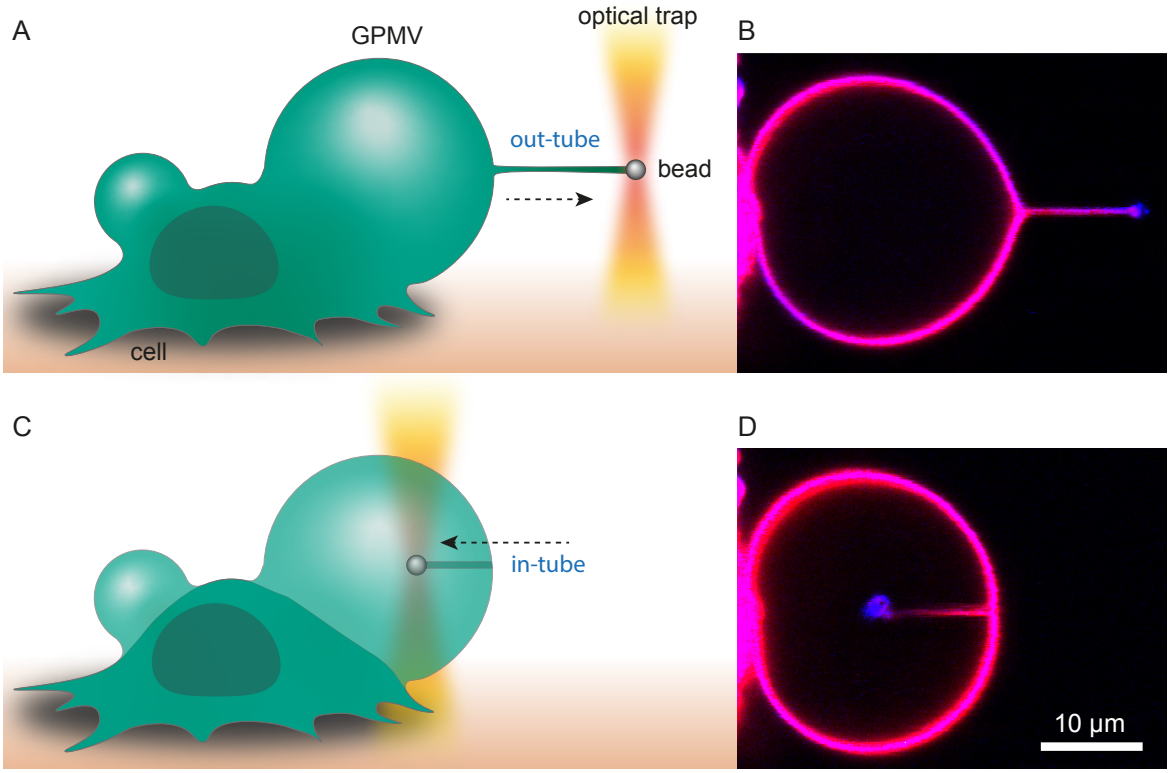

Fig. 5.1 Novel tube-pulling assay in cell-attached GPMVs. A) Schematic of the out-pull B) confocal micrograph showing an out-tube on a cell-attached GPMV with DiD (red) and NA-Δ20 protein (blue). C) Schematic of the in-pull D) confocal micrograph showing an in-tube on a cell-attached GPMV with DiD (red) and NA-Δ20 protein (blue). The polystyrene bead appears blue from the reflection of the laser. The in-tube is most intense close to the membrane where it is in the focal plane, however, closest to the bead the tube has a slightly lower intensity, indicating a slight tilt in the tube observable due to the length of the pulled tube.

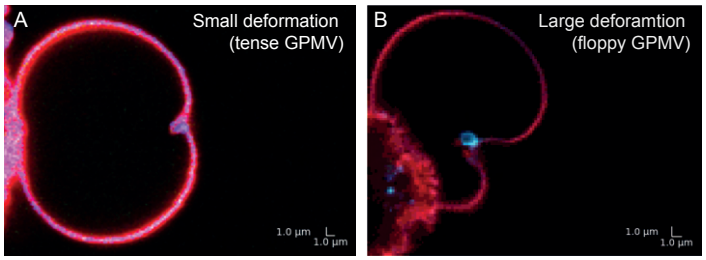

Fig. 5.2 GPMV deformations during in-pulls. A) Confocal image scan of the GPMV right before the tube collapses. A small deformation is observed, indicative of a tense vesicle. B) Confocal image scan of the GPMV showing a large deformation indicative of a 'floppy' vesicle. When the deformation is large, the in-tube is often not possible to form.

variety of tensions most readily shown by the different deformations observed during in-pulls (figure 5.2).

However, by pulling both out- and in-tubes of a single membrane vesicle, spontaneous curvature can be determined without the need for controlling tension (see section 3.2.4). Thus by pulling an out- and in-tube of the cell-attached GPMV, the spontaneous curvature of the plasma membrane expressing viral proteins can be estimated by measuring the difference in F_{out} and F_{in}[144]

$$F_{out} - F_{in} = 2\pi\sqrt{2\sigma\kappa + \kappa^2 C_s^2} - 2\pi\kappa C_s. - (2\pi\sqrt{2\sigma\kappa + \kappa^2 C_s^2} + 2\pi\kappa C_s.)$$

$$F_{out} - F_{in} = -4\pi\kappa C_s. \tag{5.3}$$

The equation is conditioned by the fact that the vesicle is stationary and is not morphologically perturbed by the in- and out-pulls, such that the tension remains constant during the whole experiment. Thus, cell-attached GPMVs provide an excellent assay where the vesicle is held steady, with little experimental preparation time. Completing the pulls on vesicles resting on a glass surface has been suggested[144], however such vesicles require firm surface adhesion, and hence become tense, and can be hard to form tubes inside due to the large perpendicular force needed to push into the membrane. Attempts on such vesicles were made during preliminary experiments and found to often lead to the vesicle being moved along the surface, perturbing the system.

To analyze the out- and in-forces it is important that the pulled tubes are visible in the focal plane when the force is determined. If this is not the case, the tube-force could likely have a large z-component, which cannot be resolved by the detection of the scattered light in the trap. Similarly, for analyzing protein sorting, it is important

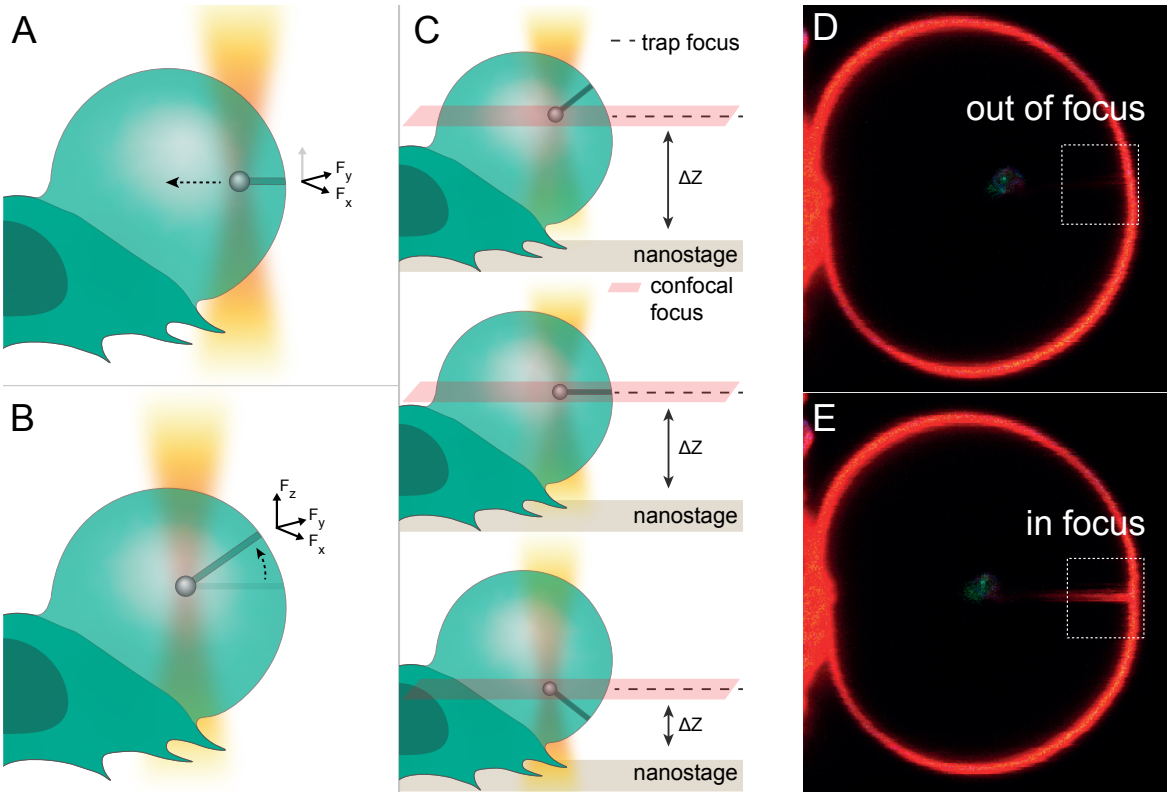

Fig. 5.3 Unpredictable z-component of in-tubes. A) A Schematic showing a short in-tube that is present in the x, y plane. As the bead is pushed further into the GPMV, the tube slides up the membrane (B), as a point further op the spherical arc is now the closest membrane point and thus the tube relaxes to this point. Now the tube exists in the x, y, z plane and has a z component to the force. C) Examples of a tether not being visible in the confocal plane (red) when the nanostage is moved so that the focal point is above or below the equator of the GPMV, allowing the tether to slide up or down out of the focal plane, while the trap is in focus. D) and E) Show a GPMV with an in-tube first out of focus (D), then moved into focus (E) by moving the nanostage and trap position.

that the tubes are in focus on the confocal image (as well as the GPMV membrane on the analyzed images). While the focus of the out-tube is easily found by moving the nanostage slightly in the z-direction, getting the in-tube in focus is more challenging, due to the geometric difference between the two pulls. As the bead is pushed into the cell, the tube will always relax to the membrane point closest to the bead, to minimize the energy in the system. When the bead is in the middle of the GPMV, the whole spherical membrane surface comes into play, and the tube can easily slip out of focus by moving in the x,y and z direction of the system (figure 5.3A,B). Indeed controlling exactly where the tube "lands" is quite tricky, and often requires short tubes, to minimize the available spherical arc the tube can relax in. Tubes pulled to the middle of the GPMV, tend to tilt, leaving only parts of the tube in focus (figure 5.1D). The tube can be maneuvered into the focal plane by moving the nanostage in

the z-direction (figure 5.3C), however the tube position was often observed to fluctuate during image scanning, complicating the acquisition. It should be noted that after tedious characterization of the optical trap, it was discovered that the calibration of the trap was only valid at the actual position where calibration was performed. Hence moving the trap would influence the spatial light distribution slightly and significantly affect the calibration parameters. This was unexpected from a commercial system where moving the trap is a standard feature. However, to overcome this shortcoming of the system all alignments should be done using the stage on which the cell is attached to instead of the trap. Moving the trap z-position was, however, required in many cases to find the in-tube during data collection. Such measurements were thus only used to quantify sorting and out-forces, as the in-force measured was unreliable.

5.3.2 Membrane tubes pulled from live cells indicate protein crowding

It is hypothesized that crowding of viral spike proteins on the membrane surface of cells induce spontaneous curvature (C_s) by generating enough pressure to overcome the bending energy threshold. To quantify this effect, the force to hold a tube pulled from a membrane can be quantified as a proxy for the spontaneous curvature, which decreases with increasing C_s for a tube in equilibrium via

$$F = 2\pi\sqrt{2\sigma\kappa + \kappa^2 C_s^2} - 2\pi\kappa C_s. \tag{5.4}$$

NA was predicted to have the largest crowding potential of the influenza A spike proteins (see section 2.3.8), thus 4 modified constructs of NA with various potential crowding potential was used to test the crowding hypothesis (figure 5.4). HEK293T cells were first transfected with the NA mutant with the highest predicted crowding potential, NAΔ20, and the holding force of pulled out-tubes was quantified (figure 5.5A,B) and compared to previously reported values for NA-FL and a control (DiD membrane dye)[208](figure 5.5C). It was previously reported that the out-forces on average increase when NA-FL is added to the membrane as compared to the control[208] (figure 5.5C, gray) and this significant increase in the average out-tube forces ($p = 0.043$: for details on all statistical analysis, see section 5.5.7) is reprinted here to provide perspective for the additional data presented in this thesis. When comparing the two NA mutants, which have the same transmembrane domains, at similar protein densities, a decrease in the force is observed between the NA-FL and NAΔ20 ($p =$

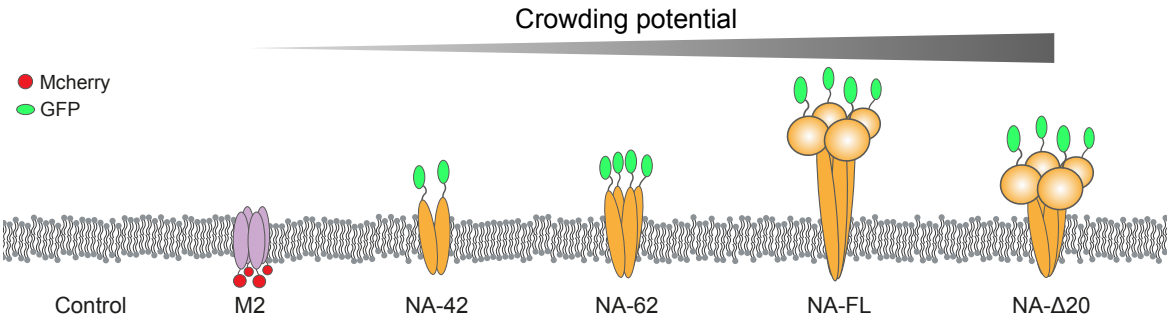

Fig. 5.4 Viral protein constructs in order of increasing crowding potential. The schematic shows M2 and neuraminidase protein constructs in a membrane depicted in sequence of their theoretically estimated crowding potential (in relative estimated scale). The neuraminidase mutants are based on the full length wildtype influenza A neuraminidase (NA-FL). It should be noted that the transmembrane domain of NA-42 is different than for the other depicted NA protein mutants, as it consists of a dimer and not a tetramer of the protein.

0.073), however the difference did not meet the statistical significance threshold of p = 0.05.

The data provides an indication that the difference in crowding potential between the two proteins can be measured by quantifying out-tube forces pulled from the plasma membrane. As the protein density is not controlled, it is relevant to observe the trend in the forces with increasing membrane coverage, as the crowding effect comes into play at high densities. In these experiments the protein density pr μm^2 has not been determined, thus the relative protein coverage is used to visualize the trend in the forces (figure 5.6D). The data points from C are plotted versus their *relative* membrane coverage, and a linear fit is plotted to guide the eye of the reader. It is not necessarily expected that any observable effects would be linear, thus it is simply used for visualization purposes of the data trends. The plot indicates that the force indeed tends to decrease as the protein density increases for both the proteins. In addition, we see that similar densities of the two proteins are represented in the box plot presented in figure 5.5C.

These experiments acquired in live cells indicating a measurable difference (minor crowding effect), motivated further studies on the crowding effect of the proteins when expressed in membrane vesicles that lack the interaction of the cytoskeleton with lipid bilayer. Reproducing the results in a vesicle system could potentially amplify the effects by isolating the bilayer from cellular interactions and processes.

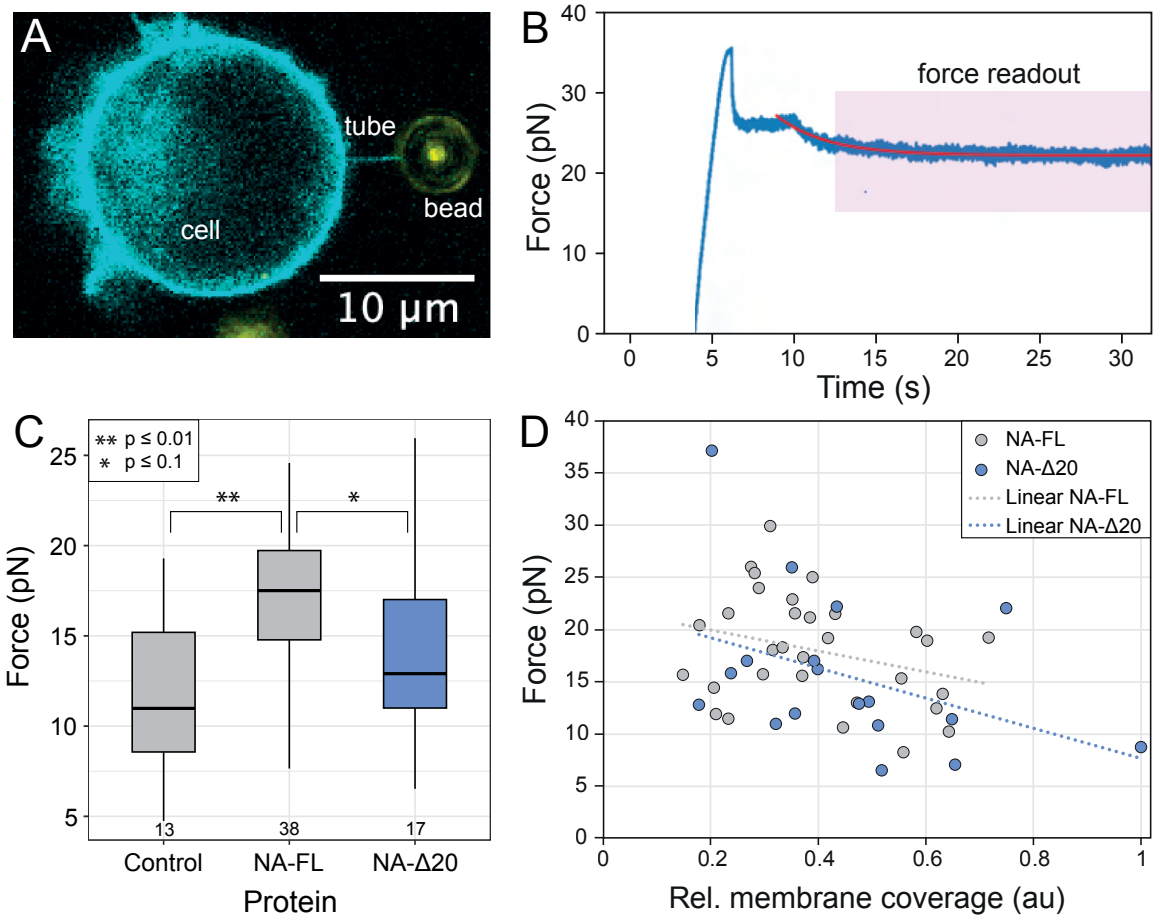

Fig. 5.5 Cell tethers show indication of protein-protein crowding. A) Micrograph of HEK293T cell transfected with NA-Δ20 protein (cyan). A 4.95 μm streptavidin coated polystyrene bead (yellow) is shown holding a tube pulled from the cell surface. B) The corresponding force plot for the tube pulled in (A). The force is shown from the start of the pull at F = 0. The pink box marks the relaxed tube region (red line is fitted exponential decay) from which the force is extracted. C) Boxplot Showing the distribution of out-tube forces measured for control HEK293T cells with DiD membrane dye and cells expressing NA-FL and NA-Δ20. The number of data points pr. protein is written above the x-axis. A statistical significant difference was observed between the control and the NA-FL cells, p = 0.0043 (Pairwise t test with pooled standard deviation, P value adjusted for multiple testing using Bejamini-Hochberg). A difference was observed between the NA-FL and NA-Δ20, p = 0.073, but did not meet the threshold requirement of p = 0.05. Part of the control data, as well as the NA-FL data are reprinted from [208] (gray). The NA-Δ20 data was collected as part of this PhD (blue). Boxes mark first and third quartiles, the line represents the median, the whiskers extent to data points within 1.5 · IQR (inter quartile range). D) For the out-pulls made for the two Neuraminidase proteins NA-FL (gray) and NA-Δ20 (blue), the force is plotted against the relative membrane coverage (protein expression) of the cell. The NA-FL data is reprinted from [208] (gray). The data shows high variance, but as a guide a linear fit of both proteins are shown, highlighting the trend of lowered force as the protein coverage on the membrane increases. NA-FL linear fit (R^2 = 0.09), NA-Δ20 (R^2 = 0.16). Figure adapted with permission from [208] . The two proteins have identical GFP-tags on the crown, thus the fluorescent intensity is assumed to be the same for each protein.

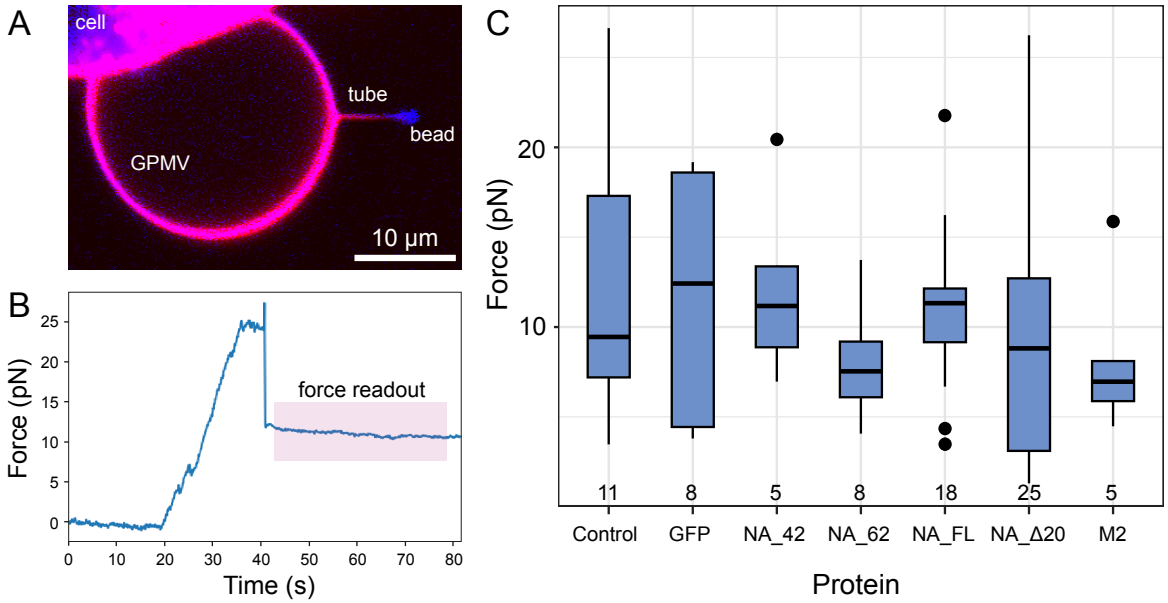

Fig. 5.6 GPMV out-tubes do not show clear crowding trends for influenza proteins. A) Micrograph of cell-attached GPMV with DiD membrane dye (red) and NA-FL protein (blue). A tube is pulled from the membrane using a 1.05 μm polystyrene bead caught in an optical trap. B) The force readout from the experiment in (A) showing force (pN) vs. time (s). The bead is in equilibrium (force = 0) at t = 0 and slightly lowered at t = 10-20 where the bead is in contact with the membrane. The pull starts at t = 20 and at t = 40 the tube is formed and shortly after the pull is stopped (at 10μm, pulling speed 0.1 μm/s). The holding force of the relaxed tube is found from the average force post relaxation (pink box). C) Boxplot of out-tube forces recorded for various proteins. Control: GPMVs with DiD, no protein, GFP: GPMVs with cytosolic GFP, NA-42/NA-62/NA-FL/NA-Δ20: GPMVs with a mutant of the IAV neuraminidase protein, M2: GPMVs with the IAV M2 protein. No statistical significance was measured between the out-tube forces pr protein for the significance threshold p = 0.05 (Wilcoxon pairwise rank sum exact test, P value adjusted for multiple testing using Benjamini-Hochberg). The data was filtered, excluding samples of low protein and lipid dye (I<10). Boxes mark first and third quartiles, the line represents the median, the whiskers extent to data points within 1.5xIQR (inter quartile range).

5.3.3 A measurable crowding effect was not observed in tubes pulled from GPMVs

Multiple viral proteins (figure 5.4) were expressed in HEK293T cells and exposed to a vesiculation buffer containing NEM, to produce GPMVs protruding from the cell membranes (figure 5.6A). The holding force of the out-tube (F_{out}) was measured for tubes pulled from these cell-attached GPMVs (figure 5.6B). No statistical difference was observed in the out-forces for the proteins tested here (figure 5.6C).

The data shows a high variance in the forces measured, which can obscure any underlying trends. Besides the spontaneous curvature C_s, the forces are affected by the tension σ and bending rigidity κ of the system. The bending rigidity of GPMVs

can vary according to the preparation procedure, e.g. vesiculation agents used and cell confluency, which can in turn contribute to a broadening of the observed forces[207]. The variety of deformations observed in experiments (figure 5.2) as well as the range in tube sizes (figure 5.7), indicate that the blebbing treatment can cause a large range of tensions in the formed GPMVs. Changes in tension between vesicles further complicates the system quantification making spontaneous curvature deductions from the measured F_{out} difficult. Comparing the force data directly without taking tension into consideration can significantly broaden the data distribution of the forces, and could contribute to the variance observed for the out-forces (figure 5.6C). Lastly, without knowing the tension, the spontaneous curvature cannot be determined for an out-tube alone.

5.3.4 Deriving spontaneous curvature from membrane tube forces

As mentioned in the introduction of this chapter, quantifying the spontaneous curvature of a membrane vesicle can be achieved by combining the measured forces of an in- and out-tube. Measuring the difference between F_{out} and F_{in} yields $\Delta F = -4\pi\kappa C_S$ (equation 5.3.1), allows for the deduction of the spontaneous curvature C_s as κ is

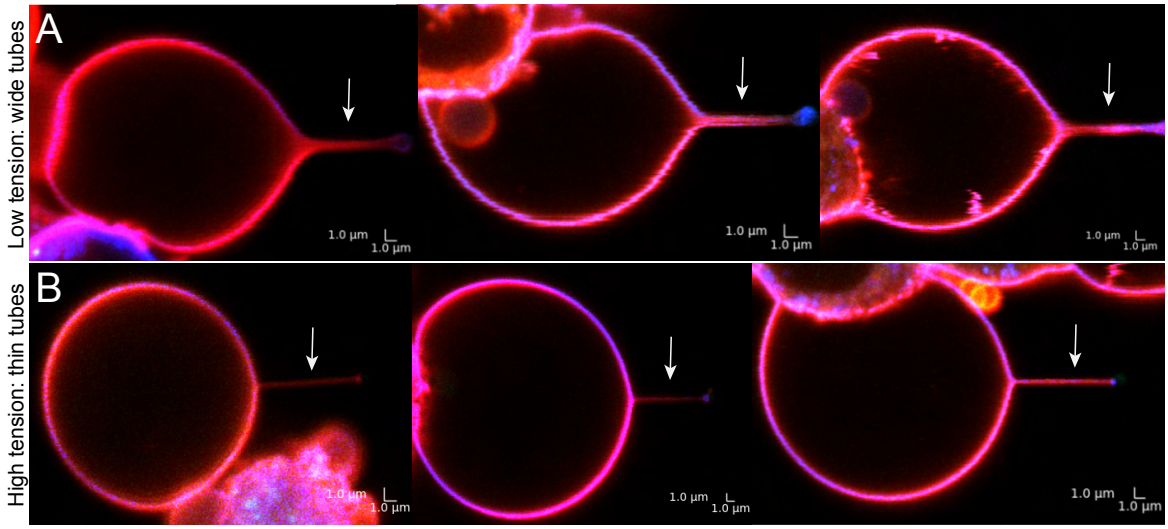

Fig. 5.7 Tube sizes indicate heterogeneity in tensions among vesicles. A) Micrographs of GPMVs with low tensions showing relatively thick tubes. B) Micrographs of GPMVs with low tension as seen by the thin tubes pulled. The white arrows point to the membrane tubes. The L in the bottom corner of each image represents a 1.0 by 1.0 μm scale bar. The images are overlays of membranes containing lipid dye DiD (red) and NA-Δ20 protein (blue). The relative tube size is inferred from the intensity of lipid dye in the tube vs. the vesicle membrane $\frac{I_{\text{lipid,tube}}}{I_{\text{lipid,GPMV}}}$.

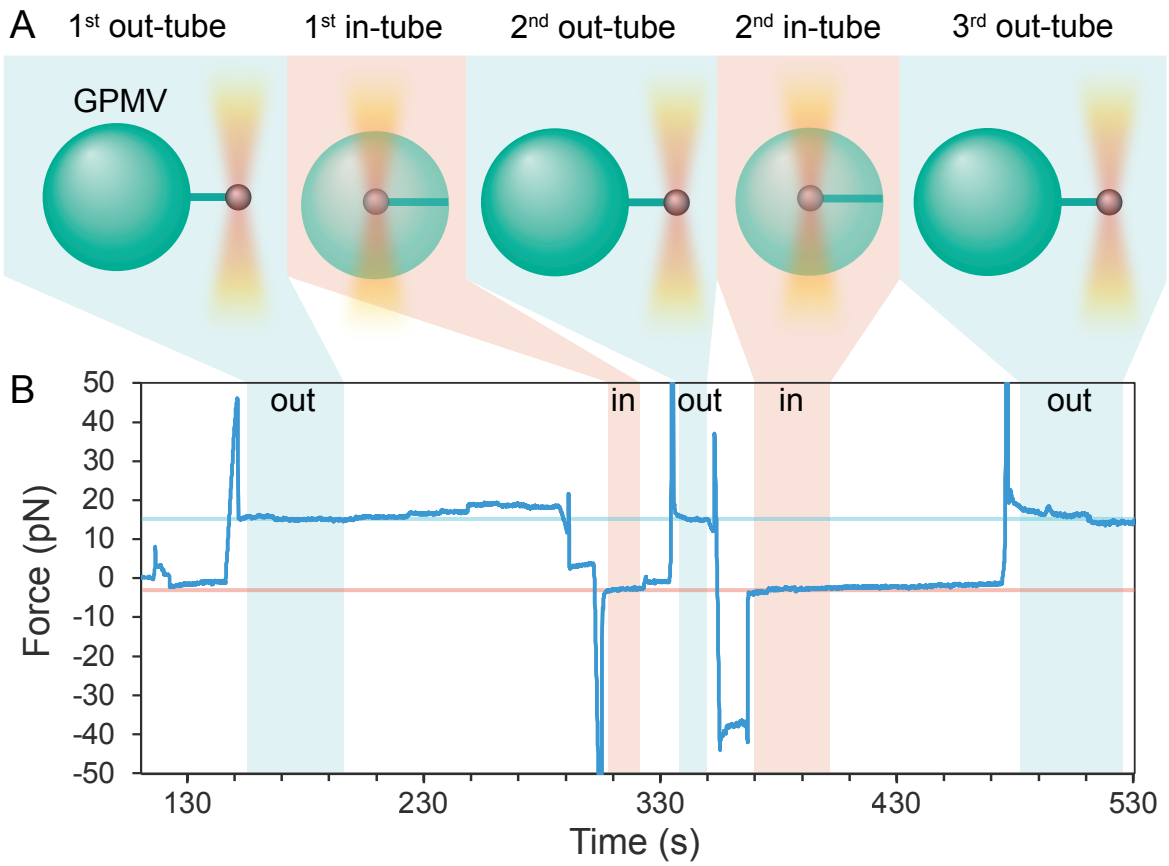

Fig. 5.8 Consecutive tube-pulls show consistent holding forces, indicating constant tension during the experiment. A) Schematic of the the out- and in-tubes pulled from a GPMV with colored areas marking where the out-tube (blue) and in-tube (red) was formed on the corresponding force plot. (B) The force plot constitutes an example showing that the vesicle is not perturbed by the pulls, and thus the forces remain the same when repeating the in- and out-pull. The horizontal lines indicate the approximate out-force (blue) and in-force (red) for easy visualization of the consistency in the measured forces.

expected to remain constant and has been measured for GPMVs to be ca. 20 K_BT[207]. It is required that the tension of the vesicle does not significantly change upon pulling the tubes, as the equations are derived based on this assumption. If the tension is not the same for the system when the in- and out-pulls are made, if e.g. the in-pull perturbs the vesicle membrane area or adhesion, then the force analysis and spontaneous curvature deduction does not hold true.

The preservation of the GPMV tension during tube pulls was tested by repeating in- and out-pulls performed on the same vesicle (figure 5.8). The forces for the out- and in-tube pulls remain the same for a total of 3 out-tubes and 2 in-tubes (figure 5.8B). This data highlights the applicability of this assay and demonstrates that spontaneous curvature measurements can indeed be made with this set-up without perturbing the

system. Completing multiple pulls for each vesicle is complicated as the change of trapping cell debris in the laser increases when it is powered on for an extended period of time, as required for multiple pulls.

To further characterize the assay, tension changes, not between vesicles, but in the same vesicle between the two pulls, are investigated. Although the notion might not be intuitive, the radius for an in- and out-tube pulled from the same membrane, will theoretically show almost no change (as discussed in section 3.2.4) given by

$$R_{out} = R_{in} = \sqrt{\frac{\kappa}{2\sigma + \kappa(C_s)^2}}. \tag{5.5}$$

Thus if the radius of the tubes stays constant, it can be inferred that the tension stays constant as κ and C_s will stay the same for a given vesicle. The intensity of lipid dye marker (DiD) in the tubes is proportional to the radius $I_{lipid,tube} \propto R_{tube}$, thus we can plot the intensity changes observed between the in-tube and out-tube radius for the same vesicle[209]. However, this relationship only holds true if the in-tube was imaged in clear focus on the inside of the GPMV. Plotting the tube intensity for the out- and in-tube of obtained confocal images from NA-Δ20 GPMVs with clear in-focus tubes, shows that the intensity of the pulled tubes show a fold change on average of 0.85 (figure 5.9). Due to the physical, technical difficulties in maintaining a steady tube in focus inside the GPMV, it is expected that the inner tube would show on average a slight decrease in intensity, even further supported by photobleaching from the membrane's exposure to light in the time spent navigating the inner GPMV to get

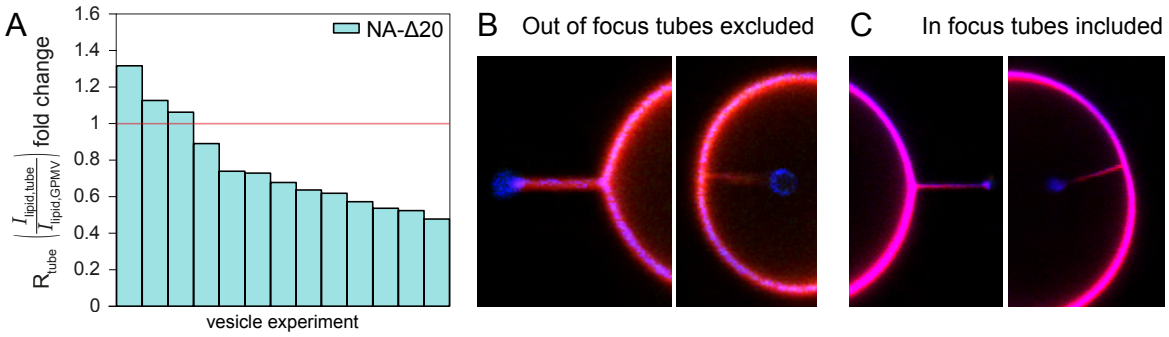

Fig. 5.9 Low variability in tension inferred from relative tube radii. A) The fold-change of the estimated tube radii ($R \propto I_{\text{lipid, tube}}/I_{\text{lipid, GPMV}}$) is plotted for selected vesicles containing NA-Δ20 and labeled with the membrane marker DiD (from which the radius is inferred). Data is filtered, excluding data where one tube was out of focus for the same vesicle, thus the shown data represents cases where both tubes (in and out) were visually in correct focus for the recorded confocal images. The red line marks a fold change of 1, indicating identical radii. B) Micrograph example of an in-tube that is visually out of focus compared to the out-tube from the same GPMV. C) Micrograph example of two tubes that are visually both in focus in the obtained confocal image of the same GPMV.

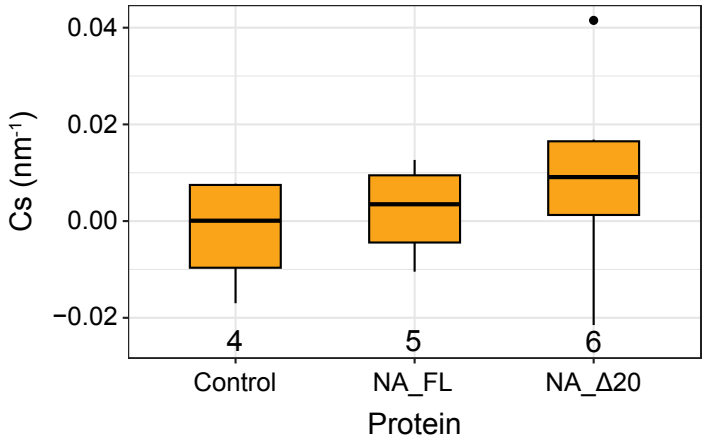

Fig. 5.10 Spontaneous curvature for neuraminidase. Boxplot of the calculated spontaneous curvature of control GPMVs with DiD and GPMVs with NA-FL and NA-Δ20. Statistical tests shown no difference between the sample means, even though a visual increase is present comparing NA-Δ20 and the control (Pairwise Wilcoxon rank sum exact test, not corrected for multiple testing). Boxes mark first and third quartiles, the line represents the median, the whiskers extent to data points within 1.5xIQR (inter quartile range).

the tube in focus. As expected, the data shows on average a lower lipid dye intensity for the in-tube (figure 5.9A), shown by a fold-change below 1 (for $\frac{R_{in}}{R_{out}}$). Considering the error on the radius from intensity measurements, these data indicate that the tension in the system is relatively constant during the experiments. Although the method has its limitations, it can be used to exclude data that might be recorded from a single vesicle showing large differences in-tube intensities indicating tension changes.

Finally, in- and out-tubes were pulled from cell-attached GPMVs containing the two neuraminidase proteins NA-FL and NA-Δ20 to quantify the spontaneous curvature induction by the proteins (figure 5.10). The spontaneous curvature was calculated from

$$C_s = -\frac{\Delta F}{4\pi\kappa} \tag{5.6}$$

where $\kappa = 20$ K_BT. The control show a median value of close to zero spontaneous curvature, while the two viral proteins examined both show an increase in C_s (figure 5.10). The C_s of NA-Δ20 is visually increased from the control, however no statistical significance was found. Collecting more data for these proteins is needed to determine if the observed trend is reproducible.

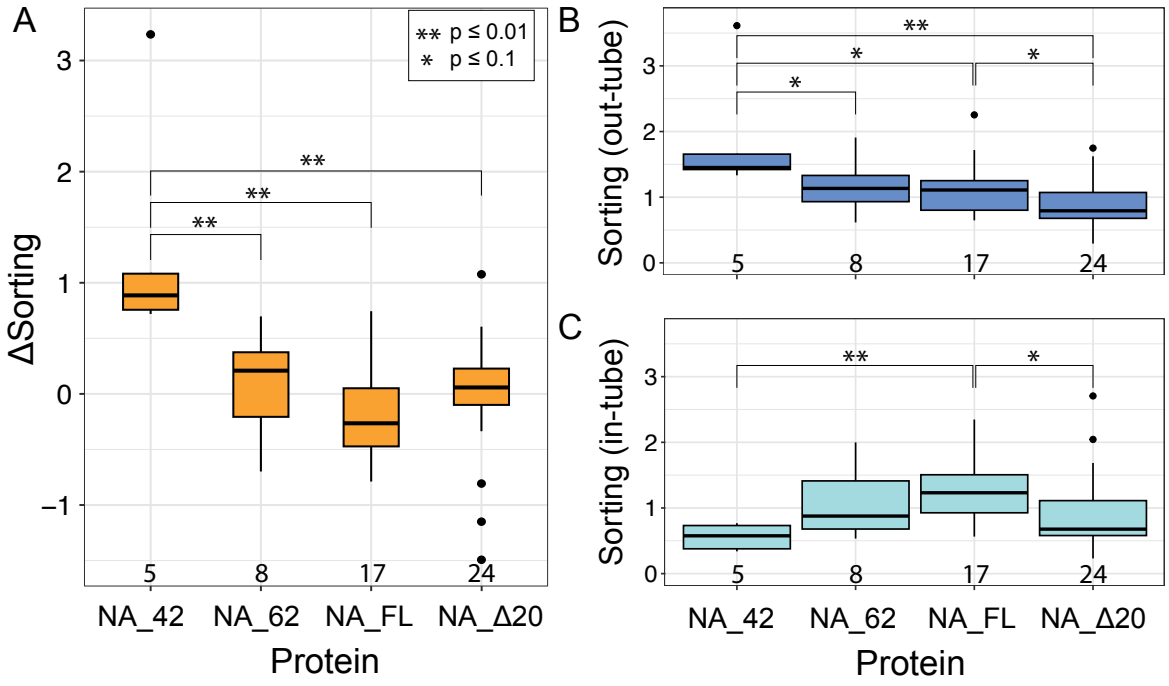

Fig. 5.11 Protein sorting for neuraminidase mutants. A) Boxplot of Δsorting vs. protein for neuraminidase protein mutants with the number of data points, N, in each box written above the x-axis. The Δsorting value represents $\Delta S = S_{out}$ - S_{in} for each protein. For NA-42 the sorting is observed to be higher in the out-tube than in-tube with an average ΔS close to 1. A statistical difference is observed in the Δsorting between NA-42 and NA-62 (p = 0.003), NA-FL (p = 0.0005) and NA-Δ20 (p= 0.0005). (B) Box plot showing only the out-sorting values pr. protein, to visual the out-sorting trends. A difference is observed between NA-42 and NA-62 (p = 0.056), and significant difference between NA-42 and NA-FL (p = 0.041) and NA-Δ20 (p = 0.0048). A difference in out-sorting was also observed between NA-FL and NA-Δ20 (p = 0.056). C) Box plot showing only the in-sorting values pr. protein, to visualize the in-sorting trends. A significant difference is observed between NA-42 and NA-FL (p = 0.0091) and between NA-FL and NA-Δ20 (p = 0.026) (Wilcoxon pairwise rank sum exact test, P value adjusted for multiple testing using Benjamini-Hochberg). The data was filtered, excluding samples of low protein and lipid dye (I<10). Boxes mark first and third quartiles, the line represents the median, the whiskers extent to data points within 1.5xIQR (inter quartile range).

5.3.5 Sorting of viral proteins in GPMVs

Proteins which induce a spontaneous curvature in the membrane are also expected to undergo membrane curvature sorting similarly to what has been shown for intrinsically curved proteins[13,90]. If influenza proteins generate curvature, it is thus possible that sorting to a certain extent can be observed for the proteins. Here an assay is presented where membrane tubes, for the first time, are pulled out from and into GPMVs attached to cells, to quantify the sorting of influenza proteins in the plasma membrane.

Proteins that crowd on the extracellular side of the membrane, such as influenza spike proteins, are hypothesized to show a slight increased preference for the out-tube

due to the added curvature, while the negative curvature of the in-tube should have the opposite effect, decreasing the sorting, as the crowding proteins would experience increased steric hindrance inside the in-tube. By comparing the fluorescent intensity of the proteins in the tubes to the intensity on the GPMV membrane, the sorting can be quantified. The membrane dye is used to quantify the size of the tubes, and the protein sorting is normalized by the tube size. This accounts for any changes in recorded protein signal for a partially out-of-focus tube. Protein sorting in the membrane tubes can be quantified by[209]

$$S = \frac{I_{\text{protein,tube}}/I_{\text{protein,GPMV}}}{I_{\text{lipid,tube}}/I_{\text{lipid,GPMV}}} \tag{5.7}$$

where $I_{\text{protein,tube}}$ and $I_{\text{lipid,tube}}$ are the protein intensity and lipid dye intensity in the tube respectively, and $I_{\text{protein,GPMV}}$ and $I_{\text{lipid,GPMV}}$ are the protein and lipid dye intensity in the GPMV membrane. The ratio $I_{\text{tube}}/I_{\text{GPMV}}$ describes any increase/decrease in the protein accumulation on the tube compared to the flat GPMV membrane. If this ratio increases, it indicates that the protein prefers the tube. The ratio for the protein is divided by the ratio for the lipid dye, so it is not wrongly concluded that the protein prefers the flat membrane if the protein ratio decreases, as this decrease could simply be from the size of the tube decreasing (or out-of-focus tube analyzed).

As NA was predicted to have the highest crowding potential of the influenza spike proteins, the 4 mutants of NA were tested for sorting behavior in GPMVs (figure 5.4). NA-42 is expected to sort the least as it does not have a large extracellular crowding domain apart from two GFPs, while NA-Δ20 is thought to have a higher sorting, due to the increased crowding potential from the ectodomain lowered close to the membrane surface. The out- and in-sorting for each protein was determined by analysis of confocal images of pulled tubes from GPMVs, and the Δsorting pr. protein, in addition to the separate out- and in-sorting, was plotted to visualize differences in the protein behavior (figure 5.11). NA-42 showed a statistically different Δsorting as compared to the other neuraminidase mutants (figure 5.11A).

For the analyzed out-tubes, a visual trend of decreased out-sorting is present as the suggested crowding potential of the protein increases (figure 5.11B and figure 5.4). A significant difference is observed between sorting for NA-42 and NA-FL ($p = 0.041$), NA-42 and NA-Δ20 ($p = 0.0048$), and a difference, not meeting the statistical significance threshold of $p = 0.05$, was observed between NA-FL and NAΔ20 ($p = 0.056$). A sorting value of 1 indicates that the protein does not have a preference for either the membrane or tube, and here we observed that both NA-62 and NA-FL show sorting of approximately 1, signifying no sorting present in this data. NA-42 shows

a preference for the out-tube, however with only 5 data points this result is vague. NA-Δ20 shows a preference for the flat membrane, which is surprising for this protein with high crowding potential, still the sorting is barely below 1, and not significantly different from NA-62 and NA-FL with sorting values S ≈ 1. It is noted that for the three proteins NA-42, NA-62 and NA-FL the average sorting value falls just above S = 1.

For the in-tube, sorting shows increased values from NA-42 to NA-FL ($p = 0.0091$), but drops for NA-Δ20 ($p = 0.026$) (figure 5.11C). If a given protein sorts in the out-tube it is likely that it will not prefer the negative curvature on the in-tube. This is observed for NA-42, that shows a decrease in sorting for the in-tube, while showing sorting into the out-tube. Again NA-62 shows an average sorting of S ≈ 1 with NA-FL showing a slight in-tube sorting, however not significantly different from NA-62. The significant drop between NA-FL and NA-Δ20 indicates that NA-Δ20 prefers the in-tube curvature, which is interesting as it also sorted into the out-tube with positive curvature. This could indicate that it might not be the ecto-domain crowding driving the sorting observed. It is noted that for the in-tube NA-42, NA-62 and NA-Δ20 show average sorting values just below S = 1.

5.4 Discussion

In this chapter a novel assay to investigate the effect of protein crowding on the spontaneous curvature of membranes was presented. Influenza proteins were investigated for their crowding ability to elucidate the role of the spike-proteins in initiating the budding event. The entropic pressure from crowding spike-proteins provides a spontaneous curvature effect to the membrane, which can be estimated by pulling tubes from crowded membranes and characterizing their mechanical properties of the membrane using optical forces.

The force trends observed in cells, indicate that a slight crowding effect could be at play, as a decrease is observed in the average out-tube force when the crowding potential of NA-FL is increased, although the observed difference fell just short of the statistical requirement of $p = 0.05$. The crowding potential was increased by decreasing the distance between the crown and the membrane, by shortening the stalk linking the TM domain with the head group (NA-Δ20). A large force increase was surprisingly observed between the the control and NA-FL protein expression. It is conceivable that this increase could stem from a change in the membrane bending rigidity due to over expression of a foreign protein. When a protein is added to the membrane, not only

does it add the crowding potential of the extracellular domain, it can also affect the spontaneous curvature of the membrane by inherent structural effects[210] and affect the rigidity of the membrane, effectively changing the κ.

Proteins with the same transmembrane domain could provide a better alternative for measuring differences in spontaneous curvature provided exclusively by stochastic collisions of the ectodomains. This was attempted by designing NA proteins with similar or identical transmembrane domains, but various extracellular domain configurations, and comparing their potential crowding contribution to the spontaneous curvature of the membrane. It was indeed observed to decrease the force slightly when the crown was lowered to the membrane (NAΔ20), increasing the crowding potential while maintaining the same transmembrane domain. The results are however limited by the low amount of data obtained.

Besides the overall trend of out-tube forces pr. protein, the measured force as a function of the membrane coverage was also investigated for cells. As the coverage increased, the forces decreased, as hypothesized. Still the observed effect was small, and in a cellular context the membrane is subjected to many underlying forces e.g. the cytoskeleton, and has been shown to exhibit varying local tension of the membranes[211]. Thus the experiments were instead carried out in cell-attached GPMVs to minimize variability.

The observed cellular trends were not reproduced in the out-forces completed in GPMVs. Here the variance of forces measured was also larger than for the cell data for many of the proteins. The average between NA-FL and NA-Δ20 was lowered, however not statistically significant. Overall, no significant differences in forces was observed for out-tubes in GPMVs with different proteins. There could be multiple explanations for this. First, the relative membrane coverage of the proteins does not provide general info of the real protein density on the membrane and we could be looking at very low densities, where differences in crowding are harder to resolve. It is possible that at the protein densities tested, no crowding effect manifests, and thus no effect on the force should be measurable. This can be determined by estimating the relationship between the fluorescent intensity and the number of proteins in the membrane[186], and calibrating the intensity data. In addition, it is possible that the vesiculation treatment affects the GPMV tension to a higher degree than pulling directly from cells, however this has not yet been investigated. Still, different tensions were observed, as demonstrated by large deformations in some vesicles. This motivated the experimental design of the presented assay to eliminate tension impact on the results by pulling in-

and out-tubes and measure, for the first time in literature, the C_s of plasma membranes expressing specific integral membrane proteins using optical tweezers.

By looking at the difference between F_{out} and F_{in} the spontaneous curvature of the membrane can be estimated and was found for a number of viral proteins as well as controls, although the limited data results did not show a significant difference in spontaneous curvature induction by viral NA-FL and NA-Δ20 proteins compared to a control. This assay is very promising for making spontaneous curvature measurements available with limited equipment and short preparation times but needs to be further tested. Theoretically the assay should solve the need for controlling tension, however the actual data gathering proved to be challenging.

The equations that provide the foundation for the spontaneous curvature measurements are only valid if the system is not perturbed during the in and out pull, rendering the tension of the given vesicle constant. A simple quantification method providing a means of estimating tension changes is measuring the radius of the in- and out-tube, which should be constant. It is shown that some variation exists in the tube radii, however the method is limited by the recorded fluorescent signal, which can vary for tubes that are placed slightly out of focus or are recorded in a slanted position, rendering parts of the analyzed tube unfocused. It was determined for a select data-set that the in-tube intensities one average were lower, confirming the notion that the in-tubes are high mobile compared to the out-tube and thus harder to capture entirely in focus. The data indicates that slight changes in tension are present and should be taken into account when using the assay to exclude large outliers, still the method is highly dependent on the quality of the confocal images obtained of the tubes. This assay is thus well suited for measurements of proteins which induce significant spontaneous curvature on the membrane and hence lead to substantial differences between in and out forces where minor tension changes can be neglected.

To push tubes into the GPMVs and avoid simply pushing the bead out of the trap, a high laser power is needed (much higher than required for pulling out-tubes). To compare the in and out forces, the same laser power is used. A high laser power sets certain requirements for the sample preparation. Maintaining high laser power in the trap for prolonged time, attracts membrane vesicles, cell debris and beads in the vicinity of the trap. Trapping such debris while measuring e.g. the out-tube will change the forces measured in the trap, rendering the experimental forces collected unreliable. Similarly, GPMVs were in certain experiments observed to encapsulate smaller vesicles or debris that entered the trap inside the GPMV lumen, affecting the force readout. Due to the intricacy of maneuvering especially the in-tube into focus, it was often not

possible to pull a second out-tube from the vesicle, as too much debris had gathered in the vesicle surroundings due to the pull from the laser. Upon attempts to complete a second out-pull this debris would come into the trap focus and interfere with the signal. To prevent these hindrances, the chamber should be as clean as possible and only a limited amount of beads added to the sample. Yet, using transiently transfected cells, a certain minimum of cells are required in the chamber to ensure that GPMVs with high expression of the proteins can be found. This limits the set-up as the additional cells create more debris in the chamber.

In addition, the system is optimized for stable trapping of larger beads (5 μm), and small movements of the of the trap (10 μm in the x, y plane in the chamber) was found to significantly impact the force read-out of a trapped 1.05 μm bead, which was used in this study. The changes were quantified and the obtained forces were calibrated to account for the movements, however it highlights the limitations of the system used. It is advised that only the nanostage is moved during experiments, especially when moving the tether into the confocal focus, to minimize any unwanted changes in the force calibration.

It requires a high density of proteins on the membrane to see the effect of crowding on the force, as modeled by Shurer et al.[31], thus to measure crowding experimentally it is important to also ensure a high protein density. In this preliminary study, the protein density was not estimated on the GPMVs, however the highest expressing GPMVs were often selected for pulls. If the protein densities investigated here fall outside of the density range where crowding starts to have a big impact on the spontaneous curvature, then that could explain the obtained results in some cases. The assay needs further validation using high expression of highly crowding proteins, such as mucins, as an assay control. This could further highlight the applicability of the presented assay.

Besides quantifying forces and spontaneous curvature, the assay can also be simultaneously used to characterize the sorting of proteins in to both the out- and in-tube of the GPMV. It was shown that NA-62 and NA-FL did not sort into either tube, and surprisingly the low crowded NA-42 showed an out-tube sorting of $\sim$1.5 while NA-Δ20 showed a slight preference for the flat membrane. NA-42 was found to show a preference for the flat membrane compared to the negative curvature of the in-tube, and similar NA-Δ20 again showed a preference for the flat membrane in this case, which would be consistent with high crowding on the negative tube. However this notion would predict NA-Δ20 preference for the out-tube, which was not observed. Sorting can be highly dependent on the size of the tubes pulled. A thin tube has a higher curvature than a thick tubes and could thus show increased sorting. Since the

tube sizes are dependent on the tension, which is not controlled in this assay, small effects might be the result of different tubes sizes rather than different sorting between proteins. To minimize this bias, tubes of similar thickness could be grouped for sorting analysis rather than combining all measurements. Here the size of the preliminary data sample obtained limited this option in practice.

5.5 Materials and methods

5.5.1 Cell culture

Human Embryonic Kidney Cells (HEK293T) were cultured at standard conditions in 25T flasks at 37°C and 5% CO2. Cells were grown in Dulbecco's Modified Eagle Medium (DMEM, high glucose, pyruvate cat. no. 11995065) supplemented with 10% fetal bovine serum (FBS, Gibco, cat. no. 11550356) and 1% Penicillin-Streptomycin (Gibco cat. no. 15140122).

5.5.2 Transfection

In this chapter, cells have been transfected with plasmids encoding for 1) cytosolic GFP, 2) Neuraminidase derivatives NA-42, NA-62, NA-FL , NA-Δ-20 3) M2 and 4) SARS-CoV-2 spike.

HEK293T cells were seeded and grown to 70% confluency over 24 h in a 6-well plate (Thermofisher Nunc™ Multidish cat. no 391-8036). The cells were then transiently transfected with the plasmid of interest using Lipofectamine™ LTX Reagent (Invitrogen, cat. no. 15338030) in accordance with the manufacturer's protocol with minor optimizations. 1.5 µg plasmid was diluted in 75 µL Opti-MEM (Gibco, cat. no. 31985070) together with 3 µL PLUS Reagent (Invitrogen, cat. no. 15338030) in an Eppendorf tube and incubated at room temperature for 5 minutes. In a separate Eppendorf tube, 3 µL Lipofectamine LTX Reagent was added to 75 µL Opti-MEM and incubated for 5 minutes. The content of the tubes was mixed together and left at room temperature for 30 minutes. The culture medium 6-well was replaced by Opti-MEM and the prepared plasmid mix added to it. After 4 h of incubation at 37°C, the culture medium was changed to growth media (specified under 'cell culture').

pre-coated for 15 minutes with 0.01% poly-L-lysine (Sigma-Aldrich, cat. no. P8920).

5.5.3 Giant plasma membrane vesicle (GPMV) preparation

GPMVs were obtained according to the protocol presented by Sezgin et al.[187]. Transfected cells were prepared as described in above. Glass slides (No. 1.5) were cleaned in ethanol and PDMS chambers (approximately 1x2 cm) placed on the slides. The chamber was coated for 15 minutes with 0.01% poly-L-lysine (Sigma-Aldrich, cat. no. P8920) then washed in PBS. The transfected cells were incubated for 5 minutes with 100 μl of TrypLE, and resuspended in 1 ml of fresh media and seeded in the chamber in low numbers, to allow for single cell experiments and incubated 24h. Next day, cells were incubated 5 minutes in a vibrant DiD (Invitrogen™ Vybrant DiD cat. no. V22887) solution containing 2 μl of 1mM DiD in 998 μl Opti-MEM (Gibco Opti-MEM™ cat. no 31985062). For M2 transfected cells, vybrant™ DiO (Invitrogen™ cat. no. V22886) was substituted for DiD. The cells were then subjected to vesiculation buffer (10 mM HEPES, 150 mM NaCl, 2 mM CaCl2, pH7.4) with 2mM N-Ethylmaleimide (NEM, Sigma-Aldrich, cat. no. E3876). After 1 h incubation at 37°C GPMVs have formed on the cells, and they are ready for experiment.

5.5.4 Tube-pulling from GPMVs and cells

For GPMV experiments 1 μm streptavidin-coated polystyrene beads (Spherotech) were added to the PDMS chamber with blebbing cells, and a sealed with a top slide. The cells were imaged in a LUMICKS C-trap using an oil condenser and 63x water objective. Trapping laser power of 15% was used for all pulls. A bead is trapped and placed in the laser at optical setting 1.7 for the trap position. The bead is calibrated in the trap 10μm from the GPMV surface (and the force is set to zero), then put in contact with the GPMV membrane ($\approx$ 20 s) and a tube is pulled by moving the bead out from the membrane a distance of 10μm with a pulling speed of 0.1 μm/s. Minimum 20 s was allowed for the tube to relax. Then the nanostage is moved slightly in the z-direction to get the tube in focus. The bead was then pushed into the GPMV by moving the trap slowly in. Upon formation of the in-tube the nanostage is moved in the z direction to attempt to get the tube in focus. For many experiments it was necessary to move the trap position to find the tube, and these experiments were not included in forces analysis requiring the in-tube force, as this becomes unreliable when moving the trap.

For membrane tubes pulled from cells the procedure outlined in [208] was followed. 4.95 μm streptavidin-coated polystyrene beads were used to pull the cell out-tubes.

5.5.5 Analysis of tube forces

The out-force is measured as the holding force of the relaxed tube, and the force is not further corrected since the trap ends up in the original calibrated position in the chamber (10 μm from the GPMV) when holding the out-tube. Upon formation of an-out tube the corresponding force plateau of the relaxed tube-force was selected and averaged to determine the force (figure 5.12A,B,C). The force is only selected when the tube is in focus (almost always the case for the immediate outpull). The force of the in-tube is similarly collected when the tube is in focus. Data where the in-tube was visible in the confocal plane upon the immediate in-pull where used in determining the spontaneous curvature. The in-force is corrected for the movement in the x,y plane of the chamber, as force calibration controls confirmed a consistent change in the force-readout upon x, y movement of the trap in the LUMICKS C-trap system (appendix figure A.3). For membrane tubes pulled from cells, the forces were determined following the procedure outlined in [208].

5.5.6 Fluorescence analysis of tubes for sorting

To determine sorting in the vesicle membrane, the fluorescent intensity of the membranes and pulled tubes need to be determined. 100 nm pixel scans were collected for the vesicles with tubes. A section of the background is marked and non-zero value pixels are averaged and used for thresholding the fluorescent channels. The GPMV shape is approximated manually with a circle (figure 5.12D), and from this circle a 180-degree arc, with an arc width of 3.1 μm, is chosen for analysis of the membrane (180 degree membrane section is necessary due to the observed polarization of the red laser). The GPMV arc crop is unwrapped using the Python library function warpPolar (figure 5.12E). Similarly the tube was selected (figure 5.12F) and a standard length of 5μm is used for the out tube (2μm for the in-tube). To correct a possible imperfect circular fit, the columns of the unwrapped membrane is shifted to align the max intensities along the center row (max shift of 5 pixels). This alignment was done for the membrane dye channel and then the same shift was applied to the protein channel. The unwrapped membrane, or the tube selection, image was then collapsed by averaging the rows along the image (figure 5.12G,H). The collapsed intensity data is fitted with a Gaussian distribution to obtain the intensity (amplitude reported as membrane/tube intensity). The intensities for the membrane and tubes can then be used to quantify sorting using

$$S = \frac{I_{\text{protein,tube}}/I_{\text{protein,GPMV}}}{I_{\text{lipid,tube}}/I_{\text{lipid,GPMV}}}. \tag{5.8}$$

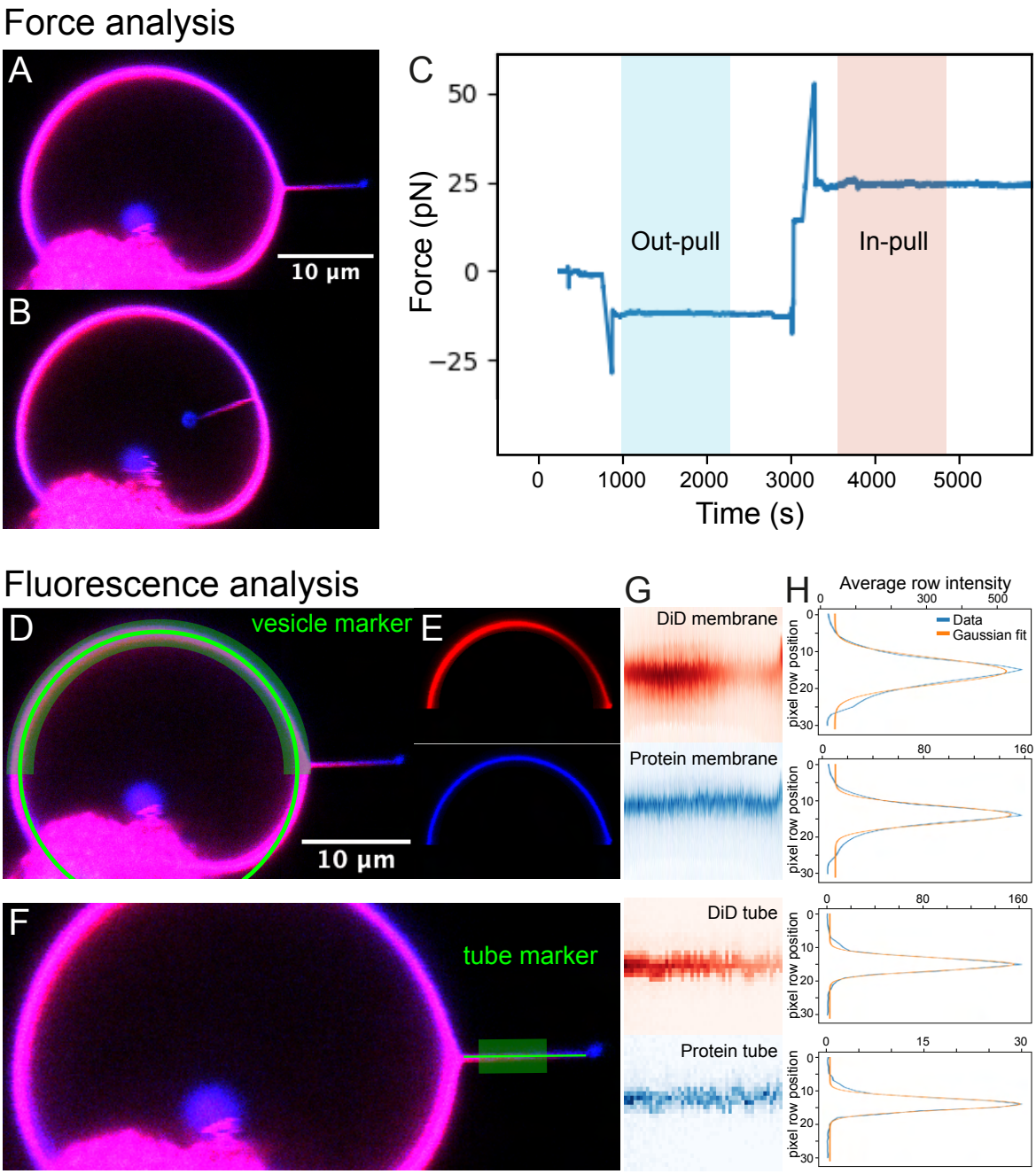

Fig. 5.12 Image analysis workflow. A) Confocal micrographs of a tether pulled out (A) and into (B) a GPMV. C) The corresponding force progression obtained from teh pulls completed in (A,B) with the out- (blue) and in-pull (red) force plateau marked. D) Spherical vesicle marker shown with a mask selecting the arc (half circle) used for membrane analysis. E) The lipid dye (red) and protein (blue) channel for the mask in (D). F) The tube marker and mask selecting (green box) used. G) The result of unwrapping the membranes from (E) and the tube marked in (F). H) The collapsed average row intensity along the tube or membrane image shown in G. Data (blue) and Gaussian fit (orange) is shown.

5.5.7 Statistical analysis

Statistical analysis was performed using the R software environment (version 4.3.1). All data was tested for normal distribution using either a Shapiro-Wilk test or visual inspection of Quantile-Quantile plots (not shown). In case of normal distribution, t-tests were performed and in case of non-normal distributed data, the Wilcoxon-rank sum test was used. Where indicated, correction for multiple testing was performed using the Benjamini-Hochberg method. All figure legends of plots where statistical analysis was performed contain exact p-values, the test performed, and if correction for multiple testing was done. Where indicated, asterisks represent different levels of significance thresholds in plots. Throughout the results section, only exact p-values were indicated for readability. The boxes of box plots represent the interquartile range (IQR) from first to third quartile (Q1, Q3), containing 50% of the data. The inside line represents the median, the whiskers represent Q1 – 1.5×IQR and Q3 + 1.5×IQR. Outliers represent datapoints outside of this range. Error bars in barplots represent Standard Deviation (SD).

Chapter 6

Conclusion and outlook

In this thesis, the biophysical mechanisms involved in promoting bud formation of progeny influenza A virions are investigated. Optical trapping combined with confocal microscopy provides the experimental foundation for new assays designed to investigate first the lateral membrane organization and then the crowding potential of IAV proteins.

Phase affinity of viral proteins

IAV proteins were successfully expressed in cells and transferred to phase-separated vesicles by utilizing a thermoplasmonic heating method for fusing isolated plasma membrane vesicles to phase-separated giant vesicles. This allowed clear identification of phase preference for a number of virus proteins and engineered variants in the fused hybrid vesicle. A strong preference for liquid disordered phase domains was observed for all the tested proteins including a tested SARS-CoV-2 spike protein. The results indicate that the liquid disordered phase matches the thickness of the transmembrane domain of the viral proteins, minimizing hydrophobic mismatch between the hydrophobic core of the bilayer and the hydrophobic transmembrane region of the proteins. The presence of a liquid ordered phase in the hybrid vesicles was confirmed with a control using a GPI anchor which showed preference for the liquid ordered phase as expected for this construct. An interesting application of this assay, is the ability to transfer plasma membrane proteins into selected domains (L_o or L_d) or even at the phase boundary, which allows for live observation of the process of protein sorting.

Altogether, the presented results show that virus proteins are highly sensitive to their membrane environment and more research has to be done at physiological conditions to investigate whether virus proteins can be made to partition into L_o domains as suggested by some research. This could be done by tuning the thickness of the phases present in the hybrid vesicles by e.g. adding more cholesterol or reducing the length of

the lipid tails, tuning the liquid ordered phase in an attempt to mimic the complex raft phases in living cells. Overall, this assay is highly valuable for investigating phase affinity of any integral membrane protein and moreover the assay does not require membrane cooling or the addition of chemical clustering agents, which are often used when investigating phases in isolated plasma membrane vesicles.

Induction of spontaneous curvature by virus proteins

Motivated by an observed crowding effect in cell tethers containing viral proteins, a novel assay was developed which has the potential to assess the spontaneous curvature induced by proteins on the cell membrane. By performing tube pulling, both inward (negative tube curvature) and outward (positive tube curvature) from cell-attached giant membrane vesicles, it was demonstrated how from the difference in these forces (ΔF) the spontaneous membrane curvature can theoretically be obtained without knowing or controlling the tension. Initial and preliminary experiments indeed show the feasibility of the assay, but several factors have to be carefully controlled in order to obtain an accurate quantification. In particular inward tubes tend to be hard to keep in focus due to the tendency of the tube-vesicle junction to migrate up or down on the vesicle membrane. This assay also allows quantification of membrane curvature sorting of the proteins on both positive and negative curvature, but here the degree of sorting was not sufficiently significant to be determined with accuracy by the assay for the given sample size.

Future directions

Viral proteins were shown to be highly sensitive to the phase state of their membrane environment and several of the investigated proteins and mutated forms have the potential to change the spontaneous curvature of cell membranes, given that the density of these proteins is sufficiently high. The tube-pulling assay has a great potential for quantifying both the spontaneous curvature and curvature sorting induced by proteins. Future work should aim at quantifying the protein density to ensure that the crowding effect is sufficiently high to be measured experimentally. In addition, mucin biopolymers could be studied as a highly crowding control protein to confirm the assay methodology. Investigation of integral membrane proteins in plasma membrane vesicles is a promising avenue for quantifying the behavior of proteins in an almost natural environment while keeping the native in-out orientation of the transmembrane proteins.

The generic assays presented in this thesis are fully applicable to any membrane protein. Refining the methods used here could be done by measuring the spontaneous curvature on isolated GPMVs. This would prevent any internal material from the donor cell to leak into the lumen of the vesicle. Furthermore, these GPMVs could be fused to phase-separated vesicles and tube pulling could be performed on phase-separated domains with concentrated protein densities. This should be possible but is certainly challenging since tube pulling necessitates adhesion and at least one of the vesicles need to be non-adhered for fusion. The here developed assays, lay the foundation for further biophysical characterization of the organization of protein in cell membranes and the physical forces behind curvature generation.

Chapter 7

External research project

As part of the Ph.D. degree I visited the Kamat Lab at Northwestern University (Evanston, IL, United States) for 5 months. Here I participated in a research project, applying my knowledge on the biophysics of membranes. The project was conceptualized by Associate professor Neha Kamat and Associate professor Stephanie Cologna, and lead by postdoc Carina Fedosejevs in the Kamat lab. In collaboration with Carina, I designed and carried out experimental data collection for the project, which is described in the following.

7.1 Introduction

Niemann-Pick disease, type C1 (NPC1) is a lysosomal storage disorder causing neurodegeneration[212]. The cause of the disease is a mutation in the cholesterol transporter gene *NPC1*, leading to misfolding of the encoded protein NCP1. This is thought to impact the intracellular transport of cholesterol, which causes cholesterol accumulation in the lysosomes. This can lead to severe neurological consequences and most treatments focus on alleviating the intracellular cholesterol buildup[213]. As cholesterol is an essential part of the lipid composition of cellular membranes, it is possible that the disease impairs membrane lipid compositions across the cell, contributing to disease progression, yet this is unexplored.

Since NPC1 is an integral membrane protein, changes in the lipid composition could increase misfolding, contributing to disease progression. Investigating changes in lipid membrane environment for diseased cells can provide insight into whether compounds affecting the membrane can be used to treat the disease, e.g. by alleviating NPC1 misfolding. Such efforts have not yet been undertaken for NPC1, and understanding

the membrane biophysical properties during disease progression could open up new avenues for lipid based therapies.

In this project a common disease mutation in NPC1, I1061T, is investigated in HeLa cell in relation to a wild type HeLa (WT) and a HeLa *NPC1* knock-out cell line (KO), to compare the biophysical properties of their cellular membranes. Although it is common to use either the KO or the NPC1-I1061T mutant (I1061T), to study the disease, the biophysical difference between these cell types have not been thoroughly examined. It is interesting to examine the difference in how the cells adapt to a mutation causing misfolding (I1061T) versus the complete knock-out of the protein. Together with Carina Fedosejevs, leading the project in the Kamat lab, I designed and carried out complementary studies to further corporate preliminary conclusions from data obtained in the lab. To investigate the biophysical properties of the membranes of the cells, the miscibility temperature of cell derived GPMVs was characterized before and after treatment with suggested drug candidates (cyclodextrins) for NPC1. Lysotracker staining was characterized to determine the cholesterol depletion of the lysosomes, visualizing the intracellular effect of the chosen treatments concentrations on the the three cell lines used in the project. In this chapter, only my own contribution to the overall project is discussed.

7.2 Results and discussion

7.2.1 Cyclodextrins alleviate lysosomal cholesterol accumulation

Lysosomal accumulation of cholesterol in diseased cells are commonly identified by filipin staining or Lysotracker incubation, and have been used to screen for NPC1 disease in patients[214,215]. Both methods were employed in this project to confirm the cholesterol accumulation in the cell lines used, and compare their initial state to post-treatment states, to quantify the effectiveness of the treatment concentrations on each cell type. Lysotracker levels in patient fibroblasts has been shown as an important predictor of NPC1 disease, particularly correlated with age of onset of neurological symptoms[216,217]. For the the diseased mutant cell line I1061T and the knock-out (KO), the staining shows clear accumulation of both Lysotracker and Filipin staining in both cell lines, as compared with the wildtype (WT) control (figure 7.1A). By quantifying the mean Lysotracker intensity pr. cell, the KO and I1061T were also found to be distinct from each other, suggesting slightly different behavior of the cell which indicates that

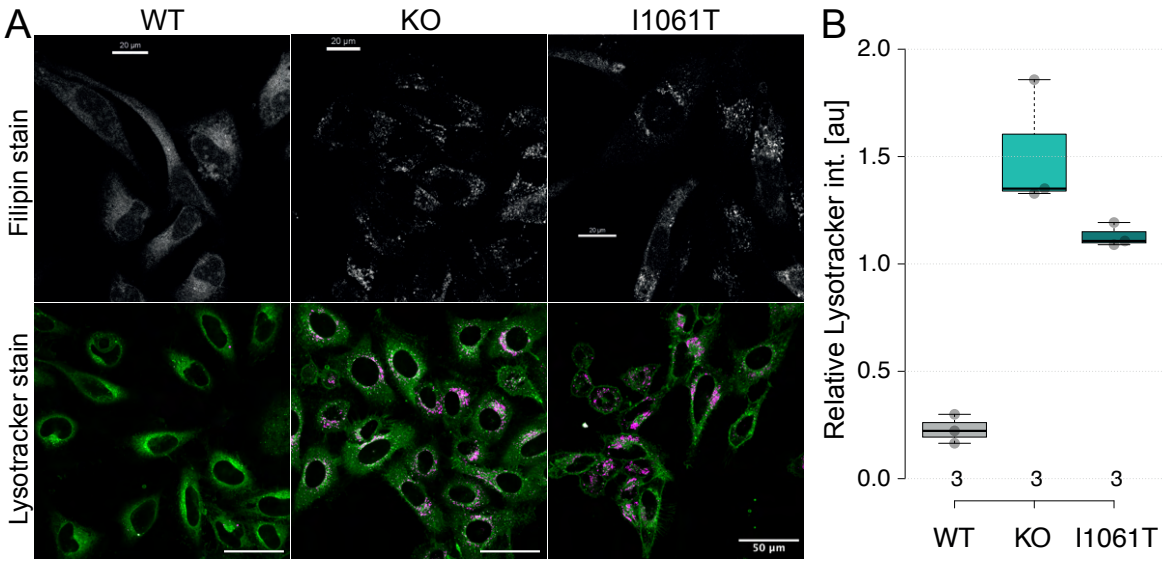

Fig. 7.1 Filipin and Lysotracker stains show a difference in lysosomal cholesterol in diseased and healthy cells. A) (Top panel) Filipin stained WT, KO and I1061T Hela cells. The images were provided by Carina Fedosejevs, postdoc in the Kamat Lab at Northwestern University. (Scale bars 20 μm). (Bottom panel) Lysotracker deep red stain (pink) and Fast DiO stain (green) for WT, KO and I1061T Hela cells. I1061T image was provided by Delfin Buyco graduate student in the Kamat at Northwestern University. (Scale bars 50 μm). The images have been modified to enhance contrast for better image visualization. B) Boxplot of the relative average Lysotracker intensity in cells. The 3 data points for each box represents the mean of a biological replicate for the cell type. Due to daily variations in the total Lysotracker intensity level, the data has been normalized with the total mean of all cell intensities recorded on the given day, $X_{norm} = X_{i,j} - X_j$, where $X_{i,j}$ is the int for cell i on day j and X_j is the mean int for all cells on day j. The total data can be found in appendix figure A.4.

the two genetic mutations have variances worth exploring. It should be noted that the data presented shows the distribution of the average Lysotracker level in three biological replicates. The data have been normalized due to daily variations in the total Lysotracker intensity level (appendix figure A.4), which could be caused by slight variations in the incubation time or dye concentration added. The data was normalized to the total mean of all cell intensities recorded on the given day, $X_{norm} = X_{i,j} - X_j$, where $X_{i,j}$ is the Lysotracker intensity for cell i on day j and Xj is the mean intensity for all cells on day j. With the baseline state of the cells characterized, the effect of treatment can be examined.

The cyclodextrin MβCD has been shown to reduce cholesterol accumulation in cells, however with varying effects[218]. Another cyclodextrin, HPβCD, is also proven to enhance lysosomal function and is currently subject of clinical trials as a potential treatment for NPC1[219,220]. Here the effect of both treatments on the cellular Lysotracker level were analyzed at concentrations of 1mM, to infer their effect on cholesterol depletion in the cells (figure 7.2). For WT and KO, both MβCD and HPβCD treatment

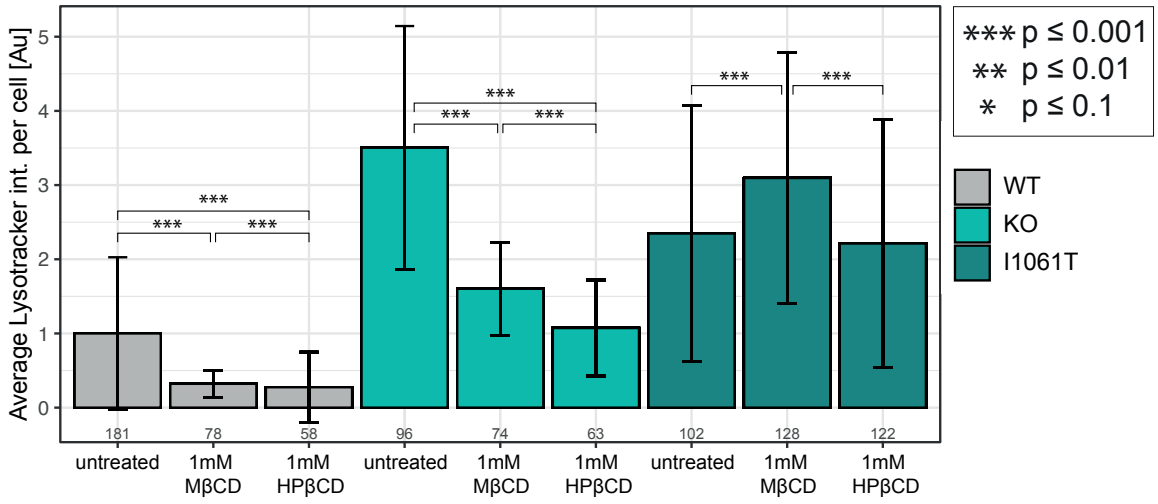

Fig. 7.2 Lysotracker levels in WT, KO and I1061T responds differently to cyclodextrin treatments. The mean Lysotracker intensity pr. cell was averaged over all analyzed cells (N noted above the x-axis) and plotted with error bars for the three cells types under treated and un-treated conditions. The data was normalized with respect to the wild type mean of the experiment day, as KO and I1061T data was recorded on different days. The data represents one biological replicate for each condition. The p-values marked with asterisk can be found in appendix figure A.5 (Wilcoxon rank sum test, adjusted for multiple testing using Benjamini-Hochberg).

resulted in a significant decrease in average Lysotracker levels in the cells. For the mutant I1061T, surprisingly an increase was observed after MβCD treatment and no change from HPβCD treatment. These results indicate that the two disease model cell lines KO and I1061T might react physically differently to the treatments. However, these results were obtained from analysis of multiple cells in one biological replicate, and should be repeated to reproduce the trend observed.

7.2.2 Treatment with MβCD and HPβCD shifts miscibility temperatures to recover wildtype behavior

GPMV miscibility temperatures (Tm) have been shown in zebra fish to correlate with the growth temperature of cells[221]. This indicates that GPMVs are a good model to reflect changes of the plasma membrane when varying the growth conditions of the cells by e.g. adding cyclodextrin (treatment) to the growing media. In [221] it is demonstrated that the GPMV Tm adjusts to changes after ca. one cell doubling time. The doubling time of HeLa cells used here are assumed to be around 24 hours, thus the treatment is left 24 hours with the cells before GPMV vesiculation was initiated. In addition GPMVs have been shown to change Tm upon varying cholesterol levels[222],

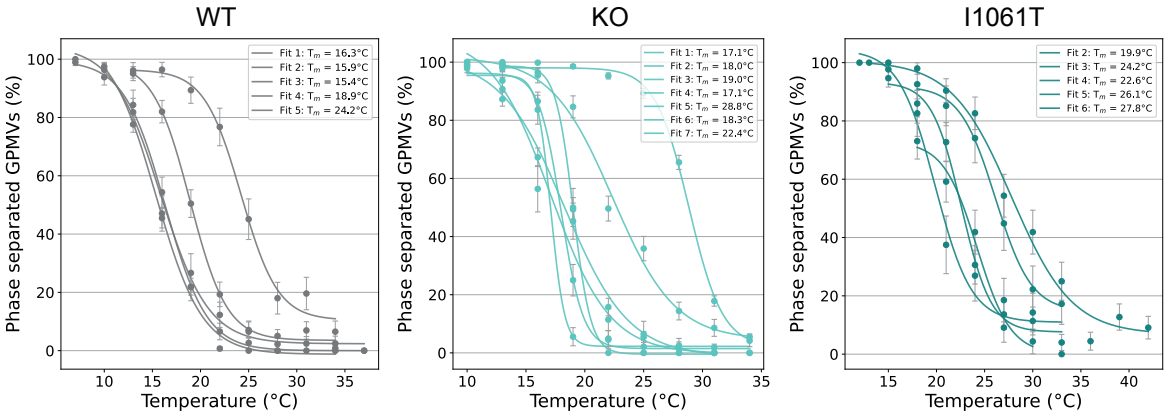

Fig. 7.3 A low reproducibility is observed in Tm measurements for WT, KO and I1061T. The plots show the analyzed Tm data for untreated cells only, and represents the baseline Tm from which changes upon cyclodextrin treatment will be compared. For WT and KO one data series lies significantly outside the range of the other recorded series. For I1061T, a general low reproducibility is observed in the recorded data. Error bars represent binomial counting statistics with error $err = \sqrt{\frac{p(1-p)}{N}}$.

thus the Tm could provide information regarding the cholesterol distribution in the cells pre and post cyclodextrin treatment.

The Tm for WT, KO and I1061T cells were determined by counting the number of phase separated vesicles at temperatures ranging from 7 to 40 degrees, and extracting the Tm from a fitted sigmoidal function (figure 7.3). The reproducibility of the Tm for each cell type was lower in the collected data than expected when compared to earlier reports[221], as seen by a large shift in the Tm among the replicates (figure 7.3). However, the observed width for each Tm fit corresponds to previously reported transition temperature spans[223]. For WT and KO, more than 70% of the data showed Tms within a few degrees distance, but for each cell an apparent outlier is present. More data is needed to determine if these outliers are representative for the normal Tm variance of the cells. For I1061T, a general low reproducibility of the Tm is observed in the recorded data. It should be noted that deviations in the Tm are expected as the growing conditions such as confluence can have a significant effect on the membrane properties[207]. Here, experimental differences in the cell confluency upon experiment initiation could add to explain the variance observed.

Next, any shift observed in the Tm post treatment with MβCD and HPβCD was quantified to investigate the biophysical effects of the treatments on the membrane properties (figure 7.4A). All treatment concentrations tested were combined in the category "treated" with either MβCD or HPβCD, as no significant difference was observed between treatment levels (appendix figure A.6). Combining all treatment

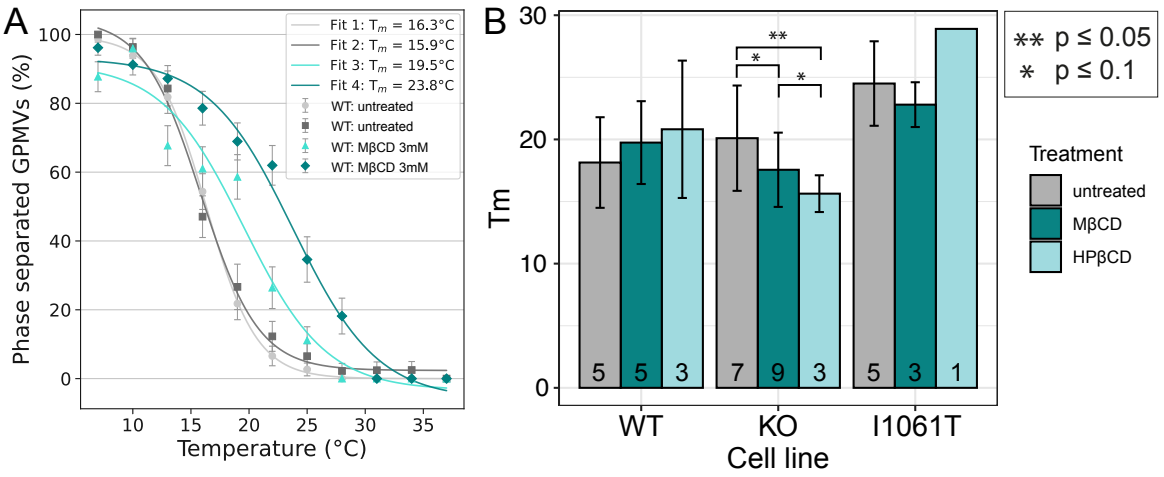

Fig. 7.4 Cyclodextrins increase Tm in healthy cell and lower Tm in diseased cells. A) Percent phase separated GPMVs vs. temperature are plotted and fitted with a sigmoid curve to extract the Tm value for the GPMV sample. An example of the phase transition plot of untreated WT cell (gray) with a Tm around 16 °C and the effect of treating with 3mM MβCD, increasing the Tm of the vesicle population. Error bars represent binomial counting statistics with error $err = \sqrt{\frac{p(1-p)}{N}}$. B) Various treatment concentrations were tested, but no significant difference between the concentration was found (appendix figure A.6), thus the Tm observed for all concentration conditions are combined in the shown plot as either HPβCD or MβCD. An increase in Tm of WT was observed post treatment, although not significant. For KO, decrease was observed post MβCD (p = 0.088) and between treatment with MβCD and HPβCD (p = 0.088). A significant decrease was demonstrated for KO upon treatment (p = 0.03). For I1061T no significant differences were observed after treatment. (Wilcoxon rank sum test, adjusted for multiple testing using Benjamini-Hochberg). The number of experiments is printed above the x-axis. Error bars show SD.

concentrations tested, the general effect observed is that the Tm of the KO is "recovered" to wildtype state after treatments (figure 7.4B).

Comparing treatments using both MβCD and HPβCD to the untreated cells, differences in Tm are observed. In general the Tm of the KO is slightly higher than the WT (not statistically significant), and when exposed to treatment with either HPβCD and MβCD it decreased, indicating a partial recovery of the wildtype state. It is clear that the treatment affects the WT differently than it affects the KO. Both cyclodextrin treatments are observed to increase the Tm, which has been reported before for MβCD[222]. Only few treatments were completed for I1061T, however the results are included here to motivate further studies on this cell type using the presented method.

7.3 Conclusion and outlook

NPC1 disease causes cholesterol accumulation in lysosomes of cells, which is caused by defects in the cholesterol transporter NPC1. The here presented findings confirm that in NPC1-KO and NPC1-I1061T mutant HeLa cell lines, cholesterol accumulates in the lysosomes. The potential drug candidates for NPC1 disease MβCD and HPβCD are thought to alleviate accumulation of cholesterol in the lysosomes. Treatment of the cellular models with MβCD and HPβCD confirmed this depletion in KO cells. However, for the I1061T mutant the depletion could not be shown. These results were unexpected and require further validation. Yet, this could be subject of new mechanistic investigations on how defects in NPC1 cause cholesterol accumulation in the lysosomes.

Defects in cholesterol transport likely affect membrane properties of diseased cells, therefore, alternative strategies for treating NPC1 disease might be lipid-based. In this study, the miscibility temperature of diseased cells was characterized, showing a measurable, but not significant increase of Tm in I1061T cells compared to WT. This can indicate that the diseased cells adapt differently to the lack or the defect of NPC1. Treatment with MβCD and HPβCD lead to additional, compositional membrane changes. These preliminary findings motivate to further investigate membrane properties in context of NPC1 disease, which might lead to new insights into disease pathophysiology or open avenues to new treatment options.

7.4 Materials and Methods

7.4.1 Cell culture

Cells were cultured in DMEM supplemented with 10% FBS and 1% Penstrep. All the cell lines were provided by the Cologna Lab (University of Illinois, Chicago). The KO cell line was observed to grow slower than the WT and I1061T cell lines, thus is was passaged with longer intervals.

7.4.2 Lysotracker staining protocol and analysis

In a glass-bottom dish 30.000 cells were seeded and grown for 24 h at 37°C and 5% CO_2. After 24 h cells subjected to cyclodextrin treatment were first washed in PBS and then incubated for 24 hours with MβCD or HPβCD in the desired concentration (0 (untreated), 250 μM, 500 μM, 1 mM and 3 mM). For cyclodextrin treatments, growth

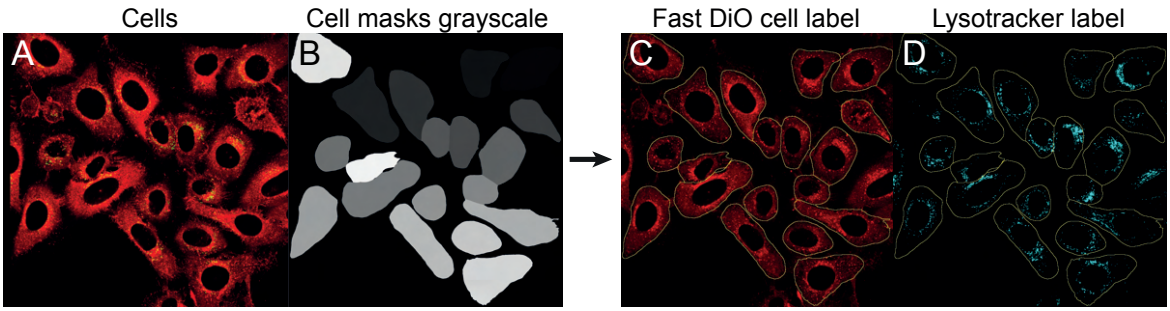

Fig. 7.5 Generating cell masks for Lysotracker analysis. Cellpose[224] was used to generate cell masks based on DiO cellular labelling. The intensity of lysotracker in the marked cells were then analyzed by determining average level pr. cell using Fiji image analysis tools[184].

media was supplemented with 25mM HEPES (to counteract acidity of MβCD) and treatment solutions with MβCD and HPβCD were made by dilution from a 100mM stock of the cyclodextrins.

On day of imaging (48 hours post initial seeding), the cells were washed twice with PBS and incubated for 1 hour with 7.5 μL Lysotracker deep red (10μM stock) added to 992.5 μL culture media to make a 75 nM Lysotracker solution. The Lysotracker fluorophore is highly selective for acidic cellular compartments, including lysosomes. The cells were then washed twice with PBS and incubated for 15 mins in a 5 μM Fast Dio solution (by mixing 8.3 μL of Fast Dio stock of 0.5 mg/ml with 992 μL culture media). The cells were again washed in PBS, and culture media was added to the well for imaging.

The cell imaging was done using a Nikon Eclipse Ti2 confocal microscope using a Plan App λ 60x Oil objective. A 488 laser (gain 20, intensity 1) was used to excite DiO and a 640 laser (gain 20, intensity 0.2) to excite the Lysotracer deep red, emission was collected at 496-550 and 650-720 respectively. The DiO signal was used to generate cells masks using CellPose[224]. The cell masks where then used to analyze the average Lysotracker level pr. cell for each cell type. The analyze workflow is depicted in figure 7.5.

7.4.3 Measuring GPMV miscibility temperatures

In a 6-well culture plate, 250.000 cells were seeded pr. well and grown at normal conditions for 21 hours. The cell were then washed in PBS and subjected to cyclodextrin treatment (0 (untreated), 250 μM, 500 μM, 1 mM and 3 mM MβCD or HPβCD) for 24 h in 25mM HEPES supplemented growth media. Cells were washed with GPMV buffer (10mM HEPES, 150nM NaCl, 2mM $CaCl_2$) and incubated 15 min with 2mM

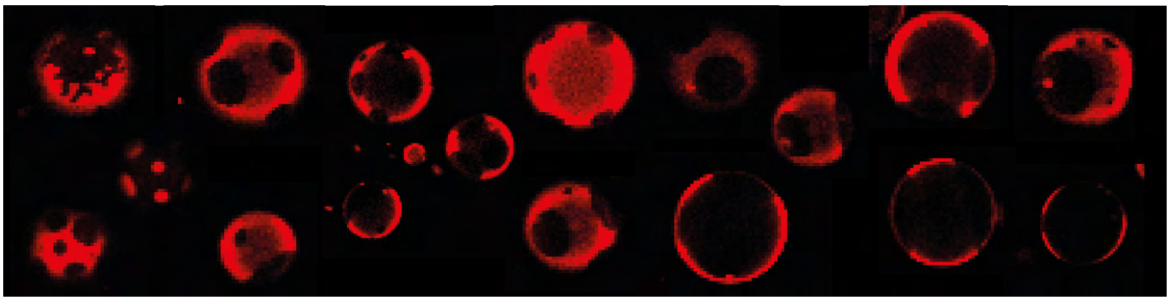

Fig. 7.6 Examples of GPMVs showing liquid ordered phases. GPMVs are from KO cells treated with MβCD at 13°C.

Rhod diluted i GPMV buffer (1M Rhodamine Liss 18:1 PE suspended in DMSO). This Rhodamine lipid was used to mark the liquid disordered phase in the GPMVs. Cell were then washed 2x and incubated with active vesiculation buffer (700 μL pr well)for 21 h at normal condition. The active vesiculation buffer was made by adding 162 μL of 4% PFA and 12 μL of 1M DTT to 9 mL GPMV buffer. After 21 h the GPMVs were harvested from the cells, by taking the cell supernatant and add to an eppendorf tubes. The GPMVs were left to sink in the tube for 4 hours.

The vesicles were collected from the bottom of the eppendorf tube and added to a small silicon chamber on a glass slide. The vesicles were then heated to 31 °C (or until all vesicles showed uniform liquid disordered domains) and slowly cooled and imaged over a range of temperatures in steps of 3 degrees. The temperature was changed by 1°C/minut and left to rest at the set temperature for 2 minutes before the vesicles were imaged. This was repeated, cycling through all the temperatures for each vesicle sample. The vesicles were imaged in a Nikon Eclipse Ti2 confocal microscope using a 20X Nikon Air objective. The heating and cooling was achieved by placing the microscope slide with sample wells on a PE100 Peltier System (Linkam).

The GPMVs were manually counted to determine the % phase-separated vesicles at each temperature. Figure 7.6 shows some examples of GPMVs that were marked as showing phases. Statistical analysis was carried out following the procedure outlined in section 5.5.7.

Bibliography

[1] Ken Jacobson, Ole G Mouritsen, and Richard GW Anderson. Lipid rafts: at a crossroad between cell biology and physics. *Nature cell biology*, 9(1):7–14, 2007.

[2] Giuseppina Turturici, Rosaria Tinnirello, Gabriella Sconzo, and Fabiana Geraci. Extracellular membrane vesicles as a mechanism of cell-to-cell communication: advantages and disadvantages. *American Journal of Physiology-Cell Physiology*, 306(7):C621–C633, 2014.

[3] Marko Kaksonen and Aurélien Roux. Mechanisms of clathrin-mediated endocytosis. *Nature reviews Molecular cell biology*, 19(5):313–326, 2018.

[4] James H Hurley, Evzen Boura, Lars-Anders Carlson, and Bartosz Różycki. Membrane budding. *Cell*, 143(6):875–887, 2010.

[5] Patrick Lajoie, Jacky G Goetz, James W Dennis, and Ivan R Nabi. Lattices, rafts, and scaffolds: domain regulation of receptor signaling at the plasma membrane. *Journal of Cell Biology*, 185(3):381–385, 2009.

[6] Veronica Astro and Ivan De Curtis. Plasma membrane–associated platforms: Dynamic scaffolds that organize membrane-associated events. *Science signaling*, 8(367):re1–re1, 2015.

[7] Peter J Woolf and Jennifer J Linderman. Self organization of membrane proteins via dimerization. *Biophysical chemistry*, 104(1):217–227, 2003.

[8] Peter I Kuzmin, Sergey A Akimov, Yuri A Chizmadzhev, Joshua Zimmerberg, and Fredric S Cohen. Line tension and interaction energies of membrane rafts calculated from lipid splay and tilt. *Biophysical journal*, 88(2):1120–1133, 2005.

[9] Félix M Goñi. "rafts": A nickname for putative transient nanodomains. *Chemistry and physics of lipids*, 218:34–39, 2019.

[10] Erdinc Sezgin, Ilya Levental, Satyajit Mayor, and Christian Eggeling. The mystery of membrane organization: composition, regulation and roles of lipid rafts. *Nature reviews Molecular cell biology*, 18(6):361–374, 2017.

[11] Ilya Levental, Kandice R Levental, and Frederick A Heberle. Lipid rafts: controversies resolved, mysteries remain. *Trends in cell biology*, 30(5):341–353, 2020.

[12] Joseph H Lorent, Blanca Diaz-Rohrer, Xubo Lin, Kevin Spring, Alemayehu A Gorfe, Kandice R Levental, and Ilya Levental. Structural determinants and functional consequences of protein affinity for membrane rafts. *Nature communications*, 8(1):1219, 2017.

[13] Guillermo Moreno-Pescador, Christoffer D Florentsen, Henrik Østbye, Stine L Sønder, Theresa L Boye, Emilie L Veje, Alexander K Sonne, Szabolcs Semsey, Jesper Nylandsted, Robert Daniels, et al. Curvature-and phase-induced protein sorting quantified in transfected cell-derived giant vesicles. *ACS nano*, 13(6):6689–6701, 2019.

[14] Jörg Nikolaus, Silvia Scolari, Elisa Bayraktarov, Nadine Jungnick, Stephanie Engel, Anna Pia Plazzo, Martin Stöckl, Rudolf Volkmer, Michael Veit, and Andreas Herrmann. Hemagglutinin of influenza virus partitions into the nonraft domain of model membranes. *Biophysical journal*, 99(2):489–498, 2010.

[15] Jonathan P Schlebach, Paul J Barrett, Charles A Day, Ji Hun Kim, Anne K Kenworthy, and Charles R Sanders. Topologically diverse human membrane proteins partition to liquid-disordered domains in phase-separated lipid vesicles. *Biochemistry*, 55(7):985–988, 2016.

[16] Ilya Levental, Daniel Lingwood, Michal Grzybek, Ünal Coskun, and Kai Simons. Palmitoylation regulates raft affinity for the majority of integral raft proteins. *Proceedings of the National Academy of Sciences*, 107(51):22050–22054, 2010.

[17] George P Leser and Robert A Lamb. Influenza virus assembly and budding in raft-derived microdomains: a quantitative analysis of the surface distribution of ha, na and m2 proteins. *Virology*, 342(2):215–227, 2005.

[18] Victoria Thusgaard Ruhoff, Guillermo Moreno-Pescador, Weria Pezeshkian, and Poul Martin Bendix. Strength in numbers: effect of protein crowding on the shape of cell membranes. *Biochemical Society Transactions*, 50(5):1257–1267, 2022.

[19] Paul Janmey. Cell membranes and the cytoskeleton. In *Handbook of biological physics*, volume 1, pages 805–849. Elsevier, 1995.

[20] Benjamin Kollmitzer, Peter Heftberger, Michael Rappolt, and Georg Pabst. Monolayer spontaneous curvature of raft-forming membrane lipids. *Soft matter*, 9(45):10877–10884, 2013.

[21] JH Lorent, Kandice R Levental, Lakshmi Ganesan, Gia Rivera-Longsworth, Erdinç Sezgin, Milka Doktorova, Edward Lyman, and Ilya Levental. Plasma membranes are asymmetric in lipid unsaturation, packing and protein shape. *Nature chemical biology*, 16(6):644–652, 2020.

[22] Patricia Bassereau, Rui Jin, Tobias Baumgart, Markus Deserno, Rumiana Dimova, Vadim A Frolov, Pavel V Bashkirov, Helmut Grubmüller, Reinhard Jahn, H Jelger Risselada, et al. The 2018 biomembrane curvature and remodeling roadmap. *Journal of physics D: Applied physics*, 51(34):343001, 2018.

[23] Mijo Simunovic, Gregory A Voth, Andrew Callan-Jones, and Patricia Bassereau. When physics takes over: Bar proteins and membrane curvature. *Trends in cell biology*, 25(12):780–792, 2015.

[24] Harvey T McMahon and Jennifer L Gallop. Membrane curvature and mechanisms of dynamic cell membrane remodelling. *Nature*, 438(7068):590–596, 2005.

[25] Emmanuel Boucrot, Adi Pick, Gamze Çamdere, Nicole Liska, Emma Evergren, Harvey T McMahon, and Michael M Kozlov. Membrane fission is promoted by insertion of amphipathic helices and is restricted by crescent bar domains. *Cell*, 149(1):124–136, 2012.

[26] Mikhail A Zhukovsky, Angela Filograna, Alberto Luini, Daniela Corda, and Carmen Valente. Protein amphipathic helix insertion: A mechanism to induce membrane fission. *Frontiers in cell and developmental biology*, 7:291, 2019.

[27] Weria Pezeshkian, Lina J NAabo, and John H Ipsen. Cholera toxin b subunit induces local curvature on lipid bilayers. *FEBS open bio*, 7(11):1638–1645, 2017.

[28] David J Busch, Justin R Houser, Carl C Hayden, Michael B Sherman, Eileen M Lafer, and Jeanne C Stachowiak. Intrinsically disordered proteins drive membrane curvature. *Nature communications*, 6(1):7875, 2015.

[29] Jeanne C Stachowiak, Eva M Schmid, Christopher J Ryan, Hyoung Sook Ann, Darryl Y Sasaki, Michael B Sherman, Phillip L Geissler, Daniel A Fletcher, and Carl C Hayden. Membrane bending by protein–protein crowding. *Nature cell biology*, 14(9):944–949, 2012.

[30] Susanne Liese, Eva Maria Wenzel, Ingrid Kjos, Rossana Rojas Molina, Sebastian W Schultz, Andreas Brech, Harald Stenmark, Camilla Raiborg, and Andreas Carlson. Protein crowding mediates membrane remodeling in upstream escrt-induced formation of intraluminal vesicles. *Proceedings of the National Academy of Sciences*, 117(46):28614–28624, 2020.

[31] Carolyn R Shurer, Joe Chin-Hun Kuo, LaDeidra Monét Roberts, Jay G Gandhi, Marshall J Colville, Thais A Enoki, Hao Pan, Jin Su, Jade M Noble, Michael J Hollander, et al. Physical principles of membrane shape regulation by the glycocalyx. *Cell*, 177(7):1757–1770, 2019.

[32] Susanne Liese and Andreas Carlson. Membrane shape remodeling by protein crowding. *Biophysical Journal*, 120(12):2482–2489, 2021.

[33] Wilton T Snead and Jeanne C Stachowiak. Structure versus stochasticity—the role of molecular crowding and intrinsic disorder in membrane fission. *Journal of molecular biology*, 430(16):2293–2308, 2018.

[34] Jure Derganc and Alenka Čopič. Membrane bending by protein crowding is affected by protein lateral confinement. *Biochimica et Biophysica Acta (BBA)-Biomembranes*, 1858(6):1152–1159, 2016.

[35] Jeanne C Stachowiak, Carl C Hayden, and Darryl Y Sasaki. Steric confinement of proteins on lipid membranes can drive curvature and tubulation. *Proceedings of the National Academy of Sciences*, 107(17):7781–7786, 2010.

[36] Yang Xu, Hediye Erdjument-Bromage, Colin KL Phoon, Thomas A Neubert, Mindong Ren, and Michael Schlame. Cardiolipin remodeling enables protein crowding in the inner mitochondrial membrane. *The EMBO Journal*, 40(23):e108428, 2021.

[37] Christine S Scheve, Paul A Gonzales, Noor Momin, and Jeanne C Stachowiak. Steric pressure between membrane-bound proteins opposes lipid phase separation. *Journal of the American Chemical Society*, 135(4):1185–1188, 2013.

[38] Michael M Kozlov, Felix Campelo, Nicole Liska, Leonid V Chernomordik, Siewert J Marrink, and Harvey T McMahon. Mechanisms shaping cell membranes. *Current opinion in cell biology*, 29:53–60, 2014.

[39] Debi P Nayak, Rilwan A Balogun, Hiroshi Yamada, Z Hong Zhou, and Subrata Barman. Influenza virus morphogenesis and budding. *Virus research*, 143(2):147–161, 2009.

[40] Chandrasekhar N Gujuluva, Amitabha Kundu, KG Murti, and Debi P Nayak. Abortive replication of influenza virus a/wsn/33 in hela229 cells: defective viral entry and budding processes. *Virology*, 204(2):491–505, 1994.

[41] Dan Dou, Rebecca Revol, Henrik Östbye, Hao Wang, and Robert Daniels. Influenza a virus cell entry, replication, virion assembly and movement. *Frontiers in immunology*, 9:1581, 2018.

[42] Audray Harris, Giovanni Cardone, Dennis C Winkler, J Bernard Heymann, Matthew Brecher, Judith M White, and Alasdair C Steven. Influenza virus pleiomorphy characterized by cryoelectron tomography. *Proceedings of the National Academy of Sciences*, 103(50):19123–19127, 2006.

[43] Qiuyu J Huang, Kangkang Song, Chen Xu, Daniel NA Bolon, Jennifer P Wang, Robert W Finberg, Celia A Schiffer, and Mohan Somasundaran. Quantitative structural analysis of influenza virus by cryo-electron tomography and convolutional neural networks. *Structure*, 30(5):777–786, 2022.

[44] Sook-San Wong and Richard J Webby. Traditional and new influenza vaccines. *Clinical microbiology reviews*, 26(3):476–492, 2013.

[45] Chih-Jen Wei, Michelle C Crank, John Shiver, Barney S Graham, John R Mascola, and Gary J Nabel. Next-generation influenza vaccines: opportunities and challenges. *Nature reviews Drug discovery*, 19(4):239–252, 2020.

[46] Taylor F Gunnels, Devin M Stranford, Roxana E Mitrut, Neha P Kamat, and Joshua N Leonard. Elucidating design principles for engineering cell-derived vesicles to inhibit sars-cov-2 infection. *Small*, 18(19):2200125, 2022.

[47] Edward C Hutchinson, Philip D Charles, Svenja S Hester, Benjamin Thomas, David Trudgian, Mónica Martínez-Alonso, and Ervin Fodor. Conserved and host-specific features of influenza virion architecture. *Nature communications*, 5(1):1–11, 2014.

[48] Paul C Roberts and Richard W Compans. Host cell dependence of viral morphology. *Proceedings of the National Academy of Sciences*, 95(10):5746–5751, 1998.

[49] Jill Seladi-Schulman, John Steel, and Anice C Lowen. Spherical influenza viruses have a fitness advantage in embryonated eggs, while filament-producing strains are selected in vivo. *Journal of virology*, 87(24):13343–13353, 2013.

[50] Matthew D Badham and Jeremy S Rossman. Filamentous influenza viruses. *Current clinical microbiology reports*, 3:155–161, 2016.

[51] Tian Li, Zhenyu Li, Erin E Deans, Eva Mittler, Meisui Liu, Kartik Chandran, and Tijana Ivanovic. The shape of pleomorphic virions determines resistance to cell-entry pressure. *Nature microbiology*, 6(5):617–629, 2021.

[52] Johan Nordholm, Diogo V da Silva, Justina Damjanovic, Dan Dou, and Robert Daniels. Polar residues and their positional context dictate the transmembrane domain interactions of influenza a neuraminidases. *Journal of Biological Chemistry*, 288(15):10652–10660, 2013.

[53] Steven J Gamblin and John J Skehel. Influenza hemagglutinin and neuraminidase membrane glycoproteins. *Journal of biological chemistry*, 285(37):28403–28409, 2010.

[54] Per A Bullough, Frederick M Hughson, John J Skehel, and Don C Wiley. Structure of influenza haemagglutinin at the ph of membrane fusion. *Nature*, 371(6492):37–43, 1994.

[55] Xingcheng Lin, Nathanial R Eddy, Jeffrey K Noel, Paul C Whitford, Qinghua Wang, Jianpeng Ma, and José N Onuchic. Order and disorder control the functional rearrangement of influenza hemagglutinin. *Proceedings of the National Academy of Sciences*, 111(33):12049–12054, 2014.

[56] Benjamin J Chen, George P Leser, Eiji Morita, and Robert A Lamb. Influenza virus hemagglutinin and neuraminidase, but not the matrix protein, are required for assembly and budding of plasmid-derived virus-like particles. *Journal of virology*, 81(13):7111–7123, 2007.

[57] Peter Palese, Kiyotake Tobita, Masahiro Ueda, and Richard W Compans. Characterization of temperature sensitive influenza virus mutants defective in neuraminidase. *Virology*, 61(2):397–410, 1974.

[58] Julie L McAuley, Brad P Gilbertson, Sanja Trifkovic, Lorena E Brown, and Jennifer L McKimm-Breschkin. Influenza virus neuraminidase structure and functions. *Frontiers in microbiology*, 10:39, 2019.

[59] Bingdong Sha and Ming Luo. Structure of a bifunctional membrane-rna binding protein, influenza virus matrix protein m1. *Nature structural biology*, 4(3):239–244, 1997.

[60] Malte Hilsch, Björn Goldenbogen, Christian Sieben, Chris T Höfer, Jürgen P Rabe, Edda Klipp, Andreas Herrmann, and Salvatore Chiantia. Influenza a matrix protein m1 multimerizes upon binding to lipid membranes. *Biophysical journal*, 107(4):912–923, 2014.

[61] Theresa Latham and Jose M Galarza. Formation of wild-type and chimeric influenza virus-like particles following simultaneous expression of only four structural proteins. *Journal of virology*, 75(13):6154–6165, 2001.

[62] Rashid Manzoor, Manabu Igarashi, and Ayato Takada. Influenza a virus m2 protein: roles from ingress to egress. *International journal of molecular sciences*, 18(12):2649, 2017.

[63] Lawrence H Pinto and Robert A Lamb. Controlling influenza virus replication by inhibiting its proton channel. *Molecular bioSystems*, 3(1):18–23, 2007.

[64] Jeremy S Rossman, Xianghong Jing, George P Leser, and Robert A Lamb. Influenza virus m2 protein mediates escrt-independent membrane scission. *Cell*, 142(6):902–913, 2010.

[65] Bastian Thaa, Ilya Levental, Andreas Herrmann, and Michael Veit. Intrinsic membrane association of the cytoplasmic tail of influenza virus m2 protein and lateral membrane sorting regulated by cholesterol binding and palmitoylation. *Biochemical Journal*, 437(3):389–397, 2011.

[66] Jesper J Madsen, John MA Grime, Jeremy S Rossman, and Gregory A Voth. Entropic forces drive clustering and spatial localization of influenza a m2 during viral budding. *Proceedings of the National Academy of Sciences*, 115(37):E8595–E8603, 2018.

[67] Masashi Yamaguchi, Radostin Danev, Kiyoto Nishiyama, Keishin Sugawara, and Kuniaki Nagayama. Zernike phase contrast electron microscopy of ice-embedded influenza a virus. *Journal of structural biology*, 162(2):271–276, 2008.

[68] Gabriele Neumann, Tokiko Watanabe, and Yoshihiro Kawaoka. Plasmid-driven formation of influenza virus-like particles. *Journal of virology*, 74(1):547–551, 2000.

[69] Paul C Roberts, Robert A Lamb, and Richard W Compans. The m1 and m2 proteins of influenza a virus are important determinants in filamentous particle formation. *Virology*, 240(1):127–137, 1998.

[70] Svetlana V Bourmakina and Adolfo García-Sastre. Reverse genetics studies on the filamentous morphology of influenza a virus. *Journal of General Virology*, 84(3):517–527, 2003.

[71] Subrata Barman, Lopa Adhikary, Alok K Chakrabarti, Carl Bernas, Yoshihiro Kawaoka, and Debi P Nayak. Role of transmembrane domain and cytoplasmic tail amino acid sequences of influenza a virus neuraminidase in raft association and virus budding. *Journal of virology*, 78(10):5258–5269, 2004.

[72] Paulino Gómez-Puertas, Carmen Albo, Esperanza Pérez-Pastrana, Amparo Vivo, and Agustin Portela. Influenza virus matrix protein is the major driving force in virus budding. *Journal of virology*, 74(24):11538–11547, 2000.

[73] Michael Veit and Bastian Thaa. Association of influenza virus proteins with membrane rafts. *Advances in virology*, 2011(1):370606, 2011.

[74] Sasa Lin, Hussein Y Naim, A Chapin Rodriguez, and Michael G Roth. Mutations in the middle of the transmembrane domain reverse the polarity of transport of the influenza virus hemagglutinin in mdck epithelial cells. *The Journal of cell biology*, 142(1):51–57, 1998.

[75] Makoto Takeda, George P Leser, Charles J Russell, and Robert A Lamb. Influenza virus hemagglutinin concentrates in lipid raft microdomains for efficient viral fusion. *Proceedings of the National Academy of Sciences*, 100(25):14610–14617, 2003.

[76] Takashi Ohkura, Fumitaka Momose, Reiko Ichikawa, Kaoru Takeuchi, and Yuko Morikawa. Influenza a virus hemagglutinin and neuraminidase mutually accelerate their apical targeting through clustering of lipid rafts. *Journal of virology*, 88(17):10039–10055, 2014.

[77] Mingtao Ge and Jack H Freed. Two conserved residues are important for inducing highly ordered membrane domains by the transmembrane domain of influenza hemagglutinin. *Biophysical journal*, 100(1):90–97, 2011.

[78] Ayub Ali, Roy T Avalos, Evgeni Ponimaskin, and Debi P Nayak. Influenza virus assembly: effect of influenza virus glycoproteins on the membrane association of m1 protein. *Journal of virology*, 74(18):8709–8719, 2000.

[79] Jie Zhang, Andrew Pekosz, and Robert A Lamb. Influenza virus assembly and lipid raft microdomains: a role for the cytoplasmic tails of the spike glycoproteins. *Journal of virology*, 74(10):4634–4644, 2000.

[80] Hong Jin, George P Leser, Jie Zhang, and Robert A Lamb. Influenza virus hemagglutinin and neuraminidase cytoplasmic tails control particle shape. *The EMBO journal*, 16(6):1236–1247, 1997.

[81] Bastian Thaa, Andreas Herrmann, and Michael Veit. Intrinsic cytoskeleton-dependent clustering of influenza virus m2 protein with hemagglutinin assessed by flim-fret. *Journal of virology*, 84(23):12445–12449, 2010.

[82] Silvia Scolari, Stephanie Engel, Nils Krebs, Anna Pia Plazzo, Rodrigo FM De Almeida, Manuel Prieto, Michael Veit, and Andreas Herrmann. Lateral distribution of the transmembrane domain of influenza virus hemagglutinin revealed by time-resolved fluorescence imaging. *Journal of Biological Chemistry*, 284(23):15708–15716, 2009.

[83] Ian A Wilson, John J Skehel, and DC Wiley. Structure of the haemagglutinin membrane glycoprotein of influenza virus at 3 å resolution. *Nature*, 289(5796):366–373, 1981.

[84] Guillermo Moreno-Pescador. Ph.d. thesis: Membrane protein dynamics studied with optical and thermoplasmonic methods in complex and simple membranes. *Niels Bohr Institute, University of Copenhagen*, 2019. https://nbi.ku.dk/english/theses/phd-theses/phd-theses-biocomplexity-biophysics/.

[85] Petr Chlanda, Oliver Schraidt, Susann Kummer, James Riches, Heike Oberwinkler, Simone Prinz, Hans-Georg Kräusslich, and John AG Briggs. Structural analysis of the roles of influenza a virus membrane-associated proteins in assembly and morphology. *Journal of virology*, 89(17):8957–8966, 2015.

[86] Zachary I Imam, Laura E Kenyon, Adelita Carrillo, Isai Espinoza, Fatema Nagib, and Jeanne Stachowiak. Steric pressure among membrane-bound polymers opposes lipid phase separation. *ACS journal of surfaces and colloids*, 32(15):3774–3784, 2016.

[87] William S Trimble and Sergio Grinstein. Barriers to the free diffusion of proteins and lipids in the plasma membrane. *Journal of Cell Biology*, 208(3):259–271, 2015.

[88] Nathan W Schmidt, Abhijit Mishra, Jun Wang, William F DeGrado, and Gerard CL Wong. Influenza virus a m2 protein generates negative gaussian membrane curvature necessary for budding and scission. *Journal of the American Chemical Society*, 135(37):13710–13719, 2013.

[89] Jan Steinkühler, Philippe De Tillieux, Roland L Knorr, Reinhard Lipowsky, and Rumiana Dimova. Charged giant unilamellar vesicles prepared by electroformation exhibit nanotubes and transbilayer lipid asymmetry. *Scientific reports*, 8(1):11838, 2018.

[90] Aurélie Bertin, Nicola De Franceschi, Eugenio de La Mora, Sourav Maity, Maryam Alqabandi, Nolwen Miguet, Aurelie Di Cicco, Wouter H Roos, Stéphanie Mangenot, Winfried Weissenhorn, et al. Human escrt-iii polymers assemble on positively curved membranes and induce helical membrane tube formation. *Nature communications*, 11(1):2663, 2020.

[91] Yi-Chih Lin, Christophe Chipot, and Simon Scheuring. Annexin-v stabilizes membrane defects by inducing lipid phase transition. *Nature communications*, 11(1):230, 2020.

[92] Guillermo S Moreno-Pescador, Dunya S Aswad, Christoffer D Florentsen, Azra Bahadori, Mohammad R Arastoo, Helena Maria D Danielsen, Anne Sofie B Heitmann, Theresa L Boye, Jesper Nylandsted, Lene B Oddershede, et al. Thermoplasmonic nano-rupture of cells reveals annexin v function in plasma membrane repair. *Nanoscale*, 14(21):7778–7787, 2022.

[93] Guillermo Moreno-Pescador, Mohammad Reza Arastoo, Victoria Thusgaard Ruhoff, Salvatore Chiantia, Robert Daniels, and Poul Martin Bendix. Thermoplasmonic vesicle fusion reveals membrane phase segregation of influenza spike proteins. *Nano Letters*, 23(8):3377–3384, 2023.

[94] Kirsten Bacia, Christina G Schuette, Nicoletta Kahya, Reinhard Jahn, and Petra Schwille. Snares prefer liquid-disordered over "raft"(liquid-ordered) domains when reconstituted into giant unilamellar vesicles*[boxs]. *Journal of Biological Chemistry*, 279(36):37951–37955, 2004.

[95] Koji Nishimura, Tomoaki Matsuura, Kazuya Nishimura, Takeshi Sunami, Hiroaki Suzuki, and Tetsuya Yomo. Cell-free protein synthesis inside giant unilamellar vesicles analyzed by flow cytometry. *Langmuir*, 28(22):8426–8432, 2012.

[96] Kerstin Göpfrich, Barbara Haller, Oskar Staufer, Yannik Dreher, Ulrike Mersdorf, Ilia Platzman, and Joachim P Spatz. One-pot assembly of complex giant unilamellar vesicle-based synthetic cells. *ACS synthetic biology*, 8(5):937–947, 2019.

[97] Zachary I Imam and George D Bachand. Multicomponent and multiphase lipid nanotubes formed by gliding microtubule-kinesin motility and phase-separated giant unilamellar vesicles. *Langmuir*, 35(49):16281–16289, 2019.

[98] Ida Louise Jørgensen, Gerdi Christine Kemmer, and Thomas Günther Pomorski. Membrane protein reconstitution into giant unilamellar vesicles: a review on current techniques. *European Biophysics Journal*, 46:103–119, 2017.

[99] Andreas Weinberger, Feng-Ching Tsai, Gijsje H Koenderink, Thais F Schmidt, Rosângela Itri, Wolfgang Meier, Tatiana Schmatko, André Schröder, and Carlos Marques. Gel-assisted formation of giant unilamellar vesicles. *Biophysical journal*, 105(1):154–164, 2013.

[100] Mark K Doeven, Joost HA Folgering, Victor Krasnikov, Eric R Geertsma, Geert van den Bogaart, and Bert Poolman. Distribution, lateral mobility and function of membrane proteins incorporated into giant unilamellar vesicles. *Biophysical journal*, 88(2):1134–1142, 2005.

[101] Garvita Dhanawat, Manorama Dey, Anirudh Singh, and Nagma Parveen. Invagination of giant unilamellar vesicles upon membrane mixing with native vesicles. *ACS omega*, 2024.

[102] Robert R Ishmukhametov, Aidan N Russell, and Richard M Berry. A modular platform for one-step assembly of multi-component membrane systems by fusion of charged proteoliposomes. *Nature communications*, 7(1):13025, 2016.

[103] Miranda L Jacobs and Neha P Kamat. Cell-free membrane protein expression into hybrid lipid/polymer vesicles. *Cell-Free Gene Expression: Methods and Protocols*, pages 257–271, 2022.

[104] Norman T Hovijitra, Jessica J Wuu, Boris Peaker, and James R Swartz. Cell-free synthesis of functional aquaporin z in synthetic liposomes. *Biotechnology and bioengineering*, 104(1):40–49, 2009.

[105] Karthika S Nair and Harsha Bajaj. Advances in giant unilamellar vesicle preparation techniques and applications. *Advances in Colloid and Interface Science*, 318:102935, 2023.

[106] Yong Zhou, Christina K Berry, Patrick A Storer, and Robert M Raphael. Peroxidation of polyunsaturated phosphatidyl-choline lipids during electroformation. *Biomaterials*, 28(6):1298–1306, 2007.

[107] Martin Lindén, Pierre Sens, and Rob Phillips. Entropic tension in crowded membranes. *PLOS Computational Biology*, 8(3):1–10, 03 2012.

[108] Guillaume Charras and Ewa Paluch. Blebs lead the way: how to migrate without lamellipodia. *Nature reviews Molecular cell biology*, 9(9):730–736, 2008.

[109] Mathew L Coleman, Erik A Sahai, Margaret Yeo, Marta Bosch, Ann Dewar, and Michael F Olson. Membrane blebbing during apoptosis results from caspase-mediated activation of rock i. *Nature cell biology*, 3(4):339–345, 2001.

[110] Robert E Scott. Plasma membrane vesiculation: a new technique for isolation of plasma membranes. *Science*, 194(4266):743–745, 1976.

[111] Brigitte Bauer, Max Davidson, and Owe Orwar. Proteomic analysis of plasma membrane vesicles. *Angewandte Chemie International Edition*, 48(9):1656–1659, 2009.

[112] Shinako Kakuda, Pavana Suresh, Guangtao Li, and Erwin London. Loss of plasma membrane lipid asymmetry can induce ordered domain (raft) formation. *Journal of lipid research*, 63(1), 2022.

[113] Erdinc Sezgin. Giant plasma membrane vesicles to study plasma membrane structure and dynamics. *Biochimica et Biophysica Acta (BBA)-Biomembranes*, 1864(4):183857, 2022.

[114] Frederick A Heberle, Milka Doktorova, Haden L Scott, Allison D Skinkle, M Neal Waxham, and Ilya Levental. Direct label-free imaging of nanodomains in biomimetic and biological membranes by cryogenic electron microscopy. *Proceedings of the National Academy of Sciences*, 117(33):19943–19952, 2020.

[115] Luisa Zartner, Martina Garni, Ioana Craciun, Tomaž Einfalt, and Cornelia G Palivan. How can giant plasma membrane vesicles serve as a cellular model for controlled transfer of nanoparticles? *Biomacromolecules*, 22(1):106–115, 2020.

[116] Lu Wang, Nicolas Hartel, Kaixuan Ren, Nicholas Alexander Graham, and Noah Malmstadt. Effect of protein corona on nanoparticle–plasma membrane and nanoparticle–biomimetic membrane interactions. *Environmental Science: Nano*, 7(3):963–974, 2020.

[117] Avinash K Gadok, David J Busch, Silvia Ferrati, Brian Li, Hugh DC Smyth, and Jeanne C Stachowiak. Connectosomes for direct molecular delivery to the cellular cytoplasm. *Journal of the American Chemical Society*, 138(39):12833–12840, 2016.

[118] Christopher V Kelly, Mary-Margaret T Kober, Päivö Kinnunen, David A Reis, Bradford G Orr, and Mark M Banaszak Holl. Pulsed-laser creation and characterization of giant plasma membrane vesicles from cells. *Journal of biological physics*, 35:279–295, 2009.

[119] Yang Li, Songyang Liu, Wanyu Xu, Kemin Wang, Fengjiao He, and Jianbo Liu. Formation of giant plasma membrane vesicles for biological and medical applications: a review. *Sensors & Diagnostics*, 2(4):806–814, 2023.

[120] Ilya Levental, Michal Grzybek, and Kai Simons. Raft domains of variable properties and compositions in plasma membrane vesicles. *Proceedings of the National Academy of Sciences*, 108(28):11411–11416, 2011.

[121] Arthur Ashkin, James M Dziedzic, and T Yamane. Optical trapping and manipulation of single cells using infrared laser beams. *Nature*, 330(6150):769–771, 1987.

[122] Jin-Der Wen, Maria Manosas, Pan TX Li, Steven B Smith, Carlos Bustamante, Felix Ritort, and Ignacio Tinoco. Force unfolding kinetics of rna using optical tweezers. i. effects of experimental variables on measured results. *Biophysical journal*, 92(9):2996–3009, 2007.

[123] Matthew J Footer, Jacob WJ Kerssemakers, Julie A Theriot, and Marileen Dogterom. Direct measurement of force generation by actin filament polymerization using an optical trap. *Proceedings of the National Academy of Sciences*, 104(7):2181–2186, 2007.

[124] Natascha Leijnse, Younes Farhangi Barooji, Mohammad Reza Arastoo, Stine Lauritzen Sønder, Bram Verhagen, Lena Wullkopf, Janine Terra Erler, Szabolcs Semsey, Jesper Nylandsted, Lene Broeng Oddershede, et al. Filopodia rotate and coil by actively generating twist in their actin shaft. *Nature communications*, 13(1):1636, 2022.

[125] Arthur Ashkin. Acceleration and trapping of particles by radiation pressure. *Physical review letters*, 24(4):156, 1970.

[126] Arthur Ashkin, James M Dziedzic, John E Bjorkholm, and Steven Chu. Observation of a single-beam gradient force optical trap for dielectric particles. *Optics letters*, 11(5):288–290, 1986.

[127] J Van Mameren, GJL Wuite, and I Heller. Introduction to optical tweezers: Background, system designs, and commercial solutions in single molecule analysis: Methods and protocols; ejg peterman, eds, 2018.

[128] Carlos J Bustamante, Yann R Chemla, Shixin Liu, and Michelle D Wang. Optical tweezers in single-molecule biophysics. *Nature Reviews Methods Primers*, 1(1):25, 2021.

[129] Lene B Oddershede. Optical tweezers techniques. *digital Encyclopedia of Applied Physics*, 2003.

[130] Poul M Bendix and Lene B Oddershede. Expanding the optical trapping range of lipid vesicles to the nanoscale. *Nano letters*, 11(12):5431–5437, 2011.

[131] Anders Kyrsting, Poul M Bendix, and Lene B Oddershede. Mapping 3d focal intensity exposes the stable trapping positions of single nanoparticles. *Nano letters*, 13(1):31–35, 2013.

[132] Christine Selhuber-Unkel, Inga Zins, Olaf Schubert, Carsten Sonnichsen, and Lene B Oddershede. Quantitative optical trapping of single gold nanorods. *Nano letters*, 8(9):2998–3003, 2008.

[133] Alexander Rohrbach. Stiffness of optical traps: Quantitative agreement<? format?> between experiment and electromagnetic theory. *Physical review letters*, 95(16):168102, 2005.

[134] Frederick Gittes and Christoph F Schmidt. Signals and noise in micromechanical measurements. *Methods in cell biology*, 55:129–156, 1997.

[135] Andrew C Richardson, Nader Reihani, and Lene B Oddershede. Combining confocal microscopy with precise force-scope optical tweezers. In *Optical Trapping and Optical Micromanipulation III*, volume 6326, pages 560–569. SPIE, 2006.

[136] Sebastian Dunst and Pavel Tomancak. Imaging flies by fluorescence microscopy: principles, technologies, and applications. *Genetics*, 211(1):15–34, 2019.

[137] W Gray Jerome and Robert L Price. *Basic confocal microscopy*. Springer, 2018.

[138] Sudheer K Cheppali, Raviv Dharan, and Raya Sorkin. Forces of change: optical tweezers in membrane remodeling studies. *The Journal of Membrane Biology*, 255(6):677–690, 2022.

[139] Imre Derényi, Frank Jülicher, and Jacques Prost. Formation and interaction of membrane tubes. *Physical review letters*, 88(23):238101, 2002.

[140] Patricia Bassereau, Benoit Sorre, and Aurore Lévy. Bending lipid membranes: experiments after w. helfrich's model. *Advances in colloid and interface science*, 208:47–57, 2014.

[141] Imre Derényi, Gerbrand Koster, Martijn M Van Duijn, András Czövek, Marileen Dogterom, and Jacques Prost. Membrane nanotubes. In *Controlled Nanoscale Motion: Nobel Symposium 131*, pages 141–159. Springer, 2007.

[142] H Moysés Nussenzveig. Cell membrane biophysics with optical tweezers. *European Biophysics Journal*, 47(5):499–514, 2018.

[143] Raktim Dasgupta and Rumiana Dimova. Inward and outward membrane tubes pulled from giant vesicles. *Journal of physics D: applied physics*, 47(28):282001, 2014.

[144] Raktim Dasgupta, Markus S Miettinen, Nico Fricke, Reinhard Lipowsky, and Rumiana Dimova. The glycolipid gm1 reshapes asymmetric biomembranes and giant vesicles by curvature generation. *Proceedings of the National Academy of Sciences*, 115(22):5756–5761, 2018.

[145] Victoria Thusgaard Ruhoff, Mohammad Reza Arastoo, Guillermo Moreno-Pescador, and Poul Martin Bendix. Biological applications of thermoplasmonics. *Nano Letters*, 24(3):777–789, 2024.

[146] Liselotte Jauffred, Akbar Samadi, Henrik Klingberg, Poul Martin Bendix, and Lene B Oddershede. Plasmonic heating of nanostructures. *Chemical reviews*, 119(13):8087–8130, 2019.

[147] Craig F Bohren and Donald R Huffman. *Absorption and scattering of light by small particles*. John Wiley & Sons, 2008.

[148] Nikolai G Khlebtsov and Lev A Dykman. Optical properties and biomedical applications of plasmonic nanoparticles. *Journal of Quantitative Spectroscopy and Radiative Transfer*, 111(1):1–35, 2010.

[149] Xiaoting Zhao, Yang Shi, Ting Pan, Dengyun Lu, Jianyun Xiong, Baojun Li, and Hongbao Xin. In situ single-cell surgery and intracellular organelle manipulation via thermoplasmonics combined optical trapping. *Nano Letters*, 22(1):402–410, 2021.

[150] Nicola De Franceschi, Maryam Alqabandi, Nolwenn Miguet, Christophe Caillat, Stephanie Mangenot, Winfried Weissenhorn, and Patricia Bassereau. The escrt protein chmp2b acts as a diffusion barrier on reconstituted membrane necks. *Journal of cell science*, 132(4):jcs217968, 2019.

[151] Poul M Bendix, S Nader S Reihani, and Lene B Oddershede. Direct measurements of heating by electromagnetically trapped gold nanoparticles on supported lipid bilayers. *ACS nano*, 4(4):2256–2262, 2010.

[152] Anders Kyrsting, Poul M Bendix, Dimitrios G Stamou, and Lene B Oddershede. Heat profiling of three-dimensionally optically trapped gold nanoparticles using vesicle cargo release. *Nano letters*, 11(2):888–892, 2011.

[153] Steven M Block, Lawrence SB Goldstein, and Bruce J Schnapp. Bead movement by single kinesin molecules studied with optical tweezers. *Nature*, 348(6299):348–352, 1990.

[154] Arthur Ashkin, Karin Schütze, JM Dziedzic, Ursula Euteneuer, and Manfred Schliwa. Force generation of organelle transport measured in vivo by an infrared laser trap. *Nature*, 348(6299):346–348, 1990.

[155] Karel Svoboda, Christoph F Schmidt, Bruce J Schnapp, and Steven M Block. Direct observation of kinesin stepping by optical trapping interferometry. *Nature*, 365(6448):721–727, 1993.

[156] Michelle D Wang, Hong Yin, Robert Landick, Jeff Gelles, and Steven M Block. Stretching dna with optical tweezers. *Biophysical journal*, 72(3):1335–1346, 1997.

[157] Iddo Heller, Tjalle P Hoekstra, Graeme A King, Erwin JG Peterman, and Gijs JL Wuite. Optical tweezers analysis of dna–protein complexes. *Chemical reviews*, 114(6):3087–3119, 2014.

[158] Kamilla Norregaard, Liselotte Jauffred, Kirstine Berg-Sørensen, and Lene B Oddershede. Optical manipulation of single molecules in the living cell. *Physical Chemistry Chemical Physics*, 16(25):12614–12624, 2014.

[159] Joel P Mills, Liangliang Qie, Ming Dao, CT Lim, and Subra Suresh. Nonlinear elastic and viscoelastic deformation of the human red blood cell with optical tweezers. *Molecular & Cellular Biomechanics*, 1(3):169, 2004.

[160] Yareni A Ayala, Bruno Pontes, Diney S Ether, Luis B Pires, Glauber R Araujo, Susana Frases, Luciana F Romão, Marcos Farina, Vivaldo Moura-Neto, Nathan B Viana, et al. Rheological properties of cells measured by optical tweezers. *BMC biophysics*, 9:1–11, 2016.

[161] Josep Mas, Andrew C Richardson, S Nader S Reihani, Lene B Oddershede, and Kirstine Berg-Sørensen. Quantitative determination of optical trapping strength and viscoelastic moduli inside living cells. *Physical biology*, 10(4):046006, 2013.

[162] Raviv Dharan, Yuwei Huang, Sudheer Kumar Cheppali, Shahar Goren, Petr Shendrik, Weisi Wang, Jiamei Qiao, Michael M Kozlov, Li Yu, and Raya Sorkin. Tetraspanin 4 stabilizes membrane swellings and facilitates their maturation into migrasomes. *Nature Communications*, 14(1):1037, 2023.

[163] Tae-Jin Kim, Chirlmin Joo, Jihye Seong, Reza Vafabakhsh, Elliot L Botvinick, Michael W Berns, Amy E Palmer, Ning Wang, Taekjip Ha, Eric Jakobsson, et al. Distinct mechanisms regulating mechanical force-induced ca2+ signals at the plasma membrane and the er in human mscs. *Elife*, 4:e04876, 2015.

[164] Claudia Arbore, Laura Perego, Marios Sergides, and Marco Capitanio. Probing force in living cells with optical tweezers: from single-molecule mechanics to cell mechanotransduction. *Biophysical reviews*, 11(5):765–782, 2019.

[165] Olga Yu Antonova, Olga Yu Kochetkova, and Igor L Kanev. Light-to-heat converting ecm-mimetic nanofiber scaffolds for neuronal differentiation and neurite outgrowth guidance. *Nanomaterials*, 12(13):2166, 2022.

[166] Nari Hong and Yoonkey Nam. Thermoplasmonic neural chip platform for in situ manipulation of neuronal connections in vitro. *Nature Communications*, 11(1):6313, 2020.

[167] Hongki Kang, Woongki Hong, Yujin An, Sangjin Yoo, Hyuk-Jun Kwon, and Yoonkey Nam. Thermoplasmonic optical fiber for localized neural stimulation. *ACS nano*, 14(9):11406–11419, 2020.

[168] Amy Sutton, Tanya Shirman, Jaakko VI Timonen, Grant T England, Philseok Kim, Mathias Kolle, Thomas Ferrante, Lauren D Zarzar, Elizabeth Strong, and Joanna Aizenberg. Photothermally triggered actuation of hybrid materials as a new platform for in vitro cell manipulation. *Nature communications*, 8(1):14700, 2017.

[169] Juan C Fraire, Gaëlle Houthaeve, Jing Liu, Laurens Raes, Lotte Vermeulen, Stephan Stremersch, Toon Brans, Gerardo Garcia-Diaz Barriga, Sarah De Keulenaer, Filip Van Nieuwerburgh, et al. Vapor nanobubble is the more reliable photothermal mechanism for inducing endosomal escape of sirna without disturbing cell homeostasis. *Journal of Controlled Release*, 319:262–275, 2020.

[170] Ruixia Chen, Jun Shi, Chongchong Liu, Jingguo Li, and Shaokui Cao. In situ self-assembly of gold nanorods with thermal-responsive microgel for multi-synergistic remote drug delivery. *Advanced Composites and Hybrid Materials*, 5(3):2223–2234, 2022.

[171] Ardeshir R Rastinehad, Harry Anastos, Ethan Wajswol, Jared S Winoker, John P Sfakianos, Sai K Doppalapudi, Michael R Carrick, Cynthia J Knauer, Bachir Taouli, Sara C Lewis, et al. Gold nanoshell-localized photothermal ablation of prostate tumors in a clinical pilot device study. *Proceedings of the National Academy of Sciences*, 116(37):18590–18596, 2019.

[172] Miao Li, Theobald Lohmuller, and Jochen Feldmann. Optical injection of gold nanoparticles into living cells. *Nano letters*, 15(1):770–775, 2015.

[173] Elina Ikonen. Roles of lipid rafts in membrane transport. *Current opinion in cell biology*, 13(4):470–477, 2001.

[174] Pallavi Varshney, Vikas Yadav, and Neeru Saini. Lipid rafts in immune signalling: current progress and future perspective. *Immunology*, 149(1):13–24, 2016.

[175] Consuelo Gajate and Faustino Mollinedo. Lipid rafts and raft-mediated supramolecular entities in the regulation of cd95 death receptor apoptotic signaling. *Apoptosis*, 20:584–606, 2015.

[176] Vincent Cottin, Joyce ES Doan, and David WH Riches. Restricted localization of the tnf receptor cd120a to lipid rafts: a novel role for the death domain. *The Journal of Immunology*, 168(8):4095–4102, 2002.

[177] Francisco S Mesquita, Laurence Abrami, Oksana Sergeeva, Priscilla Turelli, Enya Qing, Béatrice Kunz, Charlène Raclot, Jonathan Paz Montoya, Luciano A Abriata, Tom Gallagher, et al. S-acylation controls sars-cov-2 membrane lipid organization and enhances infectivity. *Developmental cell*, 56(20):2790–2807, 2021.

[178] Amir M Farnoud, Alvaro M Toledo, James B Konopka, Maurizio Del Poeta, and Erwin London. Raft-like membrane domains in pathogenic microorganisms. *Current topics in membranes*, 75:233–268, 2015.

[179] Masaya Higuchi, Kenneth M Izumi, and Elliott Kieff. Epstein–barr virus latent-infection membrane proteins are palmitoylated and raft-associated: protein 1 binds to the cytoskeleton through tnf receptor cytoplasmic factors. *Proceedings of the National Academy of Sciences*, 98(8):4675–4680, 2001.

[180] Daniel L Parton, Alex Tek, Marc Baaden, and Mark SP Sansom. Formation of raft-like assemblies within clusters of influenza hemagglutinin observed by md simulations. *PLoS Computational Biology*, 9(4):e1003034, 2013.

[181] Luke H Chamberlain. Detergents as tools for the purification and classification of lipid rafts. *FEBS letters*, 559(1-3):1–5, 2004.

[182] Tobias Baumgart, Adam T Hammond, Prabuddha Sengupta, Samuel T Hess, David A Holowka, Barbara A Baird, and Watt W Webb. Large-scale fluid/fluid phase separation of proteins and lipids in giant plasma membrane vesicles. *Proceedings of the National Academy of Sciences*, 104(9):3165–3170, 2007.

[183] Andreas Rørvig-Lund, Azra Bahadori, Szabolcs Semsey, Poul Martin Bendix, and Lene B Oddershede. Vesicle fusion triggered by optically heated gold nanoparticles. *Nano letters*, 15(6):4183–4188, 2015.

[184] Johannes Schindelin, Ignacio Arganda-Carreras, Erwin Frise, Verena Kaynig, Mark Longair, Tobias Pietzsch, Stephan Preibisch, Curtis Rueden, Stephan Saalfeld, Benjamin Schmid, et al. Fiji: an open-source platform for biological-image analysis. *Nature methods*, 9(7):676–682, 2012.

[185] Sarah L Veatch, Pietro Cicuta, Prabuddha Sengupta, Aurelia Honerkamp-Smith, David Holowka, and Barbara Baird. Critical fluctuations in plasma membrane vesicles. *ACS chemical biology*, 3(5):287–293, 2008.

[186] Nikolaj K Brinkenfeldt, André Dias, Guillermo Moreno-Pescador, Poul Martin Bendix, and Karen L Martinez. Quantitative determination of protein concentrations in living cells. *bioRxiv*, pages 2023–05, 2023.

[187] Erdinc Sezgin, Hermann-Josef Kaiser, Tobias Baumgart, Petra Schwille, Kai Simons, and Ilya Levental. Elucidating membrane structure and protein behavior using giant plasma membrane vesicles. *Nature protocols*, 7(6):1042–1051, 2012.

[188] Magdalena Kulma, Monika Hereć, Wojciech Grudziński, Gregor Anderluh, Wiesław I Gruszecki, Katarzyna Kwiatkowska, and Andrzej Sobota. Sphingomyelin-rich domains are sites of lysenin oligomerization: implications for raft studies. *Biochimica et Biophysica Acta (BBA)-Biomembranes*, 1798(3):471–481, 2010.

[189] Mohammad Fallahi-Sichani and Jennifer J Linderman. Lipid raft-mediated regulation of g-protein coupled receptor signaling by ligands which influence receptor dimerization: a computational study. *PloS one*, 4(8):e6604, 2009.

[190] Stephen A Johnson, Benjaminm M Stinson, MS Go, LM Carmona, Jason I Reminick, Xiangyi Fang Fang, and Tobias Baumgart. Temperature-dependent phase behavior and protein partitioning in giant plasma membrane vesicles. *Biochimica et Biophysica Acta (BBA)-Biomembranes*, 1798(7):1427–1435, 2010.

[191] Silvia Scolari, Katharina Imkeller, Fabian Jolmes, Michael Veit, Andreas Herrmann, and Roland Schwarzer. Modulation of cell surface transport and lipid raft localization by the cytoplasmic tail of the influenza virus hemagglutinin. *Cellular Microbiology*, 18(1):125–136, 2016.

[192] Emmie De Wit, Neeltje Van Doremalen, Darryl Falzarano, and Vincent J Munster. Sars and mers: recent insights into emerging coronaviruses. *Nature reviews microbiology*, 14(8):523–534, 2016.

[193] Massimo Pizzato, Chiara Baraldi, Giulia Boscato Sopetto, Davide Finozzi, Carmelo Gentile, Michele Domenico Gentile, Roberta Marconi, Dalila Paladino, Alberto Raoss, Ilary Riedmiller, et al. Sars-cov-2 and the host cell: a tale of interactions. *Frontiers in Virology*, 1:815388, 2022.

[194] Yuan Huang, Chan Yang, Xin-feng Xu, Wei Xu, and Shu-wen Liu. Structural and functional properties of sars-cov-2 spike protein: potential antivirus drug development for covid-19. *Acta Pharmacologica Sinica*, 41(9):1141–1149, 2020.

[195] Annett Petrich, Valentin Dunsing, Sara Bobone, and Salvatore Chiantia. Influenza a m2 recruits m1 to the plasma membrane: A fluorescence fluctuation microscopy study. *Biophysical Journal*, 120(24):5478–5490, 2021.

[196] Heiko Heerklotz. Triton promotes domain formation in lipid raft mixtures. *Biophysical journal*, 83(5):2693–2701, 2002.

[197] Charles A Day and Anne K Kenworthy. Functions of cholera toxin b-subunit as a raft cross-linker. *Essays in biochemistry*, 57:135–145, 2015.

[198] Xiangjie Sun and Gary R Whittaker. Role for influenza virus envelope cholesterol in virus entry and infection. *Journal of virology*, 77(23):12543–12551, 2003.

[199] Peter Scheiffele, Anton Rietveld, Thomas Wilk, and Kai Simons. Influenza viruses select ordered lipid domains during budding from the plasma membrane. *Journal of Biological Chemistry*, 274(4):2038–2044, 1999.

[200] Ivan V Polozov, Ludmila Bezrukov, Klaus Gawrisch, and Joshua Zimmerberg. Progressive ordering with decreasing temperature of the phospholipids of influenza virus. *Nature chemical biology*, 4(4):248–255, 2008.

[201] Sai Li, Frederic Eghiaian, Christian Sieben, Andreas Herrmann, and Iwan AT Schaap. Bending and puncturing the influenza lipid envelope. *Biophysical journal*, 100(3):637–645, 2011.

[202] Blanca B Diaz-Rohrer, Kandice R Levental, Kai Simons, and Ilya Levental. Membrane raft association is a determinant of plasma membrane localization. *Proceedings of the National Academy of Sciences*, 111(23):8500–8505, 2014.

[203] Justin A Peruzzi, Jan Steinkühler, Timothy Q Vu, Taylor F Gunnels, Vivian T Hu, Peilong Lu, David Baker, and Neha P Kamat. Hydrophobic mismatch drives self-organization of designer proteins into synthetic membranes. *Nature Communications*, 15(1):3162, 2024.

[204] Michael C Heinrich, Benjamin R Capraro, Aiwei Tian, Jose M Isas, Ralf Langen, and Tobias Baumgart. Quantifying membrane curvature generation of drosophila amphiphysin n-bar domains. *The journal of physical chemistry letters*, 1(23):3401–3406, 2010.

[205] Emmanuel Ibarboure, Martin Fauquignon, and Jean-François Le Meins. Obtention of giant unilamellar hybrid vesicles by electroformation and measurement of their mechanical properties by micropipette aspiration. *Journal of visualized experiments: JoVE*, 155:e60199, 2020.

[206] Jan Steinkühler, Piermarco Fonda, Tripta Bhatia, Ziliang Zhao, Fernanda SC Leomil, Reinhard Lipowsky, and Rumiana Dimova. Superelasticity of plasma-and synthetic membranes resulting from coupling of membrane asymmetry, curvature, and lipid sorting. *Advanced Science*, 8(21):2102109, 2021.

[207] Jan Steinkühler, Erdinc Sezgin, Iztok Urbančič, Christian Eggeling, and Rumiana Dimova. Mechanical properties of plasma membrane vesicles correlate with lipid order, viscosity and cell density. *Communications biology*, 2(1):337, 2019.

[208] Victoria Thusgaard Ruhoff. Assessment of crowding by viral spike protein neuraminidase as a potential driver for membrane budding. *Master Thesis, Niels Bohr Institute, University of Copenhagen*, 2021.

[209] Coline Prévost, Feng-Ching Tsai, Patricia Bassereau, and Mijo Simunovic. Pulling membrane nanotubes from giant unilamellar vesicles. *Journal of visualized experiments: JoVE*, e56086(130), 2017.

[210] Joshua Zimmerberg and Michael M Kozlov. How proteins produce cellular membrane curvature. *Nature reviews Molecular cell biology*, 7(1):9–19, 2006.

[211] Henry De Belly, Shannon Yan, Hudson Borja da Rocha, Sacha Ichbiah, Jason P Town, Patrick J Zager, Dorothy C Estrada, Kirstin Meyer, Hervé Turlier, Carlos Bustamante, et al. Cell protrusions and contractions generate long-range membrane tension propagation. *Cell*, 186(14):3049–3061, 2023.

[212] Marie T Vanier. Niemann-pick disease type c. *Orphanet journal of rare diseases*, 5:1–18, 2010.

[213] Benny Liu. Therapeutic potential of cyclodextrins in the treatment of niemann–pick type c disease. *Clinical lipidology*, 7(3):289, 2012.

[214] Marie T Vanier and Philippe Latour. Laboratory diagnosis of niemann–pick disease type c: the filipin staining test. In *Methods in cell biology*, volume 126, pages 357–375. Elsevier, 2015.

[215] Miao Xu, Ke Liu, Manju Swaroop, Wei Sun, Seameen J Dehdashti, John C McKew, and Wei Zheng. A phenotypic compound screening assay for lysosomal storage diseases. *Journal of Biomolecular Screening*, 19(1):168–175, 2014.

[216] Jorge L Rodriguez-Gil, Denise M Larson, Christopher A Wassif, Nicole M Yanjanin, Stacie M Anderson, Martha R Kirby, Niraj S Trivedi, Forbes D Porter, and William J Pavan. A somatic cell defect is associated with the onset of neurological symptoms in a lysosomal storage disease. *Molecular genetics and metabolism*, 110(1-2):188–190, 2013.

[217] Laura L Baxter, Dawn E Watkins-Chow, Nicholas L Johnson, Nicole Y Farhat, Frances M Platt, Ryan K Dale, Forbes D Porter, William J Pavan, and Jorge L Rodriguez-Gil. Correlation of age of onset and clinical severity in niemann–pick disease type c1 with lysosomal abnormalities and gene expression. *Scientific reports*, 12(1):2162, 2022.

[218] Rong Li, Jon Hao, Hideji Fujiwara, Miao Xu, Shu Yang, Sheng Dai, Yan Long, Manju Swaroop, Changhui Li, Mylinh Vu, et al. Analytical characterization of methyl-β-cyclodextrin for pharmacological activity to reduce lysosomal cholesterol accumulation in niemann-pick disease type c1 cells. *Assay and drug development technologies*, 15(4):154–166, 2017.

[219] Margaret Reynolds, Laura A Linneman, Sofia Luna, Barbara B Warner, Yumirle P Turmelle, Sakil S Kulkarni, Xuntian Jiang, Geetika Khanna, Marwan Shinawi, Forbes D Porter, et al. A phase 1/2 open label nonrandomized clinical trial of intravenous 2-hydroxypropyl-β-cyclodextrin for acute liver disease in infants with niemann-pick c1. *Molecular Genetics and Metabolism Reports*, 28:100772, 2021.

[220] Jessica Davidson, Elizabeth Molitor, Samantha Moores, Sarah E Gale, Kanagaraj Subramanian, Xuntian Jiang, Rohini Sidhu, Pamela Kell, Jesse Zhang, Hideji Fujiwara, et al. 2-hydroxypropyl-β-cyclodextrin is the active component in a triple combination formulation for treatment of niemann-pick c1 disease. *Biochimica et Biophysica Acta (BBA)-Molecular and Cell Biology of Lipids*, 1864(10):1545–1561, 2019.

[221] Margaret Burns, Kathleen Wisser, Jing Wu, Ilya Levental, and Sarah L Veatch. Miscibility transition temperature scales with growth temperature in a zebrafish cell line. *Biophysical journal*, 113(6):1212–1222, 2017.

[222] Ilya Levental, Fitzroy J Byfield, Pramit Chowdhury, Feng Gai, Tobias Baumgart, and Paul A Janmey. Cholesterol-dependent phase separation in cell-derived giant plasma-membrane vesicles. *Biochemical Journal*, 424(2):163–167, 2009.

[223] Erin M Gray, Gladys Díaz-Vázquez, and Sarah L Veatch. Growth conditions and cell cycle phase modulate phase transition temperatures in rbl-2h3 derived plasma membrane vesicles. *PloS one*, 10(9):e0137741, 2015.

[224] Carsen Stringer, Tim Wang, Michalis Michaelos, and Marius Pachitariu. Cellpose: a generalist algorithm for cellular segmentation. *Nature methods*, 18(1):100–106, 2021.

[225] Mohammad Reza Arastoo. Ph.d. thesis: Lateral organization of plasma membrane proteins studied using thermoplasmonics. *Niels Bohr Institute, University of Copenhagen*, 2019. https://nbi.ku.dk/english/theses/phd-theses/mohammad-reza-arastoo/.

Appendix A

Supplementary Figures

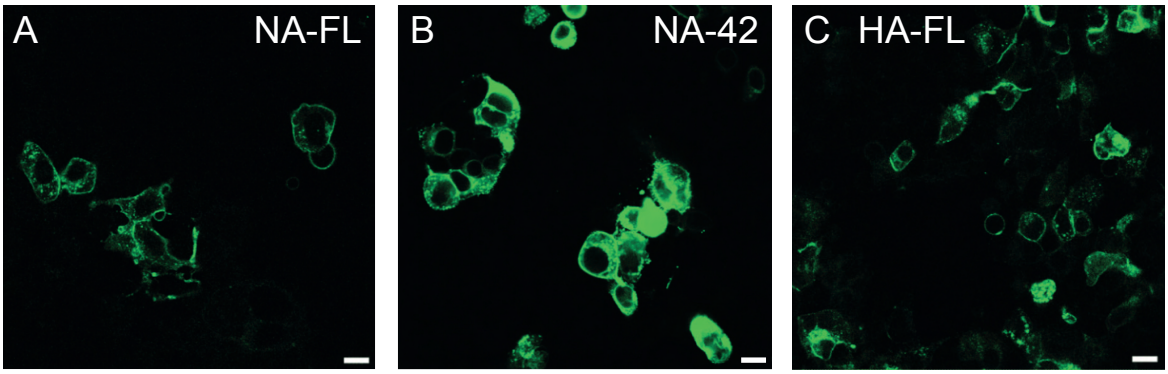

Fig. A.1 Cell expression from transfection with the constructs NA-FL, NA-42, HA-FL. NA-42 was experimentally observed to express more efficiently in cells than NA-FL and HA-FL. The images are reprinted from [225].

Protein	Phases intact post fusion?	GPMV fused to: Ld phase	Lo phase	Phase int.	Size ratio GUV/GPMV
HA	✗	✗	✗	✓	1.2
HA	✗	✗	✗	✓	1.9
HA	✗	✗	✓	✗	1.3
HA	✗	✗	✓	✗	2.1
HA	✓	✗	✓	✗	1.6
HA	✓	✗	✓	✗	2.0
HA	✓	✓	✗	✗	2.1
HA	✓	✗	✗	✓	1.6
HA	✓	✗	✓	✗	2.1
HA	✓	✗	✗	✓	2.0
HA	✓	✓	✗	✗	2.0
HA	✓	✓	✗	✗	2.8
HA	✓	✗	✗	✓	1.7
HA	✓	✗	✗	✓	2.1
HA	✓	✗	✗	✓	1.9

Protein	Phases intact post fusion?	GPMV fused to: Ld phase	Lo phase	Phase int.	Size ratio GUV/GPMV
NA	✗	✓	✗	✗	1.7
NA	✗	✗	✓	✗	1.9
NA	✗	✓	✗	✗	2.3
NA	✓	✓	✗	✗	2.1
NA	✓	✓	✗	✗	1.7
NA	✓	✓	✗	✗	2.0
NA	✓	✗	✗	✓	2.8
NA42	✗	✓	✗	✗	1.7
NA42	✓	✗	✗	✓	1.7
NA42	✓	✗	✗	✓	2.1
NA42	✓	✓	✗	✗	2.5
NA42	✓	✓	✗	✗	2.0
NA42	✓	✓	✗	✗	2.1
NA42	✓	✓	✗	✗	2.9
NA42	✓	✗	✓	✗	3.1
NA42	✓	✗	✗	✓	2.9
NA42	✓	✓	✗	✗	2.5

Fig. A.2 Overview of fusion specifics for HA-FL, NA-FL and NA-42. The table lists size ratio and site of fusion for representative data (where pre-fusion video was available) for protein constructs HA-FL (HA), NA-FL (NA) and NA-42.

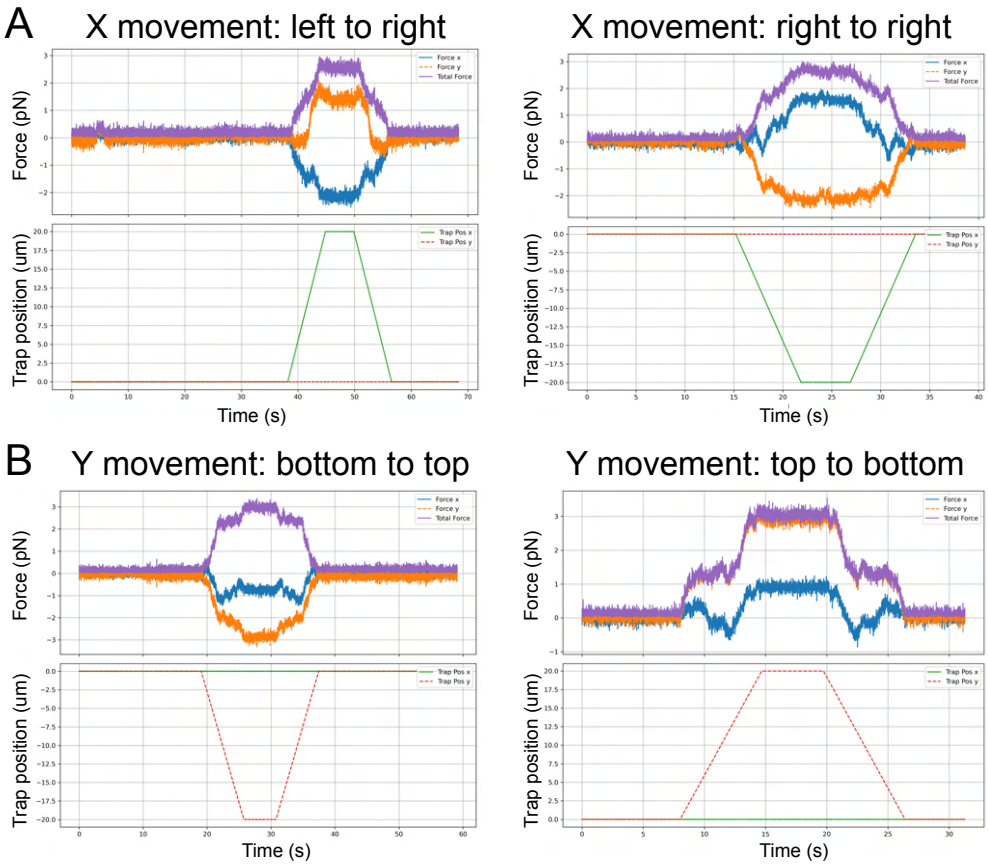

Fig. A.3 Force calibration corrections. Force plots for a 1μm bead in the trap. A) The force readouts change as the trap is moved in x direction (A) and the y direction (B) in the bright-field area. Here representative graphs are shown. An average of 3 read outs for each movement was recorded and the average change was used to calibrate the in-tube force measurements.

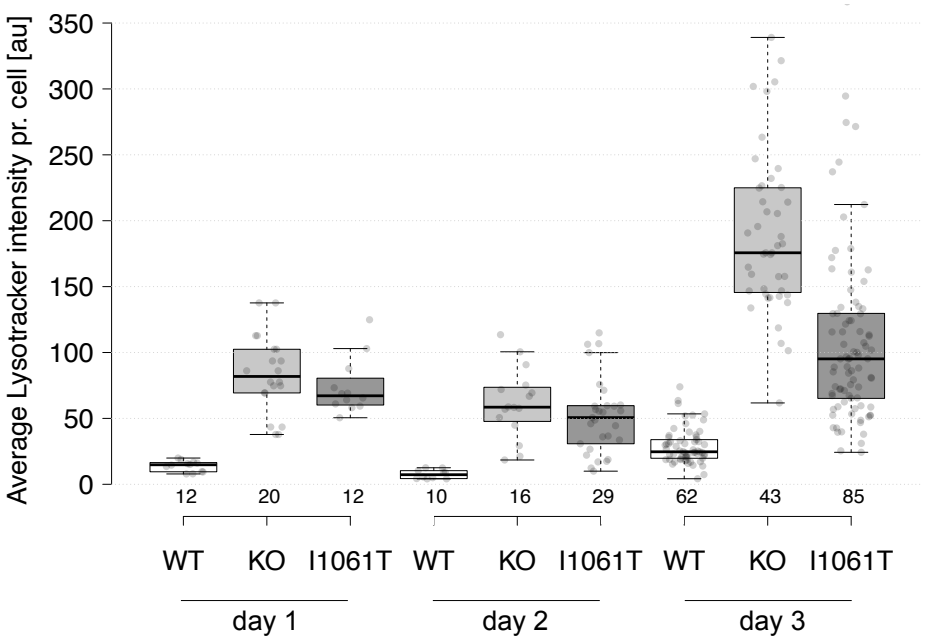

Fig. A.4 Average Lysotracker intensity in healthy and diseased cells. Boxplot showing 3 biological replicates were obtained for the average Lysotracker deep red intensity pr. cell for the healthy WT and disease cell models KO and I1061T. Jittered data points are shown and the total cells analyzed pr box shown above the x-axis.

Pairwise comparisons using Wilcoxon rank sum test with continuity correction

data: final_df_filt$norm_mean and final_df_filt$experiment

	I1061T 1mM HPCD	I1061T 1mM MBCD	I1061T untreated	KO 1mM HPCD	KO 1mM MBCD	KO untreated	WT 1mM HPCD	WT 1mM MBCD
I1061T 1mM MBCD	1.3e-06	-	-	-	-	-	-	-
I1061T untreated	0.44925	0.00018	-	-	-	-	-	-
KO 1mM HPCD	1.7e-07	< 2e-16	3.2e-08	-	-	-	-	-
KO 1mM MBCD	0.12506	8.3e-12	0.01793	1.3e-06	-	-	-	-
KO untreated	5.8e-10	0.03911	4.8e-08	< 2e-16	< 2e-16	-	-	-
WT 1mM HPCD	< 2e-16	< 2e-16	< 2e-16	< 2e-16	< 2e-16	< 2e-16	-	-
WT 1mM MBCD	< 2e-16	< 2e-16	< 2e-16	< 2e-16	< 2e-16	< 2e-16	0.00015	-
WT untreated	3.4e-15	< 2e-16	3.4e-15	0.01514	9.3e-11	< 2e-16	9.8e-12	1.9e-08

P value adjustment method: BH

Fig. A.5 P values for Lysotracker levels after treatment with cyclodextrins.

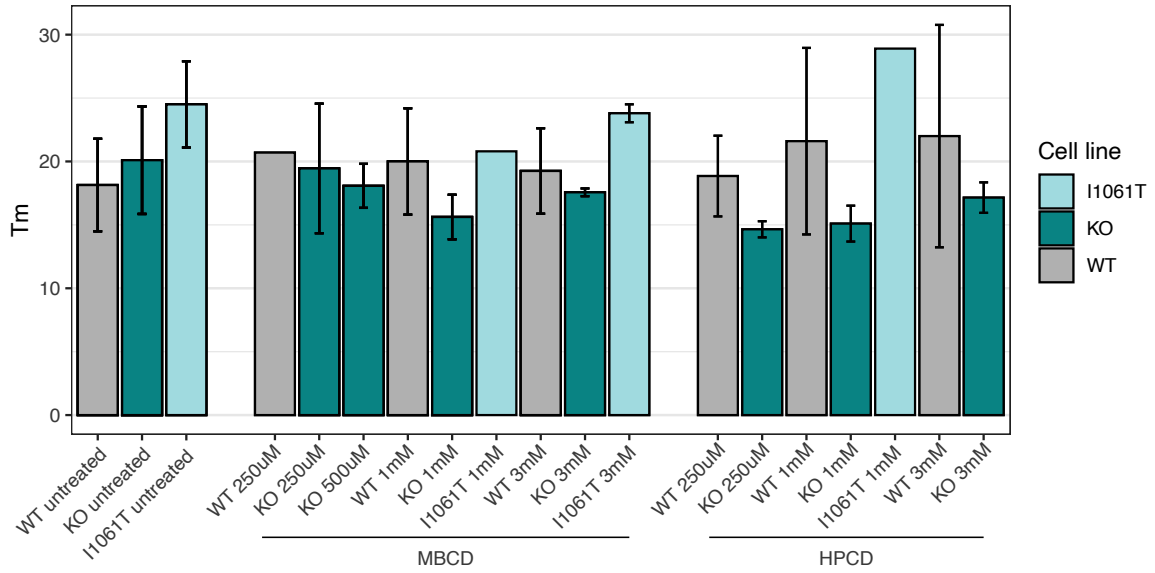

Fig. A.6 Tm variations for MβCD and HPβCD treatments. Various concentrations of MβCD and HPβCD across cells do not show a high variance, thus all treatment concentrations have been examined in groups of treated with MβCD (any concentration) and treated with and HPβCD (any concentration) in figure 7.4B.

Appendix B

Publications

B.1 Thermoplasmonic Vesicle Fusion Reveals Membrane Phase Segregation of Influenza Spike Proteins

Authors:
Guillermo Moreno-Pescador*, Mohammad Reza Arastoo*, Victoria Thusgaard Ruhoff, Salvatore Chiantia, Robert Daniels, and Poul Martin Bendix.
Status: Published

NANO LETTERS

pubs.acs.org/NanoLett Letter

Thermoplasmonic Vesicle Fusion Reveals Membrane Phase Segregation of Influenza Spike Proteins

Guillermo Moreno-Pescador,* Mohammad Reza Arastoo, Victoria Thusgaard Ruhoff, Salvatore Chiantia, Robert Daniels, and Poul Martin Bendix*

Cite This: *Nano Lett.* 2023, 23, 3377−3384 Read Online

ACCESS | Metrics & More | Article Recommendations | Supporting Information

ABSTRACT: Many cellular processes involve the lateral organization of integral and peripheral membrane proteins into nanoscale domains. Despite the biological significance, the mechanisms that facilitate membrane protein clustering into nanoscale lipid domains remain enigmatic. In cells, the analysis of membrane protein phase affinity is complicated by the size and temporal nature of ordered and disordered lipid domains. To overcome these limitations, we developed a method for delivering membrane proteins from transfected cells into phase-separated model membranes that combines optical trapping with thermoplasmonic-mediated membrane fusion and confocal imaging. Using this approach, we observed clear phase partitioning into the liquid disordered phase following the transfer of GFP-tagged influenza hemagglutinin and neuraminidase from transfected cell membranes to giant unilamellar vesicles. The generic platform presented here allows investigation of the phase affinity of any plasma membrane protein which can be labeled or tagged with a fluorescent marker.

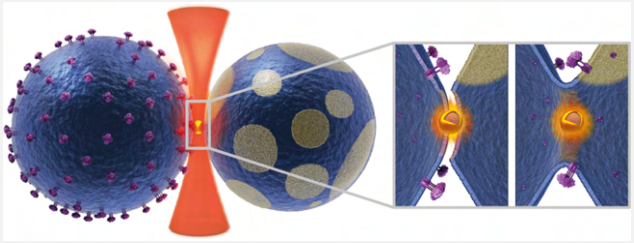

KEYWORDS: *thermoplasmonic membrane fusion, lipid raft, viral spike proteins, neuraminidase, hemagglutinin, influenza A virus*

Lipid domains play important roles in the organization of the cellular plasma membrane and hence control a number of processes[1,2] ranging from membrane trafficking[3] to apoptosis.[4,5] Additionally, they are implicated in a number of diseases including cancer emergence and invasion[6,7] and cardiovascular diseases.[8] Moreover, the discovery of a high level of cholesterol and saturated lipids in the envelope of HIV[9] together with the finding that ordered membrane domains play a role in pathogenic microorganisms[10] supports the hypothesis of a modulatory role of lipid domains in host−pathogen interactions[11] including virus entry[12] and budding.[13]

The proliferation of many enveloped viruses is intimately dependent on the structure and organization of the viral proteins in the plasma membrane. For influenza viruses, clustering of hemagglutinin (HA) and neuraminidase (NA) in the plasma membrane is crucial for the assembly and budding of progeny virions. The mechanism behind the lateral organization of proteins in the plasma membrane remains enigmatic, but the plasma membrane lipids have been proposed to be responsible for recruitment of transmembrane proteins to nanoscale budding sites of virus infected cells.[14,15] The idea of lipids being responsible for clustering virus proteins at the cell surface is appealing, and indeed colocalization, and resulting crowding, of viral envelope proteins with massive ectodomain heads could produce an asymmetric lateral pressure across the membrane capable of driving bending and thus contribute to viral budding.[16,17] Eukaryotic cell membranes have been proposed to form dynamic lipid raft structures enriched with proteins, allowing the cells to perform lateral organization of proteins into nanoscale domains.[18] The presence of rafts, initially verified using disputed detergent resistant methods, has been suggested as the driving mechanism for recruitment of viral proteins to the budding site.[2] Indeed, it was recently shown that oligomerization of GAG proteins involved in HIV virus facilitates formation of ordered lipid domains which recruited viral proteins to the budding site.[19] Such organization is critical for cell functions considering that membrane proteins constitute up to one-third of a mammalian cell proteome[20,21] and because the plasma membrane contains roughly 30000 proteins per μm^2, populating 30−55% of the membrane area.[22] Enriched in cholesterol and sphingolipids, lipid-raft domains could provide sorting platforms for both transmembrane and peripheral proteins possibly including viral proteins.[4,23−29]

The highly dynamic structure (milliseconds) and very small size (10−200 nm) of membrane domains make visual detection and investigation of rafts difficult.[30] The current

Received: January 31, 2023
Revised: March 21, 2023
Published: April 11, 2023

https://doi.org/10.1021/acs.nanolett.3c00371
Nano Lett. 2023, 23, 3377−3384

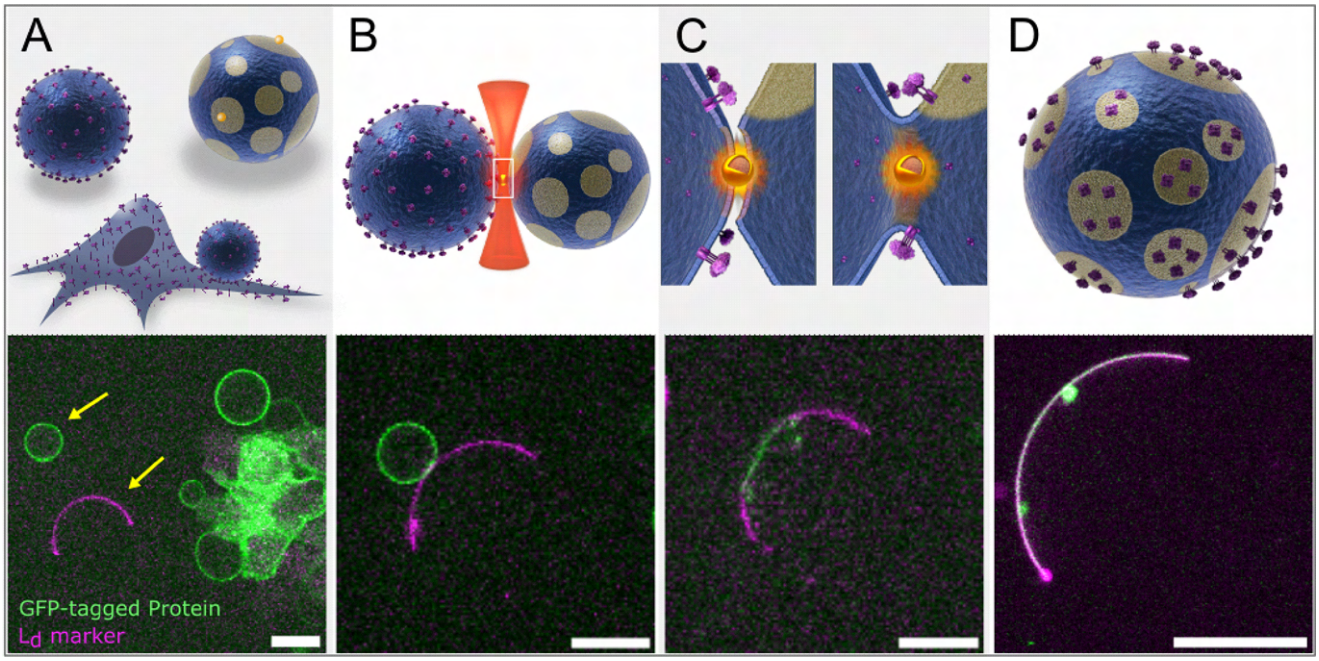

Figure 1. In vitro thermoplasmonic-based delivery of integral membrane proteins to phase-segregated model membranes. (A) HEK293T cells are transfected to express the protein of interest, here GFP-tagged hemagglutinin transmembrane domain (HA-TMD) with the ectodomain labeled with a GFP. In addition, they are treated with reagent that results in the production of GPMVs containing the expressed transmembrane protein in its correct orientation. Phase-separated giant unilamellar vesicles (GUVs) are also added to the cell culture. As the fusion mediator, 150 nm streptavidin conjugated gold nanoshells (AuNSs) are linked to the GUVs through the biotin−steptavidin interaction. Prior to fusion, a GPMV is grabbed by optical tweezers and brought in to close proximity of a GUV (yellow arrows). (B) Irradiation of the GPMV−GUV interface by the NIR laser attracts a AuNS into the laser focus where it produces local and transient heat sufficient to fuse the apposing membranes. (C) The process of lipid mixing following fusion. (D) The resultant vesicle retains its ordered and disordered phases, and the HA-TMD partitions into the liquid disordered phase (marked by 18:1 Liss Rhod. PE). The different colors in the schematics in (A−D, top panels) represent phases with different lipid order. The images have been adjusted in brightness and contrast for better visualization. Scale bars are 15 μm.

methods for studying rafts are based on biochemical, biophysical, computational, and analytical tools.[31] Biochemical tools use detergents to solubilize membrane lipids and proteins[32] which do not properly reflect the native molecular structure and organization of rafts. Biophysical tools are mainly based on model membranes,[33] including giant unilamellar vesicles (GUVs), into which membrane proteins can be reconstituted using biochemical protocols.[34,35] Despite the high resolution provided by some assays, most analytical tools require sample preparation involving tedious procedures[36] which can potentially influence the protein localization in model membranes.

Membrane proteins from influenza virus have been studied using cell-derived giant plasma membrane vesicles (GPMVs) which can exhibit large scale phase segregation only at very low temperatures (~5 °C) and by addition of the cross-linking agent cholera toxin B.[34,37] These studies have shown that NA and HA do partition into the more disordered lipid phase which is somewhat conflicting with the idea that viruses bud from cholesterol enriched domains. These findings have opened up new questions on how virus budding and plasma membrane structure are related, thus raising the possibility that raft association of virus proteins could be mediated through interactions between different proteins. However, the low temperature, and use of a toxin to trigger phase separation, raises concerns on whether this system sufficiently reflects the cellular plasma membrane.

Here, we present a general assay which can address the localization of transmembrane proteins in phase-separated membranes at a temperature set by the phase transition temperature of the lipid mixture and without the need of any chemical cross-linking agent. Phase-separated GUVs are fused with GPMVs containing the protein of interest in the correct orientation. The fused hybrid vesicle contains phase separated domains which allow us to study the localization of membrane protein phase affinity at physiologically relevant condition. We demonstrate the simplicity and efficacy of the method by investigating the phase affinity of influenza A virus membrane proteins and several chimeras containing specific domains of these proteins. Fusion of the vesicles is accomplished using thermoplasmonics and optical trapping.[38−40] This generic method can be applied to any membrane protein expressed in cells and does not require protein purification. Finally, it also holds the potential for studying interactions between either membrane proteins or between membrane and peripheral membrane binding proteins in a controlled manner under physiological conditions.

Chimeric fluorescent proteins of interest were transiently expressed in HEK293T cells to obtain the membrane proteins under physiological conditions. Following expression, a vesiculating reagent is added to the cells which triggers cells to detach part of their plasma membrane, containing the associated proteins, as giant plasma membrane vesicles (GPMVs), also known as blebs. The produced GPMVs hold the protein of interest in correct orientation with intact functionality.[37] To transfer the membrane proteins to a model membrane, we mix the GPMVs with phase-separated GUVs in a cell culture dish (Figures 1A and S1) at room temperature

https://doi.org/10.1021/acs.nanolett.3c00371
Nano Lett. 2023, 23, 3377−3384

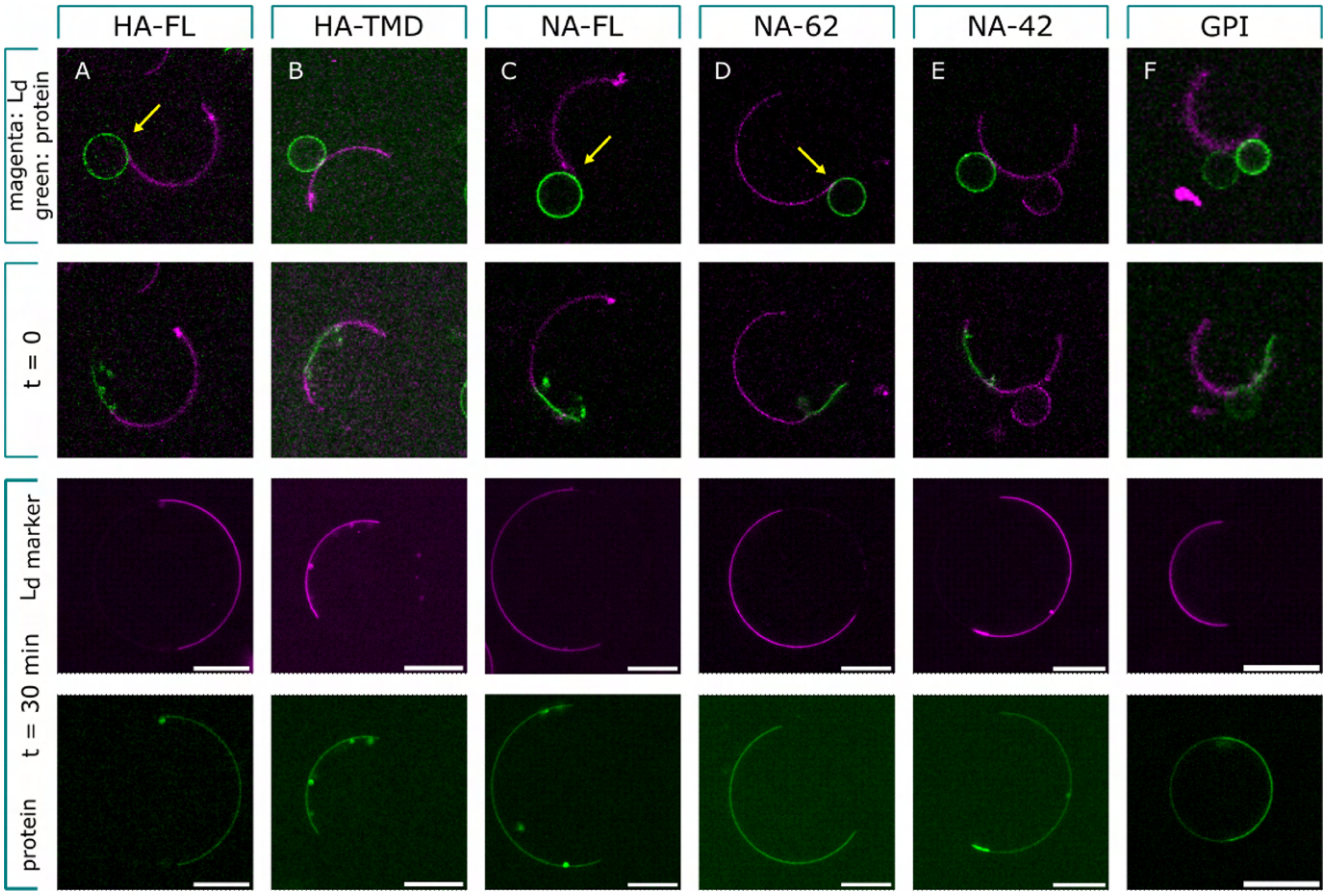

Figure 2. Phase preference of influenza HA, NA, and a GPI anchor control. The GPMVs extracted from the plasma membrane accommodate the GFP-tagged protein of interest in their membranes. The disordered phase of the GUVs is marked with the L_d marker 18:1 Liss Rhodamine PE that exclusively partitions into the disordered region. The first row shows the positions where the fusion happens (yellow arrows) at the ordered-disordered phase interface. At time zero (t = 0), the protein is mainly found near the site of fusion. The phase preference of all proteins was evaluated after 30 min (lowest two rows). (A) Full-length HA protein and (B) its transmembrane domain colocalize with the liquid disordered phase. (C) Full-length NA and two C-terminally truncated variants (NA-Δhead) (D) and (NA-TMD) (E) distribute into the disordered region. (F) GPI anchored GFP used as the positive control for liquid order phase partitioning.[64] The images have been adjusted in brightness and contrast for better visualization. Scale bars are 15 μm.

which ranged from 20 to 25 °C. The GUVs vary in size with a diameter between 10 and 80 μm and are composed of saturated fatty acids plus cholesterol and unsaturated lipids. The stoichiometry of lipids and cholesterol (Table S1) allows formation of a stable liquid-ordered phase (L_o, raft resembled domain) and liquid-disordered phase (L_d, nonraft resembled domain), respectively, at room temperature (T = 22 °C).

Because the GPMVs also differ in size, variations in the GUV's diameter enable us to select GUV−GPMVs of comparable size for a successful fusion (Figure 1B). The NIR laser (λ = 1064 nm) is then used to grab and position the GPMV of choice in close proximity to the selected GUV. We have included more details in the Supporting Information on the time scale of fusion, the protein partitioning dependence on relative vesicle sizes, and the fusion to different phases in the GUV (see Figures S2 and S3).

The 150 nm streptavidin conjugated gold nanoshells (AuNSs) are bound to biotinylated lipids in the GUV membrane. When the close contact between the GPMV and the GUV is established, the focus of the optical trap is positioned at the contact point of the two apposing membranes. The gold nanoparticles are mobile on the fluid GUV membrane and are pulled into the optical focus (Figure 1C). Irradiation of the AuNS by the NIR laser, operated at 3.04×10^{10} W m^{-2} at the sample, produces highly localized heat (on the order of $\Delta T \sim 200$ K)[40] which is sufficient to transiently open the two apposing membranes and, thereby, fuse the vesicles together to form a hybrid vesicle (Figure 1C). AuNSs produce a thermal pulse when entering the optical focus and subsequently escape the focus or become structurally degraded.[41] The membrane associated proteins are delivered to the phase-separated model membrane and are allowed to mix and partition to the phase of their preference (Figure 1D).

We examined the influenza membrane proteins HA and NA for which the phase affinity has been highly disputed in the literature.[15,42−45] Association of viral proteins with raft domains has been difficult to discern, mainly because raft domains are highly dynamic and of submicrometer size, thus making them difficult to be directly visualized in living cells. While HA has been reported to associate with rafts by cell surface analysis,[46] it has also been shown to partition into nonraft domains of model membranes.[34] However, the lipid preference of HA may be determined by the presence or absence of a palmitoyl anchor which could be responsible for recruiting it to ordered and raft-like phases.[47] Here, we used an engineered plasmid to transiently transfect HEK293T cells to

https://doi.org/10.1021/acs.nanolett.3c00371
Nano Lett. 2023, 23, 3377−3384

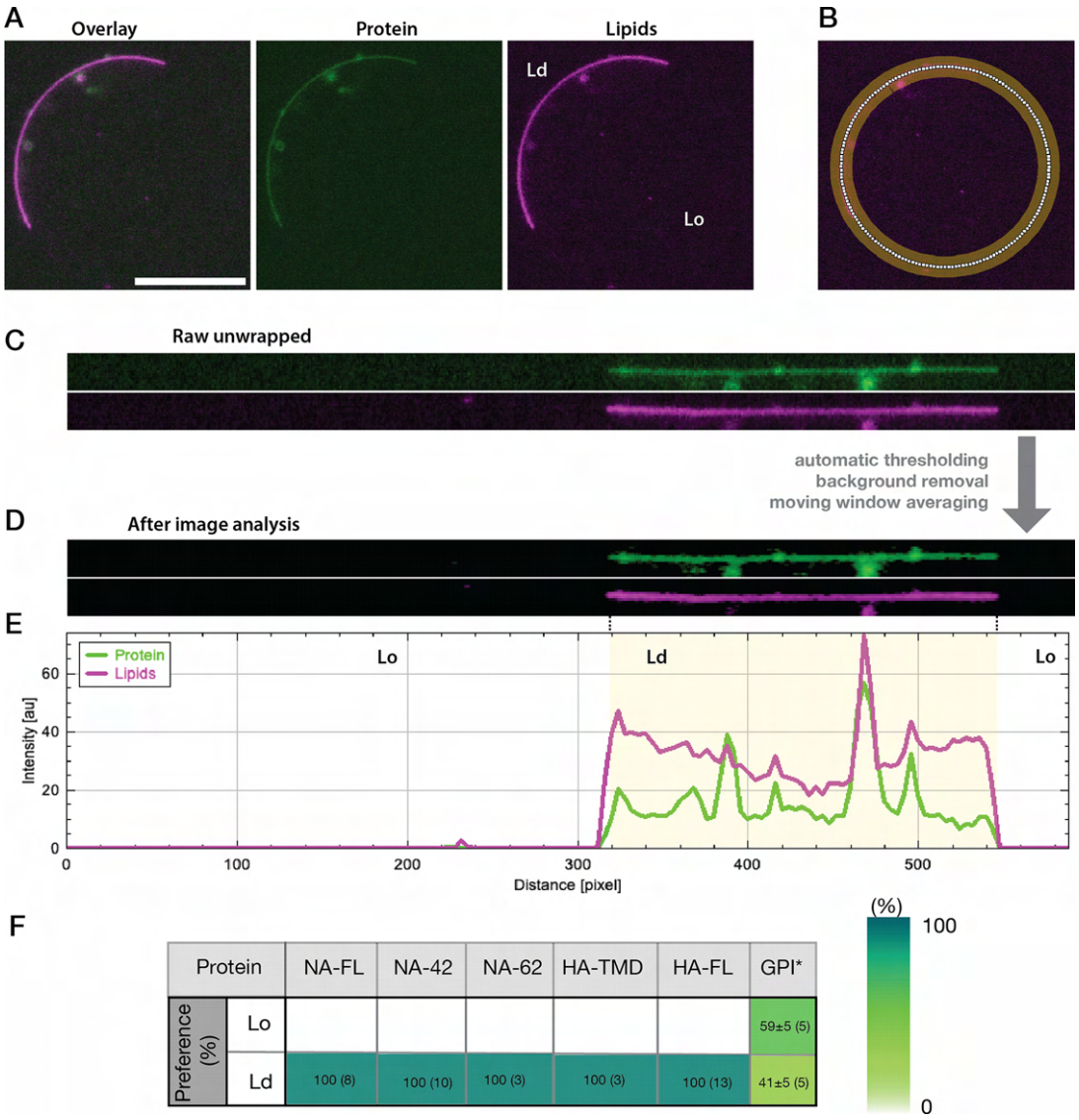

Figure 3. Quantification of protein partitioning. (A) Raw data from fusion experiment. GFP-tagged hemagglutinin transmembrane domain, abbreviated as HA-TMD (in green), and membrane (magenta) channels are overlaid. Scale bar is 15 μm. (B) Image exemplifying the selection of the vesicle by the image processing workflow. (C) Raw, unwrapped vesicle fluorescent channels. (D) Unwrapped vesicles after processing with image processing workflow. (E) Fluorescent intensity from the unwrapped vesicles from (D). L_d region is highlighted in yellow. (F) Lipid order preference from each of the proteins used in this project. We quantified the percentage of protein fluorescence signal coming from L_o and L_d lipid regions. The number in parentheses indicates the number of fusions performed for each type of protein. ∗ denotes L_o preference.

express a full-length HA (HA-FL) which has its C-terminal tagged with a green fluorescent protein (GFP) and is predominantly found to form trimers.[48] Also, we engineered a plasmid encoding for HA transmembrane domain with its N-terminal tagged with GFP which is additionally found to form both monomers and dimers.[48] We used plasmids encoding full length neuraminidase (NA-FL) and two variants that contained the NA-transmembrane domain and were C-terminally truncated at residue 42 (NA-42) or 62 (NA-62), removing the large head domain and leaving different portions of the stalk (Figure S4).[37,49] A similar strategy was followed for the GPI linked GFP control (Figure S5).

Similarly to what has been reported previously for recombinant HA reconstituted into phase-segregated vesicles,[50] we find that HA segregates into Ld domains in our hybrid vesicles after fusion (Figure 2A). Therefore, contrary to the widely accepted theory of influenza virus assembly,[15] HA expressed alone in HEK293T cells does not concentrate in cholesterol enriched lipid domains.

To exclude the possibility that the GFP label attached to the intracellular part of the HA could interfere with the palmitoylation sites, we tested the phase preference of the HA transmembrane domain (HA-TMD) with the ectodomain tagged with a GFP. However, as shown in Figure 2B, the HA-TMD also exhibited complete partitioning into the disordered phase, thus ruling out any interfering effect of the GFP label.

Influenza NA (NA-FL) displayed a preference for disordered domains, and this was confirmed by the observation of similar results using NA constructs without the enzymatic head domain (NA-62) and without both the head domain and majority of the stalk region (NA-42), as shown in Figures 2C–

https://doi.org/10.1021/acs.nanolett.3c00371
Nano Lett. 2023, 23, 3377−3384

E and S5. We note that NA-42 assembles into dimers within the membrane.

As a control, we investigated the partitioning of a GPI anchored GFP which has been found to localize preferentially into liquid ordered phases in GPMVs.[51] As expected, GPI predominantly localized into liquid ordered regions of the hybrid vesicles as shown in Figure 2F.

A total of 37 fusion experiments with varying protein constructs confirm partitioning of the proteins into the L_d phase (Figure 3). Quantification of partition coefficients was not possible due to complete partitioning of all proteins apart from the GPI control. As shown in Figures 3 and S6, all ordered phases (apart from the GPI experiment) contained no fluorescent signal after subtraction of the image background. Hence, we conclude that within the sensitivity of our imaging system, both HA and NA exhibit complete partitioning into L_d phases whereas for the GPI control we found a slight L_o preference equivalent to a partition coefficient $K_{p,raft} = 1.4$. $K_{p,raft}$ was calculated as in ref 51 where $K_{p,raft} = Int_{Lo}/Int_{Ld}$.

Our results show that both HA and NA do indeed localize into disordered domains, and it remains uncertain whether other effects like protein−protein interactions, between different types of virus proteins, could change this phase preference.

Reports on partitioning of virus proteins into L_o or L_d phases have yielded conflicting results. Early reports found that the transmembrane domain of HA interacted with sphingolipids and cholesterol as was found by isolating detergent-insoluble fractions from the plasma membrane;[52] however, the reliability of the detergent-resistant method has been questioned.[53,54] Using immuno-electron microscopy together with gold labeling, HA was shown to form nanoclusters in fixed cellular plasma membranes. However, no association between HA and rafts was found because it still clustered after depletion of the two raft constituents glycosphingolipids and cholesterol.[44] These methods entail procedures that capture raft associated proteins in a single time frame and not in a real-time manner. Other studies have found that HA partitions into raft phases only when a palmitoylation site is present.[34] Palmitoylation of proteins has been found to be a major factor for recruiting integral membrane proteins to ordered domains.[2,11,29,47] However, this ordered phase recruitment of HA, mediated by the palmitoylation site, is a mechanism which is not supported by our data. One scenario is that the cytoplasmic GFP label could interfere with the function of the palmitoylation anchor for the HA-FL. However, the HA-TMD which has its GFP label on the ectodomain still partitioned exclusively into the disordered phase. Therefore, we conclude that the palmitoylation site in HA is not sufficient to direct localization of the .HA protein into ordered phases of our hybrid vesicles.

Other factors which could influence protein partitioning are the hydrophobic match of the transmembrane domains with the thickness of the hydrophobic interior of the membrane[55] and the presence of actin. The cortical actin structure has been found to organize membrane proteins into clusters[11,27] and even affect the formation of L_o and L_d phases,[43] thus highlighting the fact that membrane organization alone is not the sole factor determining membrane protein distribution in living cells. Our results, however, show how protein partitioning behaves in the absence of actin because GPMVs, used here for the formation of hybrid vesicles, are known to be devoid of assembled cytoskeletal structure.[56] Interactions between proteins is another factor which could influence protein partitioning, as shown recently in ref 57, where a complex interaction was reported between influenza A membrane proteins during viral budding. These findings, together with our results, suggest that there could be more complex interactions at play during viral budding than previously anticipated.[58]

Delivering plasma membrane proteins to GUVs by this method provides several advantages. The control of the fusion site allowed us to test for protein partitioning after fusion into (i) the L_d phase, (ii) the L_o phase, or (iii) the L_d/L_o phase interface. An overview of protein partitioning from these three fusion sites is given in Figure S2C and shows that protein partitioning does not depend on where fusion takes place on the GUV. In addition, because the fused GPMVs are derived from transfected cells, they contain the lipid and protein diversity of the plasma membrane, although in a diluted version. Importantly, the final hybrid vesicle contains several types of proteins correctly oriented, as seen from a biological perspective, with ectodomains pointing outward.

The GPMV/GUV hybrid vesicle assay adds another biologically relevant model system to be used for studying proteins in membranes, and the question remains how the membrane in the hybrid vesicles is related to the phases in more studied GPMVs and GUVs. L_o/L_d phases in GUVs form due to interactions between cholesterol and the saturated acyl chains, and this interaction is known to form phases with significantly different lipid order as quantified by measuring the hydration level or, equivalently, the generalized polarization (G_p value) using environmentally sensitive dyes like Laurdan.[59] However, this large difference between L_o and L_d phases is known to be much attenuated in both cooled GPMVs and osmotically induced plasma membrane spheres (PMS induced at 37 °C) which should closely mimic the plasma membrane of living cells.[60] Importantly, the hybrid vesicles in our work would mimic the plasma membrane to a higher degree than GUVs, but the phases observed in these hybrid vesicles must be somewhat affected by the presence of lipids and cholesterol from the GUV. Our hybrid vesicles contain both glycans, various proteins, and a host of lipids which "smooth" the phase differences to become more cell-like with small differences in G_p value as measured by Laurdan in GPMV.[60]

The thermal damage to lipids can be neglected due to the fact that the heating region surrounding the heated nanoparticle is highly localized and transient. Our previous and extensive work on the plasmonic heating of these nanoparticles clearly show that the high temperatures ($\Delta T > 100$ °C) are only located within a distance of ca. 100 nm from the particle surface which has been confirmed in both experiments and simulations.[40,61] Morover, the time scale of fusion is on the order of a second.[62] Lipids in freestanding lipid bilayers and in GPMVs have a diffusion constant of $D \sim 5\ \mu m^2/s$ and for neuraminidase proteins $D \sim 1\ \mu m^2/s$,[37] and hence only limited mixing between the locally heated area and the rest of the large GUV/GPMVs takes place within this short time. Hence, we conclude that only minor protein and lipid damage can be expected from this method simply due to the short time a small fraction of the lipids are exposed to the heating.

We present a new technique that allows for effective transfer of membrane proteins to a phase-segregated model membrane system in which phase partitioning can be observed at physiological conditions without the addition of chemical and cross-linking reagents. With this method we demonstrate

https://doi.org/10.1021/acs.nanolett.3c00371
Nano Lett. 2023, 23, 3377−3384

that the viral spike proteins HA and NA partition predominantly into the liquid disordered phase. Further studies will reveal how coexistence of other proteins from influenza A virus embedded in a model membrane affect their mutual preference for a specific lipid phase. An extremely interesting future perspective of the current method is the possibility of combinatorial selection of proteins to be added sequentially to a hybrid GUV/GPMV model membrane. Influenza virus proteins HA, NA, M1, and M2 are populating the virus envelope, and our assay can be employed to systematically investigate possible interprotein interactions which could change their phase affinity and even other membrane remodeling behavior that these proteins could be responsible for. Also, the introduction of cytoskeletal structures into hybrid vesicles is straightforward using our method. This can be achieved by fusion of GUVs containing actin monomers and actin-membrane linkers to GPMVs which contain the cytosolic actin polymerization factors from the donor cell. In general, our method allows for generic investigation of how single proteins, and mixtures of proteins, collectively organize in heterogeneous membranes which will advance our understanding of protein function in complex biological membranes.

■ ASSOCIATED CONTENT

Data Availability Statement

The data that support the findings of this study are openly available in Zenodo at 10.5281/zenodo.7577427 in ref 63.

Supporting Information

The Supporting Information is available free of charge at https://pubs.acs.org/doi/10.1021/acs.nanolett.3c00371.

Data analysis, design and preparation of plasmids, transfection and fusion protocols, GPMV isolation, GUV formation, and additional figures (PDF)

■ AUTHOR INFORMATION

Corresponding Authors

Guillermo Moreno-Pescador − *Niels Bohr Institute, University of Copenhagen, 2100 København Ø, Denmark;* orcid.org/0000-0001-6923-9923; Email: moreno@nbi.ku.dk

Poul Martin Bendix − *Niels Bohr Institute, University of Copenhagen, 2100 København Ø, Denmark;* orcid.org/0000-0001-8838-8887; Email: bendix@nbi.ku.dk

Authors

Mohammad Reza Arastoo − *Niels Bohr Institute, University of Copenhagen, 2100 København Ø, Denmark;* orcid.org/0000-0002-7463-2321

Victoria Thusgaard Ruhoff − *Niels Bohr Institute, University of Copenhagen, 2100 København Ø, Denmark;* orcid.org/0000-0002-7986-7381

Salvatore Chiantia − *Institute of Biochemistry and Biology, University of Potsdam, 14476 Potsdam, Germany;* orcid.org/0000-0003-0791-967X

Robert Daniels − *Division of Viral Products, Center for Biologics Evaluation and Research, Food and Drug Administration, Silver Spring, Maryland 20993, United States;* orcid.org/0000-0002-5988-2920

Complete contact information is available at: https://pubs.acs.org/10.1021/acs.nanolett.3c00371

Author Contributions

G.M.-P. and M.R.A. contributed equally to this work.

Notes

The authors declare no competing financial interest.

■ ACKNOWLEDGMENTS

This work was financially supported by Danish Council for Independent Research, Natural Sciences (DFF-4181-00196) and Novo Nordisk Foundation Interdisciplinary Synergy Program (NNF18OC0034936), Novo Nordisk Foundation project grant (NNF20OC0065357), Novo Exploratory Synergy Grant (NNF20OC0064565), Novo Nordisk Infrastructure grant (NNF20OC0061176) and the German Research Foundation (254850309). We thank Henrik Østbye, who was involved in the development of the NA and NA-mutant plasmids, as previously reported in ref 37, and Annett Petrich for help with the HA plasmids. We also acknowledge Nicola De Franceschi for fruitful discussions about this project back at Patricia's Bassereau lab at the Curie Institute.

■ REFERENCES

(1) Lee, M. Y.; Ryu, J. M.; Lee, S. H.; Park, J. H.; Han, H. J. Lipid rafts play an important role for maintenance of embryonic stem cell self-renewal. *J. Lipid Res.* **2010**, *51* (8), 2082−2089.

(2) Levental, I.; Levental, K. R.; Heberle, F. A. Lipid rafts: Controversies resolved, mysteries remain. *Trends in Cell Biology* **2020**, *30* (5), 341−353.

(3) Ikonen, E. Roles of lipid rafts in membrane transport. *Curr. Opin. Cell Biol.* **2001**, *13* (4), 470−477.

(4) Cottin, V.; Doan, J. E. S.; Riches, D. W. H. Restricted Localization of the TNF Receptor CD120a to Lipid Rafts: A Novel Role for the Death Domain. *J. Immunol.* **2002**, *168* (8), 4095−4102.

(5) Gajate, C.; Mollinedo, F. Edelfosine and perifosine induce selective apoptosis in multiple myeloma by recruitment of death receptors and downstream signaling molecules into lipid rafts. *Blood* **2007**, *109* (2), 711−719.

(6) Murai, T. The role of lipid rafts in cancer cell adhesion and migration. *International Journal of Cell Biology* **2012**, *2012*, 1−6.

(7) Mollinedo, F.; Gajate, C. Lipid rafts as signaling hubs in cancer cell survival/death and invasion: Implications in tumor progression and therapy. *J. Lipid Res.* **2020**, *61* (5), 611−635.

(8) Rios, F. J. O.; Ferracini, M.; Pecenin, M.; Koga, M. M.; Wang, Y.; Ketelhuth, D. F. J.; Jancar, S. Uptake of oxLDL and IL-10 Production by Macrophages Requires PAFR and CD36 Recruitment into the Same Lipid Rafts. *PLoS One* **2013**, *8* (10), 1−13.

(9) Lorizate, M.; Sachsenheimer, T.; Glass, B.; Habermann, A.; Gerl, M. J.; Krausslich, H.-G.; Brugger, B. Comparative lipidomics analysis of HIV-1 particles and their producer cell membrane in different cell lines. *Cellular Microbiology* **2013**, *15* (2), 292−304.

(10) Farnoud, A. M.; Toledo, A. M.; Konopka, J. B.; Del Poeta, M.; London, E. Chapter Seven - Raft-Like Membrane Domains in Pathogenic Microorganisms. *Lipid Domains* **2015**, *75*, 233−268.

(11) Higuchi, M.; Izumi, K. M.; Kieff, E. Epstein-barr virus latent-infection membrane proteins are palmitoylated and raft-associated: Protein 1 binds to the cytoskeleton through tnf receptor cytoplasmic factors. *Proc. Natl. Acad. Sci. U. S. A.* **2001**, *98* (8), 4675−4680.

(12) Norkin, L. C. Simian virus 40 infection via MHC class I molecules and caveolae. *Immunological Reviews* **1999**, *168* (5), 13−22.

(13) Dick, R. A.; Goh, S. L.; Feigenson, G. W.; Vogt, V. M. HIV-1 gag protein can sense the cholesterol and acyl chain environment in model membranes. *Proc. Natl. Acad. Sci. U. S. A.* **2012**, *109* (46), 18761−18766.

(14) Barman, S.; Adhikary, L.; Chakrabarti, A. K.; Bernas, C.; Kawaoka, Y.; Nayak, D. P. Role of Transmembrane Domain and Cytoplasmic Tail Amino Acid Sequences of Influenza A Virus Neuraminidase in Raft Association and Virus Budding. *J. Virol.* **2004**, *78* (10), 5258−5269.

(15) Veit, M.; Thaa, B. Association of influenza virus proteins with membrane rafts. *Advances in Virology* **2011**, *2011*, 1−14.
(16) Guigas, G.; Weiss, M. Effects of protein crowding on membrane systems. *Biochimica et Biophysica Acta - Biomembranes* **2016**, *1858* (10), 2441−2450.
(17) Ruhoff, V. T.; Moreno-Pescador, G.; Pezeshkian, W.; Bendix, P. M. Strength in numbers: effect of protein crowding on the shape of cell membranes. *Biochem. Soc. Trans.* **2022**, *50* (5), 1257−1267.
(18) Simons, K.; Ikonen, E. Functional rafts in cell membranes. *Nature* **1997**, *387* (6633), 569−572.
(19) Sengupta, P.; Seo, A. Y.; Pasolli, H. A.; Song, Y. E.; Johnson, M. C.; Lippincott-Schwartz, J. A lipid-based partitioning mechanism for selective incorporation of proteins into membranes of HIV particles. *Nat. Cell Biol.* **2019**, *21*, 452−461.
(20) Wallin, E.; Von Heijne, G. Genome-wide analysis of integral membrane proteins from eubacterial, archaean, and eukaryotic organisms. *Protein Sci.* **1998**, *7* (4), 1029−1038.
(21) Alberts, B.; Johnson, A.; Lewis, J.; Morgan, D.; Raff, M.; Roberts, K.; Walter, P. *Molecular Biology of the Cell*, 5th ed.; W.W. Norton & Company: 2014.
(22) Lindén, M.; Sens, P.; Phillips, R. Entropic tension in crowded membranes. *PLoS Computational Biology* **2012**, *8* (3), 1−10.
(23) Ferguson, M. A. J.; Williams, A. F. Cell-Surface Anchoring of Proteins Via Glycosyl-Phosphatidylinositol Structures. *Annual review of biochemistry* **1988**, *57* (1), 285−320.
(24) Brown, D. A.; Rose, J. K. Sorting of GPI-anchored proteins to glycolipid-enriched membrane subdomains during transport to the apical cell surface. *Cell* **1992**, *68* (3), 533−544.
(25) Suzuki, K. G N; Kasai, R. S; Hirosawa, K. M; Nemoto, Y. L; Ishibashi, M.; Miwa, Y.; Fujiwara, T. K; Kusumi, A. Transient GPI-anchored protein homodimers are units for raft organization and function. *Nat. Chem. Biol.* **2012**, *8* (9), 774−783.
(26) Casey, P. J. Protein lipidation in cell signaling. *Science* **1995**, *268* (5208), 221−225.
(27) Lallemand-Breitenbach, V.; Quesnoit, M.; Braun, V.; El Marjou, A.; Pous, C.; Goud, B.; Perez, F. CLIPR-59 is a lipid raft-associated protein containing a cytoskeleton-associated protein glycine-rich domain (CAP-Gly) that perturbs microtubule dynamics. *J. Biol. Chem.* **2004**, *279* (39), 41168−41178.
(28) Horejsí, V. Transmembrane adaptor proteins in membrane microdomains: Important regulators of immunoreceptor signaling. *Immunol. Lett.* **2004**, *92* (1−2), 43−49.
(29) Diaz-Rohrer, B. B.; Levental, K. R.; Simons, K.; Levental, I. Membrane raft association is a determinant of plasma membrane localization. *Proc. Natl. Acad. Sci. U. S. A.* **2014**, *111* (23), 8500−8505.
(30) Lingwood, D.; Simons, K. Lipid rafts as a membrane-organizing principle. *Science* **2010**, *327* (5961), 46−50.
(31) Sezgin, E.; Levental, I.; Mayor, S.; Eggeling, C. The mystery of membrane organization: Composition, regulation and roles of lipid rafts. *Nat. Rev. Mol. Cell Biol.* **2017**, *18* (6), 361−374.
(32) Steck, T. L.; Yu, J. Selective solubilization of proteins from red blood cell membranes by protein perturbants. *Journal of Supramolecular and Cellular Biochemistry* **1973**, *1* (3), 220−232.
(33) Sezgin, E.; Schwille, P. Model membrane platforms to study protein-membrane interactions. *Molecular Membrane Biology* **2012**, *29* (5), 144−154.
(34) Nikolaus, J.; Scolari, S.; Bayraktarov, E.; Jungnick, N.; Engel, S.; Plazzo, A. P.; Stockl, M.; Volkmer, R.; Veit, M.; Herrmann, A. Hemagglutinin of influenza virus partitions into the nonraft domain of model membranes. *Biophys. J.* **2010**, *99* (2), 489−498.
(35) Garten, M.; Aimon, S.; Bassereau, P.; Toombes, G. E S. Reconstitution of a Transmembrane Protein, the Voltage-gated Ion Channel, KvAP, into Giant Unilamellar Vesicles for Microscopy and Patch Clamp Studies. *J. Visualized Exp.* **2015** (95), 1−16.
(36) Leser, G. P.; Lamb, R. A. Influenza virus assembly and budding in raft-derived microdomains: A quantitative analysis of the surface distribution of HA, NA and M2 proteins. *Virology* **2005**, *342* (2), 215−227.
(37) Moreno-Pescador, G.; Florentsen, C. D.; Østbye, H.; Sønder, S. L.; Boye, T. L.; Veje, E. L.; Sonne, A. K.; Semsey, S.; Nylandsted, J.; Daniels, R.; Bendix, P. M. Curvature- and Phase-Induced Protein Sorting Quantified in Transfected Cell-Derived Giant Vesicles. *ACS Nano* **2019**, *13* (6), 6689−6701.
(38) Rørvig-Lund, A.; Bahadori, A.; Semsey, S.; Bendix, P. M.; Oddershede, L. B. Vesicle fusion triggered by optically heated gold nanoparticles. *Nano Lett.* **2015**, *15* (6), 4183−4188.
(39) Bahadori, A.; Moreno-Pescador, G.; Oddershede, L. B; Bendix, P. M Remotely controlled fusion of selected vesicles and living cells: a key issue review. *Rep. Prog. Phys.* **2018**, *81* (3), 032602.
(40) Jauffred, J.; Samadi, A.; Klingberg, H.; Bendix, P. M.; Oddershede, L. B. Plasmonic heating of nanostructures. *Chem. Rev.* **2019**, *119* (13), 8087−8130.
(41) Samadi, A.; Klingberg, H.; Jauffred, L.; Kjær, A.; Bendix, P. M.; Oddershede, L. B. Platinum nanoparticles: a non-toxic, effective and thermally stable alternative plasmonic material for cancer therapy and bioengineering. *Nanoscale* **2018**, *10* (19), 9097−9107.
(42) Hess, S. T.; Kumar, M.; Verma, A.; Farrington, J.; Kenworthy, A.; Zimmerberg, J. Quantitative electron microscopy and fluorescence spectroscopy of the membrane distribution of influenza hemagglutinin. *J. Cell Biol.* **2005**, *169* (6), 965−976.
(43) Gudheti, M. V.; Curthoys, N. M.; Gould, T. J.; Kim, D.; Gunewardene, M. S.; Gabor, K. A.; Gosse, J. A.; Kim, C. H.; Zimmerberg, J.; Hess, S. T. Actin Mediates the Nanoscale Membrane Organization of the Clustered Membrane Protein Influenza Hemagglutinin. *Biophys. J.* **2013**, *104*, 2182−2192.
(44) Wilson, R. L.; Frisz, J. F.; Klitzing, H. A.; Zimmerberg, J.; Weber, P. K.; Kraft, M. L. Hemagglutinin Clusters in the Plasma Membrane Are Not Enriched with Cholesterol and Sphingolipids. *Biophys. J.* **2015**, *108* (108), 1652−1659.
(45) Rossman, J. S.; Lamb, R. A. Influenza virus assembly and budding. *Virology* **2011**, *411* (2), 229−236.
(46) Takeda, M.; Leser, G. P.; Russell, C. J.; Lamb, R. A. Influenza virus hemagglutinin concentrates in lipid raft microdomains for efficient viral fusion. *Proc. Natl. Acad. Sci. U. S. A.* **2003**, *100* (25), 14610−14617.
(47) Levental, I.; Lingwood, D.; Grzybek, M.; Coskun, U.; Simons, K. Palmitoylation regulates raft affinity for the majority of integral raft proteins. *Proc. Natl. Acad. Sci. U. S. A.* **2010**, *107* (51), 22050−22054.
(48) Dunsing, V.; Luckner, M.; Zuhlke, B.; Petazzi, R. A.; Herrmann, A.; Chiantia, S. Optimal fluorescent protein tags for quantifying protein oligomerization in living cells. *Sci. Rep.* **2018**, *8* (1), 10634.
(49) Nordholm, J.; Petitou, J.; Ostbye, H.; da Silva, D. V.; Dou, D.; Wang, H.; Daniels, R. Translational Regulation of Viral Secretory Proteins by the 5′ Coding Regions and a Viral Rna-Binding Protein. *J. Cell Biol.* **2017**, *216*, 2283−2293.
(50) Bacia, K.; Schuette, C. G.; Kahya, N.; Jahn, R.; Schwille, P. SNAREs Prefer Liquid-disordered over "Raft" (Liquid-ordered) Domains When Reconstituted into Giant Unilamellar Vesicles. *J. Biol. Chem.* **2004**, *279* (36), 37951−37955.
(51) Levental, I.; Lingwood, D.; Grzybek, M.; Coskun, U.; Simons, K. Palmitoylation regulates raft affinity for the majority of integral raft proteins. *Proc. Natl. Acad. Sci. U. S. A.* **2010**, *107* (51), 22050−22054.
(52) Scheiffele, P.; Roth, M. G.; Simons, K. Interaction of influenza virus haemagglutinin with sphingolipid−cholesterol membrane domains via its transmembrane domain. *EMBO Journal* **1997**, *16* (18), 5501−5508.
(53) Babiychuk, E. B.; Draeger, A. Biochemical characterization of detergent-resistant membranes: a systematic approach. *Biochem. J.* **2006**, *397* (3), 407−417.
(54) Heerklotz, H.; Szadkowska, H.; Anderson, T.; Seelig, J. The sensitivity of lipid domains to small perturbations demonstrated by the effect of Triton. *J. Mol. Biol.* **2003**, *329* (4), 793−799.
(55) Lorent, JH.; Levental, KR.; Ganesan, L.; Rivera-Longsworth, G.; Sezgin, E.; Doktorova, MD.; Lyman, E.; Levental, I. Plasma membranes are asymmetric in lipid unsaturation, packing, and protein shape. *Nat. Chem. Biol.* **2020**, *16* (6), 644−652.

https://doi.org/10.1021/acs.nanolett.3c00371
Nano Lett. 2023, 23, 3377−3384

(56) Scott, R. E.; Perkins, R. G.; Zschunke, M. A.; Hoerl, B. J.; Maercklein, P. B. Plasma membrane vesiculation in 3T3 and SV3T3 cells. I. Morphological and biochemical characterization. *Journal of Cell Science* **1979**, *35*, 229−243.
(57) Petrich, A.; Dunsing, V.; Bobone, S.; Chiantia, S. Influenza A M2 recruits M1 to the plasma membrane: A fluorescence fluctuation microscopy study. *Biophys. J.* **2021**, *120* (24), 5478−5490.
(58) Chen, B. J; Leser, G. P; Morita, E.; Lamb, R. A Influenza virus hemagglutinin and neuraminidase, but not the matrix protein, are required for assembly and budding of plasmid-derived virus-like particles. *J. Virol.* **2007**, *81* (13), 7111−7123.
(59) Kaiser, H. J.; Lingwood, D.; Levental, I.; Sampaio, J. L.; Kalvodova, L.; Rajendran, L.; Simons, K. Order of lipid phases in model and plasma membranes. *Proc. Natl. Acad. Sci. U. S. A.* **2009**, *106* (39), 16645−16650.
(60) Sezgin, E.; Kaiser, H.-J.; Baumgart, T.; Schwille, P.; Simons, K.; Levental, I. Elucidating membrane structure and protein behavior using giant plasma membrane vesicles. *Nat. Protoc.* **2012**, *7* (6), 1042−1051.
(61) Bendix, P. M.; Reihani, S. N. S.; Oddershede, L. B. Direct Measurements of Heating by Electromagnetically Trapped Gold Nanoparticles on Supported Lipid Bilayers. *ACS Nano* **2010**, *4* (4), 2256−2262.
(62) Rørvig-Lund, A.; Bahadori, A.; Semsey, S.; Bendix, P. M.; Oddershede, L. B. Oddershede. Vesicle Fusion Triggered by Optically Heated Gold Nanoparticles. *Nano Lett.* **2015**, *15* (6), 4183−4188.
(63) Moreno-Pescador, G.; Arastoo, M. R.; Thusgaard Ruhoff, V.; Chiantia, S.; Daniels, R.; Bendix, P. M. Data of hybrid vesicles fusion. *Zenodo*, 2023, DOI: 10.5281/zenodo.7577427.
(64) Rhee, J. M.; Pirity, M. K.; Lackan, C. S.; Long, J. Z.; Kondoh, G.; Takeda, J.; Hadjantonakis, A.-K. In vivo imaging and differential localization of lipid-modified GFP-variant fusions in embryonic stem cells and mice. *genesis* **2006**, *44* (4), 202−218.

https://doi.org/10.1021/acs.nanolett.3c00371
Nano Lett. 2023, 23, 3377−3384

Thermoplasmonic vesicle fusion reveals membrane phase segregation of influenza spike proteins

Guillermo Moreno-Pescador[1 *] ✉, Mohammad Reza Arastoo[1 *], Victoria Thusgaard Ruhoff[1], Salvatore Chiantia[2], Robert Daniels[3], and Poul Martin Bendix[1] ✉

[1]Niels Bohr Institute, University of Copenhagen, Blegdamsvej 17, 2100 København Ø, Denmark

[2]University of Potsdam, Institute of Biochemistry and Biology, Karl-Liebknecht-Str. 24-25, 14476 Potsdam, Germany

[3]Division of Viral Products, Center for Biologics Evaluation and Research, Food and Drug Administration, Silver Spring, Maryland, USA

[*]These authors contributed equally.

Supplementary Information

Materials and Methods

Cell Culture. Human Embryonic Kidney Cells (HEK293T) were cultured in Dulbecco's Modified Eagle Medium (DMEM, Gibco, cat. no. 11995065) supplemented with 10% fetal bovine serum (FBS, Gibco, cat. no. 11550356) and 100 U/mL penicillin and 100 mg/mL streptomycin (Gibco, cat. no. 15140122). Cells were grown at 37 °C in 5% CO_2 in a humidified incubator.

Cell Transfection. 3×10^5 HEK293T cells were seeded on a 35mm glass bottom dish (MatTek, cat. no. P35G-1.5-14-C) coated with 0.01% poly-L-lysine (Sigma-Aldrich, cat. no. P8920) and grown for 24 h. Then, cells were transiently transfected with the plasmid of interest using Lipofectamine™ LTX Reagent (Invitrogen, cat. no. 15338030) according to the manufacturer's protocol with minor optimization to improve expression yield. Briefly, 1.5 μg plasmid was diluted in 75 μL Opti-MEM (Gibco, cat. no. 31985070), added by 3 μL PLUS Reagent (Invitrogen, cat. no. 15338030) and incubated at room temperature for 5 minutes. In a separate Eppendorf tube, 3 μL Lipofectamine LTX Reagent was added to 75 μL Opti-MEM

and incubated for 5 minutes, after which the content of the tubes was mixed together and incubated at room temperature for 30 minutes. The culture medium was replaced by Opti-MEM and the prepared plasmid mix added to it. After 4 h of incubation at 37 °C, the culture medium was changed to DMEM supplemented with FBS and PenStrep.

Giant Plasma Membrane Vesicle (GPMV) Preparation. GPMVs were obtained according to (1). In brief, transfected cells were grown for 24 h and then washed with PBS (Gibco, cat. no. 10010023) and GPMV buffer (10 mM HEPES, 150 mM NaCl, 2 mM CaCl2, pH7.4) in succession. The vesiculation process was triggered by adding to the cells 1 mL GPMV buffer to which N-Ethylmaleimide (NEM, Sigma-Aldrich, cat. no. E3876) was added to the final concentration of 2 mM. After 2 h of incubation at 37 °C, GPMVs were ready for the experiment.

To avoid any changes to the plasma membrane proteins, GPMVs were derived from cells using N-Ethylmaleimide (NEM) rather than the reducing agent dithiothreitol (DTT); the latter is known to cut thioester-bound fatty acids and therefore, affect the raft-targeting feature of the associated protein. An alternative approach not used here is to produce plasma membrane spheres (PMS) by osmotic swelling of cells (2). Although this approach avoids the use of chemicals, it can be hard to detach the PMS from the donor cell and the resulting buffer conditions will be quite non-physiological due to the low osmolarity of the external solution.

Giant Unilamellar Vesicle (GUV) Preparation. GUVs were made according to the PVA gel-assisted hydration method (3) using a mixture of DOPC (1,2-dioleoyl-sn-glycero-3-phosphocholine, Avanti Polar Lipids, cat. no. 850375), Brain SM (Avanti Polar Lipids, cat. no. 860062) and Cholesterol (Avanti Polar Lipids, cat. no. 700000) dissolved in chloroform with a molar ratio of 2:2:1 (Supplementary Table S1). Furthermore, the lipids were mixed with the L_d marker 18:1 Liss Rhod PE (1,2-dioleoyl-sn-glycero-3-phosphoethanolamine-N-lissamine rhodamine B sulfonyl, Avanti Polar Lipids, cat. no. 810150) at 0.1 mol.%. Briefly, 90 μL of PVA gel 5% (Sigma-Aldrich, cat. no. 363065) was spread on a clean glass slide and dried at 50 °C for 50 minutes. After that, 30 μL of the lipid mix was spread on the dried PVA film and left under vacuum for 2 h. The GUVs were then grown by the addition of a growing buffer (70 mM NaCl, 80 mM sucrose, 25 mM Tris) to the prepared lipid coat and incubation at 55 °C for 1 h. Finally, the GUVs were harvested and kept at 4 °C prior to the fusion experiment.

For the GUV-GPMV fusion experiments, 0.2 mol.% of DSPE-PEG(2000) Biotin (1,2-distearoyl-sn-glycero-3-phosphoethanolamine-N-[biotinyl(polyethylene glycol)-2000], Avanti Polar Lipids, cat. no. 880129) were also added to the lipid mix. Moreover, streptavidin-coated gold nanoshells (AuNSs, nanoComposix, cat. no. GSIR150) were diluted in a so

called observation buffer (70mM NaCl, 55mM Glucose and 50mM Tris) with a ratio of approximately 1:20 (i.e. 12 μL AuNSs in 240 μL observation buffer) and briefly sonicated. Then, the same volume of this AuNS-containing buffer (i.e. 250 μL) was mixed with the prepared GUVs (i.e. 250 μL). Finally, 150 μL of this mix was added to the GPMV-producing cells just before the fusion experiment. The latter was carried out at room temperature which varied, according to the season, between 20°C - 25°C.

Optical Tweezers and Fusion. A Leica SP5 confocal microscope implemented with an optical trap based on a 1064 nm laser (Spectra Physics J201-BL-106C)) was used for confocal visualization and optical trapping (4). A Leica PL APO 63X water immersion objective with NA = 1.2 was used for sample visualization and focusing the trapping laser beam. The GFP tag and Rhodamine in the sample were excited with 488 nm and 594 nm laser lines, respectively, and their emitted intensities were collected in the spectral range of 493-553 nm and 598-700 nm. The trapping laser operated with the output power of 45 mW corresponding to an intensity of 3×10^{10} W m^{-2} in the sample and irradiation of Streptavidin-coated 150 nm AuNSs (nanoComposix, cat. no. GSIR150) in the interface of a GUV-GPMV triggers the fusion event. Also, to spot the AuNSs a 476 nm argon laser line was used and the reflected intensity was captured in the spectral range of 476-488 nm.

Design and Preparation of Plasmids. Plasmids encoding for full length hemagglutinin (HA-FL) and its transmembrane domains (HA-TMD) were engineered. Plasmid design and preparation was described in (5). $pCAG : GPI - GFP$ was a gift from Anna-Katerina Hadjantonakis (Addgene plasmid #32601, http://n2t.net/addgene:32601., $RRID : Addgene_{32601}$)

Data analysis. Image processing was all carried out in Fiji (6, 7), using macro language commands for unwrapping the vesicle signals and extracting the fluorescence intensities along the membrane. For each image of a fused vesicle, we selected manually the contours of the membrane in Fiji. After that, the macro program would unwrap flat the selected area (with a selectable width, normally in between 5-10 pixels). In the next step, the membrane signal was selected by thresholding the intensity values and the background was subsequently removed by multiplying the masked membrane signal by the original image. In the final step, the whole membrane signal was averaged by a moving window average in the x direction of 3 pixels. Afterwards the intensity of each vertical pixel column was averaged and plotted as plotted in Figure 3E and Figure S6B. The whole macro image workflow can be found in the following Github repository https://github.com/GMorenoPescador/vesicle unwrapper.

Vesicle size and time scale of mixing. To preserve the presence of membrane phases in the GUVs, we found it important to select GUVs which were at least 1.5 X larger than the GPMVs. As shown in Supplementary Figure S2A, the phases could

be lost when the GUV/GPMV size ratio approached unity, which is likely due to a large compositional change of the GUV following fusion to an equally sized GPMV. Also, we note that for our main constructs the few incidences where phases were lost do not show a clear correlation with the type of construct which was expressed in the cells (see Supplementary Figure S2B for the HA, NA or the NA-42 variant) nor the phase into which the GPMV was fused (Supplementary Figure S2C). The time scale of protein partitioning was measured to be on the order of tens of seconds (Supplementary Figure S3A). However, the time scale for protein partitioning slightly increased if fusion took place in the L_o phase of a large GUV (Supplementary Figure S3B) which increased the diffusion distance for the proteins. Neuraminidase mobility in GPMVs has been measured to be on the order of $\sim 1\mu\mathrm{m}^2/\mathrm{s}$ (5) which agrees well with the observed time scales for complete protein partitioning.

Supplementary References

1. Erdinc Sezgin, Hermann Josef Kaiser, Tobias Baumgart, Petra Schwille, Kai Simons, and Ilya Levental. Elucidating membrane structure and protein behavior using giant plasma membrane vesicles. *Nature Protocols*, 7(6):1042–1051, jun 2012. ISSN 17542189. doi: 10.1038/nprot.2012.059.
2. D. Lingwood, J. Ries, P. Schwille, and K. Simons. Plasma membranes are poised for activation of raft phase coalescence at physiological temperature. *PNAS*, 105(29):10005–10010, 2008. doi: 10.1073/pnas.0804374105.
3. Andreas Weinberger, Feng Ching Tsai, Gijsje H. Koenderink, Thais F. Schmidt, Rosângela Itri, Wolfgang Meier, Tatiana Schmatko, André Schröder, and Carlos Marques. Gel-assisted formation of giant unilamellar vesicles. *Biophysical Journal*, 105(1):154–164, 2013. ISSN 00063495. doi: 10.1016/j.bpj.2013.05.024.
4. Andrew C. Richardson, Nader Reihani, and Lene B. Oddershede. Combining confocal microscopy with precise force-scope optical tweezers. *SPIE Proceedings, Optical Trapping and Optical Micromanipulation*, 6326(632628), 2006. doi: 10.1117/12.680347.
5. Guillermo Moreno-Pescador, Christoffer D. Florentsen, Henrik Stbye, Stine L. Snder, Theresa L. Boye, Emilie L. Veje, Alexander K. Sonne, Szabolcs Semsey, Jesper Nylandsted, Robert Daniels, and Poul Martin Bendix. Curvature- and Phase-Induced Protein Sorting Quantified in Transfected Cell-Derived Giant Vesicles. *ACS Nano*, 13(6):6689–6701, 2019. ISSN 1936086X. doi: 10.1021/acsnano.9b01052.
6. Johannes Schindelin, Ignacio Arganda-Carreras, Erwin Frise, Verena Kaynig, Mark Longair, Tobias Pietzsch, Stephan Preibisch, Curtis Rueden, Stephan Saalfeld, Benjamin Schmid, Jean-Yves Tinevez, Daniel James White, Volker Hartenstein, Kevin Eliceiri, Pavel Tomancak, and Albert Cardona. Fiji: an open-source platform for biological-image analysis. *Nature Publishing Group*, 9(7):676 – 682, 07 2012. doi: 10.1038/nmeth.2019.
7. Curtis T Rueden, Johannes Schindelin, Mark C Hiner, Barry E DeZonia, Alison E Walter, Ellen T Arena, and Kevin W Eliceiri. ImageJ2: ImageJ for the next generation of scientific image data. *BMC bioinformatics*, 18(1):529 – 26, 11 2017. doi: 10.1186/s12859-017-1934-z.

Supplementary Figures

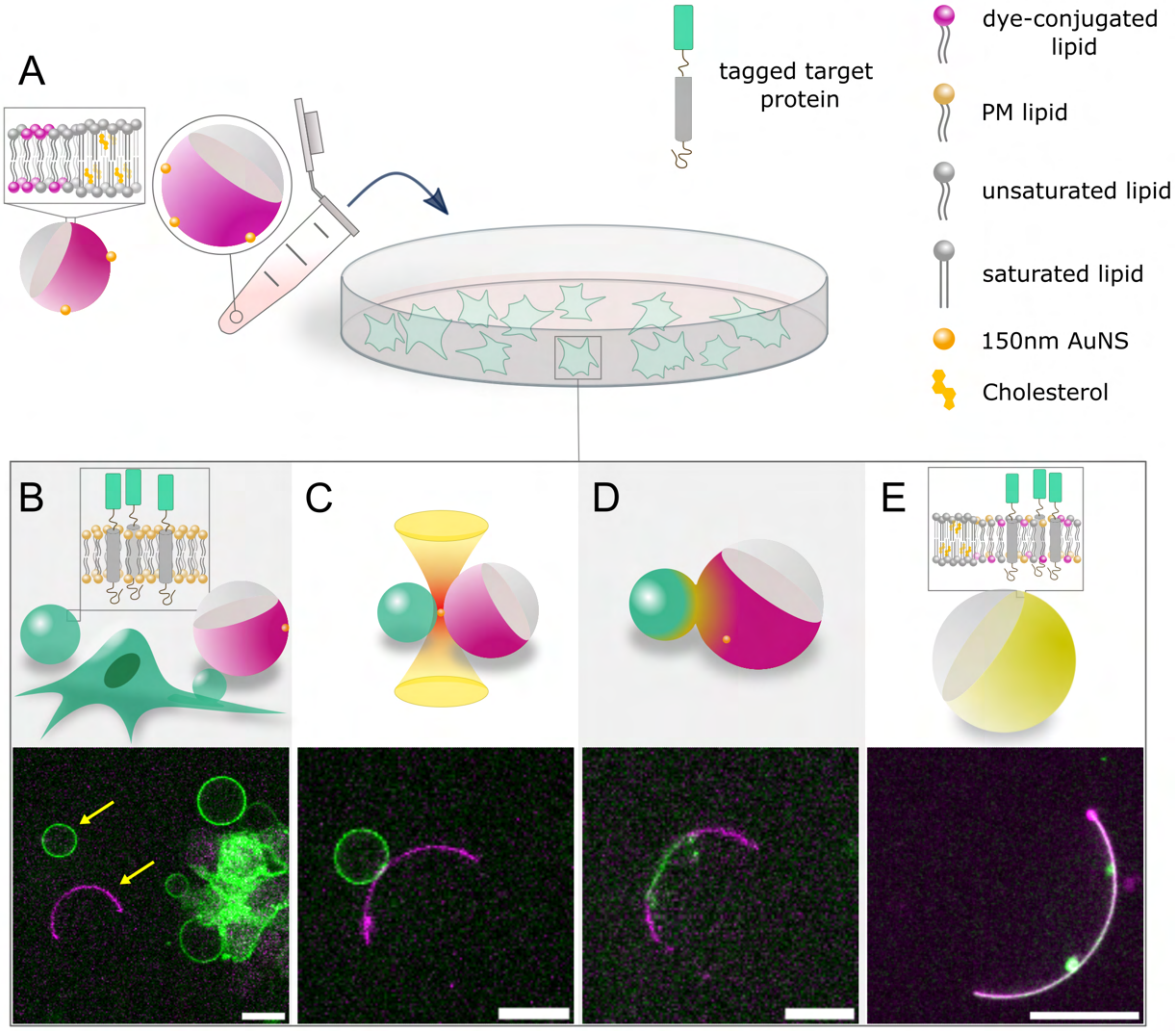

Fig. S1. Systematic delivery of membrane associated proteins into phase-separated GUVs. A. HEK293T cells are transfected to express the protein of interest that itself is a chimeric fluorescent protein, here GFP-tagged Hemagglutinin Transmembrane Domain (GFP-HA-TMD). The cells were subsequently treated with a vesiculating agent which causes cells to exclude part of their plasma membranes as GPMVs that accommodate the expressed protein on their membranes. Phase-separated GUVs are also added to the culture dish. **B.** As a result, the culture dish gets populated with GPMVs and GUVs with varying sizes that enables target selection from a pool of vesicles. A GPMV is then grabbed by the optical trap and brought into close contact with a GUV (yellow arrows). **C.** Irradiating the interface of the GPMV-GUV pair with the NIR laser pulls GUV-bound gold nanoshells into the laser focus where they produce highly localized heat. **D.** The produced heat melts the apposing membranes and fusion happens. **E.** The resultant hybrid vesicle inherits its lipid composition from the GUV-GPMV and retains its phase separation. In this way, the protein of interest has been transferred from the cell plasma membrane to the model membrane where it redistributes in its preferred phase - that is the disordered phase in this example. Insets in A, B and E show the membrane composition of each vesicle. The images in B-E are the same as in Fig. 1; the image in E has been rotated to match its phases to the depiction above. Scale bars are 15 µm.

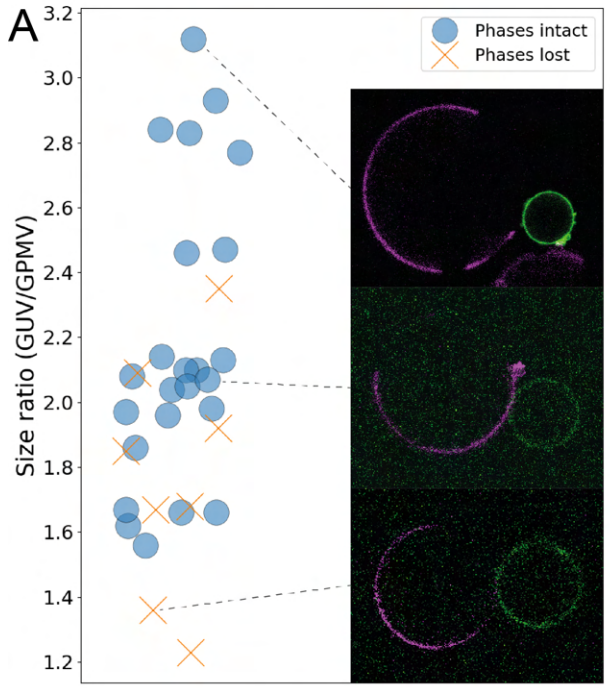

B

Protein	Phases intact post fusion?	GPMV fused to: Ld phase	Lo phase	Phase int.	Size ratio GUV/GPMV
HA	✗	✗	✗	✓	1.2
HA	✗	✗	✗	✓	1.9
HA	✗	✗	✓	✗	1.3
HA	✗	✗	✓	✗	2.1
HA	✓	✗	✓	✗	1.6
HA	✓	✗	✓	✗	2.0
HA	✓	✓	✗	✗	2.1
HA	✓	✗	✗	✓	1.6
HA	✓	✗	✓	✗	2.1
HA	✓	✗	✗	✓	2.0
HA	✓	✓	✗	✗	2.0
HA	✓	✓	✗	✗	2.8
HA	✓	✗	✗	✓	1.7
HA	✓	✗	✗	✓	2.1
HA	✓	✗	✗	✓	1.9
NA	✗	✓	✗	✗	1.7
NA	✗	✗	✓	✗	1.9
NA	✗	✓	✗	✗	2.3
NA	✓	✓	✗	✗	2.1
NA	✓	✓	✗	✗	1.7
NA	✓	✓	✗	✗	2.0
NA	✓	✗	✗	✓	2.8
NA42	✗	✓	✗	✗	1.7
NA42	✓	✗	✗	✓	1.7
NA42	✓	✗	✗	✓	2.1
NA42	✓	✓	✗	✗	2.5
NA42	✓	✓	✗	✗	2.0
NA42	✓	✓	✗	✗	2.1
NA42	✓	✓	✗	✗	2.9
NA42	✓	✗	✓	✗	3.1
NA42	✓	✗	✗	✓	2.9
NA42	✓	✓	✗	✗	2.5

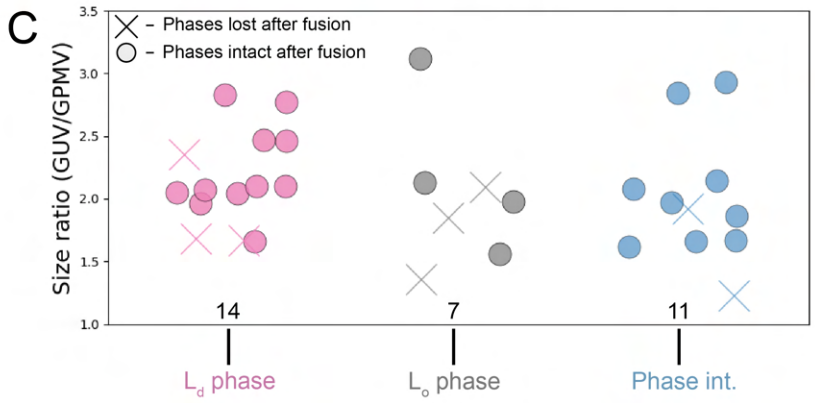

Fig. S2. Quantification of GUV:GPMV size ratio and site of fusion for fusions conducted with protein constructs HA-FL, NA-FL and NA-42. A. Random scatter of the size ratio ($\frac{GUV}{GPMV}$) of 32 attempted vesicle fusions resulting in intact phase separation (blue circle) and lost phase separation (orange cross). Inserts of 2 successful and one failed fusion are shown for visualization. Data indicates that a large size ratio is optimal, however this might result in the loss of protein signal upon diffusion into a large phase. To minimize bleaching, vesicles are imaged during the fusion process at low laser power, resulting in the variety of background noise seen in the inserts. Depending on individual GUV composition phase loss can happen at various size ratios, yet, as expected, is most common at lower ratios. Data shown represent fusion experiments where a pre-fusion video was recorded. Ratios were estimated from an average of 3 independent measurements of vesicle diameter using Fiji line analysis tools. **B.** Table listing size ratio and site of fusion for representative data (where pre-fusion video was available) for protein constructs HA-FL (HA), NA-FL (NA) and NA-42. **C.** Size ratios for fusions initiated at the L_d phase (pink), L_o phase (grey) and the phase intersection (blue) respectively. Fusions are represented at both phases and intersection for a similar range of size ratios, and indicate no immediate effect on the phase integrity post fusion.

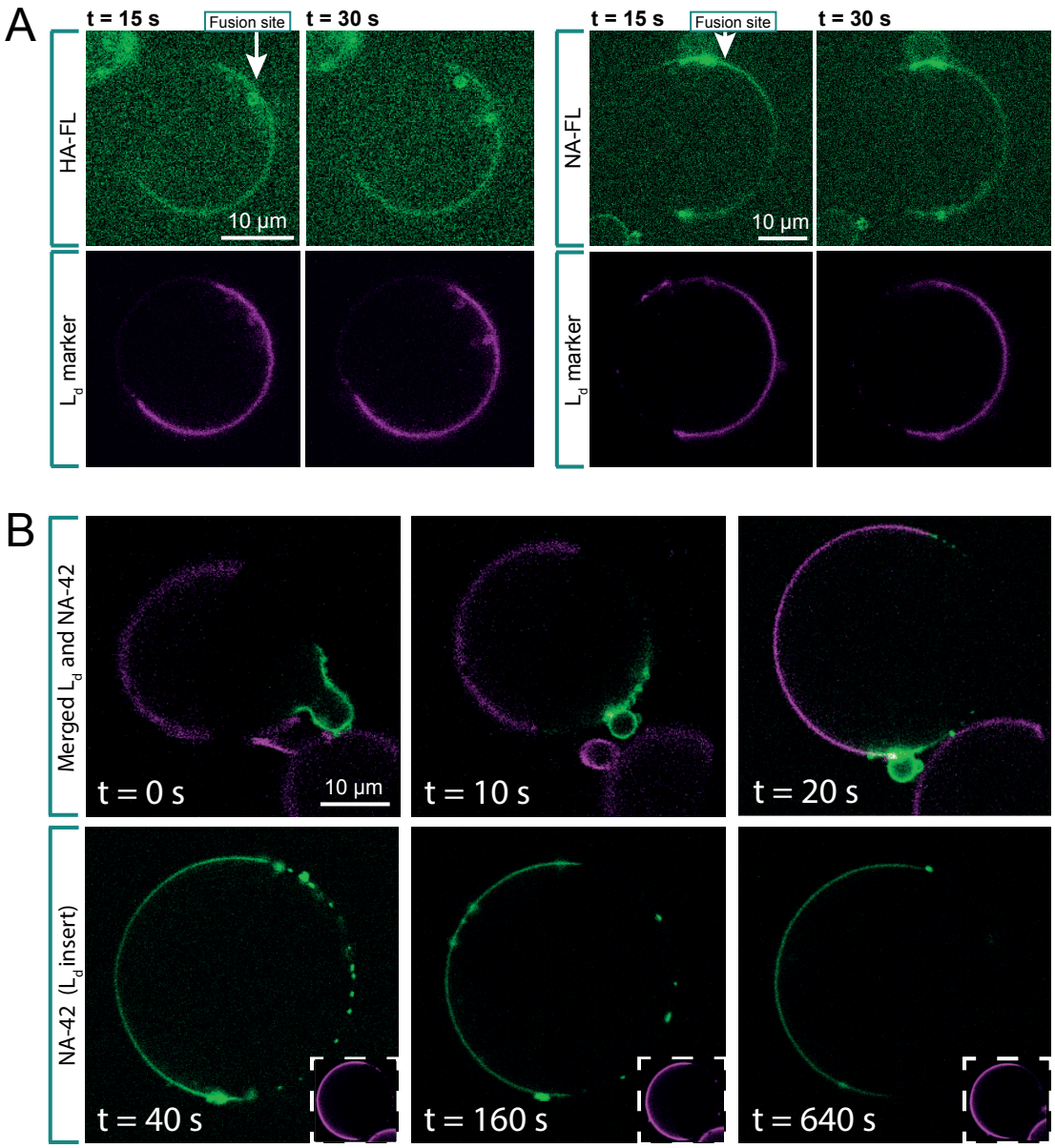

Fig. S3. Time scale of equilibrated protein diffusion into L$_d$ phase. A. Fusions into the L$_d$ phase results in equilibrium after 15 seconds. Images at t = 15 and t = 30 show complete diffusion of tagged proteins (green) into L$_d$ phase (magenta) for HA-FL (left) and NA-FL (right). **B.** An example of a fusion event where the diffusion of the proteins from the L$_o$ phase, where the fusion happened, to the L$_d$ phase had a duration of 160s. Channels are merged (top panel) and then separated (bottom panel) for clarity on the protein distribution. This time series represents the slowest observed diffusion of the 4 GPMVs fused into the L$_o$ phase, as the others were observed to equilibrate within a minute.

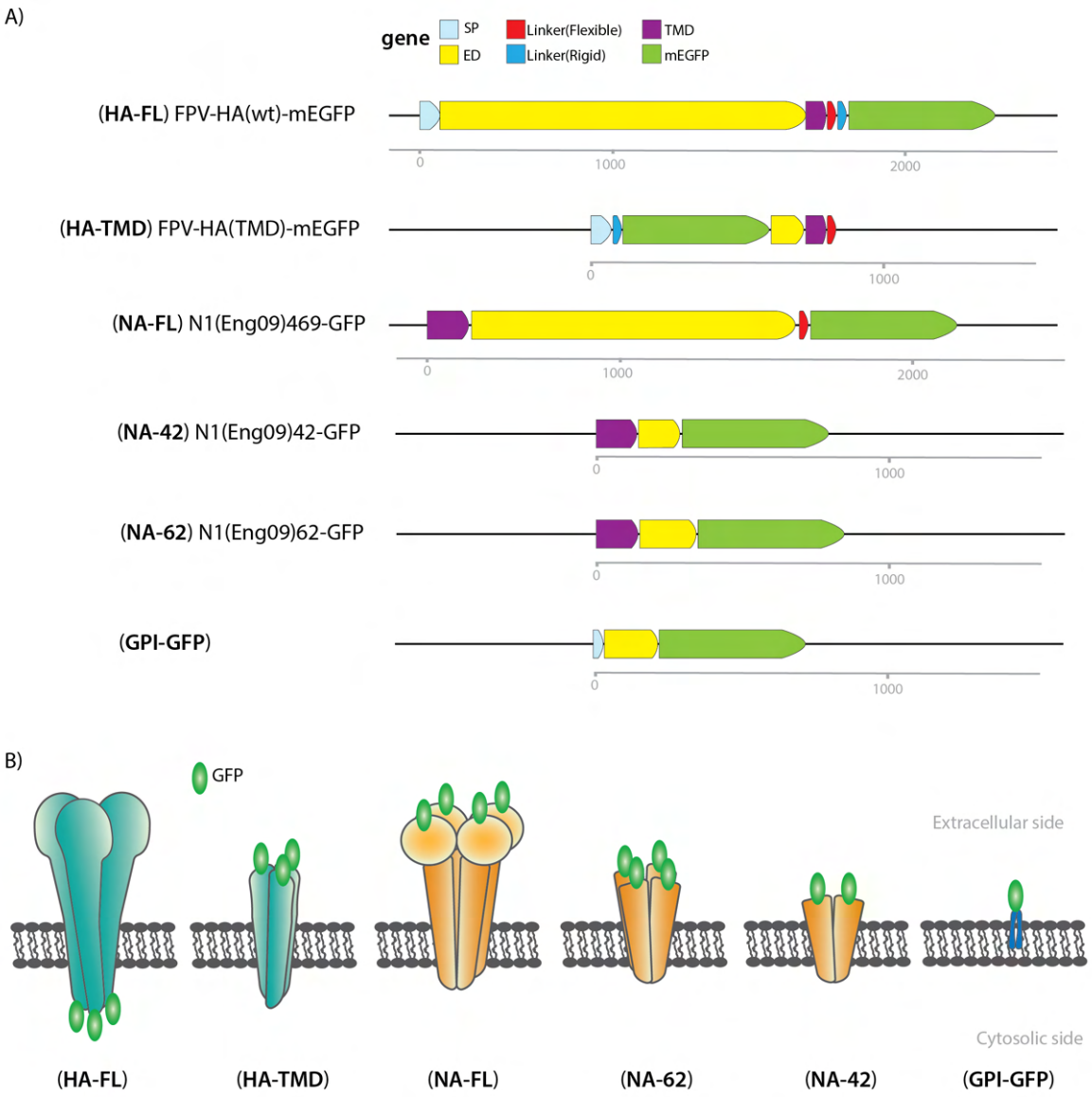

Fig. S4. HA and NA and GPI constructs. A. Schematic representation of the HA and NA and GPI constructs used in this study. **B.** Schematic version of how the protein would assemble into the membrane indicated where the GFP fluorophore sits.

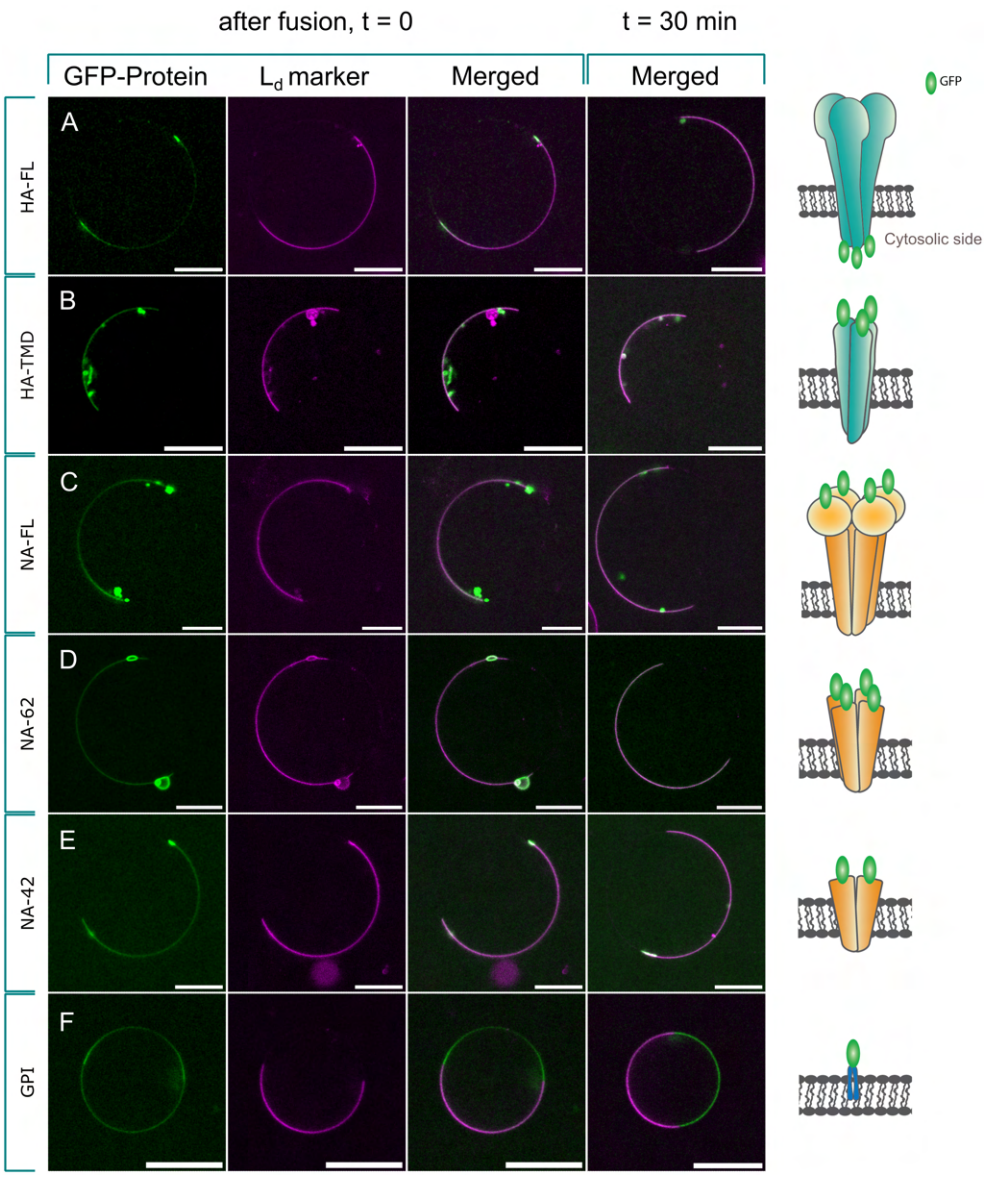

Fig. S5. Phase partitioning of influenza A virus transmembrane proteins. When the protein of interest is delivered into the phase-separated GUV, mixing is initiated. After 30 minutes from the fusion event, the hybrid vesicle is still phase separated and the protein is found in its preferred phase. The disordered phase is labeled with 18:1 liss. rhodamine PE lipid that exclusively partitions into the liquid-disordered region (colored in magenta). **A.** Full-length Hemagglutinin (HA-FL). **B.** Transmembrane domain of Hemagglutinin (HA-TMD). **C.** Full-length Neuraminidase (NA-FL). **D.** Truncated Neuraminidase that lacks the bulky head domain (NA-62). **E.** Another truncated Neuraminidase that lacks the bulky head domain and also has a shorter stem region (NA-42). NA-42 forms dimers instead of tetramers on the membrane. **F.** GPI anchored GFP as the positive control of true partitioning. The images have been adjusted in brightness and contrast for better visualization. Scale bars are 15 µm.

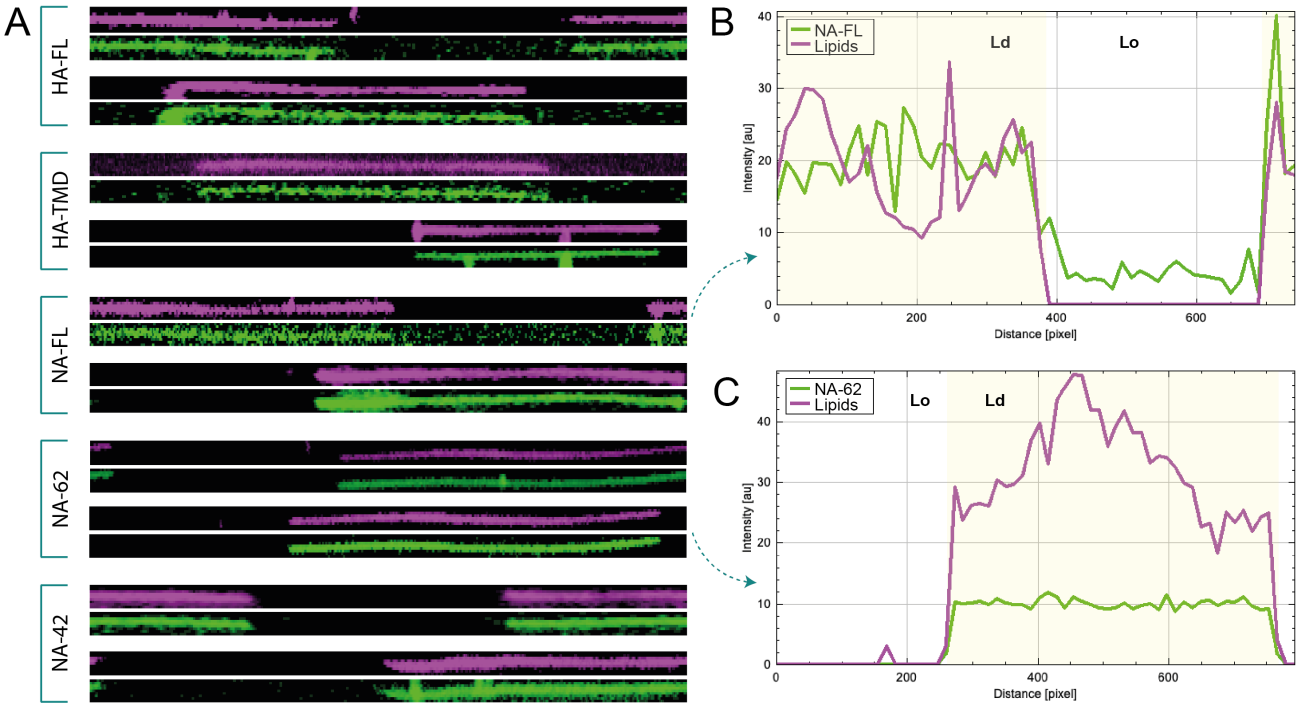

Fig. S6. Data excerpt of unwrapped vesicles for all protein constructs. A. Unwrapped phase-separated vesicle data examples for all constructs tested. Contrast and brightness have been enhanced in the images for visualization purposes. **B and C** Plot of the intensity across the two arrow-marked unwrapped vesicles. For data with high protein expression, intensity is zero outside L_o phase (C). For low protein expression, background noise is visible in the the L_o domain, but does not represent protein diffusion in this domain, as the signal is consistent with the background level (B).

Name	Volume (ml)	Solvent (ml)	Mass (mg)	Mol (µmol)	Concentration (µmol/ml)		
SM-PC-Chol.	1.00	0.854	1.00	1.427	1.427		
Lipids			**Stock**		**Mix**		
ID-L	**Name**	**MW (g/mol)**	**g/L**	**mmol/L**	**Molar ratio**	**µmol**	**µL of stock**
AVANTI, 860062	Brain SM	760.2	10.00	13.15	40.00	0.569	43.5
AVANTI, 850375	18:1 (Δ9-Cis) PC	785.6	10.00	12.73	40.00	0.569	45
AVANTI, 700000	Cholesterol	386.4	5.00	12.94	20.00	0.284	22
AVANTI, 810150	18:1 Liss Rhod PE	1301	0.100	0.077	0.100	0.0014	18.5
AVANTI, 880129	DSPE-PEG (2000) biotin	3015	0.500	0.165	0.200	0.0028	17

Table S1. Lipid specification and composition used to grow phase-separated GUVs. The ternary lipid mixture i.e. Brain SM, DOPC and Cholesterol specified here results in phase-separated GUVs. Rhodamine conjugated lipids are added to the mixture as an exclusive L_d marker. The biotin conjugated lipids are used to facilitate binding to streptavidin coated gold nanoshells used as a mediator of the membrane-fusion event. The specified values have been calculated by the LIPID MIXATOR at https://nicokiaru.github.io/LipidMixator/LipidMixator.html.

B.2 Strength in numbers: effect of protein crowding on the shape of cell membranes

Authors:
Victoria Thusgaard Ruhoff, Guillermo Moreno-Pescador, Weria Pezeshkian, and Poul Martin Bendix.
Status: Published

BIOCHEMICAL SOCIETY

PORTLAND PRESS

BIOCHEMICAL SOCIETY TRANSACTIONS

THE REVIEWS JOURNAL OF THE BIOCHEMICAL SOCIETY

VOLUME 50 ● ISSUE 5 ● OCTOBER 2022 portlandpress.com/biochemsoctrans

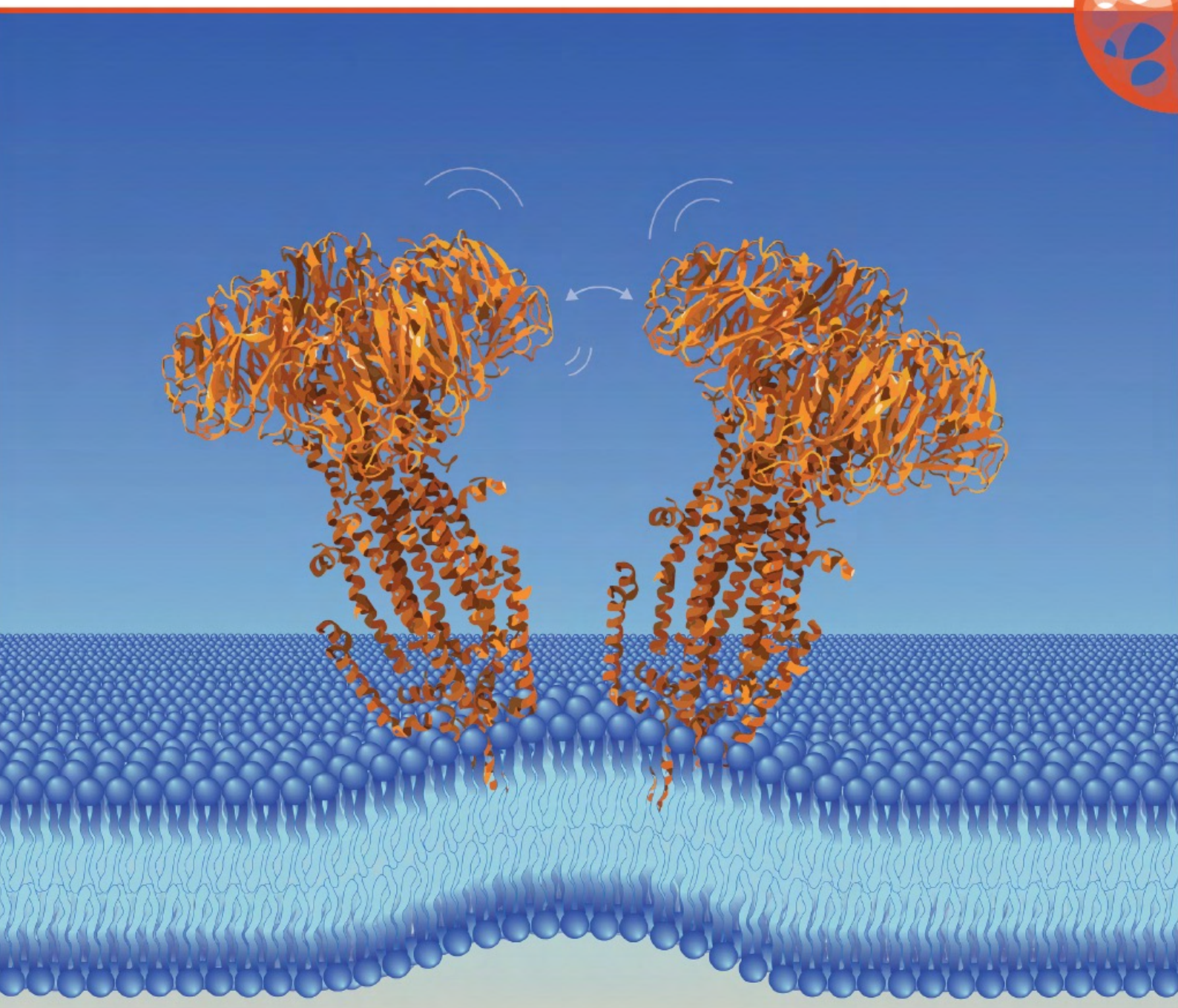

Cover art by Victoria Thusgaard Ruhoff

Biochemical Society Transactions (2022) **50** 1257–1267
https://doi.org/10.1042/BST20210883

PORTLAND PRESS

Review Article

Strength in numbers: effect of protein crowding on the shape of cell membranes

Victoria Thusgaard Ruhoff[1], Guillermo Moreno-Pescador[1], Weria Pezeshkian[2] and Poul Martin Bendix[1]

[1]Niels Bohr Institute, University of Copenhagen, Blegdamsvej 17, 2100 Copenhagen, Denmark; [2]Niels Bohr International Academy, Niels Bohr Institute, University of Copenhagen, Blegdamsvej 17, 2100 Copenhagen, Denmark

Correspondence: Poul Martin Bendix (bendix@nbi.ku.dk)

Continuous reshaping of the plasma membrane into pleomorphic shapes is critical for a plethora of cellular functions. How the cell carries out this enigmatic control of membrane remodeling has remained an active research field for decades and several molecular and biophysical mechanisms have shown to be involved in overcoming the energy barrier associated with membrane bending. The reported mechanisms behind membrane bending have been largely concerned with structural protein features, however, in the last decade, reports on the ability of densely packed proteins to bend membranes by protein–protein crowding, have challenged prevailing mechanistic views. Crowding has now been shown to generate spontaneous vesicle formation and tubular morphologies on cell- and model membranes, demonstrating crowding as a relevant player involved in the bending of membranes. Still, current research is largely based on unnatural overexpression of proteins in non-native domains, and together with efforts in modeling, this has led to questioning the *in vivo* impact of crowding. In this review, we examine this previously overlooked mechanism by summarizing recent advances in the understanding of protein–protein crowding and its prevalence in cellular membrane-shaping processes.

Introduction

The conventional textbook presentation of a plasma membrane, containing individual proteins floating in a lipid bilayer, does not provide a realistic picture of the membrane system: a heterogeneous and dynamic environment comprising domains, protein clusters and a high degree of protein coverage. Historically, the plasma membrane was viewed as a fluid-mosaic bilayer with few proteins in a vast sea of lipids [1]. This simplified view has since been replaced by an elaborate model more firmly representing the proteins heterogeneously distributed in a lipid raft-containing bilayer, influenced by dynamic interactions with cellular components like the cytoskeleton [2–6]. With this appreciation of the complexity of the membrane in place, it is not surprising that investigating and determining the role of the plasma membrane in cellular processes is a challenging task, yet necessary for our continued understanding of how the plasma membrane controls some of the most essential activities of life.

The plasma membrane is the site of action for an abundance of cellular processes, many of which require membrane shape remodeling. Membrane bending is what allows for the uptake of nutrients, waste disposal, cell migration and much intra- and extracellular communication [7–10]. Central to membrane reshaping is efficient membrane bending facilitated by proteins. The plasma membrane naturally resists bending, due to the hydrophobic and hydrophilic forces governing its structure, as well as its inherent interactions with the cell cytoskeleton [11]. Spontaneous curvature of membranes can result from asymmetric distribution of lipids within the two leaflets [12, 13]. However, the distribution of the lipids that make up the plasma membrane, cannot alone explain the large number of distinct curvature-dependent processes cells maintain. Instead, certain proteins are responsible for driving curvature, by somehow providing the energy needed to break the barrier for bending. Advanced experimental techniques including super-resolution, fluorescent microscopy techniques and

Received: 5 July 2022
Revised: 16 September 2022
Accepted: 20 September 2022

Version of Record published:
10 October 2022

PORTLAND PRESS

Biochemical Society Transactions (2022) **50** 1257–1267
https://doi.org/10.1042/BST20210883

gene editing has allowed researchers to investigate the interrelations between protein structures and the mechanics of these membrane-shaping proteins at high resolution [14–16]. These investigations have shown that a variety of proteins have the ability to bend membranes via different mechanisms [17, 18]. In cells no single protein is orchestrating curvature alone, however, shared structural protein features have long been accepted as responsible drivers of membrane reshaping. These include the insertion of wedges into the bilayer in the form of amphipathic helices [19, 20], extracellular lectins through binding to glycolipids [21] or intrinsic curvature of membrane binding domains and protein scaffolding [22, 23].

Despite a large body of research highlighting conserved structural features as the driver for membrane bending, in the last decade an overlooked and highly disputed entropic mechanism, driving membrane bending via simple protein–protein crowding, has emerged, challenging prevailing views on how membranes adopt their shapes. Crowding drives curvature generation via lateral pressure created from stochastic collisions at one side of a membrane surface if that pressure is not counteracted on the opposing side of the membrane. This entropic mechanism is emerging as a relevant player in the dynamics of membrane-shaping machinery in cells including the generation of various cell surface morphologies, sorting of cargo in clathrin coated pits and potentially virus envelope budding (Figure 1B) [24–28].

In this review, we summarize recent literature to evaluate the impact of the crowding mechanism and its interplay with other structural mechanisms, e.g. wedge insertions and scaffolding. We comment on the biological relevance of crowding by examining the ability of the cell membrane to form crowded domains, and finally suggest directions for future quantitative experimental and modeling efforts needed to further our understanding of the role that protein–protein crowding plays in membrane remodeling.

Asymmetric protein density affects membrane shape and bending

Various membrane-bound proteins continuously diffuse within the plasma membrane in a stochastic manner with frequent lateral collisions of their hydrophilic ectodomains in a narrow region above the membrane. The volume of this narrow region is controlled by the surface curvature and hence the translational entropy of the bound proteins will increase upon membrane bending. This gain of entropy will increase as the number of bound proteins increases, eventually overcoming the elastic energy penalty associated with bending. In other words, membrane bending increases the effective distance between the protein ectodomains (Figure 2A) and consequently lowers the chemical potential of the system. As a first approximation, the effect can be viewed as the buildup of pressure within a perfect gas, which is proportional to the volume and the number of bound molecules. As the concentration increases, the size of these molecules becomes important, and the excluded volume contribution must be considered [30]. If the concentration (protein coverage) continues to increase, there will be a regime where the proteins overlap and molecular interactions become important, which can cause strong membrane bending as seen e.g. for high densities of intrinsically disordered domains anchored to a membrane via BAR domains in Noguchi et al. [31].

With the heterogeneous complexity of the plasma membrane in mind, combined with estimated protein coverage of around 30–50% on the membrane surface [32, 33], it can be expected that non-specific crowding effects by proteins could play a role in biological processes involving membrane shaping. It was recently shown with a very intuitive, simple setup, that crowding of mucin biopolymers on a cell surface induces curvature, leading cells to form various morphologies dependent on the biopolymer density [26] (Figure 1A). Yet, identifying the effect from a single curvature-inducing mechanism in the complex environment of living cells is challenging, and thus the majority of experiments have been conducted in model membrane systems like giant unilamellar lipid vesicles (GUVs) (Figure 2B), where mechanisms can be readily isolated [24, 25, 34]. However, studies performed using a single type of protein incorporated in model membranes, having simple lipid compositions and no lipid leaflet asymmetry, can suffer from limited biological relevance. Other types of more biologically relevant model systems include giant plasma membrane vesicles (GPMVs) which are membranes isolated from cells. GPMVs preserve the complexity of the plasma membrane and importantly peripheral proteins preserve their inner or outer localization while integral membrane proteins retain their orientation [35–37]. Still, cell experiments provide the optimal foundation for investigating and verifying the biological relevance of membrane-shaping mechanisms.

Accumulated experimental results over the past decade have shown various protein domains are capable of inducing bending through crowding at certain threshold concentrations. Especially, attention has been on

Biochemical Society Transactions (2022) **50** 1257–1267
https://doi.org/10.1042/BST20210883

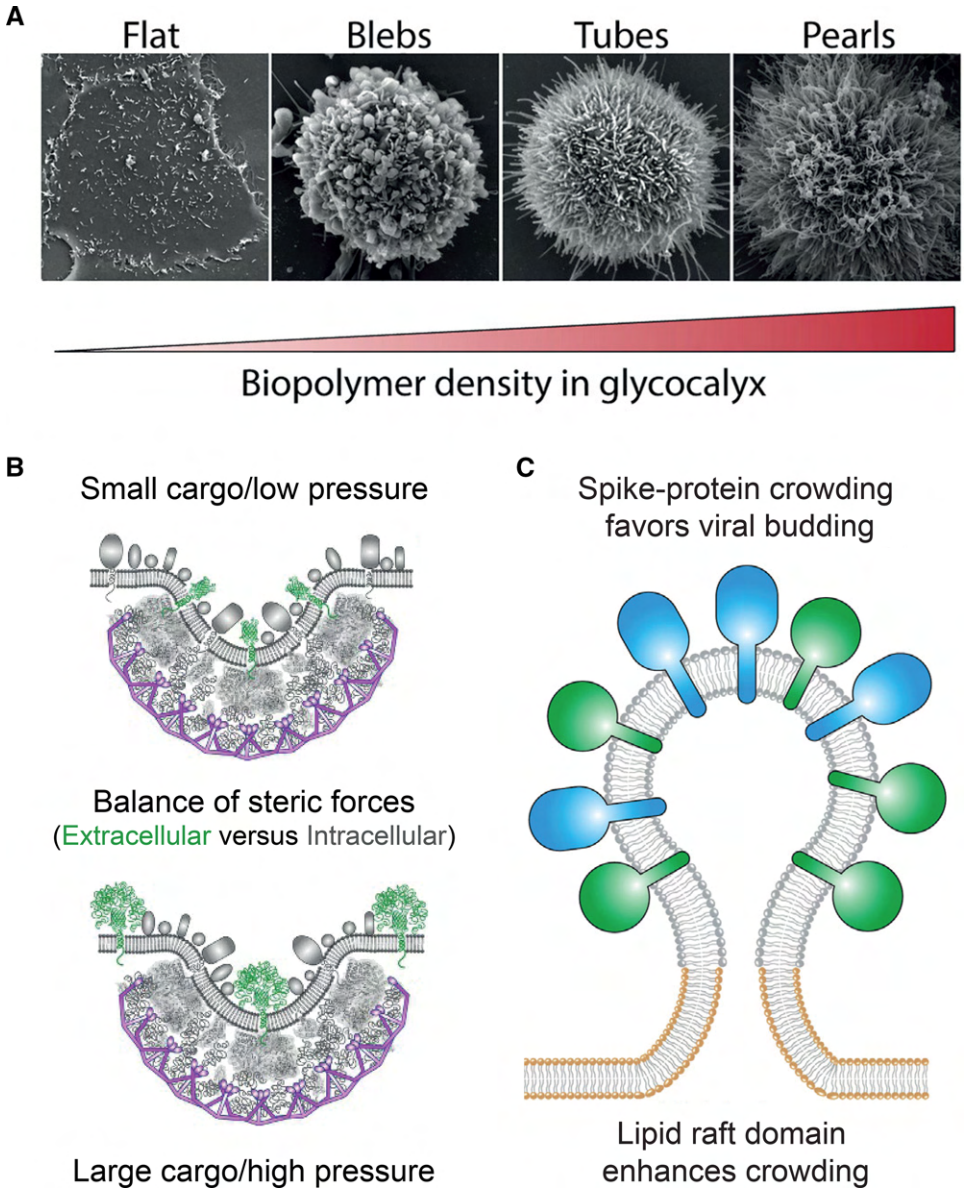

FIG. 1. Examples of crowding in biological systems.

(**A**) Crowding of mucin biopolymers on epithelial cell surfaces generate four distinct cell morphologies as a function of biopolymer denisty. From left to right the panel shows how increased crowding on the cell surface induces transitions in cell morphology from 'flat' to 'pearled'. Reprinted from [26]. (**B**) Steric pressure amongst extracellular IDP domains modulates the protein composition within the endocytotic pit. As the membrane curvature is generated on the intracellular leaflet, the resulting negative curvature on the outer side causes size dependent sorting of extracellular proteins due to steric pressure. Figure adapted from [24]. (**C**) Tentative model of viral budding from a lipid raft domain (gray) due to crowding amongst the large ectodomains of the spikeproteins (blue and green). Figure adapted from [29].

experiments concluding that proteins, generally not associated with membrane bending processes, can induce membrane curvature at high area coverage. An interesting example is GFP, a commonly used fluorescent protein, not containing any structural features associated with crowding, which has been shown to both induce spontaneous tubulation in GUVs and reduce vesicle size diameter in vesiculation experiments [14, 38]. In contrast with the notion that conserved structural features are orchestrating membrane bending, intrinsically disordered protein (IDP) domains, lacking complete 3D structure, have been identified as potential facilitators of membrane bending, via their comparably large hydrodynamic radii [24] (Figure 2C). Specifically, BAR proteins

Biochemical Society Transactions (2022) 50 1257–1267
https://doi.org/10.1042/BST20210883

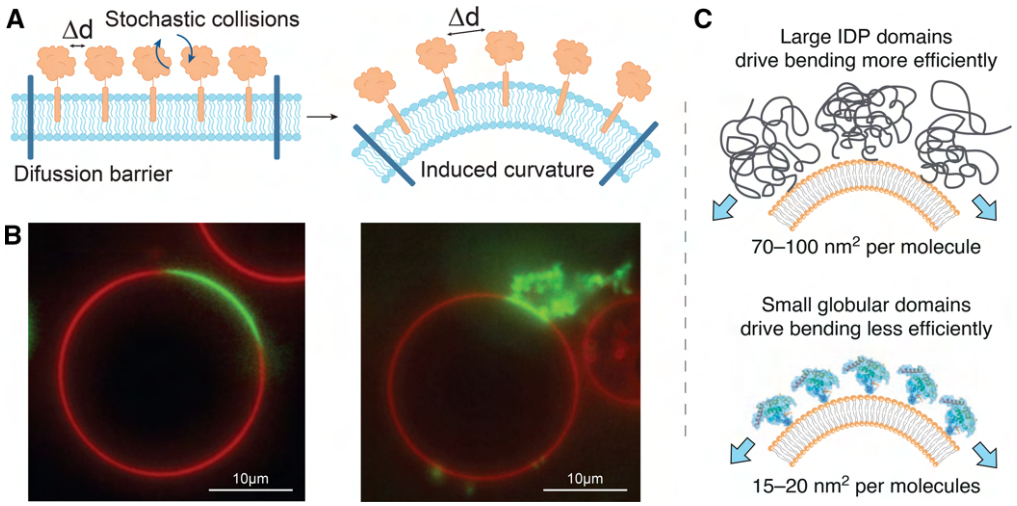

FIG. 2. Bulky ecto- and IDP domains drive tubulation in model membranes.
(**A**) Schematic illustrating how crowding between membrane-bound proteins (left panel) concentrated by a diffusion barrier can promote membrane bending, increasing Δd, to relieve the pressure (right panel). (**B**) Low (left panel) and high (right panel) density of Epsin1 ENTH domain in phase separated GUV membranes. Protein diffusion is limited by phase separation into lo (red) and ld (green) domains, resulting in spontaneous tubulation at high protein coverage in the ld domain (right panel). Reprinted from [25]. (**C**) Schematic depiction showing how IDP domains with a large hydrodynamic radius (top panel) creates membrane curvature more efficiently than smaller globular domains (lower panel). Reprinted from [24].

which have been thought to drive and stabilize membrane remodeling via a structural scaffolding mechanism, have recently been suggested by Snead et al. to be 'potent drivers of membrane fission' via crowding promoted by large IDP domains present in BAR domain containing proteins [22, 39, 40]. Recent simulations also showed that crescent-shaped BAR domains, linked to an IDP domain, induced both spherical and tubular shapes depending on the size of the IDP domain [31]. In addition, a novel method to validate the effect of crowding on membrane bending is to increase the protein volume by externally triggering unfolding of domains. Siaw et al. [41] demonstrated how steric pressure could be generated from chemically triggered protein unfolding, as proteins segregated into ordered lipid domains were shown to drive membrane deformation upon protein unfolding. Structural changes of integral proteins and membrane inserted domains are known to play a critical role in shaping membranes, but the work by Siaw et al. shows that it is relevant to account for conformational changes in the cytosolic or ectodomains when considering crowding mechanisms. This is specially important in biology as a great amount of cellular signaling pathway undergo some kind of conformational change.

The wide variety of structures and proteins associated with membranes and curvature-inducing events indicates that crowding is a mechanism with potential to influence a huge number of budding and fission processes in the cell. For example, viral budding of corona viruses or influenza viruses could partly be driven by protein crowding of various spike proteins containing large outer domains [42–44] (Figure 1C). In this context, an older theoretical study found the elastic constants of the membrane to change in the presence of anchored polymer chains on one side of the membrane. The bending rigidity of membranes was found to increase whereas the Gaussian rigidity was lowered due to the anchored polymers [45]. How this may affect budding viruses, which have saddle point curvatures before detachment from the plasma membrane, remains to be elucidated in future studies. Organelle membranes are also densely populated with proteins and exhibit highly curved regions with curvature radii that are comparable to the membrane thickness (~10 nm) [46]. Yet, such high curvatures are often generated by oligomerization of curvature-inducing proteins, which in turn undermines the crowding effect of these proteins. Therefore, despite high protein densities, crowding may not have a significant effect in the formation of these membranes.

Whether the crowding mechanism is biologically relevant, and underlying or assisting other bending mechanisms is still being debated. Especially the bending effect from helix insertion versus crowding has attracted significant attention, and although both mechanisms have been shown to induce curvature, disagreement still exists on the biological relevance and relative impact of each, since they can often be expected to

work synergistically in the same process (Figure 3). Proteins have previously been suggested to induce curvature only with a certain amphipathic helix present in the construct, as upon mutations and modification, affecting for instance the insertion depth of these helices, membrane remodeling effects were altered [15, 47]. Intriguingly, it has subsequently been demonstrated that Epsin NH_2-terminal homology (ENTH) domain, normally associated with membrane bending via wedge insertion, can actually induce spontaneous tubulation at crowding concentrations, even after deletion of its amphipathic helix [14, 25]. This observation, together with the fact that proteins have been shown to induce bending through crowding when the projected area reaches around 20% coverage, naturally suggests that crowding could provide an important contribution in facilitating membrane reshaping processes where the wedge mechanism has so far been seen as the single driver for membrane bending. For Epsin 1, the amphipathic helix is suggested to occupy at most 10% of the protein domain. Taken together with the measured size of the protein's membrane footprint, the area occupied by the helix will then be on the order of 1% for physiologically relevant densities of ENTH domain or for the larger full-length Epsin 1 protein [25]. Considering that efficient membrane bending by helix insertions requires 10–30% area coverage occupied by the helix it is, unlikely that Epsin 1 generates curvature via wedge insertion alone [25]. However, work done by Kozlov et al. [48] on ENTH found contradicting results showing that ENTH without the amphipathic wedge was not able to form highly curved membrane structures as verified by cryo-EM. These experimental results were also backed-up by modeling showing that helix insertion was more efficient than crowding in bending membranes. Comparing these two studies we wish to emphasize two major points (i) the lipid mixtures used for the experimental assays in [25] contained a small fraction of the special lipid DPhPC (1,2-diphytanoyl-sn-glycero-3-phosphocholine), which is known to lower the threshold for membrane tubulation [38]. In ref. [48], however, another Folch lipid mix was used which is derived from natural membranes. (ii) The modeling performed in [48] compared two scenarios where the helix/protein area ratio was 0.1 and 0.3, respectively. Only the latter ratio showed negligible effects of crowding whereas a ratio of 0.1 showed significant synergistic effects of crowding and helix insertion in membrane bending. In this context, the helix/protein ratio for ENTH has been reported to be 0.1 ($A_{\text{helix}}/A_{\text{ENTH}} = 1.6\ \text{nm}^2/16\ \text{nm}^2 = 0.1$) [25] and considering that the full length of the Epsin 1 protein would have an even larger projected membrane footprint, we can surmise that crowding could easily play a role for wild type Epsin's ability to bend cellular membranes. It should in this context be emphasized that both modeling and experimental assays can be designed to reveal efficient tubulation by choosing specific experimental settings, or theoretical parameters, that favor tubulation

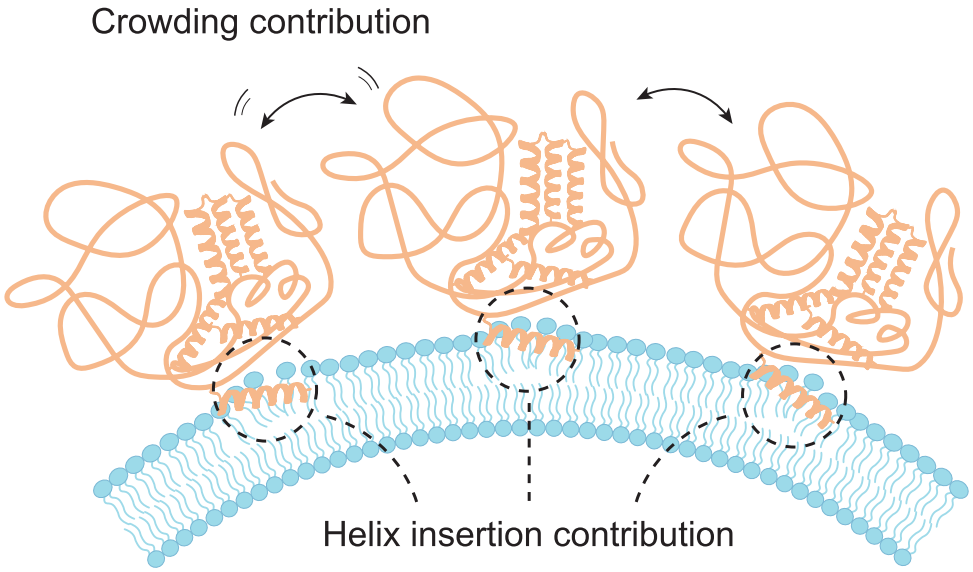

FIG. 3. Curvature generation by dual crowding and wedge mechanism.
Schematic illustration of membrane bending induced by a protein containing and IDP domain (crowding) and an amphipathic helix (wedge). Determining the driver of curvature generation *in vivo* is challenging as mechanisms such as helix insertion and crowding can work in synergy to orchestrate membrane bending.

Biochemical Society Transactions (2022) **50** 1257–1267
https://doi.org/10.1042/BST20210883

by crowding or helix insertions. To avoid biased conclusions new investigations should rather focus on identifying the conditions for which crowding does play a role in the tubulation of membranes.

Cellular processes are unlikely to employ single mechanisms for curvature generation, but rather harness multiple of these mechanisms to remodel membrane shape. Literature highlights the difficulty in separating out single mechanisms for membrane bending due to the fact that curvature-generating proteins embody a multitude of features that are associated with membrane remodeling. For example, Amphiphysin1 contains intrinsic curvature and an IDP domain, both of which are thought to effectively crowd membranes, likewise Epsin 1 could drive curvature through insertion of its amphipathic helix and via its IDP domain [49]. Certain membrane fission events have previously been reported to be dependent on a balance between two otherwise curvature-generating mechanisms, as it was promoted by amphipathic helix insertion and simultaneously restricted by BAR scaffolding [15]. Even at dilute concentrations (where steric interactions are negligible) Steinkühler et al. [50] showed that spontaneous curvature is sufficient to induce fission events in GUVs. By controlling low densities of GFP proteins bound to the membranes of cell-sized lipid vesicles, curvatures could be generated comparable to those formed by BAR domain proteins. Naturally, synergistic effects between structured and stochastic mechanisms exists [48, 49, 51] and therefore, sophisticated approaches are required to disentangle these effects and resolve the mechanisms underlying membrane curvature generation. The taxing question then becomes whether these mechanisms are actually curvature sensing or curvature inducing, and if this difference can be measured through clever experimental design.

Lateral confinement facilitates crowding

Relatively high protein coverage is needed for proteins to generate steric pressure in the 2D plane of the membrane sufficient to induce shape transitions [30]. However, local lateral confinement can assist in reaching the relevant protein densities necessary for bending a membrane [52]. In previously mentioned paper by Stachowiak et al. [25], an inhomogenous protein distribution is achieved in model membranes in the form of phase-separated GUVs containing liquid ordered (lo) and liquid disordered (ld) domains (Figure 2B). As the partitioning energy of proteins was different in different phases, each phase domain created a diffusion barrier, limiting the spread of the proteins over the entire membrane surface eventually causing enough pressure to overcome the threshold for membrane bending.

In cells, diffusion barriers consisting of membrane domains [53] or cortical actin network [54, 55], could be relevant in local and transient gathering of crowded domains needed for many small local processes such as clathrin-mediated endocytosis and viral budding. The formation of transient lipid raft domains has long been a suggested platform for the gathering of proteins, and the ability of different proteins to associate with these lipid ordered phases [56] has triggered a large interest for the biological implications of such domains. Experiments have identified some proteins to have affinity for either ordered or disordered phases in phase-separated GUV membranes [57, 58] and in isolated GPMVs [36, 59]. Although putative cell domains are most likely nanoscopic and transient, such work has served as evidence that the plasma membrane has an inherent ability to laterally organize the protein distribution in living cells. Along these lines controversial raft domains have long been thought to be the origin of processes like virus budding events [60]. Whether these domains have the ability to create sufficiently high protein–protein crowding remains unclear and has been challenged by recent work demonstrating that crowding opposes lipid phase separation [61]. This experiment, suggesting that the energetic contribution of crowding is high enough to disrupt membrane phases, highlights that lipid phase separation has obvious limitations when it comes to creating local enrichment of proteins. Yet, in [62] it was shown, in a meshless membrane model simulation, that densely anchored polymers can reduce line tension between lipid phases and thereby effectively stabilize microdomains. The effect was only verified for raft domains $\leq$100 nm. This work emphasizes the complexity of molecular interactions when considering the stability of microdomains and shows that lateral pressure from crowding and molecular effects on line tension can have opposite effects on the formation of small membrane domains.

In addition, as pointed out by Kozlov et al. [48], if upconcentration happens via protein interactive forces or oligomerization, then this inherently counteracts any crowding effect which is based on free diffusion and stochastic collisions. Therefore, the cell might need to employ more advanced machinery to crowd proteins at high surface densities. This can be achieved in many ways by the creation of diffusion barriers [6] as reviewed by Grinstein et al. [63]. Whether or not these can aid in protein crowding at the necessary concentration to break the energy barrier for bending remains to be investigated. Clustering of membrane proteins can also occur through direct and in-direct (membrane mediated) interactions, which creates a platform and seed for

growth and bending to occur as suggested to be the role of the oligomerizing Matrix protein 1 involved in influenza virus budding [64, 65]. In general for proteins to generate membrane curvature via different mechanisms, clustering is essential and we refer to Johannes et al. [66] for further reading on this subject.

Quantitative assessment of the crowding effect on membrane shape

Despite the evidence that crowding can act as a driver for membrane bending, both in cells and model membranes, the effect of crowding, and in which biological processes it plays a part, is still far from being fully elucidated. In the field, the focus has been on demonstrating crowding as a general mechanism, characterized by the spontaneous generation of membrane tubes, vesicles, pearls and similar structures [14, 24, 26]. Although the visual effect of crowding, on either a cell surface or a membrane system (GUV) can be clearly demonstrated, and relays a lot of useful information, new methods are needed which allow visualization of the bending process as it develops. This would in many cases require high resolution fluorescence imaging due to the high curvatures displayed by the biological processes relevant to crowding. Imaging the evolution of the shape changes is important to achieve a full mechanistic understanding of the crowding effect and in this context we note that methods used for characterizing the bending of membranes through percent of vesicles showing spontaneous tubulation, have been called into question by Sapp et al. [67] as they can be influenced by e.g. lipid heterogeneity effects.

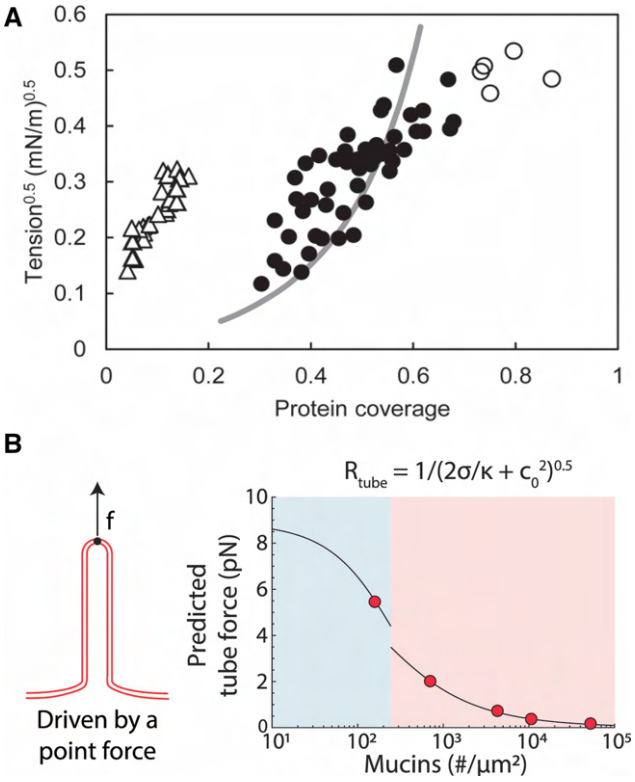

FIG. 4. Quantitative assessment of curvature-generating mechanisms using micropipette aspiration.
(**A**) Critical tension for which proteins induce shape instability in aspirated GUVs as a function of protein coverage. Endophilin BAR domains bind to the membrane via scaffolding and helix insertion (white triangles) whereas hisEGFP proteins bind to Ni-NTA lipids in the GUV and induce crowding with no helix insertion (black circles). The shaded line represents an instability theory based on repelling hard disks and empty circles represent high-density data for which the model breaks down. Using critical tension as a probe for membrane shape instability provides quantitative assessment of the crowding effect since higher tension counteracts bending. Reprinted from [34]. (**B**) Predicted tube force vs. the number of mucin biopolymers on a cell surface. The modeling reveals an expected decrease in the force needed to extract a tube from a crowded membrane as the protein density increases. Measuring tube force can serve as a measure to quantitatively assess the crowding effect. Reprinted from [26].

Biochemical Society Transactions (2022) **50** 1257–1267
https://doi.org/10.1042/BST20210883

Designing experiments to identify the underlying bending mechanisms and provide quantitative evidence for crowding is difficult, thus modeling has been a key factor when discussing biologically relevant systems. However, disagreement on the significance of the modeled crowding effect still exists in published papers [48, 67], thus separating the crowding contribution from other mechanisms has proven challenging not only in living systems, but also in theoretical modeling of biological systems. All in all, more quantitative experimental evidence, along the lines presented by Chen et al. [34], is needed to support the modeling efforts. In this work, membrane bending or shape instability on the surface of GUVs was measured as a function of membrane tension, which was regulated by the micropipette aspiration of the GUVs. The threshold for nanoscale membrane bending on the surface of GUVs was indirectly quantified from the aspirated length at a given pipette pressure. The GUVs were immersed into solutions with various concentrations of either crowding proteins or scaffolding proteins to compare the relative effect. Their conclusion provide an indication that the crowding effect is weaker compared to the suggested combined helix and scaffolding effect of BAR domain proteins (Figure 4A).

If crowding plays a significant role in driving membrane reshaping, this potential 'bending' force should be measurable with highly sensitive force detection like e.g. optical tweezers which are routinely used for extracting membrane tethers from cells [68, 69], GPMVs [35, 36] and GUVs [70]. Shurer et al. [26] has presented modeling of the point force predicted from tube formations under the influence of crowding by mucins (Figure 4B). Mimicking vesicle and tube budding with ultra-sensitive tether extraction techniques, could, therefore, provide the means to quantitatively characterize the spontaneous curvature contribution from protein crowding and hence provide a more accurate measure for the contribution from crowding in bending membranes. Other methods capable of providing relevant measurements of the crowding effect, such as a recently developed probe for measuring the lateral membrane pressure from crowding via FRET [71] or fluorescence lifetime quantification [72], will provide a deeper understanding of the mechanistic effect of crowding. Quantitative measurements of crowding should also be exploited to assess the tunable bending effects available through molecular engineering or by adjusting solution conditions [73].

Conclusion

Current knowledge obtained from multiple approaches including advanced experimental techniques and modeling has made it clear that crowding is indeed an important factor in shaping membranes at nanoscale. Looking forward, the focus must naturally shift towards identifying the processes in which crowding plays a role and characterize the relative, effective contribution of various biophysical membrane-shaping mechanisms. Advanced experimental techniques and rapid progresses in multiscale computer simulations now provide a fantastic opportunity to make a synergetic effort for decoupling and quantifying these contribution. In particular, the combination of highly sensitive force measuring tools like optical tweezers and quantitative imaging could reveal interesting details on how crowding differs for various proteins with different domain sizes and stalk lengths represented in cells. Future endeavors using a palette of experimental techniques together with modeling will undoubtedly give a more nuanced picture of the role of crowding in biology.

Perspectives

- The plasma membrane of cells is a highly crowded environment containing numerous types of proteins which give rise to phenomena such as entropic pressure, excluded volume effects and steric repulsion among the proteins. Evidence is now emerging that these physical phenomena are responsible for bending membranes and hence could be critical factors in a plethora of essential cellular functions involving membrane remodeling. In combination with molecular engineering and model systems the crowding effect can be tuned to harness effective control over membrane shapes useful for biological reconstitution and for nanotechnology applications like drug delivery.

- Current thinking explains membrane shape modulations as driven by motors or by specific protein properties like amphiphilic helix insertion or scaffolding, but is challenged by the identification of protein–protein crowding as a driver of curvature.

- An increased focus on coherent modeling and experimental design to disentangle and quantify the contribution from crowding in membrane curvature generation is needed to fully validate the importance of this interesting physical effect.

Competing Interests

The authors declare that there are no competing interests associated with the manuscript.

Funding

V.T.R. and P.M.B. acknowledge funding from Novo Nordisk Foundation (grant no. NNF20OC0065357). W.P. acknowledges funding from the Novo Nordisk Foundation (grant no. NNF18SA0035142) and INTERACTIONS, Marie Skłodowska-Curie grant agreement no. 847523.

Abbreviations

ENTH, Epsin NH_2-terminal homology; GUVs, giant unilamellar lipid vesicles; IDP, intrinsically disordered protein; GPMVs, giant plasma membrane vesicles.

References

1 Singer, S.J. and Nicolson, G.L. (1972) The fluid mosaic model of the structure of cell membranes. *Science (New York, NY)* **175**, 720–731 https://doi.org/10.1126/science.175.4023.720
2 Engelman, D.M. (2005) Membranes are more mosaic than fluid. *Nature* **438**, 578–580 https://doi.org/10.1038/nature04394
3 Enkavi, G., Javanainen, M., Kulig, W., Róg, T. and Vattulainen, I. (2019) Multiscale simulations of biological membranes: the challenge to understand biological phenomena in a living substance. *Chem. Rev.* **119**, 5607–5774 https://doi.org/10.1021/acs.chemrev.8b00538
4 Bagatolli, L. and Mouritsen, O. (2013) Is the fluid mosaic (and the accompanying raft hypothesis) a suitable model to describe fundamental features of biological membranes? What may be missing? *Front. Plant. Sci.* **4**, 457 https://doi.org/10.3389/fpls.2013.00457
5 Mouritsen, O.G. and Bagatolli, L.A. (2015) Lipid domains in model membranes: a brief historical perspective. *Essays Biochem.* **57**, 1–19 https://doi.org/10.1042/bse0570001
6 Kusumi, A., Nakada, C., Ritchie, K., Murase, K., Suzuki, K. and Murakoshi, H. et al. (2005) Paradigm shift of the plasma membrane concept from the two-dimensional continuum fluid to the partitioned fluid: high-speed single-molecule tracking of membrane molecules. *Annu. Rev. Biophys. Biomol. Struct.* **34**, 351–378 https://doi.org/10.1146/biophys.2005.34.issue-1
7 Arjonen, A., Kaukonen, R. and Ivaska, J. (2011) Filopodia and adhesion in cancer cell motility. *Cell Adh. Migr.* **5**, 421–430 https://doi.org/10.4161/cam.5.5.17723
8 Turturici, G., Tinnirello, R., Sconzo, G. and Geraci, F. (2014) Extracellular membrane vesicles as a mechanism of cell-to-cell communication: advantages and disadvantages. *Am. J. Physiol. Cell Physiol.* **306**, C621–C633 https://doi.org/10.1152/ajpcell.00228.2013
9 Kaksonen, M. and Roux, A. (2018) Mechanisms of clathrin-mediated endocytosis. *Nat. Rev. Mol. Cell Biol.* **19**, 313–326. Number: 5 Publisher: Nature Publishing Grouphttps://doi.org/10.1038/nrm.2017.132
10 Hurley, J.H., Boura, E., Carlson, L.A. and Różycki, B. (2010) Membrane budding. *Cell* **143**, 875–887 https://doi.org/10.1016/j.cell.2010.11.030
11 Janmey, P. (1995) Cell membranes and the cytoskeleton. *Handb. Biol. Phys.* **1**, 805–849 https://doi.org/10.1016/S1383-8121(06)80010-2
12 Kollmitzer, B., Heftberger, P., Rappolt, M. and Pabst, G. (2013) Monolayer spontaneous curvature of raft-forming membrane lipids. *Soft Matter* **9**, 10877–10884 https://doi.org/10.1039/c3sm51829a
13 Lorent, J.H., Levental, K.R., Ganesan, L., Rivera-Longsworth, G., Sezgin, E. and Doktorova, M. et al. (2020) Plasma membranes are asymmetric in lipid unsaturation, packing and protein shape. *Nat. Chem. Biol.* **16**, 644–652 https://doi.org/10.1038/s41589-020-0529-6
14 Snead, W.T., Hayden, C.C., Gadok, A.K., Zhao, C., Lafer, E.M. and Rangamani, P. et al. (2017) Membrane fission by protein crowding. *Proc. Natl Acad. Sci. U.S.A.* **114**, E3258–E3267 https://doi.org/10.1073/pnas.1616199114
15 Boucrot, E., Pick, A., Çamdere, G., Liska, N., Evergren, E. and McMahon, H. et al. (2012) Membrane fission is promoted by insertion of amphipathic helices and is restricted by crescent BAR domains. *Cell* **149**, 124–136 https://doi.org/10.1016/j.cell.2012.01.047
16 Isas, J.M., Ambroso, M.R., Hegde, P.B., Langen, J. and Langen, R. (2015) Tubulation by amphiphysin requires concentration-dependent switching from wedging to scaffolding. *Structure* **23**, 873–881 https://doi.org/10.1016/j.str.2015.02.014
17 Bassereau, P., Jin, R., Baumgart, T., Deserno, M., Dimova, R. and Frolov, V. et al. (2018) The 2018 biomembrane curvature and remodeling roadmap. *J. Phys. D: Appl. Phys.* **51**, 343001https://doi.org/10.1088/1361-6463/aacb98
18 Jarsch, I.K., Daste, F. and Gallop, J.L. (2016) Membrane curvature in cell biology: an integration of molecular mechanisms. *J. Cell Biol.* **214**, 375–387 https://doi.org/10.1083/jcb.201604003
19 McMahon, H.T. and Boucrot, E. (2015) Membrane curvature at a glance. *J. Cell Sci.* **128**, 1065–1070 https://doi.org/10.1242/jcs.114454
20 Zhukovsky, M.A., Filograna, A., Luini, A., Corda, D. and Valente, C. (2019) Protein amphipathic helix insertion: a mechanism to induce membrane fission. *Front. Cell Dev. Biol.* **7**, 291–290 https://doi.org/10.3389/fcell.2019.00291
21 Pezeshkian, W., Nåbo, L.J. and Ipsen, J.H. (2017) Cholera toxin B subunit induces local curvature on lipid bilayers. *FEBS Open Bio.* **7**, 1638–1645 https://doi.org/10.1002/feb4.2017.7.issue-11

22 McMahon, H.T. and Gallop, J.L. (2005) Membrane curvature and mechanisms of dynamic cell membrane remodelling. *Nature* **438**, 590–596 https://doi.org/10.1038/nature04396
23 Simunovic, M., Voth, G.A., Callan-Jones, A. and Bassereau, P. (2015) When physics takes over: BAR proteins and membrane curvature. *Trends Cell Biol.* **25**, 780–792 https://doi.org/10.1016/j.tcb.2015.09.005
24 Busch, D.J., Houser, J.R., Hayden, C.C., Sherman, M.B., Lafer, E.M. and Stachowiak, J.C. (2015) Intrinsically disordered proteins drive membrane curvature. *Nat. Commun.* **6**, 7875 https://doi.org/10.1038/ncomms8875
25 Stachowiak, J.C., Schmid, E.M., Ryan, C.J., Ann, H.S., Sasaki, D.Y. and Sherman, M.B. et al. (2012) Membrane bending by protein–protein crowding. *Nat. Cell Biol.* **14**, 944–949 https://doi.org/10.1038/ncb2561
26 Shurer, C.R., Kuo, J.C.H., Roberts, L.M., Gandhi, J.G., Colville, M.J. and Enoki, T.A. et al. (2019) Physical principles of membrane shape regulation by the glycocalyx. *Cell* **177**, 1757–1770.e21 https://doi.org/10.1016/j.cell.2019.04.017
27 Liese, S., Wenzel, E.M., Kjos, I., Rojas Molina, R., Schultz, S.W. and Brech, A. et al. (2020) Protein crowding mediates membrane remodeling in upstream ESCRT-induced formation of intraluminal vesicles. *Proc. Natl Acad. Sci. U.S.A.* **117**, 28614–28624 https://doi.org/10.1073/pnas.2014228117
28 Xu, Y., Erdjument-Bromage, H., Phoon, C.K.L., Neubert, T.A., Ren, M. and Schlame, M. (2021) Cardiolipin remodeling enables protein crowding in the inner mitochondrial membrane. *EMBO J.* **40**, e108428 https://doi.org/10.15252/embj.2021108428
29 Snead, W.T. and Stachowiak, J.C. (2018) Structure versus stochasticity–the role of molecular crowding and intrinsic disorder in membrane fission. *J. Mol. Biol.* **430**, 2293–2308 https://doi.org/10.1016/j.jmb.2018.03.024
30 Liese, S. and Carlson, A. (2021) Membrane shape remodeling by protein crowding. *Biophys. J.* **120**, 2482–2489 https://doi.org/10.1016/j.bpj.2021.04.029
31 Noguchi, H. (2022) Membrane shape deformation induced by curvature-inducing proteins consisting of chiral crescent binding and intrinsically disordered domains. *J. Chem. Phys.* **157**, 034901 https://doi.org/10.1063/5.0098249
32 Lindén, M., Sens, P. and Phillips, R. (2012) Entropic tension in crowded membranes. *PLoS Comput. Biol.* **8**, e1002431 https://doi.org/10.1371/journal.pcbi.1002431
33 Bruce, A., Johnson, A., Lewis, J., Morgan, D. and Raff, M. (2014) *Molecular Biology of the Cell*, 6th edn, Taylor & Francis Group, Oxford, UK
34 Chen, Z., Atefi, E. and Baumgart, T. (2016) Membrane shape instability induced by protein crowding. *Biophys. J.* **111**, 1823–1826 https://doi.org/10.1016/j.bpj.2016.09.039
35 Florentsen, C.D., Kamp-Sonne, A., Moreno-Pescador, G., Pezeshkian, W., Zanjani, A.A.H. and Khandelia, H. et al. (2021) Annexin A4 trimers are recruited by high membrane curvatures in giant plasma membrane vesicles. *Soft Matter* **17**, 308–318 https://doi.org/10.1039/D0SM00241K
36 Moreno-Pescador, G., Florentsen, C.D., Østbye, H., Sønder, S.L., Boye, T.L. and Veje, E.L. et al. (2019) Curvature- and phase-induced protein sorting quantified in transfected cell-derived giant vesicles. *ACS Nano* **13**, 6689–6701 https://doi.org/10.1021/acsnano.9b01052
37 Sezgin, E., Kaiser, H.J., Baumgart, T., Schwille, P., Simons, K. and Levental, I. (2012) Elucidating membrane structure and protein behavior using giant plasma membrane vesicles. *Nat. Protoc.* **7**, 1042–1051 https://doi.org/10.1038/nprot.2012.059
38 Stachowiak, J.C., Hayden, C.C. and Sasaki, D.Y. (2010) Steric confinement of proteins on lipid membranes can drive curvature and tubulation. *Proc. Natl Acad. Sci. U.S.A.* **107**, 7781–7786 https://doi.org/10.1073/pnas.0913306107
39 Snead, W.T., Zeno, W.F., Kago, G., Perkins, R.W., Richter, J.B. and Zhao, C. et al. (2018) BAR scaffolds drive membrane fission by crowding disordered domains. *J. Cell Biol.* **218**, 664–682 https://doi.org/10.1083/jcb.201807119
40 Adam, J., Basnet, N. and Mizuno, N. (2015) Structural insights into the cooperative remodeling of membranes by amphiphysin/BIN1. *Sci. Rep.* **5**, 15452 https://doi.org/10.1038/srep15452
41 Siaw, H.M.H., Raghunath, G. and Dyer, R.B. (2018) Peripheral protein unfolding drives membrane bending. *Langmuir* **34**, 8400–8407 https://doi.org/10.1021/acs.langmuir.8b01136
42 Kapoor, K., Chen, T. and Tajkhorshid, E. (2021) Post-translational modifications optimize the ability of SARS-CoV-2 spike for effective interaction with host cell receptors. *bioRxiv*
43 Dou, D., Revol, R., Östbye, H., Wang, H. and Daniels, R. (2018) Influenza A virus cell entry, replication, virion assembly and movement. *Front. Immunol.* **9**, 1581https://doi.org/10.3389/fimmu.2018.01581
44 McAuley, J.L., Gilbertson, B.P., Trifkovic, S., Brown, L.E. and McKimm-Breschkin, J.L. (2019) Influenza virus neuraminidase structure and functions. *Front. Microbiol.* **10**, 39–30 https://doi.org/10.3389/fmicb.2019.00039
45 Hiergeist, C. and Lipowsky, R. (1996) Elastic properties of polymer-decorated membranes. *J. Phys. II* **6**, 1465–1460 https://doi.org/10.1051/jp2:1996142
46 Tran, N.H., Carter, S.D., Mazière, A.D., Ashkenazi, A., Klumperman, J. and Walter, P. et al. (2021) The stress-sensing domain of activated IRE1α forms helical filaments in narrow ER membrane tubes. *Science* **374**, 52–57 https://doi.org/10.1126/science.abh2474
47 Martyna, A., Bahsoun, B., Badham, M.D., Srinivasan, S., Howard, M.J. and Rossman, J.S. (2017) Membrane remodeling by the M2 amphipathic helix drives influenza virus membrane scission. *Sci. Rep.* **7**, 44695 https://doi.org/10.1038/srep44695
48 Kozlov, M.M., Campelo, F., Liska, N., Chernomordik, L.V., Marrink, S.J. and McMahon, H.T. (2014) Mechanisms shaping cell membranes. *Curr. Opin. Cell Biol.* **29**, 53–60 https://doi.org/10.1016/j.ceb.2014.03.006
49 Zeno, W.F., Baul, U., Snead, W.T., DeGroot, A.C.M., Wang, L. and Lafer, E.M. et al. (2018) Synergy between intrinsically disordered domains and structured proteins amplifies membrane curvature sensing. *Nat. Commun.* **9**, 4152 https://doi.org/10.1038/s41467-018-06532-3
50 Steinkühler, J., Knorr, R.L., Zhao, Z., Bhatia, T., Bartelt, S.M. and Wegner, S. et al. (2020) Controlled division of cell-sized vesicles by low densities of membrane-bound proteins. *Nat. Commun.* **11**, 1–11 https://doi.org/10.1038/s41467-019-13993-7
51 Day, K.J. and Stachowiak, J.C. (2020) Biophysical forces in membrane bending and traffic. *Curr. Opin. Cell Biol.* **65**, 72–77 https://doi.org/10.1016/j.ceb.2020.02.017
52 Derganc, J. and Čopič, A. (2016) Membrane bending by protein crowding is affected by protein lateral confinement. *Biochim. Biophys. Acta - Biomembr.* **1858**, 1152–1159 https://doi.org/10.1016/j.bbamem.2016.03.009
53 van Deventer, S., Arp, A.B. and van Spriel, A.B. (2021) Dynamic plasma membrane organization: a complex symphony. *Trends Cell Biol.* **31**, 119–129 https://doi.org/10.1016/j.tcb.2020.11.004

54 Sadegh, S., Higgins, J.L., Mannion, P.C., Tamkun, M.M. and Krapf, D. (2017) Plasma membrane is compartmentalized by a self-similar cortical actin meshwork. *Phys. Rev. X* **7**, 011031 https://doi.org/10.1103/PhysRevX.7.011031
55 Heinemann, F., Vogel, S.K. and Schwille, P. (2013) Lateral membrane diffusion modulated by a minimal actin cortex. *Biophys. J.* **104**, 1465–1475 https://doi.org/10.1016/j.bpj.2013.02.042
56 Lorent, J.H., Diaz-Rohrer, B., Lin, X., Spring, K., Gorfe, A.A. and Levental, K.R. et al. (2017) Structural determinants and functional consequences of protein affinity for membrane rafts. *Nat. Commun.* **8**, 1219 https://doi.org/10.1038/s41467-017-01328-3
57 Nikolaus, J., Scolari, S., Bayraktarov, E., Jungnick, N., Engel, S. and Plazzo, A.P. et al. (2010) Hemagglutinin of influenza virus partitions into the nonraft domain of model membranes. *Biophys. J.* **99**, 489–498 https://doi.org/10.1016/j.bpj.2010.04.027
58 Schlebach, J.P., Barrett, P.J., Day, C.A., Kim, J.H., Kenworthy, A.K. and Sanders, C.R. (2016) Topologically diverse human membrane proteins partition to liquid-disordered domains in phase-separated lipid vesicles. *Biochemistry* **55**, 985–988 https://doi.org/10.1021/acs.biochem.5b01154
59 Levental, I., Lingwood, D., Grzybek, M., Coskun, U. and Simons, K. (2010) Palmitoylation regulates raft affinity for the majority of integral raft proteins. *Proc. Natl Acad. Sci. U.S.A.* **107**, 22050–22054 https://doi.org/10.1073/pnas.1016184107
60 Leser, G.P. and Lamb, R.A. (2005) Influenza virus assembly and budding in raft-derived microdomains: a quantitative analysis of the surface distribution of HA, NA and M2 proteins. *Virology* **342**, 215–227 https://doi.org/10.1016/j.virol.2005.09.049
61 Scheve, C.S., Gonzales, P.A., Momin, N. and Stachowiak, J.C. (2013) Steric pressure between membrane-bound proteins opposes lipid phase separation. *J. Am. Chem. Soc.* **135**, 1185–1188 https://doi.org/10.1021/ja3099867
62 Wu, H., Shibaa, H. and Noguchi, H. (2013) Mechanical properties and microdomain separation of fluid membranes with anchored polymers. *Soft Matter* **9**, 9907–9917 https://doi.org/10.1039/c3sm51680f
63 Trimble, W.S. and Grinstein, S. (2015) Barriers to the free diffusion of proteins and lipids in the plasma membrane. *J. Cell Biol.* **208**, 259–271 https://doi.org/10.1083/jcb.201410071
64 Saletti, D., Radzimanowski, J., Effantin, G., Midtvedt, D., Mangenot, S. and Weissenhorn, W. et al. (2017) The Matrix protein M1 from influenza C virus induces tubular membrane invaginations in an in vitro cell membrane model. *Sci. Rep.* **7**, 1–14 https://doi.org/10.1038/srep40801
65 Hilsch, M., Goldenbogen, B., Sieben, C., Höfer, C.T., Rabe, J.P. and Klipp, E. et al. (2014) Influenza A matrix protein M1 multimerizes upon binding to lipid membranes. *Biophys. J.* **107**, 912–923 https://doi.org/10.1016/j.bpj.2014.06.042
66 Johannes, L., Pezeshkian, W., Ipsen, J.H. and Shillcock, J.C. (2018) Clustering on membranes: fluctuations and more. *Trends Cell Biol.* **28**, 405–415 https://doi.org/10.1016/j.tcb.2018.01.009
67 Sapp, K. and Sodt, A.J. (2022) Observed steric crowding at modest coverage requires a particular membrane-binding scheme or a complementary mechanism. *Biophys. J.* **121**, 430–438 https://doi.org/10.1016/j.bpj.2021.12.036
68 Rosholm, K.R., Leijnse, N., Mantsiou, A., Tkach, V., Pedersen, S.L. and Wirth, V.F. et al. (2017) Membrane curvature regulates ligand-specific membrane sorting of GPCRs in living cells. *Nat. Chem. Biol.* **13**, 724–729 https://doi.org/10.1038/nchembio.2372
69 Aimon, S., Callan-Jones, A., Berthaud, A., Pinot, M., Toombes, G.E.S. and Bassereau, P. (2014) Membrane shape modulates transmembrane protein distribution. *Dev. Cell* **28**, 212–218 https://doi.org/10.1016/j.devcel.2013.12.012
70 Prévost, C., Zhao, H., Manzi, J., Lemichez, E., Lappalainen, P. and Callan-Jones, A. et al. (2015) IRSp53 senses negative membrane curvature and phase separates along membrane tubules. *Nat. Commun.* **6**, 8529 https://doi.org/10.1038/ncomms9529
71 Houser, J.R., Hayden, C.C., Thirumalai, D. and Stachowiak, J.C. (2020) A Förster resonance energy transfer-based sensor of steric pressure on membrane surfaces. *J. Am. Chem. Soc.* **142**, 20796–20805 https://doi.org/10.1021/jacs.0c09802
72 Colom, A., Derivery, E., Soleimanpour, S., Tomba, C., Molin, M.D. and Sakai, N. et al. (2018) A fluorescent membrane tension probe. *Nat. Chem.* **10**, 1118–1125 https://doi.org/10.1038/s41557-018-0127-3
73 Werner, M. and Sommer, J.U. (2010) Polymer-decorated tethered membranes under good- and poor-solvent conditions. *Eur. Phys. J. E Soft Matter.* **31**, 383–392 https://doi.org/10.1140/epje/i2010-10576-4

B.3 Close, but not too close: a mesoscopic description of (a)symmetry and membrane shaping mechanisms

Authors:
Victoria Thusgaard Ruhoff, Poul Martin Bendix, and Weria Pezeshkian.
Status: Published

BIOCHEMICAL SOCIETY
Royal Society of Biology
PORTLAND PRESS

EMERGING TOPICS IN LIFE SCIENCES

VOLUME 7 ● ISSUE 1 ● MARCH 2023
portlandpress.com/emergtoplifesci

Membrane (A)symmetry

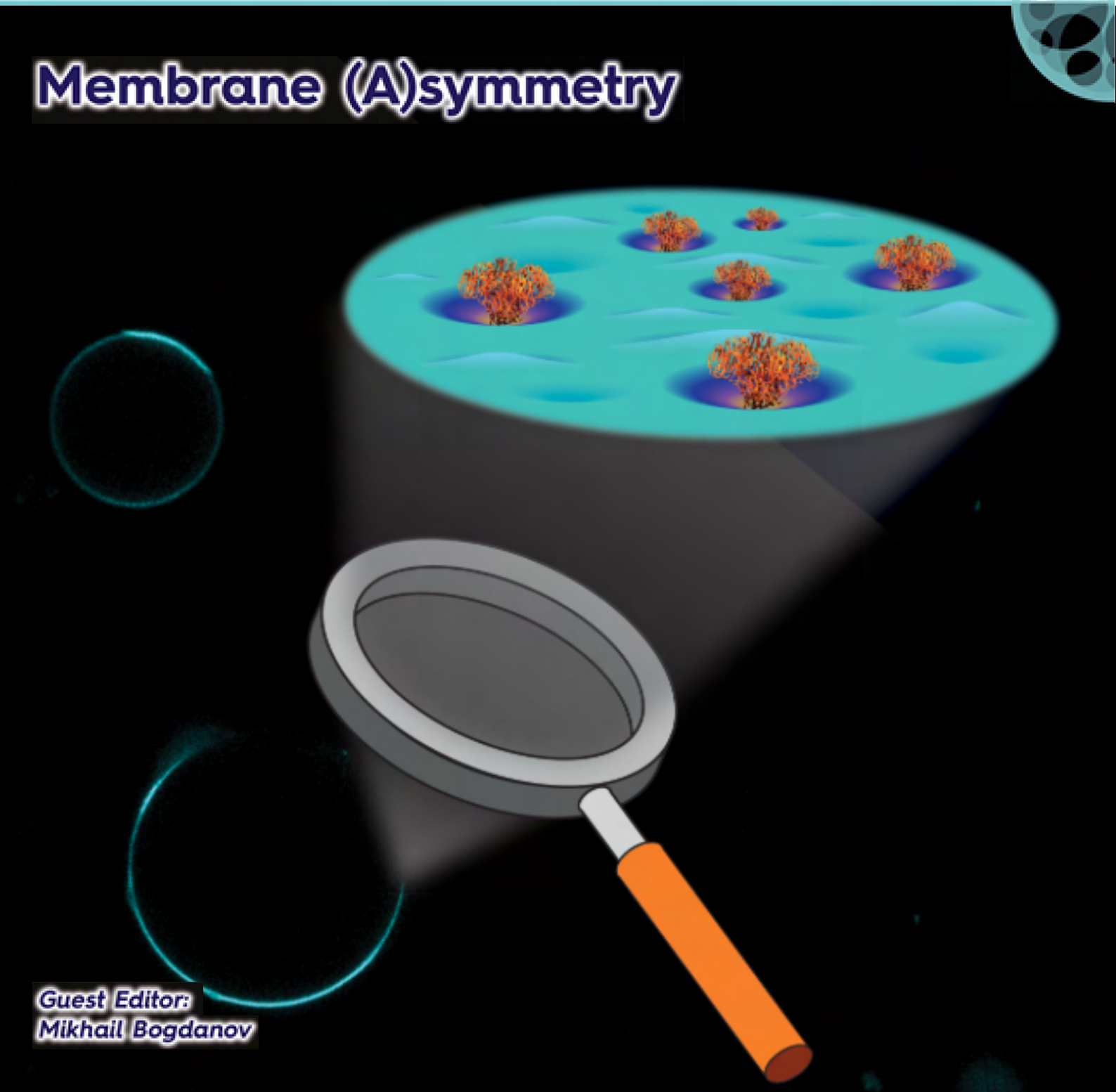

Guest Editor:
Mikhail Bogdanov

Cover art by Victoria Thusgaard Ruhoff

Emerging Topics in Life Sciences (2023) **7** 81–93
https://doi.org/10.1042/ETLS20220078

PORTLAND PRESS

Review Article

Close, but not too close: a mesoscopic description of (a)symmetry and membrane shaping mechanisms

Victoria Thusgaard Ruhoff[1], **Poul Martin Bendix**[1] and **Weria Pezeshkian**[2]

[1]Niels Bohr Institute, University of Copenhagen, Blegdamsvej 17, 2100 Copenhagen, Denmark; [2]Niels Bohr International Academy, Niels Bohr Institute, University of Copenhagen, Blegdamsvej 17, 2100 Copenhagen, Denmark

Correspondence: Weria Pezeshkian (weria.pezeshkian@nbi.ku.dk)

Biomembranes are fundamental to our understanding of the cell, the basic building block of all life. An intriguing aspect of membranes is their ability to assume a variety of shapes, which is crucial for cell function. Here, we review various membrane shaping mechanisms with special focus on the current understanding of how local curvature and local rigidity induced by membrane proteins leads to emerging forces and consequently large-scale membrane deformations. We also argue that describing the interaction of rigid proteins with membranes purely in terms of local membrane curvature is incomplete and that changes in the membrane rigidity moduli must also be considered.

Introduction

A fascinating aspect of cellular membranes is their ability to adopt a variety of shapes, a feature manifested in the rich repository of morphologies in cellular organelles [1] and essential for vital cellular processes such as endocytosis, cell migration, signaling, cell division, and cellular respiration. Genetic mutations disturbing membrane architectures are implicated in many diseases such as Parkinson's Disease and liver dysfunction [2,3]. Moreover, structures with highly curved membrane shape offer many applications for biotechnological design, for instance, for the developments of non-viral vectors [4]. Therefore, investigation of the mechanisms that control membrane shape is of particular importance for understanding both cell function, and for optimizing numerous biomedical and nanotechnological applications.

Membrane shapes have been explored under simplified and controlled conditions using biomimetic systems such as lipid bilayers and vesicles [5–7]. Such model systems have been the subject of numerous experimental, theoretical, and simulation studies during the past decades, which has given us a comprehensive picture of the equilibrium architecture of simple fluid bilayers. At a molecular scale, model systems have contributed immensely to our understanding of the coupling between proteins and membrane shape by providing quantitative data, which can be used for testing theoretical models [8–10]. Using these assays, theoretical predictions on the ability of proteins to generate and sense membrane curvature, have been measured using advanced bio-manipulation in combination with molecular imaging [11–14]. These simple model systems have also allowed us to quantify and discover dynamics of lipid domains creating asymmetry in membranes, and how such asymmetry can be coupled to membrane shape and protein-induced curvature [15–18]. At larger scales, model systems and theoretical predictions have provided an understanding of how, and under which conditions, a spherical vesicle transforms into dumbbell shapes, stomatocytes, and, more generally, multispherical structures. These shapes can be explained through a macroscopic picture merely as an interplay between membrane bending elasticity, membrane tension, and osmotic pressure [19].

Received: 28 October 2022
Revised: 13 December 2022
Accepted: 22 December 2022

Version of Record published:
16 January 2023

Emerging Topics in Life Sciences (2023) **7** 81–93
https://doi.org/10.1042/ETLS20220078

However, cellular membranes are far more complex and evidence is emerging for many molecular mechanisms which govern membrane shape. They are heterogeneous, and composed of a myriad of proteins and lipid species [20]. The protein area coverage can be as high as 30.000 proteins per μm^2 in the plasma membrane or up to 50% area coverage for internal subcellular membranes [21]. Thus, to understand cellular membrane organization, it is essential to understand how proteins are organized on membrane surfaces and how their organization affects membrane conformations. Proteins or different lipid species may be introduced to model membranes to better approximate cellular membranes. These entities, through molecular interactions, change the membrane elasticity at the nanoscale, which can lead to large-scale membrane shape remodeling. Although, the shapes of complex membranes can be similar to those described above (multispherical structures), they often exhibit different shapes with many exciting emerging phenomena, such as phase separation, protein clustering, membrane-mediated interactions, and curvature instability, in which membrane thermodynamics becomes important [22].

The purpose of this minireview is to highlight the importance of nanoscopic membrane inhomogeneity and trans-bilayer asymmetry in formation of membrane shapes and present various strategies for addressing the challenges in investigating biomembrane shapes with varying spatial and temporal extent. Finally, we sketch possible routes for future developments to finally provide a comprehensive picture of the mechanisms leading to the many interesting shapes discovered in cellular membranes.

Membrane shaping mechanisms at the mesoscale

Helfrich Hamiltonian, a function that relates membrane geometry to elastic energy, provides a steadfast description of simple lipid bilayer shapes on large scales (large compared with the membrane thickness) [23,24]. Within this formulation, supported by experimental data, a spherical vesicle can deform into a variety of shapes. By the simplest form of transbilayer asymmetry, i.e., osmotic pressure difference, three families of vesicle shapes can develop: stomatocytes (large osmotic difference), discoid (oblate), and prolate (Figure 1A) [25]. An important transbilayer symmetry-breaking parameter is the spontaneous curvature of membranes, omnipresent in cellular and artificial membranes, that leads to the formation of a plethora of membrane morphologies (Figure 1B) [19].

Spontaneous membrane curvature is the propensity of a membrane, or a segment of a membrane, to bend and is different from the intrinsic curvature of individual lipid molecules [26]. An excellent way to understand spontaneous membrane curvature at the molecular level, beyond a single lipid, is through the lateral pressure profile across the membrane (for more information see Figure 2; also see [26,27]). This profile shows the distribution of lateral stresses across the thickness of the bilayer in which the first moment is proportional to spontaneous membrane curvature. Therefore, independent of the shape of individual molecular constituents, e.g., lipids, a symmetric membrane has zero spontaneous curvature. However, transbilayer asymmetry (asymmetry between the two monolayers), can lead to a non-zero curvature that can be induced in a variety of ways (Figure 2B). For example, by an asymmetry of chemical composition, asymmetric ionic conditions, molecular adhesion, or embedding of proteins. Such spontaneous membrane curvature could be large, small, positive, or negative depending on the type and the level of asymmetry [27,28].

The above discussion assumes homogeneity of the membrane since the spontaneous curvature is laterally uniform. However, the nonzero spontaneous curvature can originate from biomolecular impurities (inclusions) (Figure 3A), that are free to diffuse laterally. If the inclusions are distributed uniformly across large distances, they can be considered as an effective mean curvature in which the previous description still applies. However, there are meso- and molecular scale mechanisms (see below) that could lead to a non-uniform inclusion density that even persist at large scale (Figure 3B). The possibility of lateral inclusion inhomogeneities leads to a plethora of emergent behaviors depending on the character of the inclusions and their interactions with the membrane. The simplest form of inclusions is the one that only induces (local) curvature and is non- or weakly interacting. A membrane decorated by these inclusions can be described by position-dependent spontaneous curvature. Theoretical and simulation results show that the entropic contribution from lateral inclusion distribution makes the membrane effectively softer, and the degree of softening depends on the inclusion concentration and local curvature (Figure 3C) [29,30]. Therefore, above a certain concentration threshold, the membrane will undergo large surface undulation [31] that leads to protein segregation into curved regions, and consequently, membrane vesiculations (Figure 3B). This behavior can explain membrane remodeling by a non-bilayer forming lipid such as ganglioside GM1 [6]. It must be noted that in this mechanism the inclusions do not modify the local rigidity directly, but the softening (curvature instability) is instead a result of the

Emerging Topics in Life Sciences (2023) **7** 81–93
https://doi.org/10.1042/ETLS20220078

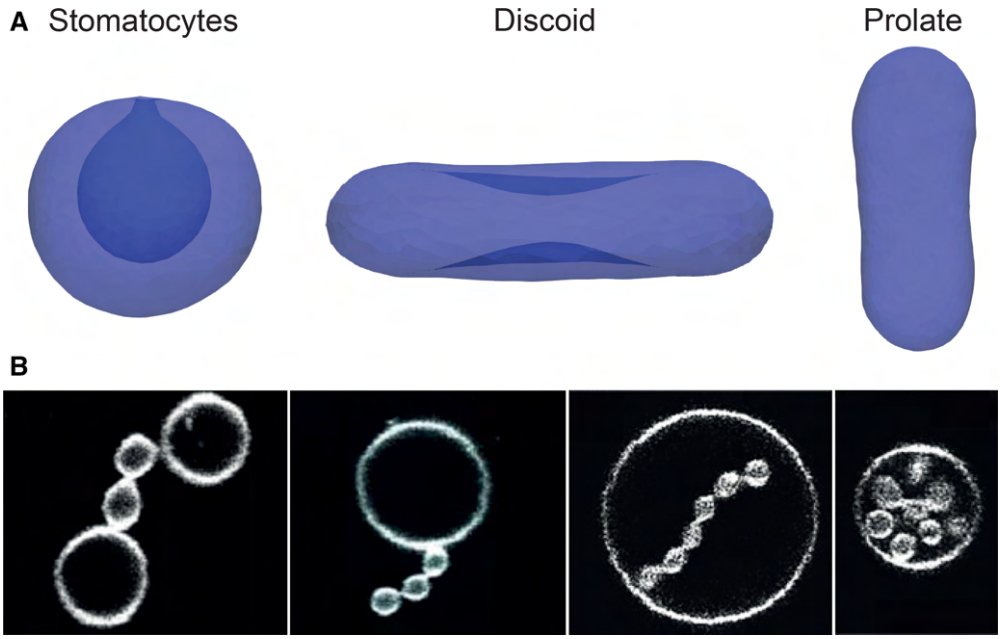

Figure 1. Vesicle deformation by transbilayer asymmetry.
(**A**) A spherical vesicle transforms into stomatocytes, oblates (discoid), and prolates through the change of reduced volume or osmotic pressure. (**B**) Multispherical structures as a result of an interplay between membrane bending elasticity, spontaneous curvature, membrane tension, and osmotic pressure. Figure adapted from [19].

cooperative action of curvature-active proteins on an undulating membrane. Therefore this behavior cannot be captured in single protein investigations or on a non-fluctuating elastic surface.

Large and rigid proteins and protein complexes prefer (impose) a well-defined membrane shape that can only be uniquely defined by Gaussian and mean curvatures. For instance, as it is depicted in Figure 4A, an infinite number of local shapes can be defined that all have identical mean curvature. In the framework of elastic energy-geometry, this means that the inclusions, in addition to inducing local membrane curvature, locally change the bending rigidity and the Gaussian modulus (Figure 4B) [13,32,33]. Such nanoscopic lateral inhomogeneities are important for large-scale membrane shape descriptions. For instance, it can lead to emergence of long-range membrane-mediated interactions like curvature mediated and Casimir-like forces, resulting in protein clustering and consequently membrane remodeling even at low concentrations as it has been shown for Shiga and cholera toxins [22,33–35]. Additionally, nanoscopic inhomogeneity in membrane rigidity can explain the tendency of certain proteins to be recruited by a narrow range of membrane curvatures, which is often referred to as membrane curvature sensing [13]. Other interesting inclusion types are the one that break in-plane rotational membrane symmetry (anisotropic proteins), e.g., such as BAR protein family, FtsZ, and dynamin A, by imposing different curvature in different directions on the bound membrane (Figure 4B) [8,36–38]. Membrane containing anisotropic inclusions can exhibit macroscopic quasi-order phases and become elongated vesicles even in absence of any direct interactions between the inclusions. The inclusions can also phase segregate through attractive curvature-mediated interactions [22,39].

As mentioned above, curvature inducing inclusions can form clusters and therefore, induce high curvature membrane deformation in a specific region of the membrane. Another mechanism behind clustering of inclusions is phase separation. Curvature inducing inclusion are recruited by different phases and even by phase boundaries of liquid ordered and disordered phases. Through this mechanism phase-induced enrichment of proteins and lipids at specific locations can assist in shaping and even contribute to fission of membrane-necks in model membranes [40]. Viral proteins have been found to be recruited, through helix insertion, to phase boundaries established in phase separated GUVs which could serve as a critical function in budding of viruses [41]. Membrane curvature can also efficiently lead to lipid sorting as shown in nanotubes extracted from GUVs which were held close to the miscibility transition temperature leading to pronounced lipid sorting between the

Emerging Topics in Life Sciences (2023) **7** 81–93
https://doi.org/10.1042/ETLS20220078

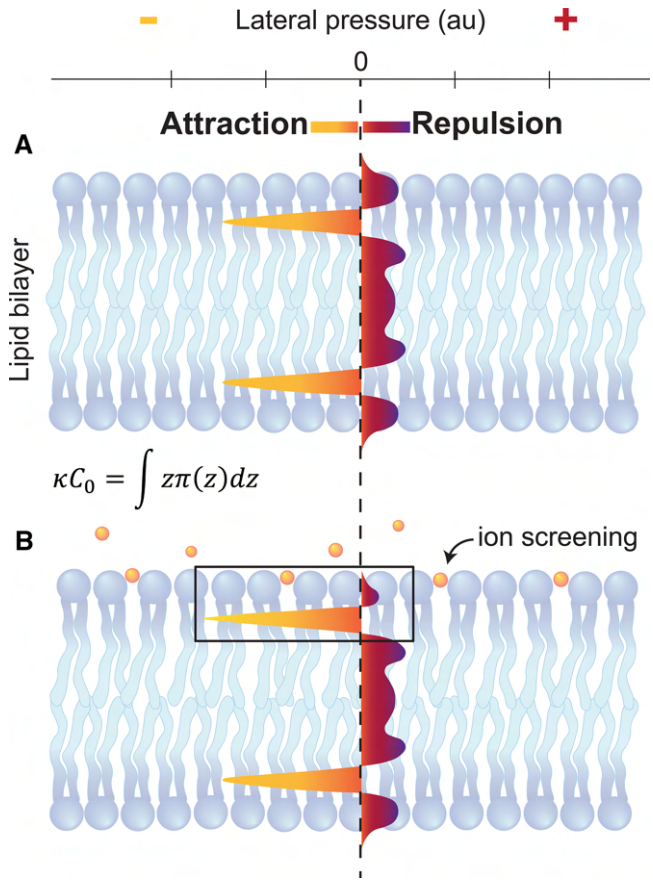

Figure 2. Lateral pressure profile of lipid bilayer.

The lateral pressure profile is the distribution of lateral stresses across the width of a lipid bilayer. It is composed of repulsive pressure components from interactions between the lipid molecules and a cohesive hydrophobic tension that favors segregation of the lipid chains from water. (**A**) The first moment of this profile is proportional to membrane spontaneous curvature. (**B**) A schematic view of how asymmetry can be induced in the profile which leads to non-zero spontaneous membrane curvature.

curved tube and the GUV [16]. Along these same lines it has been shown how curvature could control membrane phase boundaries and dynamically sort lipids and proteins in a GUV-tube model system [42]. Together these examples shed light on how membrane shapes are intimately coupled to proteins and lipids in model systems. However, investigation of membrane shapes in biological systems remains difficult primarily due to the transient nature and small scale of membrane shapes and due to the smallness of the putative nanoscopic lipid domains which are thought to be present in the membranes of living cells. Model systems in combination with advanced optical tools therefore provide an effective platform to isolate these interactions between proteins and lipid phases and hence are indispensable for gaining a deeper understanding of membrane shapes in cells.

One of the well-established features of cellular membranes is an asymmetry in the number and composition of constituent lipids and proteins between the two leaflets [20]. In recent years, several theoretical, simulation, and experimental efforts have explored the consequences (or implications) of this asymmetry. For instance, it is found that such asymmetry could affect the distribution of cholesterol in distinct manners [18,43–45], generating a mismatch in the lateral tension of the two leaflets, even for vanishing bilayer tension, leading to a multitude of behaviors such as a discontinuous increase in the bending rigidity [17,46], generation of highly ordered domains in the compressed leaflet, stress-induced flip-flop and bilayer instability (transient) to form globular micelles [47]. However, it is not fully clear yet how the composition mismatch affects membrane remodeling and shaping processes, despite the fact that the increase in bending rigidity, reorganization of lipids in different monolayers, and the ability of cholesterol (and other lipids) to flip-flop, can potentially change the behavior of

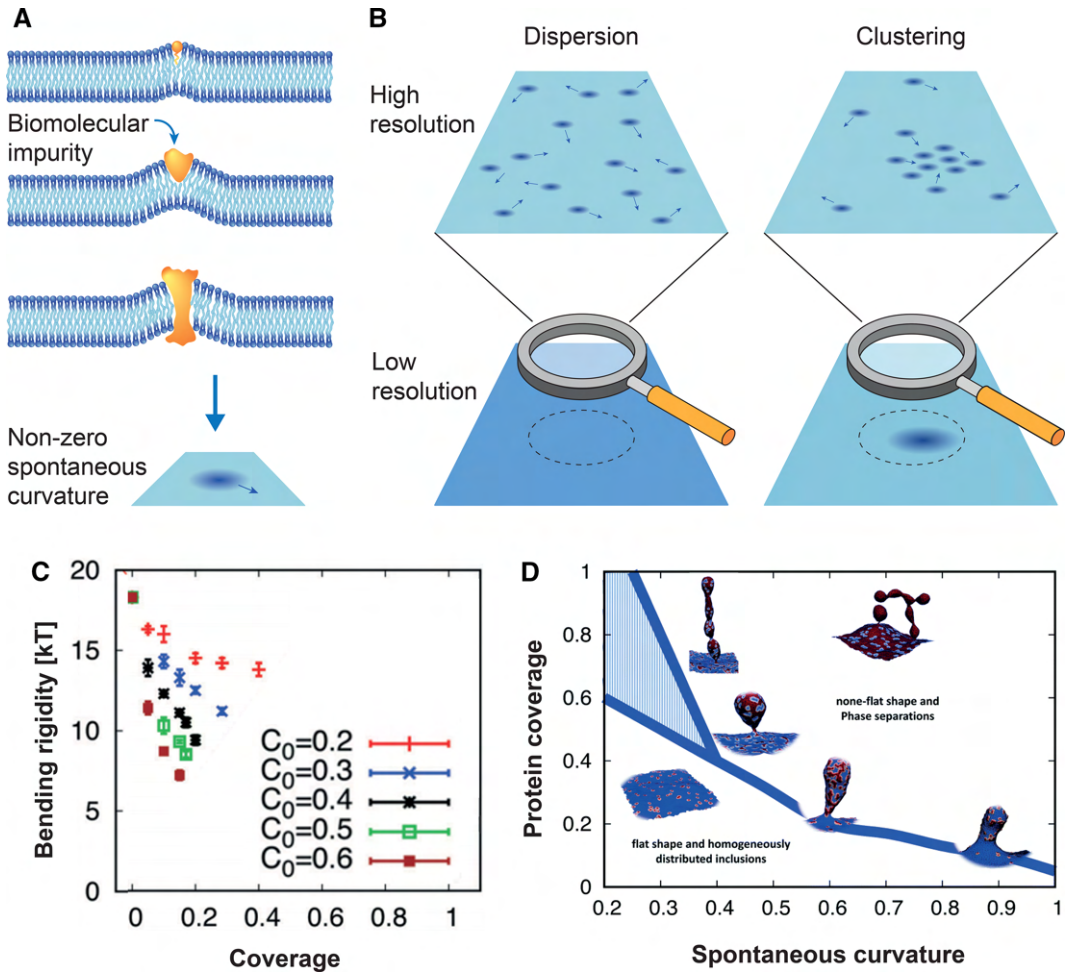

Figure 3. Non-uniform density of curvature-active inclusions can persists at large scale.

(**A**) The source of the nonzero spontaneous curvature can be some biomolecular impurities (inclusion). (**B**) The effective inclusion distribution could become non-uniform at even macroscopic scales through several possibilities for protein clustering. (**C**) As the concentration of curvature inducing inclusions increases, the effective bending rigidity decreases. (**D**) Above a certain concentration threshold, the membrane undergoes large surface undulation, that leads to protein segregation into the curved regions, and consequently, membrane vesiculations. (**C**,**D**) adapted from [29].

a membrane response to bending stress. We could envision that in the coming years more findings will shed light on this puzzle.

The above discussion indicates that the concepts of spontaneous membrane curvature and local curvature must be considered with care for complex membranes such as cellular membranes. Particularly rigid membrane proteins prefer a well-defined local shape that cannot be described by a single parameter, i.e. curvature. Three or four parameters, as depicted in Figure 4B, can provide a better approximation that can also unify the concepts of scaffolding and curvature sensing into one picture within the thermo-elastic description of membrane shape. Additionally, membrane remodeling processes must be considered as a collective phenomenon. As an example to illustrate this we can look at molecular crowding which can induce membrane bending above certain densities whereas the single molecules would not change the membrane shape on their own. Therefore, investigations at a length scale (mesoscale) a bit larger than a single biomolecule up to the length scale at which the discreetness of molecules is still relevant (5–100 nm) is essential for our understanding of complex membrane shapes. This is also supported by numerous exploratory methods that have been expanded, in recent years, to focus on these relevant length scales.

PORTLAND PRESS

Emerging Topics in Life Sciences (2023) **7** 81–93
https://doi.org/10.1042/ETLS20220078

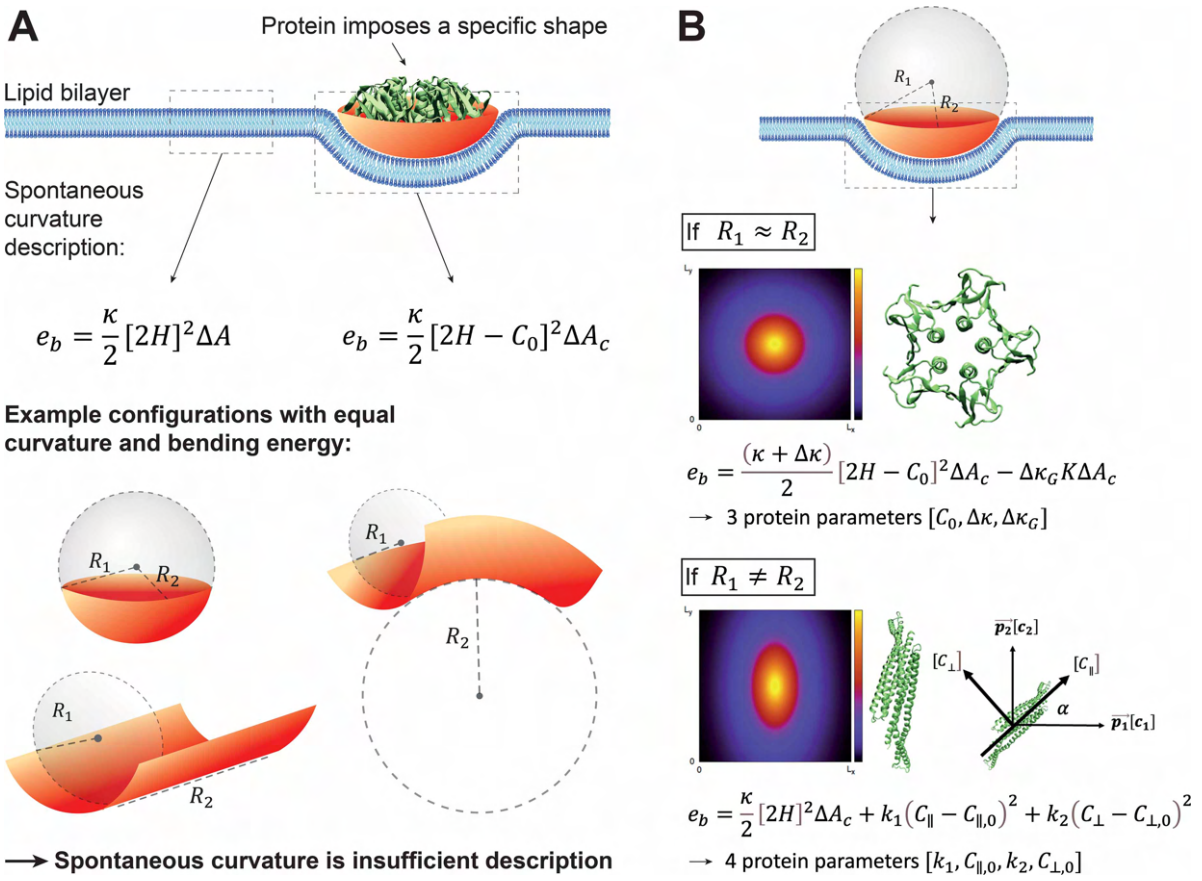

Figure 4. Describing large and rigid proteins purely in terms of local membrane curvature is incomplete.

(**A**) Large and rigid proteins and protein complexes often prefer or impose a well-defined shape on membranes. The bending energy of a membrane segment containing a rigid protein cannot be constructed by only considering spontaneous membrane curvature since there is an infinite amount of membrane shapes with the same, mean curvature and consequently the same bending energy. (**B**) A better description of the interaction of these proteins can be obtained by a three-parameter model for isotropic proteins, and a four-parameter model for anisotropic proteins. In all the equations, e_b is the bending energy of the considered segment of the membrane, κ is the membrane bending rigidity, H is the mean curvature, K is the gaussian curvature, δA is the area of the considered segment of membrane, $C_\parallel$ ($C_\perp$) is membrane curvature in the direction parallel (perpendicular) to the longest axis of the protein. (C_0, $\Delta\kappa$,$\Delta\kappa_G$) are model parameters for isotropic proteins and (k_1, k_2, $C_{\parallel,0}$, $C_{\perp,0}$) are model parameters for anisotropic proteins.

State-of-the-art techniques for exploring membrane shape

During the last few decades significant progress has been made in developing new assays for generation and detection of membrane shapes in both model membranes and living systems. New imaging platforms allow imaging below the optical diffraction limit whereas new developments in material fabrication have facilitated production of nanostructured substrates with interesting morphologies on which cells can be plated. These advances have allowed quantitative measurements of curvature affinity of proteins for both tubular, spherical and even negative gaussian curvatures [14,48].

Substantial efforts have been put into developing model membrane systems and assays to generate and detect membrane shapes. Model membranes have long been used to study lipid and protein dynamics and the complexity of these model systems has gradually increased in complexity and novelty to either enhance the biological relevance by mimicking plasma membrane or exaggerating biological effects such as lipid phase separation to study such phenomena in isolation. Both experimentally and theoretically a spectrum of systems varying from various geometries and cell-like systems, like supported lipid bilayers to cells have been used to facilitate biophysical investigation of membranes (Figure 5)

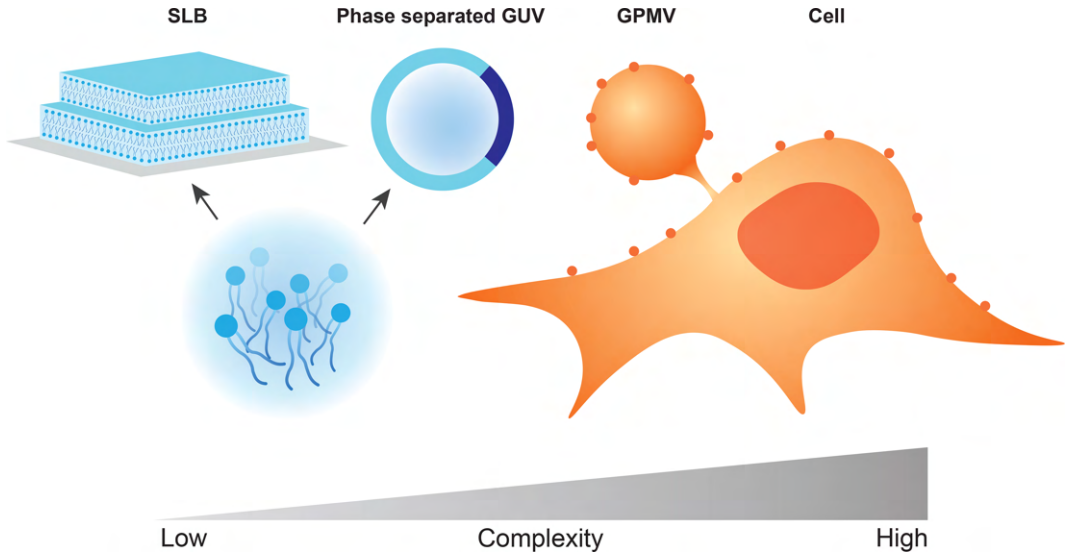

Figure 5. Model membrane systems presented in increasing complexity.

From left to right, illustrations represent four types of model membranes used in experimental investigations of membrane properties. (left) Lipids (bottom) can be used to make supported lipid bilayers (SLB) and giant unilamellar vesicles (GUVs). The latter an excellent platform to induce phase separation and explore for example protein sorting or membrane bending in 3D. (right) Giant plasma membrane vesicles (GPMVs) can be extracted from cell membranes and serve as a complex native-like membrane yet without the added complexity of i.e. the cytoskeleton and elaborate machinery governing the cell function.

3D Biomimetic systems such as GUVs remain an important experimental system for studying membrane shapes (Figure 5) as they allow researchers to insert membrane proteins into vesicles as well as create and reconstitute artificial membrane shaping agents. GUVs are, therefore, well-suited for controlling and introducing membrane asymmetry via lipid composition and protein insertions and for investigating membrane curvature effects. Lipid asymmetry in GUVs can be established simply by using electric swelling as the formation method which clearly result in large number of long nanotubes [7]. Asymmetric ionic solutions across GUV membranes also result in spontaneous membrane curvature leading to similar nanotubes [49]. Membrane tension was also shown in a GUV system to play an important role as a master regulator of membrane bending induced by N-BAR [50] or I-BAR [10]. However, GUVs are limited when it comes to studying native transmembrane proteins, as such proteins become randomly oriented in the membrane upon insertion, which does not properly reflect the inward-out orientation in biological membranes. This can be a major drawback when investigating e.g. the effect of protein crowding on membrane shapes for highly asymmetric proteins, as random inward–outward distribution will counteract any crowding effect on the transmembrane pressure profile. A promising method for obtaining vesicles with correctly oriented proteins is the extraction and isolation of giant plasma membrane vesicles (GPMVs) from cells. These membranes, harvested directly from cells, not only provide controlled conditions for transmembrane protein orientation, but also have the same lipid and and protein complexity as the plasma membrane, and therefore constitute a more complex, and native-like membrane system [13,51,52]. Recently, a new assay was developed which combines GPMVs with phase separated GUVs with the purpose of investigating phase affinity of membrane proteins, demonstrating the versatility possible when combining these two methods [53]. Yet limitations still exists with the GPMV platform, as it has recently been demonstrated that the permeability of GPMVs is much higher than for GUVs, which might significantly impact experimental studies. The origin of such permeability might stem from the invasive methods of extracting GPMVs from cell membranes [54]. However, simply mimicking the formation of spontaneous curvature and asymmetry in model membrane systems is not sufficient for gaining a quantitative understanding of membrane curvature generation, and therefore we discuss in the following how bio-manipulation tools allow for extended investigation of membrane shapes.

Optical bio-manipulation tools have been essential for quantitative investigation of membrane shapes in the above-mentioned model systems. An interesting aspect of membrane remodeling and curvature generation is

Emerging Topics in Life Sciences (2023) **7** 81–93
https://doi.org/10.1042/ETLS20220078

the presence of free membrane edges. Such free edges can be examined using stacked SLBs [55] or using high precision thermoplasmonics to puncture 3D membranes, as shown in Figure 6A, which allows membrane edges to be studied both in GUVs and in live cells [56].These new systems have not been extensively used yet, but have shown how annexin proteins exhibit a curvature-generating effect and result in rolling of membranes [55,56]. Another technique which has been extensively used to generate high curvature membranes, is the use of optical tweezers to extract nanotubes (Figure 6B). Such nanotubes can, with the use of aspiration, be tuned to specific thicknesses by changing the tension in the membrane. This assay has therefore not only proven useful in examining simple curvature sorting or membrane associated proteins linked to membrane remodeling processes [13], but also specifically to quantify the curvature sorting in relation to minute changes in the nanotube radius or membrane curvature [12]. In addition, the nanotubes function as a platform for investigation of extended biological phenomena such as protein scaffolding and phase separation of curvature sensitive molecules [16,57,58].

Recent methods are now demonstrating how to induce curvature in cellular membranes via clever cell surface manipulation. It was recently demonstrated how cells can obtain various morphologies depending on the density of mucin bio-polymers on the surface [60], a study which elegantly showed how protein–protein crowding experiments previously conducted in GUVs [9,61] could be extended to living cells. Complementary to such experiments, focusing on extracellular membrane budding, nanostructured substrates provide an

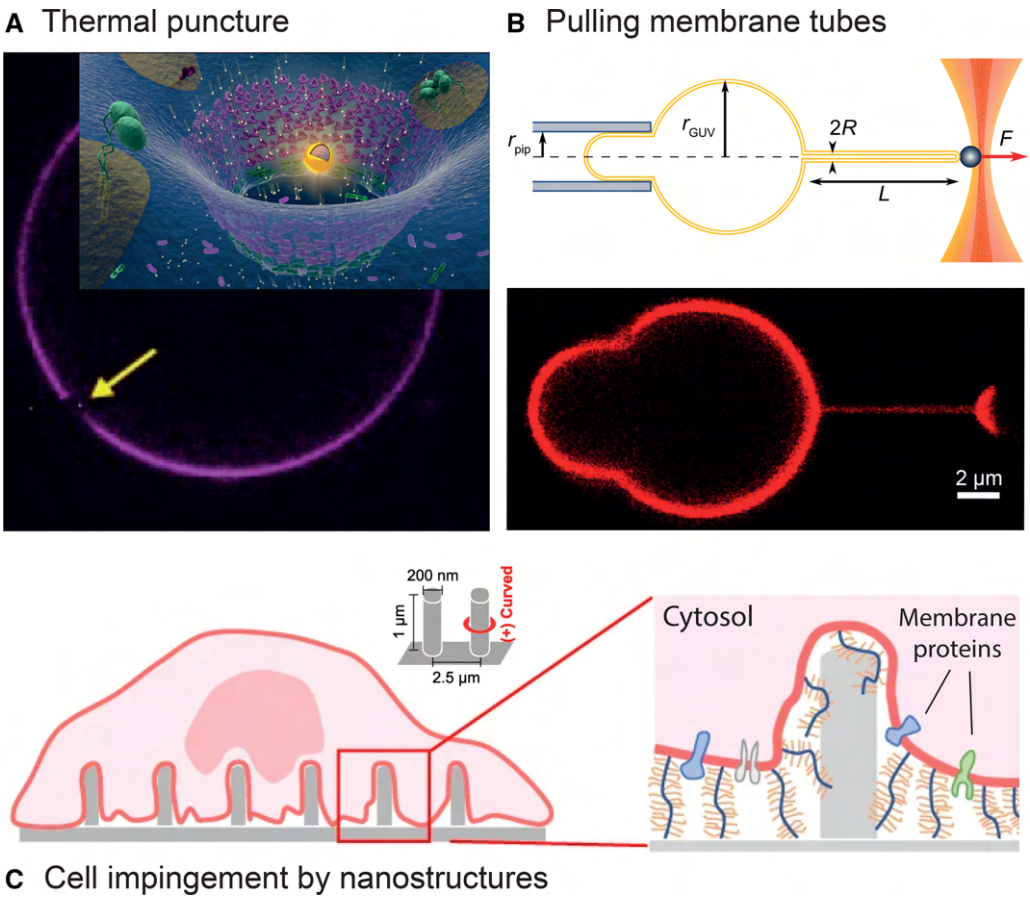

Figure 6. An advanced bio-manipulation toolbox drives research on membrane shaping mechanisms.
(**A**) Nanoscopic puncturing of a GUV using thermoplasmonic heating, creates membrane edge for investigating membrane remodeling processes at injury sites. Adapted from [56]. (**B**) Nanotubes pulled from a GUV with optical tweezers creates a platform for direct membrane probing and examination of curvature sorting of proteins. Reprinted from [59]. (**C**) Nanostructures creating curvatures by direct impingement of the cell membrane allows for in vivo investigations of protein dynamics in relation to membrane asymmetry. Adapted from [14].

excellent platform for investigation of intracellular membrane curvature effects. Such substrates have been developed to display a range of structures such as disks, spheres, rods, etc. [14,48]. Plating of living cells on such structures allows investigation of how intracellular proteins bind to membranes which are forced to wrap around these surface structures (Figure 6C). The combination of this assay with new development in protein expression, protein labeling, and fluorescent super-resolution microscopy opens up a unique door to explore protein dynamics in the intracellular environment of living cells.

The advances are not only concerning the development of model membranes and forced curvature generation, but also concerning the ways we can image and quantify membrane shapes and the physical forces driving membrane remodeling. Advanced imaging techniques, such as electron tomography and live cell imaging with super-resolution nanoscopy, have provided molecular scale information about the structure of cellular membranes. Stimulated emission by depletion (STED) microscopy can now be used to determine membrane tension without the need for invasive probing characteristic of other methods [62]. FRET imaging has recently been employed to detect changes in steric pressure at membrane surfaces, an important measure for membrane asymmetry effects [63]. In addition, a variety of crystallography techniques and cryo-EM have even provided insights into the atomistic details of membrane-shaping biomolecules [64,65]. The field is now heading toward combining all these new information to understand the shapes of membranes on all scales.

Theoretical models have also contributed eminently to our understanding of membrane shape at multiple scales. At large scales, theoretical calculations of membrane shape based on elastic energy (in particular Helfrich energy function), have provided (often) quantitative understanding of possible configurations of simple lipid bilayers that have been used for a qualitative description of cellular membrane shape [19,66,67]. At the molecular scale, concepts, such as the lipid shape model, wedging (insertion of amphipathic or hydrophobic domains), crowding (entropic repulsion between soluble domains), and scaffolding have provided a qualitative understanding of the mechanism that controls local membrane shape [27]. Additionally, curvature instability, membrane-mediated interactions, and even liquid order and liquid disorder phase coexistence have theoretical roots [29,68,69]. The rapid increase in computer power has enabled theoretical analyses of membrane organizations to take advantage of powerful numerical approaches to solve complex problems. These techniques are now developed to the point where a whole new field of study has emerged; computer simulation [70,71].

Computer simulations use theoretical models to describe the interactions between basic units, such as atoms, particles, or surface elements, and use computer power to evolve the configurations of complex systems. These techniques have been remarkably effective for exploring membrane shape remodeling at distinct scales [70–72]. Exciting examples include unraveling local membrane bending by protein complexes via atomistic and coarse-grained simulations, and protein clustering and the formation of large-scale membrane deformations by the cooperative action of proteins using mesoscopic simulations [32,33,73]. The field is now heading toward connecting distinct methods (multiscaling), to enable the modeling of realistic membranes with a full complexity at the level of cells and cell organelles [72,74]. Multiscale schemes are particularly important to bridge the gap between high-resolution simulations, which are often conducted on small system sizes, and their experimental counterparts. In the near future, we could expect highly sophisticated multiscaling methods, in particular, by adopting graphic processing computational algorithm and data driven methods [74–77]. Nevertheless, there are still several basic challenges that remain to be addressed. To name a few, atomistic and near atomistic simulations (for the major part) still relay on the simulation of segments of membranes by using periodic boundary conditions. This is, in particular, problematic for simulating asymmetric membranes [68] as for instance, in a closed membrane, where unequal stress could be released by membrane bending. While in a periodic boundary membrane, the periodicity, for small membrane bending, enforce the total membrane curvature to be zero. Another important challenge is how to extract bending capacity of membrane proteins, i.e., model parameters shown in Figure 4. Last but not least, developing a sufficiently accurate force field is still challenging. During the past few decades, state-of-the-art force fields have improved their ability to reproduce both single molecule conformations and certain collective behaviors, e.g., phase behaviors [78–80]. However, it is not clear whether the bending response of simulated membranes is equivalent to that of their experimental counterparts. For example, in both simulation and experiment, membrane bending rigidity is often determined by analyzing membrane shape fluctuations. Bending rigidity in the membrane shape fluctuations spectrum is a re-normalized quantity and changes mildly with system size which differs in simulations and experiments [31,81].

Emerging Topics in Life Sciences (2023) **7** 81–93
https://doi.org/10.1042/ETLS20220078

Outlook

The shape of fluid lipid membranes has been extensively explored experimentally, theoretically, and through computer simulations. While exciting results have been obtained, many challenges remain in order to obtain a more complete understanding of how the complex shapes of cell membranes emerge.

We should note, for example, that most of our understanding is based on the assumption that lipid membranes have a spherical topology, and our understanding of membranes of higher genera remains extremely limited. Cellular membranes, particularly those of organelles, including mitochondria and the Golgi apparatus, exhibit high genus topological shapes (topological genus g is a measure of how many handles are attached to a sphere) [72,82]. Furthermore, living cell membranes are dynamic, highly affected, and driven by non-equilibrium processes, which may result in steady-state configurations that are far from equilibrium. However, it is not fully established how non-equilibrium processes affect membrane shape, and how such structures can be characterized and modeled [83,84]. Last but not least, many proteins, especially intrinsically disordered proteins, are not randomly dispersed in the cytoplasm but are found in membrane-less organelles, commonly known as biomolecular condensates. Often, these droplets interact with cellular membranes, and we have only recently realized their significance in shaping biomembranes [85–88].

Advances in computer simulation and experimental techniques will undoubtedly provide exciting results on membrane shapes in the coming year. However, there are major bottlenecks we need to overcome. On the computational side, while the inner elements of each technique need improvement, better techniques and tools (multiscaling schemes) to reach a higher level of spatiotemporal scales and, in particular, to include the effect of molecular activities and non-equilibrium processes, must be developed. Experimentally new platforms need to be developed in which the smallest shapes can be resolved in both time and space, ideally with molecular resolution. On the imaging side new systems which combine the strengths of two different types of super-resolution imaging techniques STED and STORM (stochastic optical reconstruction microscopy) have very recently shown unprecedented fluorescent imaging with near atomic scale resolution [89]. STED microscopy has also been combined with fluorescence correlation microscopy (FCS) to allow quantification of nanoscale dynamics of molecules in membranes at high temporal resolution [90]. New reconstitution assays also need to be invented which can be used to model the intracellular systems mimicking the Golgi and ER exhibiting a wealth of complex membrane shapes. We envision that the new progress in experiments and simulations will together be able to link the molecular origin leading to different membrane shapes.

Summary

- Mesoscale, a length scale in the range of 5–100 nm, is essential for our understanding of cellular membrane shapes.
- Describing the interaction of proteins with membranes purely in terms of local membrane curvature is incomplete.
- Membrane remodeling mechanisms must be considered as a collective phenomenon.

Competing Interests

The authors declare that there are no competing interests associated with the manuscript.

Funding

W.P. acknowledges funding from the Novo Nordisk Foundation (grant no. NNF18SA0035142) and INTERACTIONS, Marie Skłodowska-Curie grant agreement no. 847523. V.T.R. and P.M.B. acknowledge funding from Novo Nordisk Foundation (grant no. NNF20OC0065357).

Abbreviations

GPMVs, giant plasma membrane vesicles; GUVs, giant unilamellar vesicles; SLB, supported lipid bilayers.

References

1 Heinrich, L., Bennett, D. and Ackerman, D. (2021) Whole-cell organelle segmentation in volume electron microscopy. *Nature* **599**, 141–146 https://doi.org/10.1038/s41586-021-03977-3
2 Valdinocci, D., Simões, R.F., Kovarova, J., Cunha-Oliveira, T., Neuzil, J. and Pountney, D.L. (2019) Intracellular and intercellular mitochondrial dynamics in Parkinson's disease. *Front. Neurosci.* **13**, 930 https://doi.org/10.3389/fnins.2019.00930
3 Perkins, H.T. and Allan, V. (2021) Intertwined and finely balanced: endoplasmic reticulum morphology, dynamics, function, and diseases. *Cells* **10**, 2341 https://doi.org/10.3390/cells10092341
4 Aguilar, M., Bassereau, P., Bastos, M., Beales, P., Bechinger, B. and Bonev, B. et al. (2021) Peptide–membrane interactions and biotechnology; enabling next-generation synthetic biology: general discussion. *Faraday Discuss.* **232**, 463–481 https://doi.org/10.1039/D1FD90068D
5 Cheney, P.P., Weisgerber, A.W., Feuerbach, A.M. and Knowles, M.K. (2017) Single lipid molecule dynamics on supported lipid bilayers with membrane curvature. *Membranes* **7**, 15 https://doi.org/10.3390/membranes7010015
6 Dasgupta, R., Miettinen, M.S., Fricke, N., Lipowsky, R. and Dimova, R. (2018) The glycolipid GM1 reshapes asymmetric biomembranes and giant vesicles by curvature generation. *Proc. Natl Acad. Sci. U.S.A.* **115**, 5756–5761 https://doi.org/10.1073/pnas.1722320115
7 Steinkühler, J., Tillieux, P., Knorr, R.L., Lipowsky, R. and Dimova, R. (2018) Charged giant unilamellar vesicles prepared by electroformation exhibit nanotubes and transbilayer lipid asymmetry. *Sci. Rep.* **8**, 11838 https://doi.org/10.1038/s41598-018-30286-z
8 Jarin, Z., Tsai, F.C., Davtyan, A., Pak, A.J., Bassereau, P. and Voth, G.A. (2019) Unusual organization of I-BAR proteins on tubular and vesicular membranes. *Biophys. J.* **117**, 553–562 https://doi.org/10.1016/j.bpj.2019.06.025
9 Snead, W.T., Hayden, C.C., Gadok, A.K., Zhao, C., Lafer, E.M. and Rangamani, P. et al. (2017) Membrane fission by protein crowding. *Proc. Natl Acad. Sci. U.S.A.* **114**, E3258–E3267 https://doi.org/10.1073/pnas.1616199114
10 Chen, Z., Shi, Z. and Baumgart, T. (2015) Regulation of membrane-shape transitions induced by I-BAR domains. *Biophys. J.* **109**, 298–307 https://doi.org/10.1016/j.bpj.2015.06.010
11 Bendix, P.M., Simonsen, A.C., Florentsen, C.D., Häger, S.C., Mularski, A. and Zanjani, A.A.H. et al. (2020) Interdisciplinary synergy to reveal mechanisms of annexin-mediated plasma membrane shaping and repair. *Cells* **9**, 1029 https://doi.org/10.3390/cells9041029
12 Dharan, R., Goren, S., Cheppali, S.K., Shendrik, P., Brand, G. and Vaknin, A. et al. (2022) Transmembrane proteins tetraspanin 4 and CD9 sense membrane curvature. *Proc. Natl Acad. Sci. U.S.A.* **119**, e2208993119 https://doi.org/10.1073/pnas.2208993119
13 Florentsen, C.D., Kamp-Sonne, A., Moreno-Pescador, G., Pezeshkian, W., Zanjani, A.A.H. and Khandelia, H. et al. (2021) Annexin A4 trimers are recruited by high membrane curvatures in giant plasma membrane vesicles. *Soft Matter* **17**, 308–318 https://doi.org/10.1039/D0SM00241K
14 Lu, C.H., Pedram, K., Tsai, C.T., Jones, T., Li, X. and Nakamoto, M.L. et al. (2022) Membrane curvature regulates the spatial distribution of bulky glycoproteins. *Nat. Commun.* **13**, 3093 https://doi.org/10.1038/s41467-022-30610-2
15 Beltrán-Heredia, E., Tsai, F.C., S. Salinas-Almaguer, Cao, F.J., Bassereau, P. and Monroy, F. (2019) Membrane curvature induces cardiolipin sorting. *Commun. Biol.* **2**, 1–7 https://doi.org/10.1038/s42003-019-0471-x
16 Sorre, B., A. Callan-Jones, Manneville, J.B., Nassoy, P., Joanny, J.F. and Prost, J. et al. (2009) Curvature-driven lipid sorting needs proximity to a demixing point and is aided by proteins. *Proc. Natl Acad. Sci. U.S.A.* **106**, 5622–5626 https://doi.org/10.1073/pnas.0811243106
17 Hossein, A. and Deserno, M. (2021) Stiffening transition in asymmetric lipid bilayers: the role of highly ordered domains and the effect of temperature and size. *J. Chem. Phys.* **154**, 014704 https://doi.org/10.1063/5.0028255
18 Courtney, K.C., Pezeshkian, W., Raghupathy, R., Zhang, C., Darbyson, A. and Ipsen, J.H. et al. (2018) C24 sphingolipids govern the transbilayer asymmetry of cholesterol and lateral organization of model and live-cell plasma membranes. *Cell Rep.* **24**, 1037–1049 https://doi.org/10.1016/j.celrep.2018.06.104
19 Lipowsky, R. (2022) Multispherical shapes of vesicles highlight the curvature elasticity of biomembranes. *Adv. Colloid Interface Sci.* **301**, 102613 https://doi.org/10.1016/j.cis.2022.102613
20 Lorent, J.H., Levental, K.R., Ganesan, L., G. Rivera-Longsworth, Sezgin, E. and Doktorova, M. et al. (2020) Plasma membranes are asymmetric in lipid unsaturation, packing and protein shape. *Nat. Chem. Biol.* **16**, 644–652 https://doi.org/10.1038/s41589-020-0529-6
21 Paul, Q., Griffiths, G. and Warren, G. (1984) Density of newly synthesized plasma membrane proteins in intracellular membranes II. Biochemical studies. *J. Cell Biol.* **98**, 2142–2147 https://doi.org/10.1083/jcb.98.6.2142
22 Johannes, L., Pezeshkian, W., Ipsen, J.H. and Shillcock, J.C. (2018) Clustering on membranes: fluctuations and more. *Trends Cell Biol.* **28**, 405–415 https://doi.org/10.1016/j.tcb.2018.01.009
23 Ghosh, R., Satarifard, V., A. Grafmüller and Lipowsky, R. (2021) Budding and fission of nanovesicles induced by membrane adsorption of small solutes. *ACS Nano* **15**, 7237–7248 https://doi.org/10.1021/acsnano.1c00525
24 Fiorin, G., Marinelli, F. and J.D. Faraldo-Gómez (2020) Direct derivation of free energies of membrane deformation and other solvent density variations from enhanced sampling molecular dynamics. *J. Comput. Chem.* **41**, 449–459 https://doi.org/10.1002/jcc.v41.5
25 Ghosh, R., Satarifard, V., A. Grafmüller and Lipowsky, R. (2019) Spherical nanovesicles transform into a multitude of nonspherical shapes. *Nano Lett.* **19**, 7703–7711 https://doi.org/10.1021/acs.nanolett.9b02646
26 Lipowsky, R. and Dimova, R. (2021) Introduction to remodeling of biomembranes. *Soft Matter* **17**, 214–221 https://doi.org/10.1039/D0SM90234A
27 Kozlov, M.M. and Taraska, J.W. (2022) Generation of nanoscopic membrane curvature for membrane trafficking. *Nat. Rev. Mol. Cell Biol.* **24**, 63–78 https://doi.org/10.1038/s41580-022-00511-9
28 Has, C. and Das, S.L. (2021) Recent developments in membrane curvature sensing and induction by proteins. *Biochim. Biophys. Acta* **1865**, 129971 https://doi.org/10.1016/j.bbagen.2021.129971
29 Pezeshkian, W. and Ipsen, J.H. (2019) Fluctuations and conformational stability of a membrane patch with curvature inducing inclusions. *Soft Matter* **15**, 9974–9981 https://doi.org/10.1039/C9SM01762C
30 Leibler, S. (1986) Curvature instability in membranes. *J. Phys.* **47**, 507–516 https://doi.org/10.1051/jphys:01986004703050700
31 Pezeshkian, W. and Ipsen, J.H. (2021) Creasing of flexible membranes at vanishing tension. *Phys. Rev. E* **103**, L041001 https://doi.org/10.1103/PhysRevE.103.L041001
32 Pezeshkian, W., L.J. Nåbo and Ipsen, J.H. (2017) Cholera toxin B subunit induces local curvature on lipid bilayers. *FEBS Open Bio* **7**, 1638–1645 https://doi.org/https://doi.ord/10.1002/2211-5463.12321

33 Sadeghi, M. and F. Noé (2021) Thermodynamics and kinetics of aggregation of flexible peripheral membrane proteins. *J. Phys. Chem. Lett.* **12**, 10497–10504 https://doi.org/10.1021/acs.jpclett.1c02954
34 Pezeshkian, W., Gao, H., Arumugam, S., Becken, U., Bassereau, P. and Florent, J.C. et al. (2017) Mechanism of shiga toxin clustering on membranes. *ACS Nano* **11**, 314–324 https://doi.org/10.1021/acsnano.6b05706
35 E. Alizadeh-Haghighi, A. Karaei Shiraz and Bahrami, A.H. (2022) Membrane-mediated interactions between disk-like inclusions adsorbed on vesicles. *Front. Phys.* **10** https://doi.org/10.3389/fphy.2022.1020619
36 Jarin, Z., Pak, A.J., Bassereau, P. and Voth, G.A. (2021) Lipid-composition-mediated forces can stabilize tubular assemblies of I-BAR proteins. *Biophys. J.* **120**, 46–54 https://doi.org/10.1016/j.bpj.2020.11.019
37 N. De Franceschi, Pezeshkian, W., Fragasso, A., Bruininks, B.M.H., Tsai, S. and Marrink, S.J. et al. (2022) Synthetic membrane shaper for controlled liposome deformation. *ACS Nano* https://doi.org/10.1021/acsnano.2c06125
38 Kumar, G., Ramakrishnan, N. and Sain, A. (2019) Tubulation pattern of membrane vesicles coated with biofilaments. *Phys. Rev. E* **99**, 022414 https://doi.org/10.1103/PhysRevE.99.022414
39 Kwiecinski, J.A., Goriely, A. and Chapman, S.J. (2020) Interactions of anisotropic inclusions on a fluid membrane. *SIAM J. Appl. Math.* **80**, 2448–2471 https://doi.org/10.1137/20M1332694
40 Schmidt, N.W., Mishra, A., Wang, J., DeGrado, W.F. and Wong, G.C.L. (2013) Influenza virus A M2 protein generates negative gaussian membrane curvature necessary for budding and scission. *J. Am. Chem. Soc.* **135**, 13710–13719 https://doi.org/10.1021/ja400146z
41 Rossman, J.S., Jing, X.H., Leser, G.P. and Lamb, R.A. (2010) Influenza virus M2 protein mediates ESCRT-independent membrane scission. *Cell* **142**, 902–913 https://doi.org/10.1016/j.cell.2010.08.029
42 Heinrich, M., Tian, A., Esposito, C. and Baumgart, T. (2010) Dynamic sorting of lipids and proteins in membrane tubes with a moving phase boundary. *Proc. Natl Acad. Sci. U.S.A.* **107**, 7208–7213 https://doi.org/10.1073/pnas.0913997107
43 Karlsen, M.L., Bruhn, D.S., Pezeshkian, W. and Khandelia, H. (2021) Long chain sphingomyelin depletes cholesterol from the cytoplasmic leaflet in asymmetric lipid membranes. *RSC Adv.* **11**, 22677–22682 https://doi.org/10.1039/D1RA01464A
44 Allender, D.W., Sodt, A.J. and Schick, M. (2019) Cholesterol-dependent bending energy is important in cholesterol distribution of the plasma membrane. *Biophys. J.* **116**, 2356–2366 https://doi.org/10.1016/j.bpj.2019.03.028
45 Steck, T.L. and Lange, Y. (2018) Transverse distribution of plasma membrane bilayer cholesterol: picking sides. *Traffic* **19**, 750–760 https://doi.org/10.1111/tra.2018.19.issue-10
46 Elani, Y., Purushothaman, S., Booth, P.J., Seddon, J.M., Brooks, N.J. and Law, R.V. et al. (2015) Measurements of the effect of membrane asymmetry on the mechanical properties of lipid bilayers. *Chem. Commun.* **51**, 6976–6979 https://doi.org/10.1039/C5CC00712G
47 Sreekumari, A. and Lipowsky, R. (2022) Large stress asymmetries of lipid bilayers and nanovesicles generate lipid flip-flops and bilayer instabilities. *Soft Matter* **18**, 6066–6078 https://doi.org/10.1039/D2SM00618A
48 Zhao, W., Hanson, L., Lou, H.Y., Akamatsu, M., Chowdary, P.D. and Santoro, F. et al. (2017) Nanoscale manipulation of membrane curvature for probing endocytosis in live cells. *Nat. Nanotechnol.* **12**, 750–756 https://doi.org/10.1038/nnano.2017.98
49 Karimi, M., J. Steinkühler, Roy, D., Dasgupta, R., Lipowsky, R. and Dimova, R. (2018) Asymmetric ionic conditions generate large membrane curvatures. *Nano Lett.* **18**, 7816–7821 https://doi.org/10.1021/acs.nanolett.8b03584
50 Shi, Z. and T. Tobias Baumgart (2015) Membrane tension and peripheral protein density mediate membrane shape transitions. *Nat. Commun.* **6**, 5974 https://doi.org/10.1038/ncomms6974
51 Sezgin, E., Kaiser, H.J., Baumgart, T., Schwille, P., Simons, K. and Levental, I. (2012) Elucidating membrane structure and protein behavior using giant plasma membrane vesicles. *Nat. Protoc.* **7**, 1042–1051 https://doi.org/10.1038/nprot.2012.059
52 G. Moreno-Pescador, Florentsen, C.D., Ostbye, H., Sonder, S.L., Boye, T.L. and Veje, E.L. et al. (2019) Curvature- and phase-induced protein sorting quantified in transfected cell-derived giant vesicles. *ACS Nano* **13**, 6689–6701 https://doi.org/10.1021/acsnano.9b01052
53 G. Moreno-Pescador, Arastoo, M.R., Chiantia, S., Daniels, R. and Bendix, P.M. (2022) Thermoplasmonic induced vesicle fusion for investigating membrane protein phase affinity. bioRxiv. Available from: https://www.biorxiv.org/content/early/2022/09/19/2022.09.19.508467
54 Sezgin, E. (2022) Giant plasma membrane vesicles to study plasma membrane structure and dynamics. *Biochim. Biophys. Acta Biomembr.* **1864**, 183857 https://doi.org/10.1016/j.bbamem.2021.183857
55 Boye, T.L., Jeppesen, J.C., Maeda, K., Pezeshkian, W., Solovyeva, V. and Nylandsted, J. et al. (2018) Annexins induce curvature on free-edge membranes displaying distinct morphologies. *Sci. Rep.* **8**, 10309 https://doi.org/10.1038/s41598-018-28481-z
56 G.S. Moreno-Pescador, Aswad, D.S., Florentsen, C.D., Bahadori, A., Arastoo, M.R. and Danielsen, H.M.D. et al. (2022) Thermoplasmonic nano-rupture of cells reveals annexin V function in plasma membrane repair. *Nanoscale* **14**, 7778–7787 https://doi.org/10.1039/D1NR08274D
57 Simunovic, M., Evergren, E., Golushko, I., C. Prévost, Renard, H.F. and Johannes, L. et al. (2016) How curvature-generating proteins build scaffolds on membrane nanotubes. *Proc. Natl Acad. Sci. U.S.A.* **113**, 11226–11231 https://doi.org/10.1073/pnas.1606943113
58 Prevost, C., Zhao, H.X., Manzi, J., Lemichez, E., Lappalainen, P. and A. Callan-Jones et al. (2015) IRSp53 senses negative membrane curvature and phase separates along membrane tubules. *Nat. Commun.* **6**, 8529 https://doi.org/10.1038/ncomms9529
59 C. Prévost, Tsai, F.C., Bassereau, P. and Simunovic, M. (2017) Pulling membrane nanotubes from giant unilamellar vesicles. *J. Vis. Exp.* **130**, e56086 https://doi.org/10.3791/56086
60 Shurer, C.R., Kuo, J.C.H., Roberts, L.M., Gandhi, J.G., Colville, M.J. and Enoki, T.A. et al. (2019) Physical principles of membrane shape regulation by the glycocalyx. *Cell* **177**, 1757–1770.e21 https://doi.org/10.1016/j.cell.2019.04.017
61 Ruhoff, V.T., G. Moreno-Pescador, Pezeshkian, W. and Bendix, P.M. (2022) Strength in numbers: effect of protein crowding on the shape of cell membranes. *Biochem. Soc. Trans.* **50**, 1257–1267 https://doi.org/10.1042/BST20210883
62 Roy, D., Steinkuhler, J., Zhao, Z.L., Lipowsky, R. and Dimova, R. (2020) Mechanical tension of biomembranes can be measured by super resolution (STED) microscopy of force-induced nanotubes. *Nano Lett.* **20**, 3185–3191 https://doi.org/10.1021/acs.nanolett.9b05232
63 Houser, J.R., Hayden, C.C., Thirumalai, D. and Stachowiak, J.C. (2020) A Forster resonance energy transfer-based sensor of steric pressure on membrane surfaces. *J. Am. Chem. Soc.* **142**, 20796–20805 https://doi.org/10.1021/jacs.0c09802
64 Frost, A., Perera, R., Roux, A., Spasov, K., Destaing, O. and Egelman, E.H. et al. (2008) Structural basis of membrane invagination by F-BAR domains. *Cell* **132**, 807–817 https://doi.org/10.1016/j.cell.2007.12.041

65 J. Moser von Filseck, Barberi, L., Talledge, N., Johnson, I.E., Frost, A. and Lenz, M. et al. (2020) Anisotropic ESCRT-III architecture governs helical membrane tube formation. *Nat. Commun.* **11**, 1–9 https://doi.org/10.1038/s41467-020-15327-4
66 Zucker, B. and Kozlov, M.M. (2022) Mechanism of shaping membrane nanostructures of endoplasmic reticulum. *Proc. Natl Acad. Sci. U.S.A.* **119**, e2116142119 https://doi.org/10.1073/pnas.2116142119
67 Al-Izzi, S.C., Sens, P. and Turner, M.S. (2020) Shear-driven instabilities of membrane tubes and dynamin-induced scission. *Phys. Rev. Lett.* **125**, 018101 https://doi.org/10.1103/PhysRevLett.125.018101
68 Haussman, R.C. and Deserno, M. (2014) Effective field theory of thermal Casimir interactions between anisotropic particles. *Phys. Rev. E* **89**, 062102 https://doi.org/10.1103/PhysRevE.89.062102
69 Gao, J., Hou, R., Li, L. and Hu, J. (2021) Membrane-mediated interactions between protein inclusions. *Front. Mol. Biosci.* **8**, 811711 https://doi.org/10.3389/fmolb.2021.811711
70 Marrink, S.J., Corradi, V., Souza, P.C.T., H.I. Ingólfsson, Tieleman, D.P. and Sansom, M.S.P. (2019) Computational modeling of realistic cell membranes. *Chem. Rev.* **119**, 6184–6226 https://doi.org/10.1021/acs.chemrev.8b00460
71 Enkavi, G., Javanainen, M., Kulig, W., T. Róg and Vattulainen, I. (2019) Multiscale simulations of biological membranes: the challenge to understand biological phenomena in a living substance. *Chem. Rev.* **119**, 5607–5774 https://doi.org/10.1021/acs.chemrev.8b00538
72 Pezeshkian, W. and Marrink, S.J. (2021) Simulating realistic membrane shapes. *Curr. Opin. Cell Biol.* **71**, 103–111 https://doi.org/10.1016/j.ceb.2021.02.009
73 Mandal, T., Lough, W., Spagnolie, S.E., Audhya, A. and Cui, Q. (2020) Molecular simulation of mechanical properties and membrane activities of the ESCRT-III complexes. *Biophys. J.* **118**, 1333–1343 https://doi.org/10.1016/j.bpj.2020.01.033
74 Pezeshkian, W., M. König, Wassenaar, T.A. and Marrink, S.J. (2020) Backmapping triangulated surfaces to coarse-grained membrane models. *Nat. Commun.* **11**, 2296 https://doi.org/10.1038/s41467-020-16094-y
75 Lee, C.T., Laughlin, J.G., N.A. de La Beaumelle, Amaro, R.E., McCammon, J.A. and Ramamoorthi, R. et al. (2020) 3D mesh processing using GAMer 2 to enable reaction-diffusion simulations in realistic cellular geometries. *PLoS Comput. Biol.* **6**, e1007756 https://doi.org/10.1371/journal.pcbi.1007756
76 Casalino, L., Dommer, A.C., Gaieb, Z., Barros, E.P., Sztain, T. and Ahn, S.H. et al. (2021) AI-driven multiscale simulations illuminate mechanisms of SARS-CoV-2 spike dynamics. *Int. J. High Perform. Comput. Appl.* **35**, 432–451 https://doi.org/10.1177/10943420211006452
77 H.I. Ingólfsson, Neale, C., Carpenter, T.S., Shrestha, R., C.A. López and Tran, T.H. et al. (2022) Machine learning–driven multiscale modeling reveals lipid-dependent dynamics of RAS signaling proteins. *Proc. Natl Acad. Sci. U.S.A.* **119**, e2113297119 https://doi.org/10.1073/pnas.2113297119
78 Pezeshkian, W., Khandelia, H. and Marsh, D. (2018) Lipid configurations from molecular dynamics simulations. *Biophys. J.* **114**, 1895–1907 https://doi.org/10.1016/j.bpj.2018.02.016
79 Leonard, A.N., Wang, E., V. Monje-Galvan and Klauda, J.B. (2019) Developing and testing of lipid force fields with applications to modeling cellular membranes. *Chem. Rev.* **119**, 6227–6269 https://doi.org/10.1021/acs.chemrev.8b00384
80 Souza, P.C.T., Alessandri, R. and Barnoud, J. et al. (2021) Martini 3: a general purpose force field for coarse-grained molecular dynamics. *Nat. Methods* **18**, 382–388 https://doi.org/10.1038/s41592-021-01098-3
81 Terzi, M.M. and Deserno, M. (2017) Novel tilt-curvature coupling in lipid membranes. *J. Chem. Phys.* **147**, 084702 https://doi.org/10.1063/1.4990404
82 Zucker, B., Golani, G. and Kozlov, M.M. (2022) Model for ring closure in ER tubular network dynamics. *Biophys. J.* **122**, 1–11 https://doi.org/10.1016/j.bpj.2022.10.005
83 Sachin Krishnan, T.V. and Sunil Kumar, P.B. (2022) Active membrane recycling induced morphology changes in vesicles. *Front. Phys.* **10** https://doi.org/10.3389/fphy.2022.1003558
84 Vutukuri, H.R., Hoore, M., C. Abaurrea-Velasco, L. van Buren, Dutto, A. and Auth, T. et al. (2020) Active particles induce large shape deformations in giant lipid vesicles. *Nature* **586**, 52–56 https://doi.org/10.1038/s41586-020-2730-x
85 Shillcock, J.C., Thomas, D.B., Beaumont, J.R., Bragg, G.M., Vousden, M.L. and Brown, A.D. (2022) Coupling bulk phase separation of disordered proteins to membrane domain formation in molecular simulations on a bespoke compute fabric. *Membranes* **12**, 17 https://doi.org/10.3390/membranes12010017
86 Day, K.J., Kago, G., Wang, L., Richter, J.B., Hayden, C.C. and Lafer, E.M. et al. (2021) Membrane bending by protein phase separation. *Nat. Cell Biol.* **23**, 366–376 https://doi.org/10.1038/s41556-021-00646-5
87 Case, L.B., Ditlev, J.A. and Rosen, M.K. (2019) Regulation of transmembrane signaling by phase separation. *Annu. Rev. Biophys.* **48**, 465–494 https://doi.org/10.1146/annurev-biophys-052118-115534
88 Tesei, G., Schulze, T.K., Crehuet, R. and K. Lindorff-Larsen (2021) Accurate model of liquid–liquid phase behavior of intrinsically disordered proteins from optimization of single-chain properties. *Proc. Natl Acad. Sci. U.S.A.* **118**, e2111696118 https://doi.org/10.1073/pnas.211169611
89 Gwosch, K.C., Pape, J.K., Balzarotti, F., Hoess, P., Ellenberg, J. and Ries, J. et al. (2020) MINFLUX nanoscopy delivers 3D multicolor nanometer resolution in cells. *Nat. Methods* **17**, 217–224 https://doi.org/10.1038/s41592-019-0688-0
90 Sezgin, E., Schneider, F., Galiani, S., I. Urbančič, Waithe, D. and Lagerholm, B.C. et al. (2019) Measuring nanoscale diffusion dynamics in cellular membranes with super-resolution STED-FCS. *Nat. Protoc.* **14**, 1054–1083 https://doi.org/10.1038/s41596-019-0127-9

B.4 Biological Applications of Thermoplasmonics

Authors:
Victoria Thusgaard Ruhoff, Mohammad Reza Arastoo, Guillermo Moreno-Pescador, and Poul Martin Bendix
Status: Published

NANO LETTERS

January 24, 2024
Volume 24, Number 3
pubs.acs.org/NanoLett

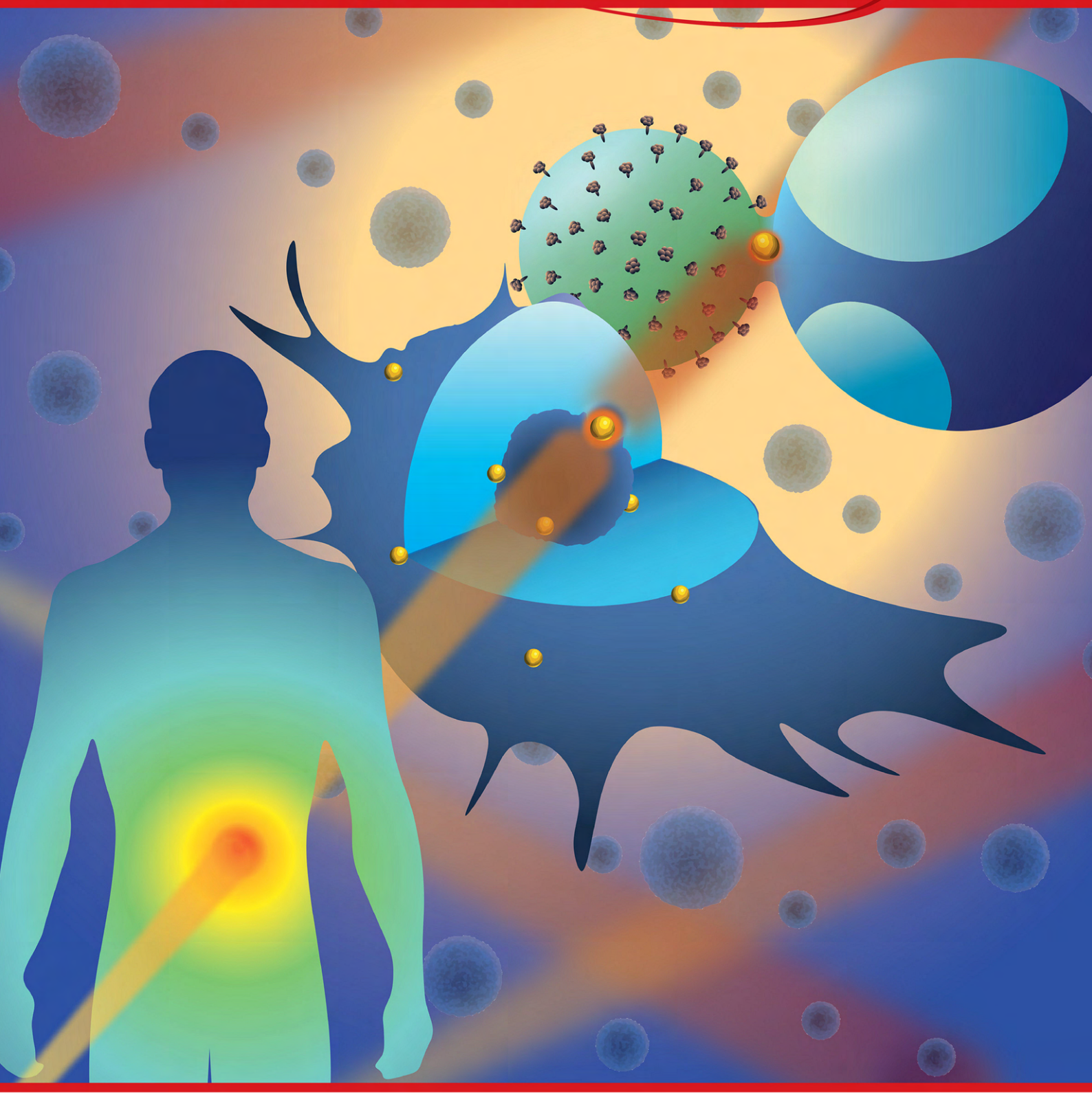

ACS Publications
Most Trusted. Most Cited. Most Read.

www.acs.org

Cover art by Victoria Thusgaard Ruhoff

NANO LETTERS

Editors' Choice
Open Access

pubs.acs.org/NanoLett

Mini-Review

Biological Applications of Thermoplasmonics

Victoria Thusgaard Ruhoff, Mohammad Reza Arastoo, Guillermo Moreno-Pescador, and Poul Martin Bendix*

Cite This: *Nano Lett.* 2024, 24, 777−789

Read Online

ACCESS | Metrics & More | Article Recommendations

ABSTRACT: Thermoplasmonics has emerged as an extraordinarily versatile tool with profound applications across various biological domains ranging from medical science to cell biology and biophysics. The key feature of nanoscale plasmonic heating involves remote activation of heating by applying laser irradiation to plasmonic nanostructures that are designed to optimally convert light into heat. This unique capability paves the way for a diverse array of applications, facilitating the exploration of critical biological processes such as cell differentiation, repair, signaling, and protein functionality, and the advancement of biosensing techniques. Of particular significance is the rapid heat cycling that can be achieved through thermoplasmonics, which has ushered in remarkable technical innovations such as accelerated amplification of DNA through quantitative reverse transcription polymerase chain reaction. Finally, medical applications of photothermal therapy have recently completed clinical trials with remarkable results in prostate cancer, which will inevitably lead to the implementation of photothermal therapy for a number of diseases in the future. Within this review, we offer a survey of the latest advancements in the burgeoning field of thermoplasmonics, with a keen emphasis on its transformative applications within the realm of biosciences.

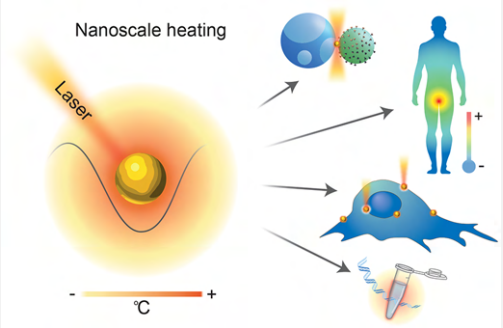

KEYWORDS: *photothermal therapy, thermoplasmonics, plasmonic heating, drug delivery, COVID detection, plasmonic PCR, membrane fusion, cell manipulation, stem cell differentiation*

The application of localized heating has unveiled remarkable potential for harnessing control over biological functions and manipulating biomaterials. Through the use of laser irradiation of nanoparticles, often made from noble metals like gold, it has become feasible to generate heat in biological samples, that is highly localized in both space and time. This kind of laser-induced heating was first considered an inadvertent thermal side effect in plasmonics-related applications, but recently, this photoinduced nanoparticle heating has found use in a range of applications in experimental research. The phenomenon, now termed thermoplasmonics or plasmonic heating, has undergone a transition into a promising new field of research that has opened up a vast number of new possible applications within various disciplines spanning chemistry, physics, biology, and medicine.

Light scattering and absorption by nanoparticles are ancient phenomena used for coloring glass paintings, but with the advent of lasers and the synthesis of precisely engineered plasmonic nanoparticles, a new world of opportunities has emerged to harness light and heating at the molecular scale. Together with the sensitivity of biomaterials to heat, thermoplasmonics will allow unprecedented manipulative control over biological processes in living cells and molecular and biomimetic systems.[1]

Thermoplasmonics can be applied for different purposes in biological systems. The local heat produced by laser-irradiated nanoparticles can activate cell sensing and has been employed to study temperature-induced changes in transmembrane potentials in neurons with consequent induction of action potentials,[2] activation of heat shock proteins (HSPs),[3] and modulation of cell differentiation.[4] These effects illustrate the potential of manipulating biological functions. In addition, thermoplasmonics allows for precise ablation at the subcellular or cellular level, which has been used for photothermal therapy in cancer[5] and investigation of cellular membrane repair to nanoscopic injuries induced by local heating in living cells.[1] This form of thermal nanosurgery has also proven to be effective in the manipulation of biomimetic systems like fusion of giant unilamellar lipid vesicles (GUVs) for studying membrane−protein interactions[6,7] or selective fusion of cancer cells with immune cells.[8] At the molecular level, thermoplas-

Received: September 15, 2023
Revised: December 15, 2023
Accepted: December 18, 2023
Published: January 6, 2024

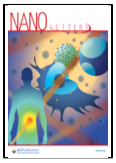

https://doi.org/10.1021/acs.nanolett.3c03548
Nano Lett. 2024, 24, 777−789

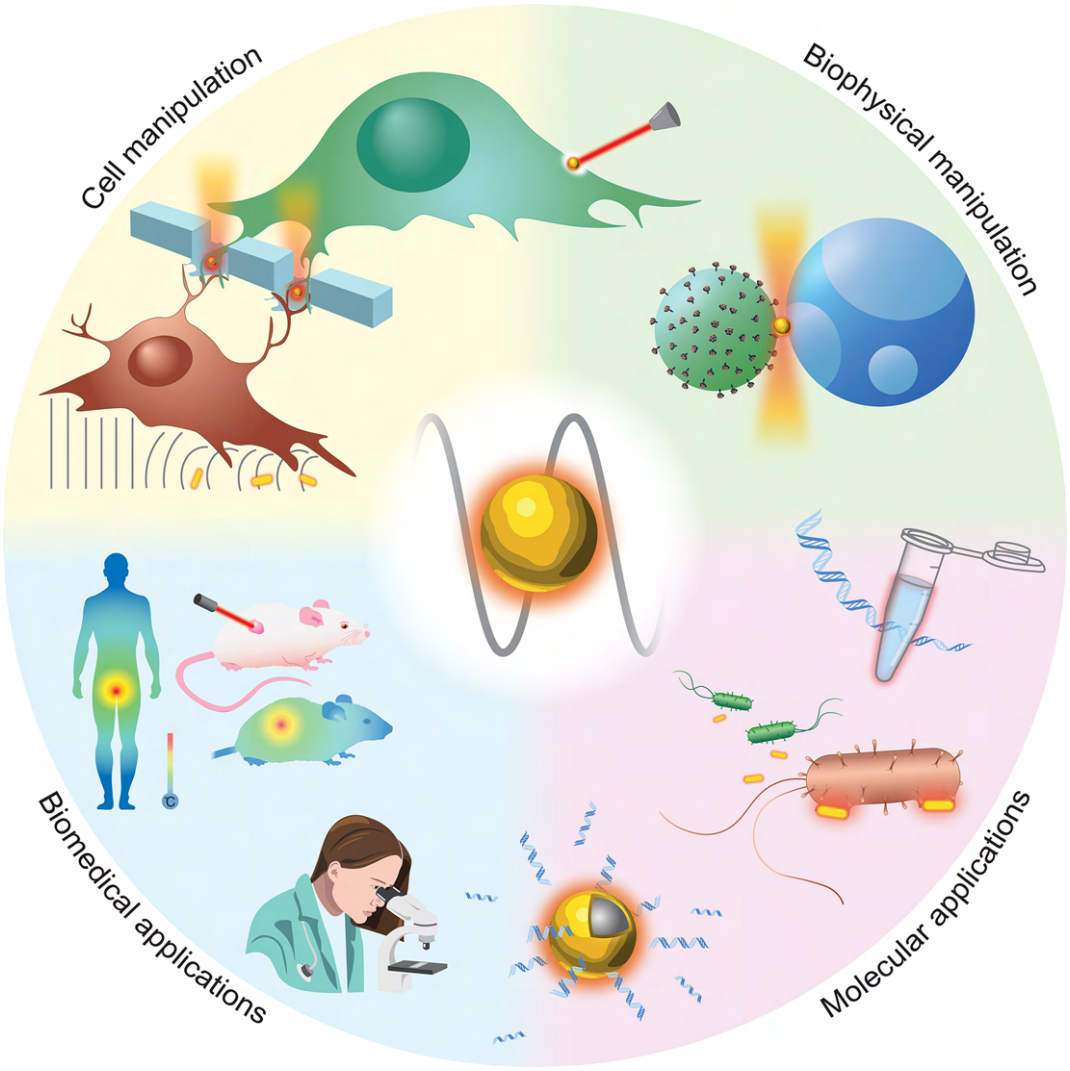

Figure 1. Applications of thermoplasmonics in four biological areas. Each shaded area is discussed as a topic in this review.

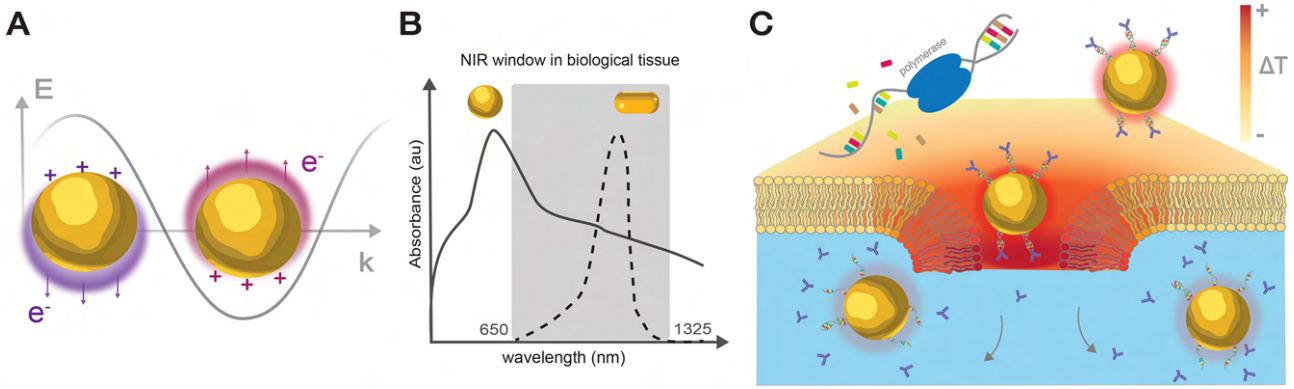

Figure 2. Plasmonic heating for biological applications. (A) Laser irradiation of plasmonic nanoparticles excites electronic oscillations in the particle, which causes heating. The heating reaches a maximum at a wavelength corresponding to the localized surface plasmon frequency of the particle. (B) Schematic of the spectra of spherical and rod-shaped gold nanoparticles showing how the peak absorption can be tuned by the shape factor to coincide with the wavelengths at which biological tissue is most transparent (shaded region). (C) Local heating for molecular and supramolecular applications. Here, heating of AuNPs results in membrane perforation, release of conjugated antibodies, and polymerase activation for usage in ultrafast PCR.

monics can be used to study and enhance biological processes. Localized heating shows promise in investigations of protein denaturation effects and thermal control of the hybridization of RNA and DNA nucleotides.[9] These molecular-level manipu-

https://doi.org/10.1021/acs.nanolett.3c03548
Nano Lett. 2024, 24, 777−789

lations have found applications in drug delivery and other therapeutic strategies.

The concept of thermoplasmonics has been seamlessly integrated into many fields of science. We refer the interested reader to comprehensive reviews on plasmonics with a particular focus on thermoplasmonics in chemistry and physics.[10−15] Here we will first provide a brief introduction to optical heating of plasmonic nanoparticles followed by important and recent applications of thermoplasmonics in several areas of science, as highlighted in Figure 1, with a focus on cellular, biophysical, molecular, and biomedical applications, including photothermal therapy and drug delivery.

Surface plasmon resonances occur when light excites the free electrons on the surface of a metallic material, leading to collective electronic oscillations and charge displacements. In the case of nanoparticles (Figure 2A), this excitation leads to so-called localized plasmon resonance when the free electrons in the metal are spatially confined. When a small spherical metallic nanoparticle is irradiated by light, the oscillating electric field causes the conduction electrons to oscillate coherently, leading to an oscillating charge dipole that resonates with specific wavelengths determined by the particle shape, size, and material property. The absorption of incoming light increases significantly at this resonance, and substantial heat can be generated at the resonance due to the thermal relaxation of the oscillating electron cloud. This property of metallic nanoparticles to convert light to heat is what has generally been termed thermoplasmonics or plasmonic heating. The optical response of a nanoparticle to light can be described through its extinction cross section (C_{ext}), which is defined as the sum of scattering and absorption cross sections ($C_{ext} = C_{abs} + C_{scat}$).

The extinction cross section of a nanoparticle embedded in a dielectric medium with permittivity ε_m and irradiated at wavelength λ can be described by the optical theorem as[16]

$$C_{ext} = \kappa \, \mathrm{Im}(\alpha) \tag{1}$$

where the wavenumber is $\kappa = 2\pi\sqrt{\varepsilon_m}/\lambda$ and for small particle sizes (compared to the wavelength of light used) the scattering is negligible, and we find that the absorption that equals the extinction cross section can be approximated as

$$C_{abs} \approx \kappa \, \mathrm{Im}(\alpha) \tag{2}$$

Polarizability α for spherical particles that are small compared to the wavelength of light is given by

$$\alpha = 3V\frac{\varepsilon(\omega) - \varepsilon_m}{\varepsilon(\omega) + \phi\varepsilon_m} \tag{3}$$

where V is the volume of the particle, ε_m is the dielectric permittivity of the medium, ε is the dielectric permittivity of the particle at frequency ω, and ϕ is a shape-dependent parameter[17] that for a sphere equals 2.

On the basis of the latter, it is apparent that the localized surface plasmon resonance (i.e., maximum absorption and scattering cross section of the particle) can be tuned on the basis of the shape, size, and composition of the nanoparticle. All of these parameters are being extensively explored by researchers and have led to novel particle designs (shells, rods, stars, cubes, etc.) with peak absorption at specific wavelengths extending into the near-infrared region where biological materials exhibit minimum absorption.

By solving the heat transfer equation,[18] we can calculate the temperature increase in the vicinity of an irradiated nanoparticle through the relation[19]

$$\Delta T(r) = \frac{I}{4\pi K r}C_{abs} \tag{4}$$

This expression is valid for only small nanoparticles. C_{abs} is the absorption cross section from eq 2, which is defined as the ratio between the power absorbed by the particles and the total incoming laser intensity (power per area). I is the laser intensity on the particle, r the distance from the center of the particle, and K the thermal conductivity of the medium in which the particle is suspended. C_{abs} is given above for small particles, but for larger particle having a spherical shape, the absorption cross section can be found using Mie's solutions to the Maxwell equations.[19] For nonspherical particles, the optical cross sections are calculated by using finite-element modeling, which allows the absorption cross section to be computed for any particle shape that has been demonstrated for a number of particle types.[12]

Due to the large diversity of commercially available plasmonic nanoparticles, including gold nanoparticles (AuNPs), gold nanoshells (AuNSs), nanomatryoshkas, nanostars, nanorods, and many more, it is now possible to choose nanoparticles with a large absorption cross section at practically any wavelength in the optical and near-infrared (NIR) regime (Figure 2B). Other materials used in optical heating applications include platinum[20] and titanium,[21] which have shown great photothermal effects, and nanoparticles made from platinum have also been successfully trapped using optical tweezers.[22] The heating effect of a nanoparticle is highly localized to the vicinity of the particle (Figure 2C), rendering the thermoplasmonic effect of nanoparticles as an extremely versatile and adaptable tool for diverse biological applications,[23] as we will discuss below.

It should be noted here that nanoscale heating exceeding ∼240 °C can result in gas bubbles on the particle surface, which drastically changes the heating. Such bubbles have size-dependent lifetimes that are analytically solved in ref 24.

Moreover, we note that collective effects can occur through plasmonic coupling between two particles or a lattice of many particles. This can broaden the parameters of the thermoplasmonic effect. It has been shown recently for thermoplasmonic applications that when identical nanoparticles are arranged in a periodic array, they can support collective modes known as lattice resonances.[25] These resonances produce a much larger temperature increase per particle than for arrays that do not support resonance conditions, and their absorption peak can be tuned to wavelengths where the single nanoparticles cannot.

In the following, we will discuss a number of important applications in thermoplasmonics in which such nanoparticles have been used to answer biological questions and as a tool for the manipulation of biological matter. Most applications to date have used nanoshells and nanorods that can be tuned with respect to absorption resonance wavelengths and hence can also be used in the near-infrared region, but the exploration of new types of particles is an active area of research.

The combination of optical trapping and heating of plasmonic nanoparticles has recently shown great potential in applications, such as the study of protein biophysics. In particular, for the study of interactions of proteins with membranes, thermoplasmonics has offered a unique way to

https://doi.org/10.1021/acs.nanolett.3c03548
Nano Lett. 2024, 24, 777−789

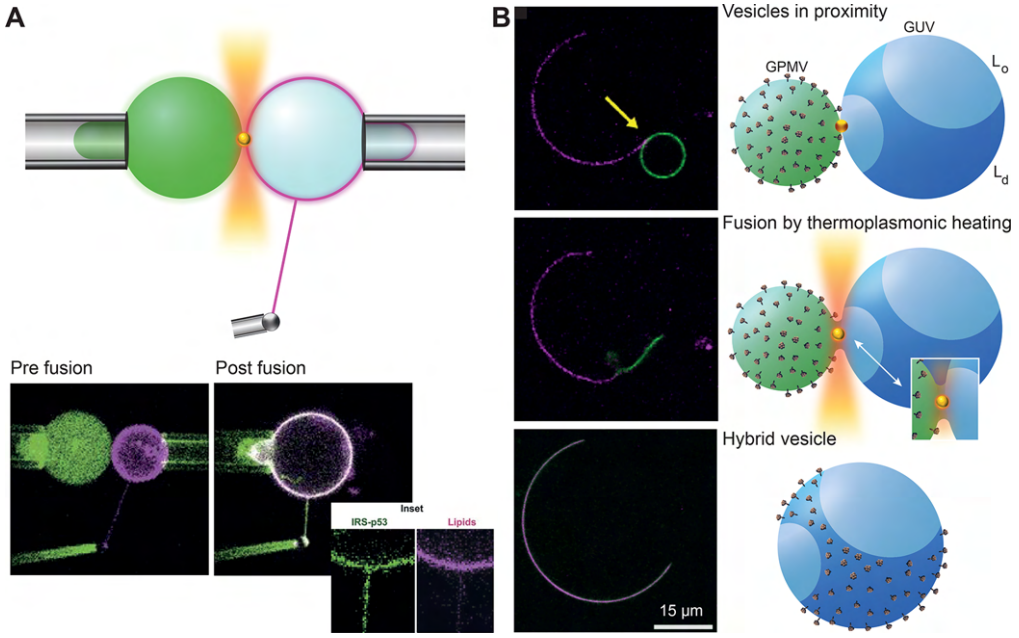

Figure 3. Thermoplasmonically induced remodeling of biomembranes for studying protein dynamics. (A) Via the combination of aspiration using micropipettes with optical trapping of plasmonic nanoparticles, it is possible to fuse two vesicles by locally heating the contact point between the apposing membranes. The bottom panels show an example in which a giant unilamellar lipid vesicle (GUV), containing the I-BAR protein domain of IRSp53 (green) in the lumen, is fused to another GUV that is composed of anionic lipids. The fused vesicle thereby contains anionic lipids that facilitate binding of IRSp53. The bottom right inset shows membrane curvature sensing of IRSp53 within a nanotube pulled from the hybrid GUV. Panel A was adapted with permission from ref 7. Copyright 2019 The Company of Biologists Publishing. (B) Fusion can also be achieved between vesicles resting on a surface, as shown here where a giant plasma membrane vesicle (GPMV) and a GUV are fused to investigate the phase affinity of integral membrane proteins found in influenza virus.[6] First, the GPMV is brought into the proximity of a phase-separated GUV using an optical trap. Fusion takes place after a nanoparticle is trapped at the contact point between the vesicles (top), and upon fusion (middle), the proteins and lipids mix within seconds. After fusion (bottom), the affinity of the proteins for the disordered lipid phase can be detected.[6]

control protein binding and allow both time-resolved imaging of protein binding and monitoring of how membrane geometry affects protein recruitment.[7,26,27] The applicability of thermoplasmonics in this realm lies in the ability of laser-heated nanoparticles to remodel biomembranes via, for example, fusion of membranes or via pore formation. Examples of thermoplasmonic fusion[27] (Figure 3) include studies of membrane binding proteins like ESCRT[26] or the I-BAR domain from IRSp53.[7] These proteins were encapsulated within GUVs made from zwitterionic lipids and subsequently delivered, via thermoplasmonically induced membrane fusion, to other vesicles having a different lipid composition that favored protein binding (Figure 3A). A similar approach was applied in the study of the membrane phase affinity of transmembrane influenza virus proteins.[6] Here giant plasma membrane vesicles (GPMVs) were harvested from cells expressing fluorescently tagged virus proteins followed by fusion of the GPMVs to phase-segregated GUVs, which allowed for investigation of the lateral segregation of proteins (Figure 3B). Such studies offer a unique way to investigate the membrane phase affinity of integral membrane proteins and also membrane-shape remodeling of proteins in real time by mixing biomimetic membranes and natural membranes harvested from cells. This strategy can readily be extended for investigation of any transmembrane/integral protein, including proteins from other viruses like SARS-CoV-1/2. Possible future studies along these lines are numerous and should include the possibility of fusing living cells and biomimetic membranes[28,15] and investigating cellular functions like membrane repair.[1]

The ability of plasmonic nanoparticles to inflict nanoscopic membrane damage has been exploited in the delivery of nanoparticles to vesicles and cells.[29,30] Nanoparticles were optically injected across the membrane in cells[29] and GUVs[30] by using a pulsed laser, which both triggered a light pressure on the particle and softened the membrane by local heating and facilitated delivery across the membrane (Figure 4A). Recently, a NIR continuous wave (CW) laser was also used for membrane perforation to study pore formation in GUVs and cells by locally disrupting the membrane and subsequently monitoring the recruitment of membrane repair proteins to the annular ring of the nanoscopic injury (Figure 4B,C).[1] This approach offers a unique way to study the physical and biological aspects of pore formation in membranes in the presence or absence of proteins. Gentler plasmonic heating can be applied to study local phase behavior by locally heating GUVs existing in an ordered lipid state.[31] This strategy allowed the long-standing question concerning the discrete nature of the melting-induced permeability of membranes[32] to be answered and was also used for quantification of nanoparticle mobility on gel versus fluid lipid membranes.[33] The local effect of heat from a nanoparticle on a membrane was recently modeled using course grained simulation of a fluid and a gel membrane interacting with 7 nm particles.[34] These simulations showed that heat affects the two leaflets of the bilayer differently and leads to the bending and wrapping of the membrane around the nanoparticle. A complete understanding of the nanoparticle−membrane interaction remains elusive, and additional work needs to be done to carefully design experiments that can be modeled accurately.

https://doi.org/10.1021/acs.nanolett.3c03548
Nano Lett. 2024, 24, 777−789

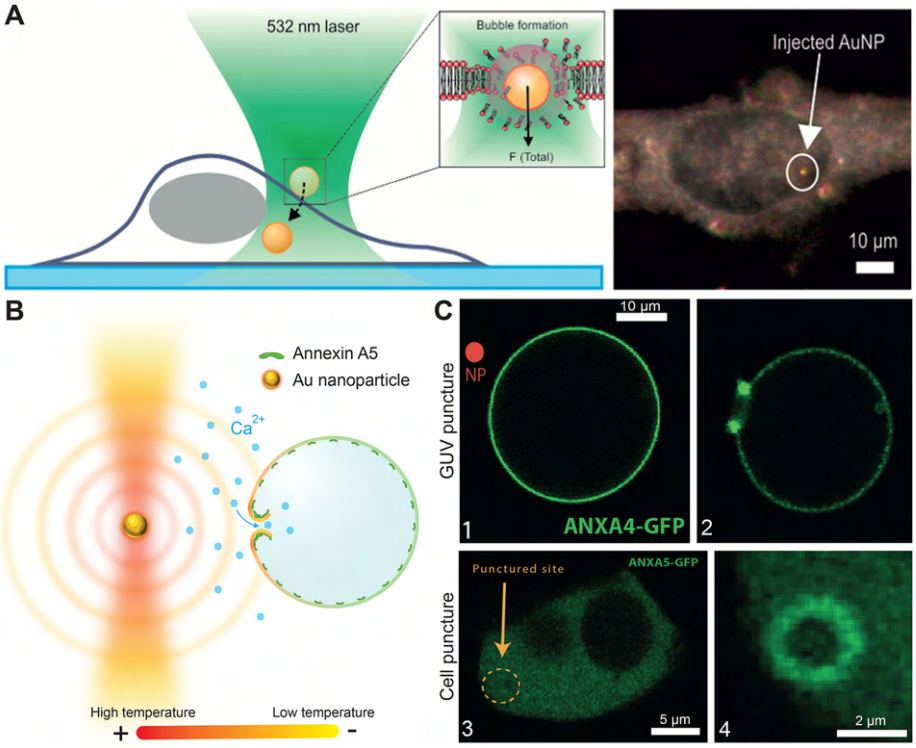

Figure 4. Opto-injection and pore formation in biomembranes using thermoplasmonics. (A) Injection of AuNPs using a CW laser with a λ of 532 nm. The AuNP was first immobilized on the cell membrane by using optical forces. Subsequent focusing of the laser beam on the particle facilitated translocation across the membrane due to a local high temperature and optical forces. Panel A was reproduced from ref 29. Copyright 2015 American Chemical Society. (B) Schematic of an experiment for investigation of the response of membrane repair proteins (GFP-labeled annexins, green) to membrane pore formation in GUVs by optically trapping and consequently heating a AuNP in the vicinity of the membrane, thus inducing a pore. Panel B was adapted with permission from ref 1. Copyright 2022 Royal Society of Chemistry. (C) (1) Image showing an intact GUV containing annexin A4 (green). (2) Recruitment of annexin A4 (green) to a membrane pore induced in a GUV results in local enrichment at the pore annulus and curving of the membrane. (3) Living cell expressing GFP-labeled annexin A5. (4) Thermoplasmonically induced puncturing of the cell also results in the recruitment of annexin A5 around the site of injury. Panel C was adapted with permission from ref 1. Copyright 2022 Royal Society of Chemistry.

Proteins respond to heat by changing their binding and folding kinetics. Unfolding of proteins at high temperatures is predicted by Boltzmann's statistics, and studies involving protein function should always raise concerns regarding potential irreversible molecular damage caused by high local temperatures. However, in most applications involving the study of proteins and lipids, the spatial extent of heat exposure has a nanoscopic length scale and levels off quickly beyond a distance corresponding to the particle radius. Also, the brief exposure of <1 s significantly limits molecular damage. Because both cells and GUVs have dimensions of >10 μm and consist of mobile lipids and proteins, which therefore are only transiently exposed to heat, it is estimated that the overall molecular damage can be kept at a minmum.

Alterations in protein structure and even damage are certainly taking place in some applications and can even be a desired effect. Plasmonic nanorods have been found to be efficient in dissolution of protein aggregations formed by Aβ amyloids that are abundant in the brains of people with Alzheimer's disease.[35] In vitro studies have confirmed that Aβ fibers of various lengths are susceptible to breakage, unfolding, or other structural changes when conjugated to irradiated gold nanorods.[36] Together with improved delivery of nanorods across the blood–brain barrier (BBB),[37] this will allow the therapeutic possibility of treating people with neurodegenerative diseases like Alzheimer's.

Nanoparticles delivered to the bloodstream have a tendency to become decorated with a protein corona, which affects the nanoparticle circulatory lifetime and the conjugation of the particle to cell receptors of interest (targeting). Plasmonic nanoparticles coated with proteins from a commonly used culture medium containing fetal bovine serum (FBS), which resembles the protein composition in the blood, were studied before and after laser irradiation. This study showed that the protein composition was found to be significantly altered upon laser heating because of denaturation and destruction of proteins on the particle surface.[38]

We conclude that biophysical applications of plasmonic nanoparticles have shown great promise as a tool for resolving questions concerning the biological and biophysical functions of proteins and biomembranes. The steep gradient in temperature from irradiated plasmonic nanoparticles makes it possible to manipulate biological systems with nanosurgical precision and keep protein degradation extremely local. The scope of applications is currently in its early stage, and future experiments should be tailored by using cleverly designed nanoparticle shapes and sizes and by introducing novel particles like Janus particles. Janus particles allow generation of anisotropic thermal distributions and have been shown to exhibit very high thermal gradients as high as 40 K/nm in the vicinity of the particle surface.[39]

https://doi.org/10.1021/acs.nanolett.3c03548
Nano Lett. 2024, 24, 777−789

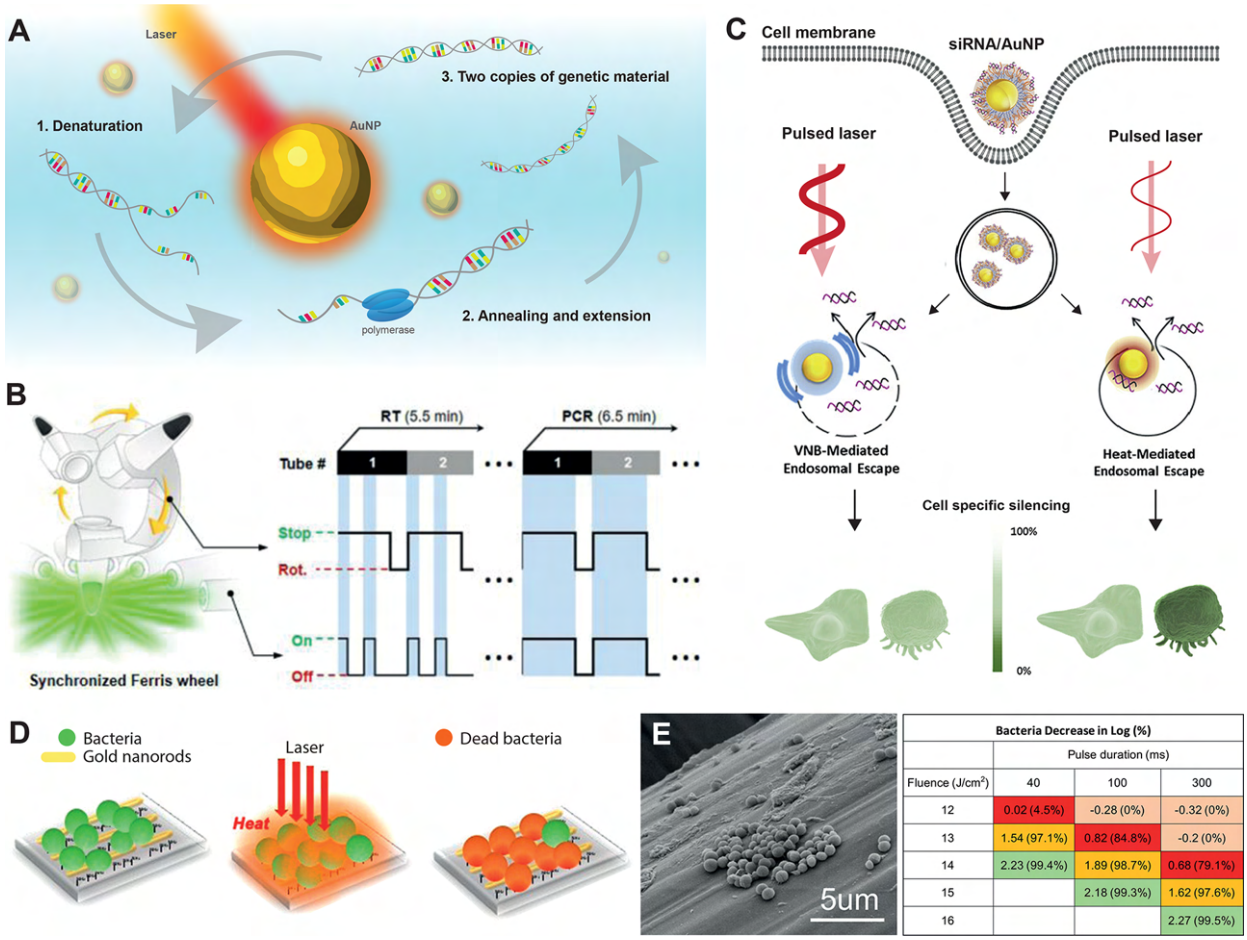

Bacteria Decrease in Log (%)			
	Pulse duration (ms)		
Fluence (J/cm^2)	40	100	300
12	0.02 (4.5%)	-0.28 (0%)	-0.32 (0%)
13	1.54 (97.1%)	0.82 (84.8%)	-0.2 (0%)
14	2.23 (99.4%)	1.89 (98.7%)	0.68 (79.1%)
15		2.18 (99.3%)	1.62 (97.6%)
16			2.27 (99.5%)

Figure 5. Thermoplasmonics in molecular biology and microbiology. (A) Laser heating of plasmonic nanoparticles allows rapid thermal cycling for conducting nano-PCR. (B) Detection of SARS-CoV-2 RNA using high-speed nano-PCR for reverse transcription PCR. A spinning wheel, containing tubes with RNA and nanoparticles, is rotated to allow periodic laser irradiation of the tube content leading to thermal cycling. Panel B was reproduced with permission from ref 9. Copyright 2020 Springer Nature. (C) Mechanism of cellular uptake and intracellular release of nucleotides from AuNPs. Two release mechanisms are proposed on the basis of a thermal mechanism and a nonthermal mechanism. The nonthermal disruption of the endocytic envelope is based on a mechanical effect due to vapor nanobubble formation during pulsed laser irradiation. Laser irradiation with a lower pulse energy results in heating, which depends on the number of particles taken up. Endosomal escape of nucleotides and gene silencing is therefore cell type specific as indicated in the bottom part of the panel. Panel C was modified from ref 56. Copyright 2020 Elsevier. (D) Disinfection of surgical mesh using plasmonic heating of AuNRs. The surgical mesh is functionalized with AuNRs, and subsequent inoculation with *Staphylococcus aureus* leads to biofilm formation. (E) Laser irradiation kills the bacteria as shown by scanning electron microscopy or by cell counting. Panels D and E were reproduced with permission from ref 62. Copyright 2019 American Chemical Society.

The sensitivity of molecules and proteins has led to numerous applications of plasmonic heating in molecular systems. An application, in which plasmonic heating has had a significant impact, is the acceleration of the analysis of DNA using polymerase chain reaction (PCR). PCR is a method of amplifying nucleic acids with high specificity and sensitivity[40] that has been applied in areas ranging from biology to medicine[41] and agriculture.[42] The reaction requires repeated cycles of heating and cooling between temperatures necessary for dehybridization and hybridization of a target sequence. Conventional thermocyclers employ a heating block based on the Peltier element and have a limited rate of heating and cooling so that the entire amplification process is completed within 1−2 h. Because of the desire to rapidly diagnose viral infections caused by viruses like SARS-CoV-2, the use of plasmonic heating offers a promising approach to accelerate DNA or RNA detection.[9]

Rapid heating and cooling can be performed using thermoplasmonics and have recently led to a strategy termed photonic PCR that was successfully exploited to accelerate PCR.[9,43−46] Both plasmonic nanoparticles and plasmonic substrates can be used for rapid heat cycling. Plasmonic excitation of a Au film resulted in 30 successive heating/cooling cycles within 5 min.[47] A heating rate of 12.79 ± 0.93 °C s^{-1} was achieved by irradiating a Au film using a light-emitting diode (LED) with a wavelength of 450 nm. When the diode was switched off, the heat dissipated through the Au film, and the reaction mixture cooled at a rate of 6.6 ± 0.29 °C s^{-1}. A rapid heat cycling using nanoparticles was recently used for the detection of SARS-CoV-2 RNA, via reverse transcription, by performing nano-PCR using a mobile device achieving a detection time of 17 min (Figure 5A,B).[9] Despite the recent advances achieved in accelerating the thermal cycles, it is important to note that the completion of a single PCR cycle still faces a time limit of ∼1 s, which is set by the kinetic limitations of PCR such as DNA denaturation, primer annealing, and polymerase extension.[48]

https://doi.org/10.1021/acs.nanolett.3c03548
Nano Lett. 2024, 24, 777−789

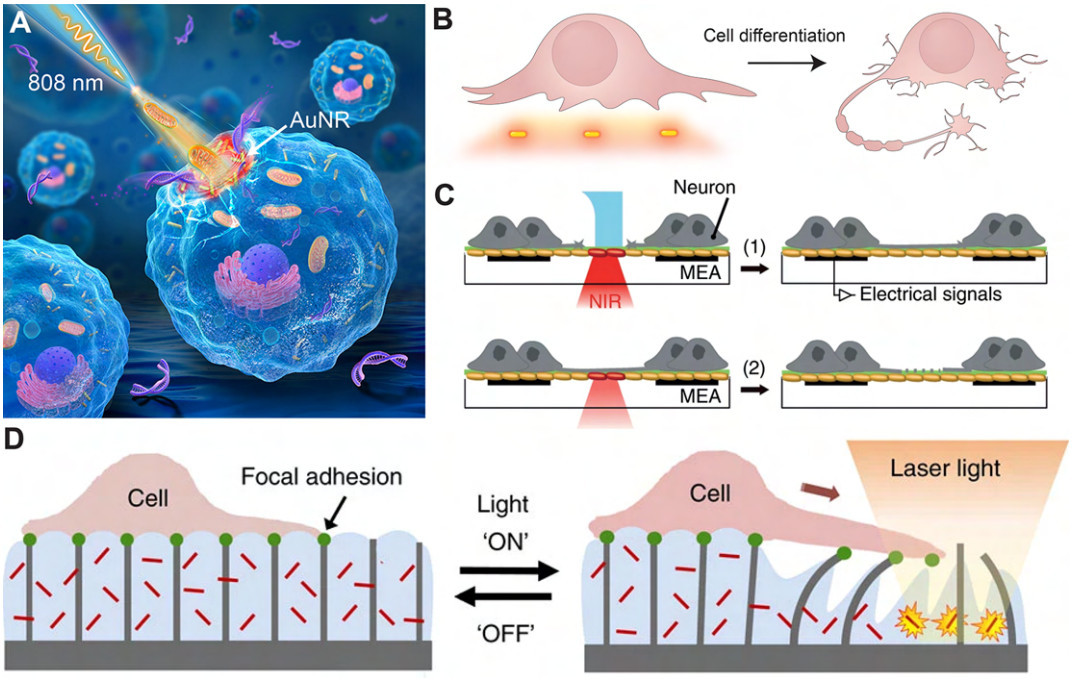

Figure 6. Optical manipulation of single cells using thermoplasmonics. (A) Perforation of a cell by irradiation of AuNRs near the cell surface. Intracellular manipulations following perforation were made possible by combining optical trapping with a micropipette. Panel A was reproduced from ref 67. Copyright 2021 American Chemical Society. (B) Induction of neurite outgrowth and (C) interrogation of neuronal cell signaling by plasmonic heating. Cell−cell interconnections can be ablated through plasmonic heating or allowed to form by ablation of a barrier consisting of a heat sensitive hydrogel containing plasmonic nanoparticles. Panel C was reproduced from ref 2. Copyright 2020 Springer Nature. (D) Active substrate material for subcellular mechanical actuation of adhered cells. The thermally sensitive hydrogel containing plasmonic nanoparticles contracts upon irradiation and thereby stretches the adhered cell. Panel D was reproduced from ref 68. Copyright 2017 Springer Nature.

Plasmonic heating has been successfully applied in drug delivery primarily to release molecular content conjugated to the plasmonic nanostructures or to facilitate permeation of the plasma membrane to allow the influx of small interfering RNA.[49] In particular, gene silencing, using plasmonic nanostructures conjugated with silencing RNA,[50] can be triggered from laser heating of the nanostructure and has shown great promise in the downregulation of protein synthesis in cell studies.[51,52] As a proof of principle, green fluorescent protein (GFP) is often chosen as the target for interference with gene expression. Other more biologically relevant examples, which have been successfully downregulated using plasmonic heating of gold nanostructures, include HSPs,[53] oncogenes,[54] and proteins controlling transcription like NF-κB.[50]

A major challenge in drug delivery involves the two membrane barriers that have to be penetrated during delivery of the drug of interest. Nanoparticles are excellent for carrying drugs across the cell membrane simply through particle endocytosis.[55] Once endocytosed, the nanoparticles and their molecular content become trapped within the endosome, and here the molecules are in danger of losing their therapeutic effect due to degradation by enzymes and the low pH of the endosomal environment. The release from the endocytic compartment has been shown to be feasible through laser irradiation, which can both release the molecules from the nanoparticle via, e.g., dehybridization of nucleotide strands and disruption of the endosome membrane.[56] However, by testing molecular release using pulsed and CW lasers, it was found that the mechanisms behind these two escape phenomena were more complex than just simple thermally triggered release. It was found[56] that pulsed lasers were more efficient in silencing gene expression in cells when high-energy pulses were used. The authors discriminated between a thermal mechanism when the pulse energy was low and a nonthermal mechanism when the pulse energy was sufficiently high to cause formation of vapor nanobubbles (VNBs) (Figure 5C). This finding was corroborated by other studies that found pulsed lasers trigger release with reproducibility and efficiency that are both higher than those of CW lasers.[57−59] Release triggered by CW lasers, on the contrary, was found to be dependent on the aggregation status of the NPs within the endosome, which has a great impact on the total light absorption. Wang et al.[60] concluded that the optical extinction of aggregated gold nanoparticles (sizes of ∼30 nm) increased significantly at NIR wavelengths, which is the relevant range for PTT. Interestingly, the mechanism of molecular release from NPs can also proceed through other nonthermal effects involving electrochemical effects arising from so-called hot electrons[61] or photoinduced free radicals generated during irradiation with resonant light.[59] It is noteworthy that the laser intensities used in CW applications are on the order of 10 W cm^{-2}, which are not sufficient to generate any significant heat from a single nanoparticle. However, due to the large number of closely spaced nanoparticles found in endosomes, the extent of heating is increased; however, the degree of endosomal heating is quite uncertain, and the spatial configuration of the nanoparticles is uncontrollable in such an environment. Although these studies provide some insight into the nanoscale mechanisms at play, during nanoparticle heating in cells, we stress the need for further mechanistic studies using, for

https://doi.org/10.1021/acs.nanolett.3c03548
Nano Lett. 2024, 24, 777−789

example, bioimimetic vesicles as models for the cell and endosomal membrane.

Thermoplasmonically assisted sterilization and disinfection are other emerging fields that utilize plasmonic nanoparticles to produce heat to kill pathogens via molecular targets. Plasmonic nanoparticles can be functionalized to recognize and bind specific targets on the bacterial wall, which allows selective killing of bacteria within a bacterial population by irradiating the sample with laser light.[63] Sterilization of surgical implants has also been suggested by plasmonically assisted overheating. Implant contamination often occurs because of bacterial growth. If the bacterial growth develops further into biofilms, it becomes more resistant to the host immune system and even antimicrobial agents. Via decoration of a surgical polymer mesh with plasmonic gold nanorods, it was possible to eliminate a biofilm of bacteria formed at the surface of the polymer meshes by laser irradiation, thus proposing an alternative disinfection method to the existing biochemical approaches[62] (Figure 5D,E). This photothermal disinfection has recently been extended to create reusable face masks.[64,65] This innovation was driven by the global demand for personal hygiene, including wearing face masks during the COVID-19 pandemic, which quickly led to a shortage of professional face masks. Consequently, using reusable face masks that utilize plasmonic nanoheaters in their structure and take advantage of the same plasmonics principle for pathogen decontamination was proposed.

Studying and probing living cells remain challenging despite new developments in micromanipulation techniques. Thermoplasmonic heating provides entirely new opportunities for single-cell interrogation and manipulation and moreover allows investigation of both isolated cells and selective interference of cells within a cell culture while leaving neighboring cells unaffected. Both extra- and intracellular manipulation have been achieved using plasmonic heating, which is made possible by the efficient nanoparticle delivery through endocytosis. In addition to the natural endocytic pathways, thermoplasmonics provides an interesting alternative for nanoparticle delivery by using optically triggered injection. Researchers reported high cellular viability upon effective delivery of gold nanoparticles utilizing plasmonic heating and optical pushing at the membrane site to push the particles swiftly through the lipid bilayer.[29] To avoid the cellular uptake of metallic particles and consequent entrapment of the particles within endosomes, an alternative approach could be to use a plasmonic nanocavity substrate on which cells can be plated to provide high-throughput delivery of very large molecules and possibly nanoparticles upon laser irradiation.[66] Such thermoplasmonic perforation has paved the way for new in situ single-cell nano- and microsurgery. Manipulation and extraction of intracellular organelles from a single living cell, through transient light-induced membrane perforations, were achieved using plasmonic heating in combination with optical trapping and micropipette manipulation[67] (Figure 6A). By controlling the optical power, one can achieve both induced membrane perforation and membrane repair by the respective lipid fluidities achieved at high and mild temperatures. This application is an elegant mix of optical heating and optical trapping that pushes the boundaries of what is possible at the single-cell level, thus advancing thermoplasmonic membrane manipulation to another level.

Perforating the cellular membrane using thermoplasmonics is, however, relevant for not only the delivery of molecules but also intracellular organelle manipulation and extraction. Nanoscopic membrane injury via heating has revealed the dynamics of the subsequent cellular repair response and involved proteins, e.g., how annexin proteins are recruited to injury sites following laser induced puncture of cells[1] (Figure 4C). Annexin proteins are highly upregulated in various cancer cell lines and thus are a target for cancer therapy. This technique can be employed to investigate other membrane-repairing proteins that could play an important role in identifying components in the membrane repair machinery and hence for the development of new therapeutic interventions with the goal of downregulating membrane repair mechanisms in cancer cells.

Transcriptional regulation can also be modulated using thermoplasmonics on single cells, as demonstrated by several studies. Recently, it was demonstrated that thermal heating of nanoparticles can guide the directed differentiation of dental pulp stem cells[69] through regulation of the mitochondrial metabolism. A similar approach using laser heating of copper nanoparticles was used to induce mesenchymal stem cell differentiation into fibroblasts and hence accelerate wound healing.[70] Copper ions have traditionally been used to trigger this differentiation, but by using laser irradiation of copper nanoparticles, it was possible to thermally induce the mesenchymal differentiation and simultaneously weaken the side effects of having free copper ions in the blood. Remote modulation of myotube[71] and neuronal[4,72] cell differentiation was also achieved using plasmonic heating (Figure 6B), and while the mechanism behind the observed biological effects remains poorly understood, it has been shown that several proteins are regulated through thermally altered gene expression, including HSP and other stress sensitive proteins.[50,71] We envisage that plasmonic heating will provide a useful tool in research on stem cell-based therapeutics and tissue engineering by remote heating and wireless stimulation of muscle cells. To gain a more complete understanding of how local hyperthermia works in different cell types, future research should seek to elucidate the underlying mechanisms of how local heat can alter the genetic state of cells.

Plasmonic heating has been extensively used to manipulate cells by thermally triggering changes in the extracellular environment. By embedding cells in thermally sensitive hydrogels, one can turn cellular connections on and off using local heating, allowing for the study of how cellular stimuli propagate in a neuronal cellular network.[2] To this end, neural cells were placed on a layer of gold nanorods, which could be locally heated by laser irradiation. The plated cells were separated by the heat sensitive hydrogel, and hence, the selected connections could be allowed to grow by selective ablation of specific areas of the gel (Figure 6C). Additionally, this platform allowed suppression of neuronal spike activity by selective ablation of existing neural connections like local heat ablation (Figure 6C). Thermally induced contraction of hydrogels has also been used to apply subcellular mechanical stress by embedding a contractile hydrogel between polymeric pillars onto which cells were adhered[68] (Figure 6D). While hydrogels offer a unique manipulation tool for cellular studies, we also emphasize other studies that offer some more flexibility due to the absence of a hydrogel. For example, a micropatterned plasmonic substrate[72] or a mobile optical fiber, functionalized with gold nanorods at the tip, was successfully used to selectively modulate neuronal signals in cell cultures.[73]

https://doi.org/10.1021/acs.nanolett.3c03548
Nano Lett. 2024, 24, 777−789

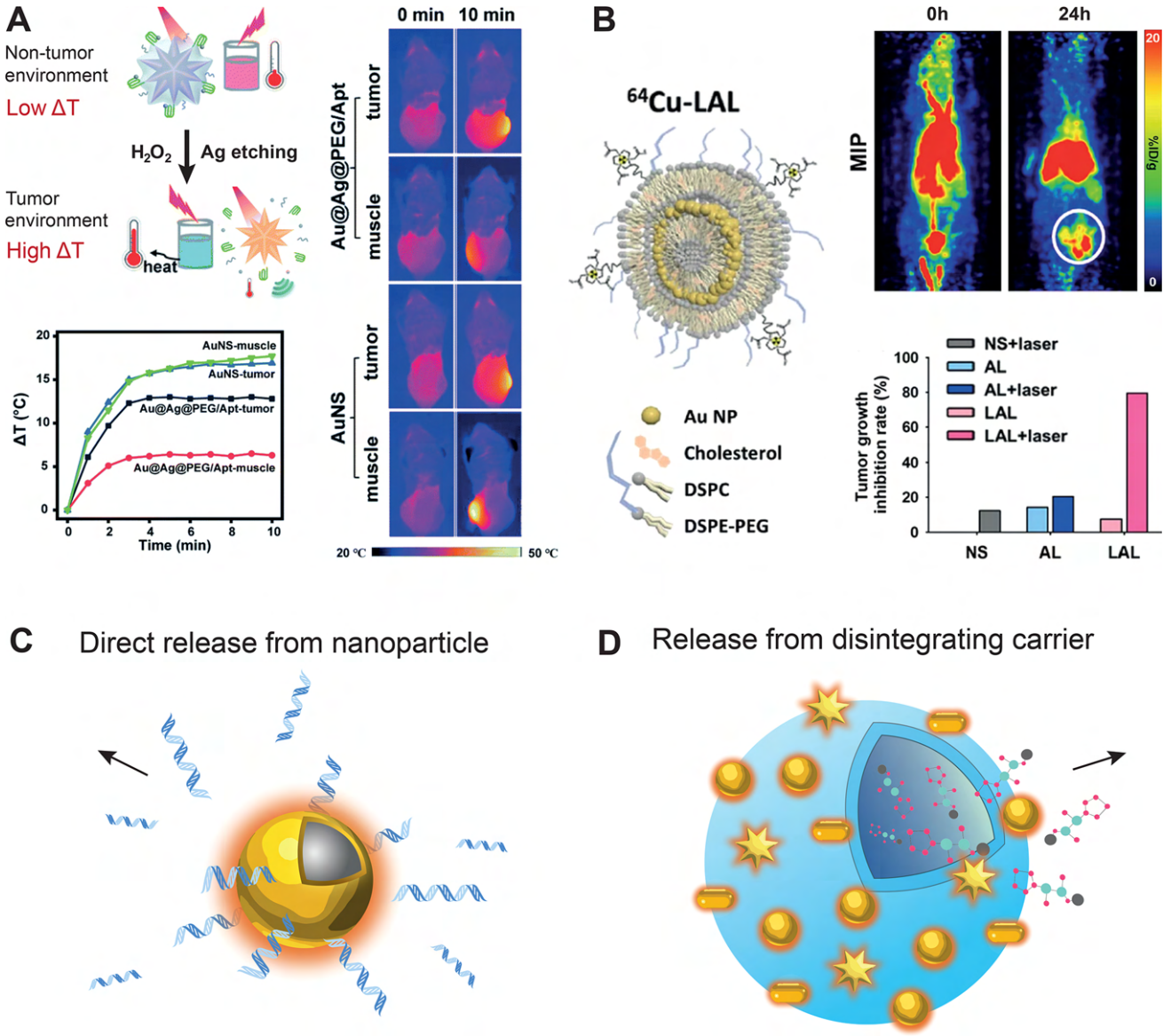

Figure 7. Plasmonic heating used in photothermal therapy and for triggering release in drug delivery. (A) Photothermal therapy using gold nanostars coated with silver as a switchable pro-drug agent. Upon entry into the tumor environment, the silver coating is etched off due to the high levels of H_2O_2 in tumor cells. The bare gold nanostars exhibit higher absorption within the near-infrared wavelength region and hence become activated within the tumor environment. The measured difference in heating between bare gold nanostars and silver-coated nanostars is shown in the graph and by thermal imaging for the tumor and muscle tissue. Panel A was modified from ref 83. Copyright 2021 Royal Society of Chemistry. (B) Multilayer theranostic nanoparticles synthesized with a liposomal core, a shell of gold nanoparticles, and an additional outer lipid bilayer. The outer lipid bilayer is labeled with radioisotopes for positron emission tomography (PET) imaging. Data show treatment with PEG lipids containing liposomes and gold (AL) and liposomes, gold, and an outer lipid bilayer (LAL) for improving immune evasiveness and increasing the rate of delivery to tumor site. Laser treatment with LAL showed efficient tumor inhibition compared to laser treatment with normal saline (NS) and also efficient delivery and imaging capabilities as shown by PET imaging. Panel B was reproduced from ref 87. Copyright 2021 Springer Nature. (C and D) General approach for using plasmonic heating in drug delivery. (C) Thermally triggered release of molecular cargo conjugated to the particle surface and (D) thermally triggered permeability changes in temperature sensitive materials (e.g., liposomes or hydrogels) containing drugs.

Here we have highlighted a few applications for studying cell cultures using thermoplasmonics, but it is not hard to imagine endless opportunities for combining new developments in substrate engineering with thermoplasmonics, which will offer many new applications for investigating and manipulating cell−substrate and cell−cell interactions.

Nanoparticles have now been investigated extensively as photothermal agents for cancer therapy often combined with drug delivery[5,74] or in combination with photodynamic therapy (PDT) in which light-absorbing molecules can act as photosensitizers for the generation of reactive oxygen species.[75,76] During photothermal therapy (PTT), nanoparticles accumulate at tumor sites in tissue by the enhanced permeability and retention (EPR) effect and are irradiated with NIR light to ablate the cancerous cells.[77] After some years with animal testing and lab research, photothermal therapy is these days entering a new era, following some new unpublished data from a recently completed clinical trial. These data show that prostate cancer was successfully treated via laser irradiation with gold nanoshells with remarkably few side effects. Here, we

https://doi.org/10.1021/acs.nanolett.3c03548
Nano Lett. 2024, 24, 777−789

briefly touch upon these new results and a few recent advances made in this field and point to where the research is heading to improve clinical applications of these smart therapeutic particles.

A challenge in PTT is to design biocompatible nanoparticles that can effectively extravasate into the cancer tumor environment.[78] The leaky vasculature supplying tumors with blood allows the extravasation of NPs (<200 nm) into the tumor tissue. The optimal particle diameter used in the systemic delivery of NPs is approximately 100−200 nm, whereas much smaller NPs are cleared via the renal system.[79,80] Several promising approaches have been adopted to make the nanoparticle evade the immune system by camouflaging nanoparticles with biomimetic coatings, thus increasing their circulation time and their likelihood of reaching their target. At the target site, therapeutic effects are achieved upon irradiation, leading to the efficient treatment of tumors in mice. Such a therapeutic approach has just been finalized in a clinical trial for testing ablation of tumors using gold nanoshells (clinical trial NCT04240639).[5,81] Patients in this trial received gold nanoshells (total diameter of ∼150 nm) intravenously. The particle surface was passivated with short polyethylene glycol (molecular weight of 6 kDa) for immune evasion to allow for accumulation in the tumor via the EPR effect. Subsequent irradiation with low-power NIR light (810 nm) resulted in efficient ablation of the tumor with very few side effects observed during a long follow-up observation. Although data from this trial have not been published in final form, preliminary data from this trial can be found in ref 81, which clearly show the convincing effect of PTT on prostate cancer.

Further developments are focused on testing thermoplasmonic particles that function as pro-drugs. These efforts are driving the field toward more clinically safe therapeutics with minimal side effects.[82] For instance, researchers have developed nanoparticles that are plasmonically dormant until activated by the H_2O_2 environment at tumor sites, inhibiting thermal effects of irradiation in other tissues where the particles may also accumulate[83] (Figure 7A). More recently, to address limitations of selectivity and imaging of therapeutic particles, multimodal systems combining plasmonic and magnetic properties have been proposed.[84−86] A two-layer Au-liposome (LAL) labeled with ^{64}Cu was recently shown to exhibit a very high level of accumulation in tumors while also being effective for in vivo PET imaging and tumor ablation by PTT in mice models[87] (Figure 7B). Such hybrid particles pave the way for the next generation of cancer theranostics by providing a platform that simultaneously serves as a contrast agent for imaging and a source of plasmonically induced hyperthermia.

Plasmonic heating of nanoparticles is also being extensively investigated in the field of drug delivery for light-triggered release of therapeutic molecules, as also discussed above in relation to the delivery of small RNA for genetic interference. There are two generic approaches for using thermoplasmonics in drug delivery: (i) conjugating drugs directly to the surface of nanoparticles, such that the drug will be released when irradiation causes heating of the system (Figure 7C), and (ii) employing a thermosensitive drug container made from, e.g., hydrogels or lipids, to release the content[88,89] (Figure 7D). A hybrid polymeric microcarrier with gold bipyramidal nanoparticles has, e.g., been used to release a therapeutic molecule for diabetic retinopathy upon NIR irradiation.[90] Combination therapy, in which the discussed thermoplasmonic effects are used for both on-site delivery of drugs or genetic material and simultaneous heat-induced hyperthermia, has been proven to be an effective strategy for combating cancer cells.[91,92] There are several advantages of this approach, including the sensitivity of cancer cells to heat and the stronger therapeutic effect of some drugs at higher temperatures. With early thermoplasmonic particle systems already in clinical trials, innovation on combination therapies involving thermal release and thermal therapy is likely to continue.

Future perspectives in this field include further development of substrate engineering and development of smart materials, which are expected to inspire new applications in thermoplasmonics. Many materials exhibit high thermal sensitivity and hence can act as heat-triggered actuators inside cells or in materials that are interfacing with biological specimens. Also, the existing strategies outlined in this review have other applications. For instance, intracellular or nuclear repair in cells should be possible to investigate using endocytosed nanoparticles that are known, during cellular uptake, to travel from the cell surface toward the nucleus along the endocytic pathway. Also, microchemistry, using thermoplasmonic fusion of GUVs, has great potential beyond what is shown with the biophysical applications presented in this review. Monitoring polymerization or other active molecular events is readily possible by combining reagents in a stepwise manner through fusion and remains to be explored.

Photothermal therapy has now been shown in clinical trials to be efficient in cancer therapy with remarkably few side effects, and future studies should focus on testing PTT on additional types of cancer. Successful outcomes in cancer therapy will also lead to expansion of the same PTT methodology to other diseases like Alzheimer's disease as mentioned in ref 93 or in phage therapy with the aim of killing multiresistant bacteria.[74] Future developments should also focus on molecular mechanisms affected by heating[94] that will strengthen the impact of PTT in combination with other scientific disciplines.

AUTHOR INFORMATION

Corresponding Author

Poul Martin Bendix − *Niels Bohr Institute, University of Copenhagen, 2100 København Ø, Denmark;* orcid.org/0000-0001-8838-8887; Email: bendix@nbi.ku.dk

Authors

Victoria Thusgaard Ruhoff − *Niels Bohr Institute, University of Copenhagen, 2100 København Ø, Denmark;* orcid.org/0000-0002-7986-7381

Mohammad Reza Arastoo − *Niels Bohr Institute, University of Copenhagen, 2100 København Ø, Denmark;* orcid.org/0000-0002-7463-2321

Guillermo Moreno-Pescador − *Niels Bohr Institute, University of Copenhagen, 2100 København Ø, Denmark; Copenhagen Plant Science Center, Department of Plant and Environmental Sciences, University of Copenhagen, 1871 Frederiksberg, Denmark;* orcid.org/0000-0001-6923-9923

Complete contact information is available at: https://pubs.acs.org/10.1021/acs.nanolett.3c03548

Notes

The authors declare no competing financial interest.

https://doi.org/10.1021/acs.nanolett.3c03548
Nano Lett. 2024, 24, 777−789

■ ACKNOWLEDGMENTS

P.M.B., M.R.A., and V.T.R. received funding from the Novo Foundation (Grants NNF18OC0034936, NNF20OC0065357, NNF20OC0064565, and NNF20OC0061176), and G.M.-P. received funding from the Novo Foundation (Grant NNF22OC0079093).

■ REFERENCES

(1) Moreno-Pescador, G. S.; Aswad, D. S.; Florentsen, C. D.; Bahadori, A.; Arastoo, M. R.; Danielsen, H. M. D.; Heitmann, A. S. B.; Boye, T. L.; Nylandsted, J.; Oddershede, L. B.; Bendix, P. M.; et al. Thermoplasmonic nano-rupture of cells reveals annexin v function in plasma membrane repair. *Nanoscale* **2022**, *14* (21), 7778−7787.
(2) Hong, N.; Nam, Y. Thermoplasmonic neural chip platform for in situ manipulation of neuronal connections in vitro. *Nat. Commun.* **2020**, *11* (1), 6313.
(3) Robert, H. M. L.; Savatier, J.; Vial, S.; Verghese, J.; Wattellier, B.; Rigneault, H.; Monneret, S.; Polleux, J.; Baffou, G. Photothermal control of heat-shock protein expression at the single cell level. *Small* **2018**, *14* (32), 1801910.
(4) Antonova, O. Yu.; Kochetkova, O. Yu.; Kanev, I. L. Light-to-heat converting ecm-mimetic nanofiber scaffolds for neuronal differentiation and neurite outgrowth guidance. *Nanomaterials* **2022**, *12* (13), 2166.
(5) Li, X.; Lovell, J. F.; Yoon, J.; Chen, X. Clinical development and potential of photothermal and photodynamic therapies for cancer. *Nat. Rev. Clin. Oncol.* **2020**, *17* (11), 657−674.
(6) Moreno-Pescador, G.; Arastoo, M. R.; Ruhoff, V. T.; Chiantia, S.; Daniels, R.; Bendix, P. M. Thermoplasmonic vesicle fusion reveals membrane phase segregation of influenza spike proteins. *Nano Lett.* **2023**, *23* (8), 3377−3384.
(7) De Franceschi, N.; Alqabandi, M.; Miguet, N.; Caillat, C.; Mangenot, S.; Weissenhorn, W.; Bassereau, P. The escrt protein chmp2b acts as a diffusion barrier on reconstituted membrane necks. *J. Cell Sci.* **2019**, *132* (4), jcs217968.
(8) Yeheskely-Hayon, D.; Minai, L.; Golan, L.; Dann, E. J.; Yelin, D. Optically induced cell fusion using bispecific nanoparticles. *Small* **2013**, *9* (22), 3771−3777.
(9) Cheong, J.; Yu, H.; Lee, C. Y.; Lee, J.-u.; Choi, H.-J.; Lee, J.-H.; Lee, H.; Cheon, J. Fast detection of SARS-CoV-2 RNA via the integration of plasmonic thermocycling and fluorescence detection in a portable device. *Nat. Biomed. Eng.* **2020**, *4*, 1159−1167.
(10) Baffou, G.; Quidant, R. Thermo-plasmonics: using metallic nanostructures as nano-sources of heat. *Laser Photonics Rev.* **2013**, *7* (2), 171−187.
(11) Baffou, G.; Cichos, F.; Quidant, R. Applications and challenges of thermoplasmonics. *Nat. Mater.* **2020**, *19* (9), 946−958.
(12) Jauffred, L.; Samadi, A.; Klingberg, H.; Bendix, P. M.; Oddershede, L. B. Plasmonic heating of nanostructures. *Chem. Rev.* **2019**, *119* (13), 8087−8130.
(13) Xin, H.; Namgung, B.; Lee, L. P Nanoplasmonic optical antennas for life sciences and medicine. *Nat. Rev. Mater.* **2018**, *3* (8), 228−243.
(14) Sharifi, M.; Attar, F.; Saboury, A. A.; Akhtari, K.; Hooshmand, N.; Hasan, A.; El-Sayed, M. A.; Falahati, M. Plasmonic gold nanoparticles: Optical manipulation, imaging, drug delivery and therapy. *J. Controlled Release* **2019**, *311-312*, 170−189.
(15) Bahadori, A.; Moreno-Pescador, G.; Oddershede, L. B; Bendix, P. M Remotely controlled fusion of selected vesicles and living cells: a key issue review. *Rep. Prog. Phys.* **2018**, *81* (3), 032602.
(16) Bohren, C. F.; Huffman, D. R. *Absorption and Scattering of Light by Small Particles*; Wiley-VCH Verlag GmbH & Co. KGaA, 1998.
(17) Khlebtsov, N. G.; Dykman, L. A. Optical properties and biomedical applications of plasmonic nanoparticles. *J. Quant. Spectrosc. Radiat. Transfer* **2010**, *111* (1), 1−35.
(18) Govorov, A. O.; Zhang, W.; Skeini, T.; Richardson, H.; Lee, J.; Kotov, N. A. Gold nanoparticle ensembles as heaters and actuators: melting and collective plasmon resonances. *Nanoscale Res. Lett.* **2006**, *1* (1), 84−90.
(19) Bendix, P. M.; Reihani, S. N. S.; Oddershede, L. B. Direct measurements of heating by electromagnetically trapped gold nanoparticles on supported lipid bilayers. *ACS Nano* **2010**, *4* (4), 2256−2262.
(20) Samadi, A.; Klingberg, H.; Jauffred, L.; Kjær, A.; Bendix, P. M.; Oddershede, L. B. Platinum nanoparticles: a non-toxic, effective and thermally stable alternative plasmonic material for cancer therapy and bioengineering. *Nanoscale* **2018**, *10* (19), 9097−9107.
(21) Ifijen, I. H.; Maliki, M. A comprehensive review on the synthesis and photothermal cancer therapy of titanium nitride nanostructures. *Inorg. Nano-Met. Chem.* **2023**, *53* (4), 366−387.
(22) Samadi, A.; Bendix, P. M.; Oddershede, L. B. Optical manipulation of individual strongly absorbing platinum nanoparticles. *Nanoscale* **2017**, *9* (46), 18449−18455.
(23) Guglielmelli, A.; Pierini, F.; Tabiryan, N.; Umeton, C.; Bunning, T. J.; De Sio, L. Thermoplasmonics with gold nanoparticles: A new weapon in modern optics and biomedicine. *Adv. Photonics Res.* **2021**, *2* (8), 2000198.
(24) Baffou, G.; Polleux, J.; Rigneault, H.; Monneret, S. Superheating and micro-bubble generation around plasmonic nanoparticles under cw illumination. *J. Phys. Chem. C* **2014**, *118* (9), 4890−4898.
(25) Zundel, L.; Malone, K.; Cerdan, L.; Martinez-Herrero, R.; Manjavacas, A. Lattice Resonances for Thermoplasmonics. *ACS Photonics* **2023**, *10* (1), 274−282.
(26) Bertin, A.; de Franceschi, N.; de la Mora, E.; Maity, S.; Alqabandi, M.; Miguet, N.; di Cicco, A.; Roos, W. H.; Mangenot, S.; Weissenhorn, W.; Bassereau, P.; et al. Human escrt-iii polymers assemble on positively curved membranes and induce helical membrane tube formation. *Nat. Commun.* **2020**, *11* (1), 2663.
(27) Rørvig-Lund, A.; Bahadori, A.; Semsey, S.; Bendix, P. M.; Oddershede, L. B. Vesicle fusion triggered by optically heated gold nanoparticles. *Nano Lett.* **2015**, *15* (6), 4183−4188.
(28) Bahadori, A.; Oddershede, L. B.; Bendix, P. M. Hot-nanoparticle-mediated fusion of selected cells. *Nano Res.* **2017**, *10*, 2034−2045.
(29) Li, M.; Lohmuller, T.; Feldmann, J. Optical injection of gold nanoparticles into living cells. *Nano Lett.* **2015**, *15* (1), 770−775.
(30) Urban, A. S.; Pfeiffer, T.; Fedoruk, M.; Lutich, A. A.; Feldmann, J. Single-step injection of gold nanoparticles through phospholipid membranes. *ACS Nano* **2011**, *5* (5), 3585−3590.
(31) Andersen, T.; Bahadori, A.; Ott, D.; Kyrsting, A.; Reihani, S N. S; Bendix, P. M Nanoscale phase behavior on flat and curved membranes. *Nanotechnology* **2014**, *25* (50), 505101.
(32) Andersen, T.; Kyrsting, A.; Bendix, P. M. Local and transient permeation events are associated with local melting of giant liposomes. *Soft Matter* **2014**, *10* (24), 4268−4274.
(33) Urban, A. S.; Fedoruk, M.; Horton, M. R.; Radler, J. O.; Stefani, F. D.; Feldmann, J. Controlled nanometric phase transitions of phospholipid membranes by plasmonic heating of single gold nanoparticles. *Nano Lett.* **2009**, *9* (8), 2903−2908.
(34) Chen, H.; Dong, X.; Ou, L.; Ma, C.; Yuan, B.; Yang, K. Thermal-controlled cellular uptake of "hot" nanoparticles. *Nanoscale* **2023**, *15* (30), 12718−12727.
(35) Michaels, T. C. T.; Saric, A.; Curk, S.; Bernfur, K.; Arosio, P.; Meisl, G.; Dear, A. J.; Cohen, S. I. A.; Dobson, C. M.; Vendruscolo, M.; Linse, S.; Knowles, T. P. J. Dynamics of oligomer populations formed during the aggregation of alzheimer's aβ42 peptide. *Nat. Chem.* **2020**, *12* (5), 445−451.
(36) Lin, D.; Qian, Z.; Bagnani, M.; Hernandez-Rodriguez, M. A.; Corredoira-Vazquez, J.; Wei, G.; Carlos, L. D.; Mezzenga, R. Probing the protein folding energy landscape: Dissociation of amyloid-β fibrils by laser-induced plasmonic heating. *ACS Nano* **2023**, *17* (10), 9429−9441.
(37) Wang, C.; Wu, B.; Wu, Y.; Song, X.; Zhang, S.; Liu, Z. Camouflaging nanoparticles with brain metastatic tumor cell membranes: a new strategy to traverse blood−brain barrier for

https://doi.org/10.1021/acs.nanolett.3c03548
Nano Lett. 2024, 24, 777−789

imaging and therapy of brain tumors. *Adv. Funct. Mater.* **2020**, *30* (14), 1909369.
(38) Mahmoudi, M.; Lohse, S. E.; Murphy, C. J.; Fathizadeh, A.; Montazeri, A.; Suslick, K. S. Variation of protein corona composition of gold nanoparticles following plasmonic heating. *Nano Lett.* **2014**, *14* (1), 6−12.
(39) Jiang, M.; Chapman, A.; Olarte-Plata, J. D.; Bresme, F. Controlling local thermal gradients at molecular scales with janus nanoheaters. *Nanoscale* **2023**, *15*, 10264−10276.
(40) Mullis, K.; Faloona, F.; Scharf, S.; Saiki, R.; Horn, G.; Erlich, H. Specific enzymatic amplification of dna in vitro: The polymerase chain reaction. *Cold Spring Harbor Symposia on Quantitative Biology* **1986**, *51*, 263−273.
(41) Zhu, H.; Zhang, H.; Xu, Y.; Laššáková, S.; Korabečná, M.; Neužil, P. PCR past, present and future. *BioTechniques* **2020**, *69*, 317−325.
(42) Postollec, F.; Falentin, H.; Pavan, S.; Combrisson, J.; Sohier, D. Recent advances in quantitative PCR (qPCR) applications in food microbiology. *Food Microbiol.* **2011**, *28*, 848−861.
(43) Lee, S. H.; Park, S.-m.; Kim, B. N.; Kwon, O. S.; Rho, W.-Y.; Jun, B.-H. Emerging ultrafast nucleic acid amplification technologies for next-generation molecular diagnostics. *Biosens. Bioelectron.* **2019**, *141*, 111448.
(44) Monshat, H.; Wu, Z.; Pang, J.; Zhang, Q.; Lu, M. Integration of plasmonic heating and on-chip temperature sensor for nucleic acid amplification assays. *J. Biophotonics* **2020**, *13*, 7.
(45) Kang, B.-H.; Jang, K.-W.; Yu, E.-S.; Na, H.; Lee, Y.-J.; Ko, W.-Y.; Bae, N.; Rho, D.; Jeong, K.-H. Ultrafast plasmonic nucleic acid amplification and real-time quantification for decentralized molecular diagnostics. *ACS Nano* **2023**, *17*, 6507−6518.
(46) Nabuti, J.; Fath Elbab, A. R.; Abdel-Mawgood, A.; Yoshihisa, M.; Shalaby, H. M.H. Highly efficient photonic PCR system based on plasmonic heating of gold nanofilms. *Biosens. Bioelectron.: X* **2023**, *14*, 100346.
(47) Son, J. H.; Cho, B.; Hong, S.; Lee, S. H.; Hoxha, O.; Haack, A. J; Lee, L. P Ultrafast photonic PCR. *Light: Sci. Appl.* **2015**, *4*, No. e280.
(48) Millington, A. L.; Houskeeper, J. A.; Quackenbush, J. F.; Trauba, J. M.; Wittwer, C. T. The kinetic requirements of extreme qpcr. *Biomol. Detect. Quantif.* **2019**, *17*, 100081.
(49) Hasanzadeh Kafshgari, M.; Agiotis, L.; Largilliere, I.; Patskovsky, S.; Meunier, M. Antibody-functionalized gold nanostar-mediated on-resonance picosecond laser optoporation for targeted delivery of rna therapeutics. *Small* **2021**, *17* (19), 2007577.
(50) Lu, W.; Zhang, G.; Zhang, R.; Flores, L. G.; Huang, Q.; Gelovani, J. G.; Li, C. Tumor site-pecific silencing of NF-κ B p65 by targeted hollow gold nanosphere-mediated photothermal transfection. *Cancer Res.* **2010**, *70*, 3177−3188.
(51) Paunovska, K.; Loughrey, D.; Dahlman, J. E. Drug delivery systems for RNA therapeutics. *Nat. Rev. Genet.* **2022**, *23*, 265−280.
(52) Florentsen, C. D.; West, A.-K. V.; Danielsen, H. M. D.; Semsey, S.; Bendix, P. M.; Oddershede, L. B. Quantification of loading and laser-assisted release of RNA from single gold nanoparticles. *Langmuir* **2018**, *34*, 14891−14898.
(53) Wang, Z.; Li, S.; Zhang, M.; Ma, Y.; Liu, Y.; Gao, W.; Zhang, J.; Gu, Y. Laser-triggered small interfering rna releasing gold nanoshells against heat shock protein for sensitized photothermal therapy. *Adv. Sci.* **2017**, *4* (2), 1600327.
(54) Huo, S.; Gong, N.; Jiang, Y.; Chen, F.; Guo, H.; Gan, Y.; Wang, Z.; Herrmann, A.; Liang, X.-J. Gold-dna nanosunflowers for efficient gene silencing with controllable transformation. *Sci. Adv.* **2019**, *5* (10), No. eaaw6264.
(55) Graczyk, A.; Pawlowska, R.; Jedrzejczyk, D.; Chworos, A. Gold nanoparticles in conjunction with nucleic acids as a modern molecular system for cellular delivery. *Molecules* **2020**, *25* (1), 204.
(56) Fraire, J. C.; Houthaeve, G.; Liu, J.; Raes, L.; Vermeulen, L.; Stremersch, S.; Brans, T.; Garcia-Diaz Barriga, G.; De Keulenaer, S.; Van Nieuwerburgh, F.; et al. Vapor nanobubble is the more reliable photothermal mechanism for inducing endosomal escape of sirna without disturbing cell homeostasis. *J. Controlled Release* **2020**, *319*, 262−275.
(57) Huschka, R.; Barhoumi, A.; Liu, Q.; Roth, J. A.; Ji, L.; Halas, N. J. Gene silencing by gold nanoshell-mediated delivery and laser-triggered release of antisense oligonucleotide and sirna. *ACS Nano* **2012**, *6* (9), 7681−7691.
(58) Braun, G. B.; Pallaoro, A.; Wu, G.; Missirlis, D.; Zasadzinski, J. A.; Tirrell, M.; Reich, N. O. Laser-activated gene silencing via gold nanoshell- sirna conjugates. *ACS Nano* **2009**, *3* (7), 2007−2015.
(59) Krpetic, Z.; Nativo, P.; See, V.; Prior, I. A.; Brust, M.; Volk, M. Inflicting controlled nonthermal damage to subcellular structures by laser-activated gold nanoparticles. *Nano Lett.* **2010**, *10* (11), 4549−4554.
(60) Wang, Y.; Gao, Z.; Han, Z.; Liu, Y.; Yang, H.; Akkin, T.; Hogan, C. J.; Bischof, J. C. Aggregation affects optical properties and photothermal heating of gold nanospheres. *Sci. Rep.* **2021**, *11* (1), 898.
(61) Huschka, R.; Zuloaga, J.; Knight, M. W.; Brown, L. V.; Nordlander, P.; Halas, N. J. Light-induced release of dna from gold nanoparticles: nanoshells and nanorods. *J. Am. Chem. Soc.* **2011**, *133* (31), 12247−12255.
(62) de Miguel, I.; Prieto, I.; Albornoz, A.; Sanz, V.; Weis, C.; Turon, P.; Quidant, R. Plasmon-based biofilm inhibition on surgical implants. *Nano Lett.* **2019**, *19* (4), 2524−2529.
(63) Zharov, V. P.; Mercer, K. E.; Galitovskaya, E. N.; Smeltzer, M. S. Photothermal nanotherapeutics and nanodiagnostics for selective killing of bacteria targeted with gold nanoparticles. *Biophys. J.* **2006**, *90*, 619−627.
(64) Akouibaa, A.; Masrour, R.; Benhamou, M.; Derouiche, A. Thermoplasmonics Decontamination of Respirators Face Masks Using Silver Nanoparticles: A New Weapon in the Fight Against COVID-19 Pandemic. *Plasmonics* **2022**, *17* (6), 2307−2322.
(65) De Sio, L.; Ding, B.; Focsan, M.; Kogermann, K.; Pascoal-Faria, P.; Petronela, F.; Mitchell, G.; Zussman, E.; Pierini, F. Personalized reusable face masks with smart nano-assisted destruction of pathogens for covid-19: A visionary road. *Chem. - Eur. J.* **2021**, *27* (20), 6112−6130.
(66) Madrid, M.; Saklayen, N.; Shen, W.; Huber, M.; Vogel, N.; Mazur, E. Laser-activated self-assembled thermoplasmonic nanocavity substrates for intracellular delivery. *ACS Appl. Bio Mater.* **2018**, *1* (6), 1793−1799.
(67) Zhao, X.; Shi, Y.; Pan, T.; Lu, D.; Xiong, J.; Li, B.; Xin, H. In situ single-cell surgery and intracellular organelle manipulation via thermoplasmonics combined optical trapping. *Nano Lett.* **2022**, *22* (1), 402−410.
(68) Sutton, A.; Shirman, T.; Timonen, J. V. I.; England, G. T; Kim, P.; Kolle, M.; Ferrante, T.; Zarzar, L. D; Strong, E.; Aizenberg, J. Photothermally triggered actuation of hybrid materials as a new platform for in vitro cell manipulation. *Nat. Commun.* **2017**, *8* (1), 14700.
(69) Wang, J.; Qu, X.; Xu, C.; Zhang, Z.; Qi, G.; Jin, Y. Thermoplasmonic regulation of the mitochondrial metabolic state for promoting directed differentiation of dental pulp stem cells. *Anal. Chem.* **2022**, *94* (27), 9564−9571.
(70) Xiao, Y.; Peng, J.; Liu, Q.; Chen, L.; Shi, K.; Han, R.; Yang, Q.; Zhong, L.; Zha, R.; Qu, Y.; Qian, Z. Ultrasmall cus@ bsa nanoparticles with mild photothermal conversion synergistically induce mscs-differentiated fibroblast and improve skin regeneration. *Theranostics* **2020**, *10* (4), 1500.
(71) Marino, A.; Arai, S.; Hou, Y.; Degl'Innocenti, A.; Cappello, V.; Mazzolai, B.; Chang, Y.-T.; Mattoli, V.; Suzuki, M.; Ciofani, G. Gold nanoshell-mediated remote myotube activation. *ACS Nano* **2017**, *11* (3), 2494−2508.
(72) Andolfi, A.; Arnaldi, P.; Lisa, D. D.; Pepe, S.; Frega, M.; Fassio, A.; Lagazzo, A.; Martinoia, S.; Pastorino, L. A micropatterned thermoplasmonic substrate for neuromodulation of in vitro neuronal networks. *Acta Biomater.* **2023**, *158*, 281−291.

https://doi.org/10.1021/acs.nanolett.3c03548
Nano Lett. 2024, 24, 777−789

(73) Kang, H.; Hong, W.; An, Y.; Yoo, S.; Kwon, H.-J.; Nam, Y. Thermoplasmonic optical fiber for localized neural stimulation. *ACS Nano* **2020**, *14* (9), 11406−11419.
(74) Peng, H.; Borg, R. E.; Dow, L. P.; Pruitt, B. L.; Chen, I. A. Controlled phage therapy by photothermal ablation of specific bacterial species using gold nanorods targeted by chimeric phages. *Proc. Natl. Acad. Sci. U. S. A.* **2020**, *117* (4), 1951−1961.
(75) Kong, C.; Chen, X. Combined photodynamic and photothermal therapy and immunotherapy for cancer treatment: a review. *Int. J. Nanomed.* **2022**, *17*, 6427−6446.
(76) Guo, S.; Gu, D.; Yang, Y.; Tian, J.; Chen, X. Near-infrared photodynamic and photothermal co-therapy based on organic small molecular dyes. *J. Nanobiotechnol.* **2023**, *21* (1), 348.
(77) Lv, Z.; He, S.; Wang, Y.; Zhu, X. Noble metal nanomaterials for nir-triggered photothermal therapy in cancer. *Adv. Healthcare Mater.* **2021**, *10* (6), 2001806.
(78) Otero, C. M.; Simal, G. B.; Scocozza, M. F.; Rubert, A.; Grillo, C. A.; Hannibal, L.; Lavorato, G.; Huergo, M. A.; Murgida, D. H.; Vericat, C. Optimized biocompatible gold nanotriangles with nir absorption for photothermal applications. *ACS Appl. Nano Mater.* **2022**, *5* (1), 341−350.
(79) Fang, J. Epr effect-based tumor targeted nanomedicine: A promising approach for controlling cancer. *J. Pers. Med.* **2022**, *12* (1), 95.
(80) Longmire, M.; Choyke, P. L.; Kobayashi, H. Clearance properties of nano-sized particles and molecules as imaging agents: considerations and caveats. *Nanomedicine* **2008**, *3*, 703−717, DOI: 10.2217/17435889.3.5.703.
(81) Rastinehad, A. R.; Anastos, H.; Wajswol, E.; Winoker, J. S.; Sfakianos, J. P.; Doppalapudi, S. K.; Carrick, M. R.; Knauer, C. J.; Taouli, B.; Lewis, S. C.; et al. Gold nanoshell-localized photothermal ablation of prostate tumors in a clinical pilot device study. *Proc. Natl. Acad. Sci. U. S. A.* **2019**, *116* (37), 18590−18596.
(82) Ali, M. R. K.; Rahman, M. A.; Wu, Y.; Han, T.; Peng, X.; Mackey, M. A.; Wang, D.; Shin, H. J.; Chen, Z. G.; Xiao, H.; et al. Efficacy, long-term toxicity, and mechanistic studies of gold nanorods photothermal therapy of cancer in xenograft mice. *Proc. Natl. Acad. Sci. U. S. A.* **2017**, *114* (15), E3110−E3118.
(83) Liu, Y.; Mo, F.; Hu, J.; Jiang, Q.; Wang, X.; Zou, Z.; Zhang, X.-Z.; Pang, D.-W.; Liu, X. Precision photothermal therapy and photoacoustic imaging by in situ activatable thermoplasmonics. *Chem. Sci.* **2021**, *12* (29), 10097−10105.
(84) Muzzi, B.; Albino, M.; Gabbani, A.; Omelyanchik, A.; Kozenkova, E.; Petrecca, M.; Innocenti, C.; Balica, E.; Lavacchi, A.; Scavone, F.; et al. Star-shaped magnetic-plasmonic au@ fe3o4 nanoheterostructures for photothermal therapy. *ACS Appl. Mater. Interfaces* **2022**, *14* (25), 29087−29098.
(85) Henderson, L.; Neumann, O.; Kadria-Vili, Y.; Gerislioglu, B.; Bankson, J.; Nordlander, P.; Halas, N. J Plasmonic gadolinium oxide nanomatryoshkas: Bifunctional magnetic resonance imaging enhancers for photothermal cancer therapy. *PNAS Nexus* **2022**, *1* (4), pgac140.
(86) Griaznova, O. Yu.; Belyaev, I. B.; Sogomonyan, A. S.; Zelepukin, I. V.; Tikhonowski, G. V.; Popov, A. A.; Komlev, A. S.; Nikitin, P. I.; Gorin, D. A.; Kabashin, A. V.; Deyev, S. M. Laser synthesized core-satellite fe-au nanoparticles for multimodal in vivo imaging and in vitro photothermal therapy. *Pharmaceutics* **2022**, *14* (5), 994.
(87) Jeon, M.; Kim, G.; Lee, W.; Baek, S.; Jung, H. N.; Im, H.-J. Development of theranostic dual-layered au-liposome for effective tumor targeting and photothermal therapy. *J. Nanobiotechnol.* **2021**, *19*, 262.
(88) Wang, C.; Vazquez-Gonzalez, M.; Fadeev, M.; Sohn, Y. S.; Nechushtai, R.; Willner, I. Thermoplasmonic-triggered release of loads from dna-modified hydrogel microcapsules functionalized with au nanoparticles or au nanorods. *Small* **2020**, *16* (22), 2000880.
(89) Chen, R.; Shi, J.; Liu, C.; Li, J.; Cao, S. In situ self-assembly of gold nanorods with thermal-responsive microgel for multi-synergistic remote drug delivery. *Adv. Compos. Hybrid Mater.* **2022**, *5* (3), 2223−2234.
(90) Stoia, D.; Pop, R.; Campu, A.; Nistor, M.; Astilean, S.; Pintea, A.; Suciu, M.; Rugina, D.; Focsan, M. Hybrid polymeric therapeutic microcarriers for thermoplasmonic-triggered release of resveratrol. *Colloids Surf., B* **2022**, *220*, 112915.
(91) Zhao, Q.; Yang, Y.; Wang, H.; Lei, W.; Liu, Y.; Wang, S. Gold nanoparticles modified hollow carbon system for dual-responsive release and chemo-photothermal synergistic therapy of tumor. *J. Colloid Interface Sci.* **2019**, *554*, 239−249.
(92) Tao, W.; Cheng, X.; Sun, D.; Guo, Y.; Wang, N.; Ruan, J.; Hu, Y.; Zhao, M.; Zhao, T.; Feng, H.; et al. Synthesis of multi-branched au nanocomposites with distinct plasmon resonance in nir-ii window and controlled crispr-cas9 delivery for synergistic gene-photothermal therapy. *Biomaterials* **2022**, *287*, 121621.
(93) Sanati, M.; Khodagholi, F.; Aminyavari, S.; Ghasemi, F.; Gholami, M.; Kebriaeezadeh, A.; Sabzevari, O.; Hajipour, M. J.; Imani, M.; Mahmoudi, M.; Sharifzadeh, M. Impact of gold nanoparticles on amyloid β-induced alzheimer's disease in a rat animal model: Involvement of stim proteins. *ACS Chem. Neurosci.* **2019**, *10* (5), 2299−2309.
(94) Ali, M. R. K.; Wu, Y.; Tang, Y.; Xiao, H.; Chen, K.; Han, T.; Fang, N.; Wu, R.; El-Sayed, M. A. Targeting cancer cell integrins using gold nanorods in photothermal therapy inhibits migration through affecting cytoskeletal proteins. *Proc. Natl. Acad. Sci. U. S. A.* **2017**, *114* (28), E5655−E5663.

B.5 Filopodia: integrating cellular functions with theoretical models

Authors:
Victoria Thusgaard Ruhoff, Natascha Leijnse, Amin Doostmohammadi, and Poul Martin Bendix
Status: In press, published online

Trends in Cell Biology

CellPress

Review

Filopodia: integrating cellular functions with theoretical models

Victoria Thusgaard Ruhoff[1], Natascha Leijnse[1], Amin Doostmohammadi[1], and Poul Martin Bendix[1,*]

Filopodia, widely distributed on cell surfaces, are distinguished by their dynamic extensions, playing pivotal roles in a myriad of biological processes. Their functions span from mechanosensing and guidance to cell–cell communication during cellular organization in the early embryo. Filopodia have significant roles in pathogenic processes, such as cancer invasion and viral dissemination. Molecular mapping of the filopodome has revealed generic components essential for filopodia functions. In parallel, recent insights into biophysical mechanisms governing filopodia dynamics have provided the foundation for broader investigations of filopodia's biological functions. We highlight recent discoveries of engagement of filopodia in various stages of development and pathogenesis and present an overview of intricate molecular and physical features of these cellular structures across a spectrum of cellular activities.

Highlights

Filopodia are increasingly recognized as essential structures in various cellular processes such as embryogenesis, neurogenesis, and cardiogenesis, where they play a crucial role in signaling and coordinating morphogenetic events.

Viral infections, including severe acute respiratory syndrome coronavirus 2 (SARS-CoV-2), induce filopodia growth by reprogramming cell signaling pathways, thereby promoting the efficient spread of the virus.

Theoretical modeling offers fresh mechanistic insights into the dynamic functions of filopodia, elucidating processes such as retraction, pushing, and rotation.

The use of optical tweezers and molecular tension sensors enables a comprehensive mechanical examination, providing detailed insights into the forces acting along filopodia.

Diverse perspectives on filopodia function in cellular activities

Filopodia are thin, finger-like dynamic protrusions of the plasma membrane (100–300 nm in diameter [1]). They are filled with parallel bundles of crosslinked filamentous actin (F-actin) and typically have lengths ranging from 5 μm to several cell diameters. The dynamic actin-filled filopodia structure serves as a pivotal component in diverse cellular functions within metazoan cells. The conservation of a substantial portion of filopodial machinery throughout evolution [2] leads to generic phenotypes, as seen across different cell types. Sensing and guidance of, for example, neuronal cells, was originally discovered as a prominent task of filopodia, but recent findings have extensively expanded the repertoire of functions to include a host of chemical and mechanical tasks as well as transport of molecular, vesicular, and viral cargo between cells.

In this review we present an updated overview on the biological functions carried out by filopodia and provide examples from both developmental and differentiated cells, as well as from pathogenesis such as viral infection and cancer growth. First, we provide a short overview of some important and recently discovered functions of filopodia in cellular activities (Figures 1 and 2) followed by a description of the molecular and physical mechanisms that underlie filopodia dynamics (Figure 3). The main focus will be to provide a description of the chemical and physical processes within filopodia that are essential for filopodia functions and to integrate theoretical models with observed cellular functions. We keep the emphasis primarily on recently discovered functions of filopodia and **cytonemes** (see Glossary) and we do not focus on description of the molecular composition of filopodia (reviewed elsewhere [1,3]) or on cognate structures like **tunneling nanotubes (TNTs)**, **invadopodia, and podosomes** (also reviewed elsewhere [4,5]).

Filopodia are essential structures across all stages of life

Filopodia carry out their functions by dynamically pushing, pulling, and spatially exploring their three-dimensional (3D) environment through rotary movement to perform mechanical work and

[1]Niels Bohr Institute, University of Copenhagen, Blegdamsvej 17, 2100 København Ø, Denmark

*Correspondence: bendix@nbi.ku.dk (P.M. Bendix).

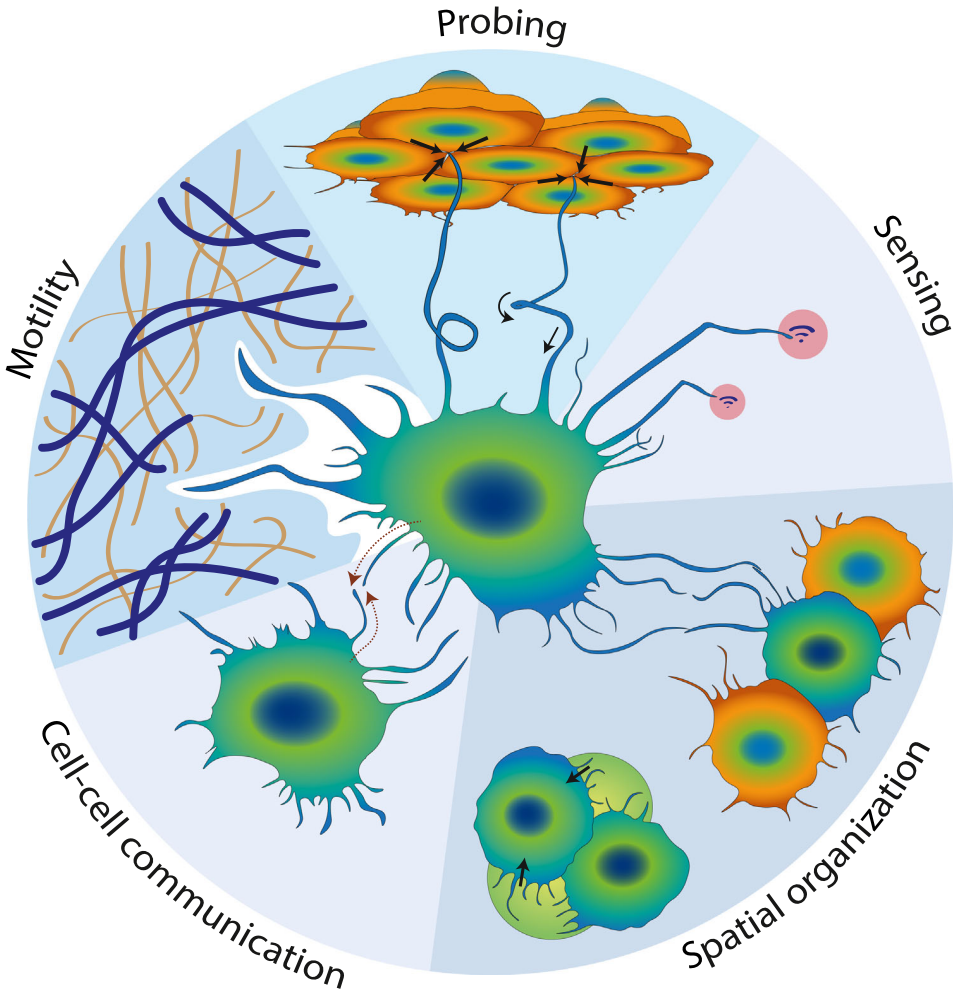

Cellular functions	Examples	Refs
Tissue reorganization	Embryonic compaction	(9, 16)
	Invadopodia in cancer invasion	(5)
	Multiciliated cell precursor remodel epithelial sheet	(17)
Cell-cell matching and communication	Cytonemes for cargo transport	(11, 13, 18–21)
	Cytonemes in development	(22, 23)
	Wound healing	(24–27)
	Model for assisting actin ring in wound closure	(28)
Pathogenesis	Viral spreading	(8, 29–34)
	Cancer metastasis	(15, 35)

Trends in Cell Biology

Figure 1. (Top illustration) Overview of cellular functions of filopodia. Filopodia are generic structures present in virtually all cell types and are responsible for cellular activities such as spatial organization, motility, probing, and transport of molecules, vesicles, and viruses. (Bottom table) Brief overview of specific work related to filopodia functions in various stages of life ranging from development to pathogenesis See [5,8,9,11,13,15–35].

Glossary

Brillouin microscopy: a label-free novel microscopy technique to measure the 3D viscoelastic properties of material including biological samples. It is based on scattering of light by material density (acoustic) waves which allows measurements of both relative stiffness and tension within the material.
Buckling: deformation of a material in response to a load (such as compression or shear) above a critical threshold.
Cytonemes: specialized types of long F-actin filled filopodia used for exchange of signalling molecules between cells.
E-cadherin: calcium dependent adhesion molecule found in adherens junctions which allow epithelial cells to adhere to each other.
Epithelial vertex: point in an epithelial cell layer where three or more cell boundaries meet.
Growth cone: Actin rich extension on neurites which guides the growth of an axon and assists the neurite in finding its synaptic target.
Hydrodynamic instability: an instability in the flow field of a fluid caused by a small perturbation which disturbs the regular stable flow.
Invadopodia and podosomes: Filopodia-like actin filled plasma membrane protrusions found in cancer cells which degrade the ECM during cancer invasion and metastasis by releasing extracellular matrix dissolving proteases. A characteristic of these structures is the existence of a ring of actin associated proteins at the base. These structures are much shorter than filopodia and their actin structure can include branched actin.
Kelvin-Voigt model: a viscoelastic model commonly used in rheology to describe the behavior of materials exhibiting both elastic and viscous properties. It incorporates a linear spring (representing elasticity) and a dashpot (representing viscosity) in parallel, allowing it to simulate both instantaneous deformation and delayed relaxation in response to applied stress.
Laser ablation: using laser light to remove material from a sample (e.g tissue) via generation of heat or plasma in the irradiated tissue.
Molecular clutch model: a theoretical framework used to describe how cells adhere to and exert forces on their surrounding environment during processes such as migration and tissue remodeling. It is based on the

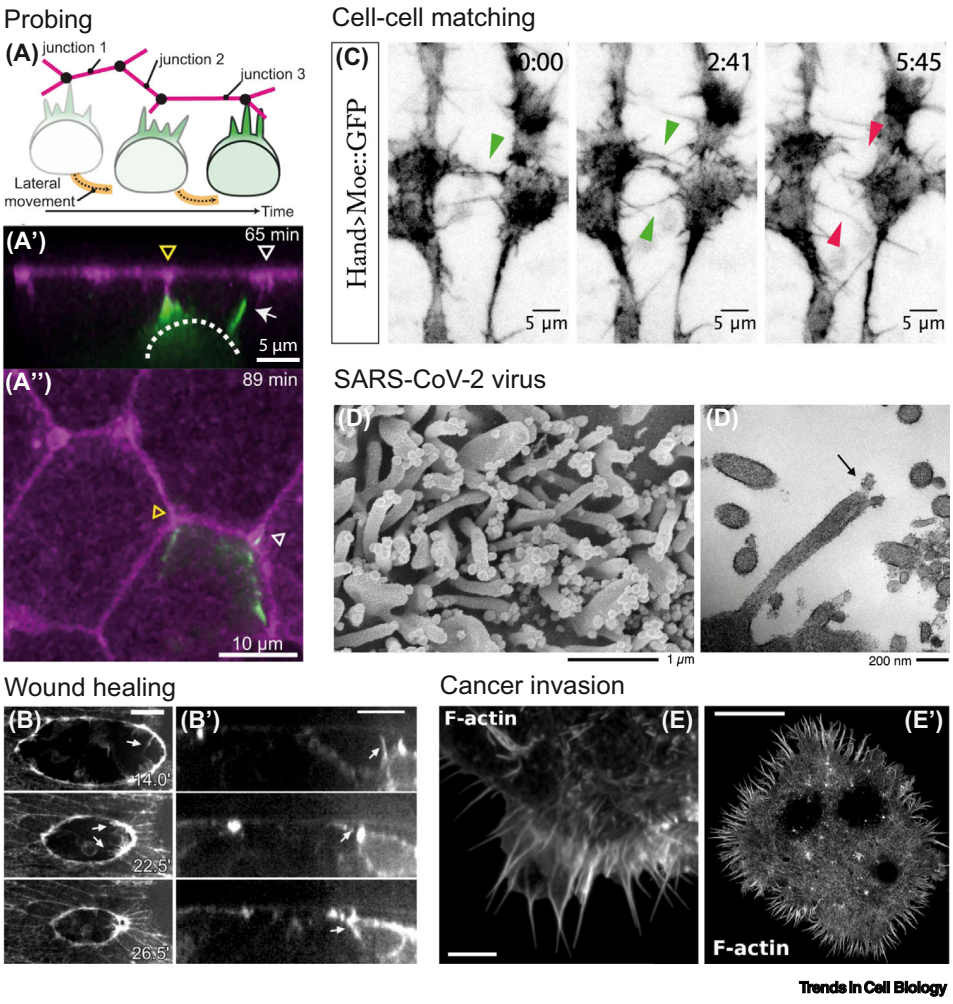

Figure 2. Biological examples of filopodia functions in various biological contexts. (A, A′, A″) Vertex probing carried out by multiciliated cell precursors (MCCs) from the *Xenopus* embryo. The MCCs (pseudocolor green, F-actin) mechanically probe the vertex stiffness of the epithelium (pseudocolor magenta, nectin) for decision-making prior to insertion. Reprinted, with permission, from [17]. (B, B') Filopodia of a stage 15 embryo (expression actin) exploring the gap during epithelial wound repair in *Drosophila*. Arrows point to filopodia. Scale bars 10 µm. Reprinted, with permission, from [24]. (C) Cell–cell matching during embryogenesis by embryonic wing heart precursor cells. Reprinted, with permission, from [47] (D, D') Budding of severe acute respiratory syndrome coronavirus 2 (SARS-CoV-2) virus from Vero E6 cell filopodia. Scanning electron microscopy image (D) and transmission electron microscopy (D') images showing the budding sites for SARS-CoV-2 virions. Reprinted, with permission, from [30]. (E, E') Total internal reflection microscopy improved using structural illumination of filopodia from MDA-MB-231 cancer cells and (E') from NK-92 natural killer cells (both stained for F-actin). Scale bars 5 µm (E) and 10 µm (E'). Reprinted, with permission, from [48].

convey extracellular biomechanical cues into the cell [6–8]. These abilities enable them to fulfill a vast variety of physiological and pathological roles ranging from chemical sensing, mechanical probing, and cell guidance to shaping and remodeling their environment. Filopodia also facilitate cell motility and can act as bridges that allow long-distance cell–cell communication (Figure 1). Next, we discuss the various roles of filopodia, grouped based on the developmental stages at which they occur: starting out with the role of filopodia in the compaction of early embryonic cells, before implantation [9], to guiding in **neurogenesis** [10], **morphogen** exchange via cytonemes [11–14], and the function of filopodia for motility in wound healing and cancer [15].

mechanism that cell adhesion molecules act like "clutches," dynamically engaging and disengaging to transmit mechanical forces between the cell's internal cytoskeleton and the extracellular matrix, to regulate cellular traction forces.
Molecular tension probe: a fluorescent probe which is sensitive to changes in molecular tensions. A common type of sensor is based on Fluorescent energy transfer (FRET) between a donor and acceptor fluorophore which are conjugated to the molecular system.
Morphogen: signalling molecule secreted by specific cell types during tissue development which instructs differentiation within the surrounding neighbourhood depending on its local, diffusion-dependent concentration. An example of a morphogen is SHH (Sonic Hedgehog).
Multiciliated cell precursors: Stem cells which have committed to develop into multiciliated cells which are specialized epithelial cells decorated with many motile cilia responsible for driving fluid flow across an epithelium.
Neurogenesis: formation of neurons in the brain during embryonal development as well as in later stages in life.
Optical trap: a device using focused light to hold (trap) a small object with a refractive index which is higher than the surrounding medium's refractive index.
Retrograde actin flow: the rearward movement of individual actin monomers which constitute an actin filament caused by continuous polymerization at the plus end in balance with depolymerizion at the minus end.
SARS-CoV-2: strain of severe-acute-respiratory-syndrome-related coronavirus (SARSr-CoV) which caused the Coronavirus disease 2019 (COVID-19) pandemic in 2019/20.
Tunneling nanotubes (TNTs) and airinemes: Filopodia-like long protrusion of the plasma membrane that connect cells over long distances and allow for organelle exchange. TNTs can contain actin filaments as well as microtubules and/or intermediate filaments. Airinemes are less straight than TNTs and are found in pigment cells from zebrafish.

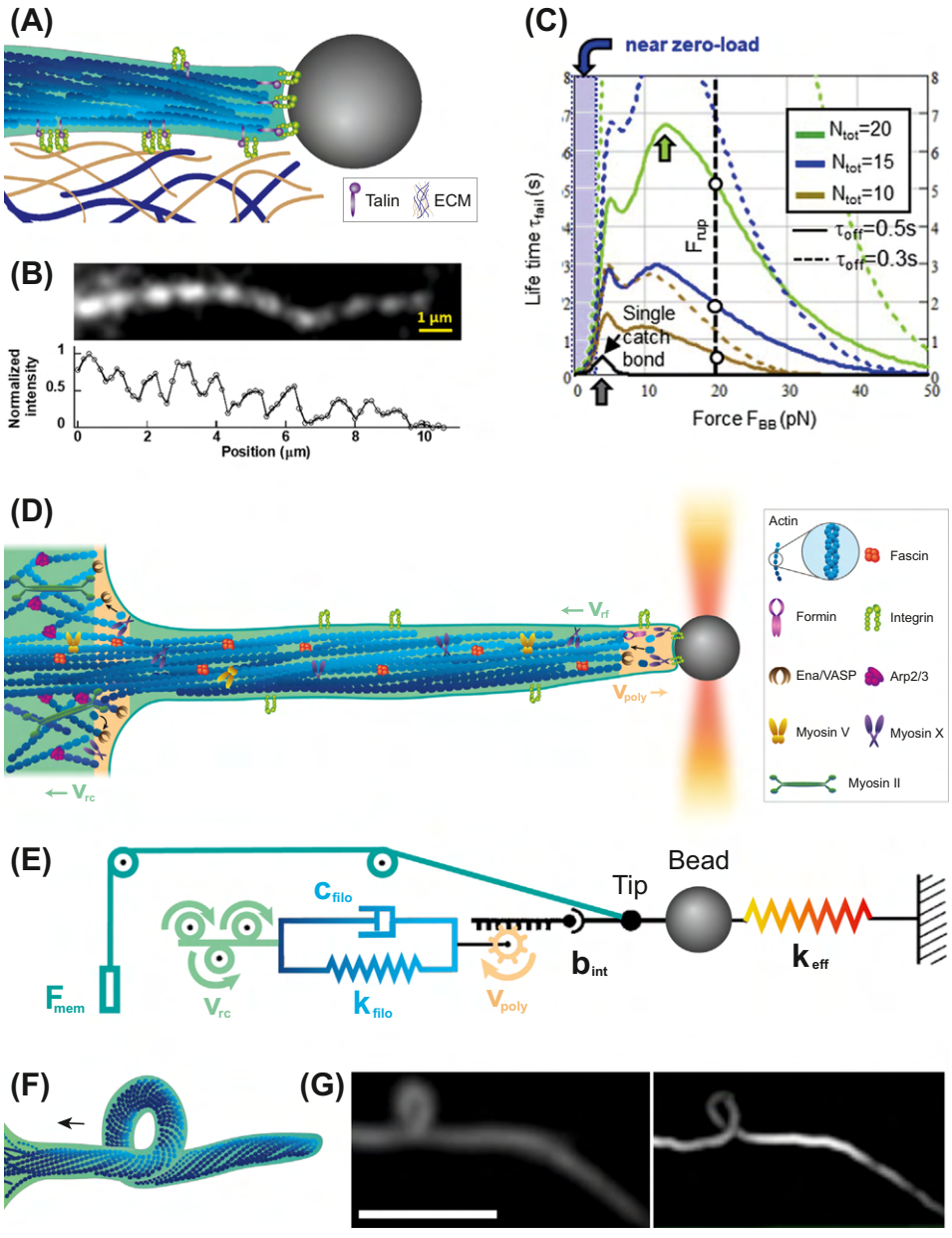

Trends in Cell Biology

Figure 3. Physical mechanisms underlying filopodia function. (A) Adhesive pulling by filopodia is regulated by a clutch mechanism based on talin/vinculin connecting integrins to the filopodial actin shaft. Activation of the adhesive clutch can lead to (B) traction on the substrate/extracellular matrix (ECM) induced by the retrograde flow [61] or a pushing force at the tip induced by polymerization at the tip while the actin is fixed at an adhesion point. The fluorescent nodes displayed in (B) represent a relatively higher force that originates from a filopodia integrin tension sensor, which emits light once the tension on the integrin exceeds 10 pN. (C) The strong dependence of bond life-time on tip forces and on off rates is demonstrated using mathematical modeling [63]. (D) Retrograde flow is driven by: (i) actin polymerization at the tip and depolymerization at the base, and (ii) frictional coupling of lamellipodium actin with the filopodium actin shaft, which is rooted in the lamellipodium. Filaments polymerizing against the plasma membrane provide a frictional force on the actin shaft and hence contribute to a pulling force extending into the filopodium [6]. (E) Kelvin-Voigt mechanical model of filopodia function capturing the physical effects present in (D) [6]. F_{mem} is the force due to the membrane tension, v_{rc} is the

(Figure legend continued at the bottom of the next page.)

Box 1. Molecular architecture and formation of filopodia

Actin filaments (F-actin), the main constituents of filopodia, consist of ATP bound G-actin monomers, which are added at the fast growing 'plus-end' (barbed end) located at the tip of the filopodium. The barbed end grows five to ten times faster than the minus end, thus contributing to **retrograde actin flow** [40]. Two models have been proposed to describe the initial step in filopodia formation: the 'convergent elongation model' and the 'tip nucleation model' [41]. The convergent elongation model [42] states that filopodia originate from the lamellipodium. The lamellipodial actin network is assembled through the nucleating activity of actin-related protein-2/3 (Arp2/3) complexes. Barbed end-associated elongation factors, such as formins and/or enabled/vasodilator-stimulated phosphoprotein (Ena/VASP) proteins assist to reorganize this actin network by promoting actin filament elongation and oligomerization. The tips of these filaments cluster at the plasma membrane (e.g., transported laterally by myosin X) and elongate together to protrude the plasma membrane. In contrast, the 'tip nucleation model' states that filopodia can form *de novo* from nucleation points on the plasma membrane, which contain clustered formins that directly produce elongating actin filaments. From here on, both models overlap: actin filament assembly at the tip is assisted by formins and Ena/VASP proteins, which are delivered by myosin X, and are both located at the fast-growing plus ends of F-actin, where they help attach new actin monomers to the filament and prevent capping proteins from stopping the elongation.

Membrane adaptor proteins with distinct molecular curvatures, such as IRSp53 (insulin-receptor substrate p53) [43,44], or other I-BAR domain-containing proteins, F-BAR or N-BAR, assemble at the nucleation point and at the tip to assist membrane bending. Some redundancy and stochasticity has been observed regarding which molecules should be present in an initiation complex for filopodia formation [45]. Interestingly, formation of filopodia-like structures was observed when pulling membrane tethers from active areas of cells [7,8,44], indicating that membrane deformation may be a sufficient cue to initiate the formation of a filopodium shaft.

When filopodia form, the polymerizing actin structure has to overcome the tension of the plasma membrane. Theoretical calculations have shown that at least a bundle of ten crosslinked actin filaments is needed in order to overcome the compressive force arising from the membrane tension [46]. Actin crosslinking proteins such as fascin or α-actinin are abundant in filopodia and prevent **buckling** by providing stiffness to the actin shaft.

The molecular architecture of filopodia enables diverse biological functions

Filopodia formation and dynamics require a complex regulation of molecular players (Box 1). The internal structure of filopodia differs depending on cell type; however, the main components, a crosslinked actin bundle of ~20 actin filaments, the plasma membrane, and membrane associated proteins are found in all filopodia. Actin filaments in filopodia are typically assumed to be continuous from the base to the tip and hence the major molecular activity is expected to take place at the tip region. However, in fast growing filopodia a more fragmented actin organization is found, as revealed by electron microscopy in *Dictyostelium discoideum* amoeba filopodia, which could contribute to remodeling activity along the filopodium [36]. This type of fragmentation was also observed in mouse catecholaminergic neuronal cells where the actin filaments in long filopodia were predominantly found to be short, with only 15% of them exceeding 1 µm in length [37]. Despite the simple geometry and nano-scale width of filopodia, the molecular complexity is high and we refer to recent literature for a more detailed overview of the mapped composition of filopodia [38] and the molecular architecture [1,3].

Reorganization of tissue by filopodia

One of the earliest known occurrence of filopodia is observed during early embryonic development, in the eight-cell stage. Long filopodia decorated with E-cadherin adhesion receptors are seen extending over neighboring cells, which pull cells together to enhance the contact areas between the cells and aid in the formation of the epithelial-like structure required for compaction [9]. Whether filopodia are able to directly deform or penetrate neighboring cells during compaction is uncertain,

velocity of cortical retrograde flow, k_{filo} is the stiffness of the filopodium, c_{filo} is the viscosity or dissipation in the filopodium, v_{poly} is the velocity of actin polymerization against the plasma membrane, and b_{int} and k_{eff} represent the filopodium-bead contact and optical trap stiffness, respectively. (F) Twist-induced helical buckling is frequently observed in filopodia and can, together with retrograde flow, lead to contraction and hence pulling [8,65]. (G) Z-projection of the 3-dimensional 3D volume containing a coiling filopodium (Gabor and Gaussian blur filtered) (left) and segmentation of the filopodium in a 3D view (obtained using the 'Simple Neurite Tracer' plugin in ImageJ) (right). Scale bar is 2 µm, adapted from [8].

but this has been observed for other cell types [39]. While no quantitative measure of the forces involved could be obtained during the compaction process, **laser ablation** of individual filopodia revealed shape changes, which clearly indicated that filopodia sustained tension needed to compact the embryo. Whether the filopodia are essential for generating the tension required for compaction was later questioned [16]. Instead, compaction of the early embryo was found to be driven by pulsatile cortical actomyosin contractions and found to be independent of both the presence of filopodia or neighboring cells (i.e., adhesion) [16].

Further research needs to be done to bridge these two important studies and to identify the exact role of filopodia in compaction of pre-implant embryos. Nevertheless, the presence of filopodia and their role in significantly deforming neighboring cells, as during embryonic compaction, is an interesting observation and implies that filopodia pushing could be more powerful than just merely overcoming the membrane tension barrier for protrusion. Alternatively, the actomyosin cortex of the neighboring cell could play a role in filopodia's ability to extend over neighboring cells, by providing traction on the invading filopodium. It is rare to see filopodia with strong protrusive forces that are able to deform adjacent cells or external stiff matrices. Such protrusive abilities are mostly observed for a cognate structure called invadopodia, which possesses this ability by invading extracellular matrices (ECMs) through chemical dissolution of the ECM near the tip [5].

A recent example of remodeling and reshaping of cellular junctions by filopodia was presented in **multiciliated cell precursors** in the *Xenopus* embryo. Filopodia were found to remodel the epithelia by both probing and remodeling the vertices of the overlying epithelial sheet (Figure 2A). The filopodia were employed by incoming cells to sense the **epithelial vertex** stiffness and thus identify the preferred positions for cell integration into the tissue. Subsequently, the filopodia additionally remodeled the vertices to facilitate integration into the tissue [17]. The presence of a filopodium-mediated traction force was inferred from laser ablation of cellular junctions leading to recoil movement of the neighboring vertices. Interestingly, integration of progenitor cells primarily took place at stiff vertices having higher order connections. This is an elegant example in which filopodia have dual functions involved in both remodeling and sensing of the architecture of the host cell layer.

Intercellular matching and communication is facilitated by filopodia

Specific cell–cell connections play a crucial role in coordination of morphogenetic processes in multicellular organisms. In addition to gap junctions, synapses, and TNTs, which are intercellular cell–cell communication structures, cells use specialized filopodia, called cytonemes, to form contacts between distant cells. Cytonemes [13,18,49], are one example of long-range actin-rich filopodia-like structures reaching up to 150 μm in length and are capable of transporting signaling components to neighboring cells via ligand-receptor-mediated transfer of surface-associated cargoes such as morphogens (e.g., Sonic Hedgehog [11,19]) and growth factors (e.g., Wnt [20,21]), which are essential regulators of cell proliferation, differentiation, and oncogenesis. In addition, cytonemes are essential for brain development through a tight coupling between angiogenesis and neurogenesis. Cytonemes growing from endothelial cells on nascent blood vessels couple with cytonemes from neural stem cells and have been found to fine-tune the behavior of the neural stem cells [22]. The importance of neurovascular cytonemes in regulation of brain development was also observed [23], where blood flow acted as a switch to control cytoneme contact between endothelial cells and neuroblasts, which was found to regulate neuroblast differentiation.

Wound healing constitutes a masterpiece of tissue remodeling in which filopodia play a pivotal role in knitting the wound together during the final stage of closure, as observed in *Drosophila* [24,25] (Figure 2B) and mammalian cells [26]. The initial phase of wound closure involves assembly and contraction of a supracellular 'purse string' structure, which is a continuous actomyosin

ring extending from cell to cell at the wound periphery [24]. At the final stages of wound closure filopodia reach out and pair with contralateral cells on the opposing side and seamlessly knit the wound together [24,25]. Interestingly, microtubules were found inside filopodia during wound healing in *Drosophila* embryos, which may facilitate stronger pushing forces than by actin polymerization alone [24]. In ctenophores, filopodia were also found to grow laterally, connecting to neighboring cells during the early phase of wound closure, whereas during the final stages of closure, filopodia growth was perpendicular to the cell surface [27]. The exact mechanical function of filopodia with respect to the actomyosin ring in wound closure is still debated. Mathematical modeling suggested that protrusions from the edge had a fluidizing effect on the periphery and could relieve the tension that builds up during contraction of the actomyosin ring [28].

Filopodia's role in the process of dorsal closure during *Drosophila* embryo development bears some resemblance to filopodia during wound closure. Collective cell migration facilitates closure of the epidermal sheet, concluding with filopodia reaching out to connect with opposing filopodia growing from the contralateral side of the gap. However, a primary role of these filopodia is instead to ensure proper cell matching [47] (Figure 2C). Differential cell adhesion across the gap is facilitated by expression of adhesion molecules with different strengths, thus allowing specific pairing of cells necessary for normal embryogenesis.

Measurements of the filopodia interactions during cell–cell pairing processes taking place in neurogenesis, angiogenesis, and epithelial closures are difficult to obtain using traditional force measurements with, for example, **optical traps**. However, new developments in optics like **Brillouin microscopy** can directly image mechanical stresses in tissues [50] and the development of fluorescence-based force sensors [51] may provide useful tools for detection of stresses during closure of epithelial gaps. Such measurements have the potential to answer outstanding questions on whether filopodia are actually providing a pulling force to seal the remaining gap or whether filopodia may act merely as chemical sensory antennae searching for signals and guiding the lamellipodium towards the correct opposing cell.

Filopodia play critical roles in pathogenesis

The intricate molecular machinery of filopodia and their ability to establish connections between cells constitutes a dynamic platform for the initiation and progression of diseases. Filopodia are shown to play a role in important pathogenic processes such as viral entry [30] and rapid tissue invasion during metastasis [35]. Investigating how viruses utilize filopodia for efficient viral entry and viral dissemination and how filopodia facilitate rapid tissue invasion by metastatic cells can provide insight into potential therapeutic strategies for combating viral infections and impeding cancer metastasis.

Manipulation of the cellular cytoskeleton by viruses. Filopodia play a significant role in viral spread and infection, serving as conduits for viral entry and transport between host cells [52]. Several viruses, such as severe acute respiratory syndrome coronavirus 2 **(SARS CoV-2)**, Ebola, vaccinia, and Marburg have been found to hijack cellular functions like internal signaling and the cytoskeletal machinery [29,30]. Following infection, cells may produce unusually long, highly branched filopodia, which are more efficient for intercellular spreading of viruses, as seen for SARS-CoV-2 in a non-human cell line [30]. Also, the number of filopodia per cell increases following cellular contact with human papillomavirus (HPV)16 viruses and the rates of infection were found to correlate with the presence of high number of filopodia [53].

Virions are found to be transported towards the cell body by 'surfing' along filopodia [54,55] or by filopodia 'grabbing' facilitated by retraction or actin retrograde flow [56]. Viruses can also hijack myosin motors to become actively transported towards the tip of filopodia [31] and ultrastructure

images of infected cells show how new virus particles indeed also bud from the tip [30] (Figure 2D) in a similar fashion as observed with shedding of extracellular vesicles from macrophage filopodia tips [32]. Viruses tweak the cellular biochemistry and cytoskeleton to improve the chance of infecting neighboring cells by rewiring the signaling through phosphorylation of proteins. Further research should be focused on identifying the molecular interactions between viruses and the filopodium to identify the surface receptors involved and the connectivity to the internal actin shaft, inspired by recent research showing that synthetic particles, connected to the internal actin shaft through the transmembrane integrin receptor [8], can be used as a model system for viruses surfing on a filopodium.

Guiding metastatic cells. In the context of cancer, filopodia have emerged as key players in promoting invasion and metastasis through their ability to facilitate adhesion and sensing of the environment. Their ability to sense and navigate the microenvironment allows cancer cells to invade surrounding tissues and disseminate to distant sites, much like immune cells (Figure 2E and E') [48]. Invasiveness of cancer cells correlates with filopodia number and clinical outcomes negatively correlate with upregulation of filopodia-specific proteins such as integrins, myosin X, and fascin [15]. Myosin X transports integrins towards the tip and enables the cell to establish adhesion sites in 3D matrices. These adhesion sites then allow the cell to probe the stiffness of the ECM, which has been shown to be an important factor in cancer invasiveness [35]. Overall, filopodia have a pivotal role in cancer invasion, together with other protrusive structures like invadopodia. Understanding how filopodia adhere to the ECM and use mechanosensing (e.g., through calcium signaling) [57] to probe the ECM stiffness, provides a promising direction for therapeutic interventions [58].

Physical models of filopodia dynamics

The interplay between mechanical behavior and molecular components in the function and formation (Box 1) of filopodia has been investigated both experimentally and theoretically. Physical movements of filopodia include traction, pushing, rotation, and sideward movement. The forces involved in filopodia retraction have been shown to originate from actomyosin dynamics taking place within the filopodium and at the lamellipodium.

Actomyosin activity governs filopodia function

Filopodial actin exhibits continuous retrograde flow driven by actin polymerization and motor activity within the lamellipodium. Tip polymerization and depolymerization at the base alone lead to retrograde movement of the actin and, additionally, the retrograde activity within the lamellipodium contributes to the rearward pulling of the actin within the filopodium. Retrograde movement within the filopodium continues until adhesive contacts are established along the filopodium, thus leading to arrest of the retrograde flow. The adhesive contact has been modeled as a **molecular clutch** mechanism that triggers tip elongation of the actin structure due to simultaneous fixation of the actin bundle to the substrate combined with actin polymerization at the tip. Differential adhesive contact among different filopodia was suggested as a mechanism for guided growth of **growth cones**, leading to amplified elongation along those filopodia, which established substrate adhesive points [59]. Activation of the clutch, mediated by contact with the adhesive substrate, also leads to force transduction to the substrate, which has been quantified experimentally [60,61]. The force transduced to the substrate has been shown to be periodically spaced along the filopodium with a period of 1 μm and was found to originate from retrograde forces due to its dependence on both actin polymerization and myosin II (Figure 3A,B) [61]. Additionally, myosin IIa has also been found to be involved in formin dependent mechanosensitivity during filopodia adhesion [62]. Force measurements at the filopodium tip have revealed a tip clutch mechanism based on interactions between actin and the mechanosensitive talin/integrin complex [63]. These interactions displayed catch bond behavior, which exhibited load-dependent strength (Figure 3C).

Filopodia generate significant traction. A direct relation between the actin polymerization and the generated filopodia traction has been demonstrated [6,8]. Polymerization of actin against the lamellipodium plasma membrane was found to generate a traction force due to frictional coupling between the cortical actin network and the actin shaft, which is often deeply rooted in the lamellipodium [6] (Figure 3D,E). This mechanism was captured in a proposed **Kelvin-Voigt mechanical model** of filopodia retraction, which also includes other effects such as polymerization at the tip and the passive membrane tension. The frictional coupling can be facilitated through the actin branching protein Arp2/3 and possibly through myosin motors [6], (Figure 3D). Sensitive measurements of the pulling force in macrophages additionally revealed a stepwise retraction with step length of 36 ± 13 nm (mean ± standard deviation), which could indicate involvement of molecular motors or simultaneous depolymerization of chunks of actin filaments [64]. Indeed, a simple mathematical model predicted an involvement of a stepwise motor in the pulling force, but silencing of several myosins and inhibition of myosin II using blebbistatin did not eliminate the stepwise pulling observed in macrophages [64]. Therefore, from these studies it remains enigmatic how molecular motors contribute to the retraction force in macrophage filopodia. We also emphasize that other recently discovered mechanisms, such as internal twist within the actin structure, are also contributing to the retraction force (Box 2).

Measured filopodia forces are in the range of tens of piconewtons, which are typically obtained using optical tweezers to trap a bead that is attached to the tip of the filopodium. The measured force is limited by the strength of the tip conjugation to the trapped bead. However, traction force measurements in substrate-attached filopodia, which are more firmly attached along the whole filopodium length, revealed very large forces reaching nanonewton range for macrophages [66]. A more detailed probe of the molecular tension along a single filopodium can be obtained using a **molecular tension probe** [61] (Figure 3A,B).

Filopodia pushing is limited by buckling instability. The pushing effect of filopodia is also activated by the clutch mechanism constituted by the simultaneous adhesion to the substrate and tip polymerization. This force is typically much lower than the magnitude of the pulling force and originates from the polymerization of actin at the tip. Biologically, a pushing mechanism is necessary

Box 2. Filopodia rotation and buckling

Recent work has revealed that filopodia frequently exhibit interesting signatures of helical shapes [7,8], (see Figure 2F,G in the main text). Theoretical predictions have suggested such shape transitions of the actin shaft should occur due to the compressive force from the membrane tension [65], however, the buckling still takes place when the force from the membrane tension is relieved by using an optical trap at the tip [7]. This implies that it is not the compressive force from the membrane that is responsible for the buckling. Instead another intrinsic mechanism for buckling could be the axial rotation or twisting of the actin shaft, which is emerging as a generic property of filopodia dynamics [7,8]. The axial twist in straight filopodia was confirmed by optically trapping single filopodia that contained a tracer particle on the side, linked to the actin core through a vitronectin-integrin bond. Such particles move along with the retrograde flow towards the cell body along a spiral path, revealing a rotating shaft. Free filopodia also showed a similar rotational movement with periods of approximately 3 minutes. To explain this rotary or twisting behavior of filopodia the acto-myosin was modeled as an active material, which was confined in a space mimicking the confinement posed by the filopodial tubular membrane. A rotational twist in the structure emerged due to a **hydrodynamic instability activated by the twisting deformation of model filaments. The molecular activity within filopodia that causes this hydrodynamic instability could arise from myosin V** [67] and myosin X [68], which are frequently found at the base of filopodia or inside filopodia at high densities [68,69]. These myosins have the ability to walk around actin bundles filopodium along a helical and anticlockwise path towards the tip [70,71]. This chirality of myosin transport is consistent with a predominant clockwise rotation of filopodia measured experimentally for both neuronal cells [67,72] and cancer cell lines [8]. Indeed, silencing these motors resulted in slower rotations in HEK293 cells, thus suggesting the contribution of these motors to the twist.

The effect of molecular motors on filopodia dynamics is still poorly understood and further studies should focus on biomechanical single molecule studies of myosins to reveal how they contribute to retraction force and shape instabilities. An interesting observation was recently reported on chiral growth of filopodia observed in substrate-attached cells, which was attributed to spiral movement of motors (myosin X) around the actin shaft [73]. Whether filopodia rotations and 2D chiral growth of filopodia have some common mechanism is currently not understood.

for filopodia elongation and the magnitude of pushing measured in neuronal growth cone filopodia reached as high as 20 pN [74]. Moreover, in processes like the compaction of embryos, in which filopodia reach over neighboring cells [9], some initial protrusive force is expected, which is hard to assess experimentally. The instability against buckling of extending filopodia has been modeled by considering factors such as G-actin diffusion to the tip, the buckling resistance of the bundled actin shaft, and the membrane tension [46]. However, this model can only predict stable and straight filopodia of a few micrometers and hence cannot explain the types of filopodia or cytonemes that have been observed to extend several cell diameters [14,75]. It remains an open question how these long actin bundles can sustain a straight shape against the membrane tension.

Taken together, recent progress has made it evident that actomyosin dynamics in filopodia is governing filopodia function during development and in pathogenesis.

Novel approaches for investigating filopodia

Detailed investigations of filopodia functions have primarily been carried out using advanced optics and smart substrates that allow quantification of minuscule forces during, for example, sensing of chemical and mechanical cues [60,63]. Still, most quantitative measurements have been conducted on isolated cells; however, new developments in optics and substrate synthesis will likely provide insight into the intercellular function of filopodia structures in their native environment. Already, Brillouin microscopy can map local stress generation in tissues [50] and fluorescent energy transfer (FRET) sensors can give extremely detailed information regarding molecular tension at cell junctions [76]. Alternatively, synthetic reconstitution of filopodia-like structures in vesicle systems [44,77] can enhance our understanding, however, more work is needed to shed light on the minimal machinery and protein components needed to initiate a filopodium. More advanced reconstitution should include myosin motors, adhesion molecules, membrane-shaping proteins, and dynamic actin polymerization/depolymerization with the aim of recapitulating dynamic behaviors such as retraction and rotation. One challenge here is to encapsulate the molecular ensemble in membrane vesicles, but recent work has provided solutions for encapsulation of larger structures [78,79].

Concluding remarks

Filopodia are continuously identified in diverse cell types and are found to be responsible for an increasing number of functions, such as mechanochemical sensing, force production, and cell guidance. While filopodia are found across virtually all cell types, future studies should be focused on differences between these filopodia and on elucidating common principles behind their fundamental functions, despite the various context they appear in. Additionally, mapping the functions of individual molecular components is critical; however, we also emphasize the need for physical modeling of filopodia, which has provided significant insight into filopodia function arising from collective self-organization of actin-motor protein complexes [6,8].

Finally, filopodia also play a pivotal role in cellular disorders, such as in cancer and for viral infections. Cancer cells use filopodia for efficient invasion of tissue and seem to copy the strategies seen for immune cells, which need similar ability to invade tissue for their repair. Viruses seem to take advantage of the ability of filopodia to spread signals and material among cells and infected cells are found to be upregulated in terms of filopodia number and lengths. Many questions remain unanswered (see Outstanding questions) and the importance of filopodia in pathogenesis highlights the importance of pinpointing the molecular components involved and also elucidates the possibility of discovering therapeutics preventing viruses and cancer cells from hijacking the filopodia.

Outstanding questions

What is the role of filopodia in mechanosensing and transducing external mechanical cues into cellular responses?

How do abnormalities in filopodia formation and function contribute to diseases such as cancer, neurodegenerative disorders, or other pathologies?

Can targeting filopodia be a viable therapeutic strategy for interfering with virus transmission or cancer metastasis?

How do very long filopodia (>70 micrometers) sustain from buckling under the compressive load from the plasma membrane tension?

What is the role of filopodia during embryonic compaction?

Do filopodia have the ability to penetrate neighboring cells?

How diverse are filopodia across cell types in terms of mechanism and composition?

Is the fragmented or continuous structure of actin in filopodia cell type specific?

Acknowledgments

P.M.B. acknowledges funding from the Novo Nordisk Foundation (grant nos. NFF20OC0065357 and NFF20OC0061176). A.D. acknowledges funding from the Novo Nordisk Foundation (grant no. NNF18SA0035142 and NERD grant no. NNF21OC0068687), Villum Fonden grant no. 29476, and the European Union via the ERC-Starting Grant PhysCoMeT, grant no. 101041418.

Declaration of interests

The authors declare no competing financial interests.

References

1. Mattila, P.K. and Lappalainen, P. (2008) Filopodia: molecular architecture and cellular functions. *Nat. Rev. Mol. Cell Biol.* 9, 446–454
2. Sebé-Pedrós, A. *et al.* (2013) Insights into the origin of metazoan filopodia and microvilli. *Mol. Biol. Evol.* 30, 2013–2023
3. Blake, T.C.A. and Gallop, J.L. (2023) Filopodia in vitro and in vivo. *Annu. Rev. Cell Dev. Biol.* 39, 307–329
4. Zurzolo, C. (2021) Tunneling nanotubes: reshaping connectivity. *Curr. Opin. Cell Biol.* 71, 139–147
5. Linder, S. *et al.* (2023) Mechanisms and roles of podosomes and invadopodia. *Nat. Rev. Mol. Cell Biol.* 24, 86–106
6. Bornschlögl, T. *et al.* (2013) Filopodial retraction force is generated by cortical actin dynamics and controlled by reversible tethering at the tip. *Proc. Natl. Acad. Sci. U. S. A.* 110, 18928–18933
7. Leijnse, N. *et al.* (2015) Helical buckling of actin inside filopodia generates traction. *Proc. Natl. Acad. Sci. U. S. A.* 112, 136–141
8. Leijnse, N. *et al.* (2022) Filopodia rotate and coil by actively generating twist in their actin shaft. *Nat. Commun.* 13, 1636
9. Fierro-González, J.C. *et al.* (2013) Cadherin-dependent filopodia control preimplantation embryo compaction. *Nat. Cell Biol.* 15, 1424–1433
10. Wit, C.B. and Hiesinger, P.R. (2023) Neuronal filopodia: from stochastic dynamics to robustness of brain morphogenesis. *Semin. Cell Dev. Biol.* 133, 10–19
11. Sanders, T.A. *et al.* (2013) Specialized filopodia direct long-range transport of SHH during vertebrate tissue patterning. *Nature* 497, 628–632
12. Daly, C.A. *et al.* (2022) Regulatory mechanisms of cytoneme-based morphogen transport. *Cell. Mol. Life Sci.* 79, 119
13. Zhang, C. and Scholpp, S. (2019) Cytonemes in development. *Curr. Opin. Genet. Dev.* 57, 25–30
14. Kornberg, T.B. (2017) Distributing signaling proteins in space and time: the province of cytonemes. *Curr. Opin. Genet. Dev.* 45, 22–27
15. Jacquemet, G. *et al.* (2015) Filopodia in cell adhesion, 3D migration and cancer cell invasion. *Curr. Opin. Cell Biol.* 36, 23–31
16. Maître, J.-L. *et al.* (2015) Pulsatile cell-autonomous contractility drives compaction in the mouse embryo. *Nat. Cell Biol.* 17, 849–855
17. Ventura, G. *et al.* (2022) Multiciliated cells use filopodia to probe tissue mechanics during epithelial integration in vivo. *Nat. Commun.* 13, 6423
18. Korenkova, O. *et al.* (2020) Fine intercellular connections in development: TNTs, cytonemes, or intercellular bridges? *Cell Stress* 4, 30
19. Gonzalez-Mendez, L. *et al.* (2017) Cytoneme-mediated cell-cell contacts for hedgehog reception. *Elife* 6, e24045
20. Routledge, D. *et al.* (2022) The scaffolding protein flot2 promotes cytoneme-based transport of wnt3 in gastric cancer. *Elife* 11, e77376
21. Brunt, L. *et al.* (2021) Vangl2 promotes the formation of long cytonemes to enable distant wnt/β-catenin signaling. *Nat. Commun.* 12, 2058
22. Di Marco, B. *et al.* (2020) Reciprocal interaction between vascular filopodia and neural stem cells shapes neurogenesis in the ventral telencephalon. *Cell Rep.* 33, 108256
23. Taberner, L. *et al.* (2020) Sensory neuroblast quiescence depends on vascular cytoneme contacts and sensory neuronal differentiation requires initiation of blood flow. *Cell Rep.* 32, 107903
24. Abreu-Blanco, M.T. *et al.* (2012) *Drosophila* embryos close epithelial wounds using a combination of cellular protrusions and an actomyosin purse string. *J. Cell Sci.* 125, 5984–5997
25. Rothenberg, K.E. and Fernandez-Gonzalez, R. (2019) Forceful closure: cytoskeletal networks in embryonic wound repair. *Mol. Biol. Cell* 30, 1353–1358
26. Miles, R.R. *et al.* (2021) The eIF2 kinase GCN2 directs keratinocyte collective cell migration during wound healing via coordination of reactive oxygen species and amino acids. *J. Biol. Chem.* 297, 101257
27. Ramon-Mateu, J. *et al.* (2019) Regeneration in the ctenophore *Mnemiopsis leidyi* occurs in the absence of a blastema, requires cell division, and is temporally separable from wound healing. *BMC Biol.* 17, 1–25
28. Staddon, M.F. *et al.* (2018) Cooperation of dual modes of cell motility promotes epithelial stress relaxation to accelerate wound healing. *PLoS Comput. Biol.* 14, e1006502
29. Leite, F. and Way, M. (2015) The role of signalling and the cytoskeleton during vaccinia virus egress. *Virus Res.* 209, 87–99
30. Bouhaddou, M. *et al.* (2020) The global phosphorylation landscape of SARS-CoV-2 infection. *Cell* 182, 685–712
31. Matozo, T. *et al.* (2022) Myosin motors on the pathway of viral infections. *Cytoskeleton* 79, 41–63
32. Zhu, X. *et al.* (2023) Macrophages release IL11-containing filopodial tip vesicles and contribute to renal interstitial inflammation. *Cell Commun. Signal.* 21, 293
33. Heusermann, W. *et al.* (2016) Exosomes surf on filopodia to enter cells at endocytic hot spots, traffic within endosomes, and are targeted to the ER. *J. Cell Biol.* 213, 173–184
34. Salas, N. *et al.* (2023) Role of cytoneme structures and extracellular vesicles in *Trichomonas vaginalis* parasite-parasite communication. *Elife* 12, e86067
35. Jahin, I. *et al.* (2023) Extracellular matrix stiffness activates mechanosensitive signals but limits breast cancer cell spheroid proliferation and invasion. *Front. Cell Dev. Biol.* 11, 1292775
36. Medalia, O. *et al.* (2007) Organization of actin networks in intact filopodia. *Curr. Biol.* 17, 79–84
37. Sartori-Rupp, Anna A. *et al.* (2019) Correlative cryo-electron microscopy reveals the structure of TNTs in neuronal cells. *Nat. Commun.* 10, 342
38. Jacquemet, G. *et al.* (2019) Filopodome mapping identifies p130Cas as a mechanosensitive regulator of filopodia stability. *Curr. Biol.* 29, 202–216
39. Frei, D.M. *et al.* (2015) Novel microscopy-based screening method reveals regulators of contact-dependent intercellular transfer. *Sci. Rep.* 5, 12879
40. Cooper, G.M. (2000) Structure and organization of actin filaments. In *The cell: a molecular approach* (2), pp. 445–446
41. Yang, C. and Svitkina, T. (2011) Filopodia initiation: focus on the Arp2/3 complex and formins. *Cell Adhes. Migr.* 5, 402–408
42. Svitkina, T.M. *et al.* (2003) Mechanism of filopodia initiation by reorganization of a dendritic network. *J. Cell Biol.* 160, 409–421
43. Scita, G. *et al.* (2008) Irsp53: crossing the road of membrane and actin dynamics in the formation of membrane protrusions. *Trends Cell Biol.* 18, 52–60
44. Tsai, F.-C. *et al.* (2022) Activated I-BAR IRSp53 clustering controls the formation of VASP-actin–based membrane protrusions. *Sci. Adv.* 8, eabp8677
45. Dobramysl, U. *et al.* (2021) Stochastic combinations of actin regulatory proteins are sufficient to drive filopodia formation. *J. Cell Biol.* 220, e202003052
46. Mogilner, A. and Rubinstein, B. (2005) The physics of filopodial protrusion. *Biophys. J.* 89, 782–795
47. Zhang, S. *et al.* (2018) Selective filopodia adhesion ensures robust cell matching in the *Drosophila* heart. *Dev. Cell* 46, 189–203
48. Jacquemet, G. *et al.* (2017) Filoquant reveals increased filopodia density during breast cancer progression. *J. Cell Biol.* 216, 3387–3403

49. Casas-Tintó, Sergio and Portela, Marta (2019) Cytonemes, their formation, regulation, and roles in signaling and communication in tumorigenesis. *Int. J. Mol. Sci.* 20, 5641
50. Prevedel, R. *et al.* (2019) Brillouin microscopy: an emerging tool for mechanobiology. *Nat. Methods* 16, 969–977
51. Eder, D. *et al.* (2017) Challenging FRET-based E-cadherin force measurements in *Drosophila*. *Sci. Rep.* 7, 13692
52. Chang, K. *et al.* (2016) Filopodia and viruses: an analysis of membrane processes in entry mechanisms. *Front. Microbiol.* 7, 300
53. Biondo, A. and Meneses, P.I. (2022) The process of filopodia induction during HPV infection. *Viruses* 14, 1150
54. Chang, K. *et al.* (2022) Induction of filopodia during cytomegalovirus entry into human iris stromal cells. *Front. Microbiol.* 13, 834927
55. Lehmann, M.J. *et al.* (2005) Actin-and myosin-driven movement of viruses along filopodia precedes their entry into cells. *J. Cell Biol.* 170, 317–325
56. Zhang, Y. *et al.* (2023) Single particle tracking reveals SARS-CoV-2 regulating and utilizing dynamic filopodia for viral invasion. *Sci. Bull.* 68, 2210–2224
57. Efremov, A.K. *et al.* (2022) Application of piconewton forces to individual filopodia reveals mechanosensory role of L-type Ca2+ channels. *Biomaterials* 284, 121477
58. Winkler, J. *et al.* (2020) Concepts of extracellular matrix remodelling in tumour progression and metastasis. *Nat. Commun.* 11, 5120
59. Kerstein, P.C. *et al.* (2015) Mechanochemical regulation of growth cone motility. *Front. Cell. Neurosci.* 9, 244
60. Chan, C.E. and Odde, D.J. (2008) Traction dynamics of filopodia on compliant substrates. *Science* 322, 1687–1691
61. Tu, Y. *et al.* (2022) Filopodial adhesive force in discrete nodes revealed by integrin molecular tension imaging. *Curr. Biol.* 32, 4386–4396
62. Alieva, N.O. *et al.* (2019) Myosin iia IIA and formin dependent mechanosensitivity of filopodia adhesion. *Nat. Commun.* 10, 3593
63. Michiels, R. *et al.* (2022) Pulling, failing, and adaptive mechanotransduction of macrophage filopodia. *Biophys. J.* 121, 3224–3241
64. Kress, H. *et al.* (2007) Filopodia act as phagocytic tentacles and pull with discrete steps and a load-dependent velocity. *Proc. Natl. Acad. Sci. U. S. A.* 104, 11633–11638
65. Pronk, S. *et al.* (2008) Limits of filopodium stability. *Phys. Rev. Lett.* 100, 258102
66. Zidovska, A. and Sackmann, E. (2011) On the mechanical stabilization of filopodia. *Biophys. J.* 100, 1428–1437
67. Tamada, A. and Igarashi, M. (2017) Revealing chiral cell motility by 3D Riesz transform-differential interference contrast microscopy and computational kinematic analysis. *Nat. Commun.* 8, 2194
68. Shangguan, J. and Rock, R.S. (2023) Pushed to the edge: hundreds of myosin 10s pack into filopodia and could cause traffic jams on actin. *bioRxiv*, published online May 8, 2024. https://doi.org/10.1101/2023.06.26.546598
69. Wang, F.-S. *et al.* (1996) Function of myosin-V in filopodial extension of neuronal growth cones. *Science* 273, 660–663
70. Sun, Y. *et al.* (2010) Single-molecule stepping and structural dynamics of myosin X. *Nat. Struct. Mol. Biol.* 17, 485–491 ISSN 1545-9985
71. Ali, M.Y. *et al.* (2002) Myosin V is a left-handed spiral motor on the right-handed actin helix. *Nat. Struct. Biol.* 9, 464–467
72. Tamada, A. *et al.* (2010) Autonomous right-screw rotation of growth cone filopodia drives neurite turning. *J. Cell Biol.* 188, 429–441
73. Li, W. *et al.* (2023) Chiral growth of adherent filopodia. *Biophys. J.* 122, 3704–3721
74. Cojoc, D. *et al.* (2007) Properties of the force exerted by filopodia and lamellipodia and the involvement of cytoskeletal components. *PLoS One* 2, e1072
75. Zhang, C. *et al.* (2024) Cytoneme-mediated transport of active Wnt5b–Ror2 complexes in zebrafish. *Nature* 625, 126–133
76. Zhang, W. *et al.* (2023) Curved adhesions mediate cell attachment to soft matrix fibres in three dimensions. *Nat. Cell Biol.* 25, 1453–1464
77. Litschel, T. *et al.* (2021) Reconstitution of contractile actomyosin rings in vesicles. *Nat. Commun.* 12, 2254
78. Blosser, M.C. *et al.* (2016) cDICE method produces giant lipid vesicles under physiological conditions of charged lipids and ionic solutions. *Soft Matter* 12, 7364–7371
79. Ruhoff, V.T. *et al.* (2024) Biological applications of thermoplasmonics. *Nano Lett.* 24, 777–789